ABSTRACT

PETERSON, ELLEN R. Flow of Thin Liquid Films with Surfactant: Analysis, Numerics, and Experiment. (Under the direction of Dr. Michael Shearer.)

When surfactant is deposited on a thin layer of fluid the liquid is instantaneously set into motion. This striking effect is caused by a surface force, the Marangoni force, induced by a surface tension gradient produced by the local presence of surfactant. We investigate the motion of the fluid, and associated spreading of surfactant, in two scenarios: spreading on a horizontal solid substrate, where surface tension is the sole driving force, and on an inclined substrate, where gravity provides an additional force. The governing equations in both cases are derived from the Navier Stokes equations applying the lubrication approximation. The resulting fourth order system of nonlinear PDE consists of two equations: one for the height of the fluid free surface and the other for the distribution of surfactant.

On a horizontal substrate, we introduce a droplet of insoluble surfactant on a film with initially uniform height. Neglecting the physical and smoothing effects of gravity, capillarity, and surface diffusion the development of a numerical method is complicated by the loss of smoothness at the leading edge of surfactant. We address this issue by transforming the spatial variable to a fixed domain and using the jump conditions of the simplified system as boundary conditions. These numerical results are then compared to a known similarity scaling and solution developed by Jensen and Grotberg [34, 35] for the region of the solution near the leading edge of the surfactant. We further this investigation by examining the solution near the center of the droplet. Using a phase plane analysis we determine that a similarity solution does exist for this region of the solution. However, this solution contradicts the behavior observed in the numerical simulations and we turn to an asymptotic analysis to determine the structure of the solution, which does not have self-similarity but agrees with numerical simulations.

We compare the spreading behavior of the thin film and surfactant to the results of an innovative experiment in which the location of the surfactant molecules and the deformation of the free surface of the film are recorded simultaneously. We compare numerical simulations (now including the physical parameters) to experimental results for the location and spreading of the maximum film height and leading edge of surfactant, as well as the shape of the film height and surfactant profiles. We find agreement between the model and experiment for the spreading of both the deformation of the film and the surfactant concentration. While we are able to align the experimental and numerical height profiles, the lack of agreement between experiment and simulations with regard to the surfactant profiles brings into question the model for surfactant distribution.

On an inclined plane, we investigate the stability of a triple-step traveling wave. We use

the dispersion relation of the one-dimensional system (without gravity, capillarity or surface diffusion) to determine that the solution is stable to small perturbations. When these physical effects are included we use the Evans function and stability indicator function to determine the analysis is consistent with the solution being stable. In two dimensions we find the inclusion of surfactant merely introduces a smoothing effect which results in the stability determined by properties of the height equation, analogous to the work of Bertozzi and Brenner [6].

Finally, we explore the spreading behavior of a droplet of surfactant placed on an initially uniform film on an inclined plane. The film develops into two waves and we examine the dynamics of this spreading.

Flow of Thin Liquid Films with Surfactant: Analysis, Numerics, and Experiment

by
Ellen R. Peterson

A dissertation submitted to the Graduate Faculty of
North Carolina State University
in partial fulfillment of the
requirements for the Degree of
Doctor of Philosophy

Applied Mathematics

Raleigh, North Carolina

2010

APPROVED BY:

_____   _____
Dr. Alina Chertock   Dr. Karen E. Daniels

_____   _____
Dr. Mansoor A. Haider   Dr. Michael Shearer
                                                     Chair of Advisory Committee

BIOGRAPHY

Ellen Peterson hails from Ada, Ohio a small farming community in rural northwestern Ohio. While growing up, she thrived on involvement in various activities ranging from music to sports to leadership roles. These opportunities and the ability to balance and multitask numerous responsibilities are a cornerstone of her being. A small university in Ada complemented the small town experience to develop a spirit full of ambition, enthusiasm, and determination.

The benefits of a closely-knit community were always apparent to Ellen. When choosing a college she was determined to find a place that could challenge her but also provide the essential support network that she had come to rely on. She found the perfect combination at Wittenberg University where she earned a Bachelor of Science in Mathematics. While she loved every minute spent on campus, she quickly realized that her full potential could not be reached if she relied solely on the opportunities available at this small school. The summer after her junior year of college she participated in a REU at the University of Nebraska-Lincoln. This experience exposed her for the first time to the challenge, rigor, and excitement of research. She returned to Wittenberg in the fall with a new drive and a resolution to continue onto graduate school. Without complete understanding of the nature of the subject, she decided to pursue an advanced degree in applied mathematics.

In search of an adventure, she enrolled in North Carolina State University to pursue her Ph.D. Ellen blossomed during her time at NC State. She developed a true love of research but also, through the Preparing the Professoriate Program, realized a desire to encourage young students both in and outside of the classroom.

In the fall, Ellen will cultivate both her love of research and teaching during a post-doc at Carnegie Mellon University. She will always recognize the influence of the encouragement and support she has experienced throughout her development and will strive to offer this inspiration to future students.

ACKNOWLEDGEMENTS

TABLE OF CONTENTS

LIST OF TABLES

LIST OF FIGURES

xi

Chapter 1

Introduction

The modern theory of the dynamics of fluids begins in the early nineteenth century, around 1822, the time of Navier's formulation of what is now called the Navier-Stokes equations. These equations describe the flow of viscous fluids. While Navier is credited with the original derivation, this derivation failed to recognize the full importance of viscosity. In 1845, Stokes published a derivation which is most commonly used today. While Navier and Stokes assume a majority of the credit for the creation of this model, Euler, Cauchy, Poisson, and Barre de Saint-Venant all contributed to the development of the Navier-Stokes equations [1].

One interesting property of fluids is the attraction that occurs between the molecules at interfaces. This attraction is known as capillarity and helps explain why fluid travels up a small tube and wine fingers down the side of a wine glass. Thomson observed this phenomenon as part of his investigation into the behavior of wine [76]. He introduced wine into a layer of water and observed that the water moved away from the area in which wine was introduced and in some cases even began to climb up the sides of the glass. Thomson hypothesized that the surface tension of the fluid was what induced the movement of the film [76]. This began the study of surface tension as a driving force for liquids. Marangoni further investigated the effects of surface tension; surface stresses are now commonly referred to as Marangoni forces [52]. Pockels and Rayleigh also contributed to the early understanding of the effects of surface tension and how contamination of a fluid alters the flow of a liquid [61].

Reynolds performed various experiments to examine the flow of fluid in a tube. The goal of the experiments was to determine the relation between the velocity and pressure of the flow and the viscosity, temperature of the fluid, and the diameter of the tube. These investigations resulted in a grouping of parameters into what we now call the Reynolds number

$$Re = \frac{UL}{\nu},\tag{1.0.1}$$

where U is the mean velocity of the fluid, L is a characteristic length scale (diameter of the tube in Reynolds' experiments) and ν is the kinematic viscosity of the fluid [66]. Fluids with high Reynolds number ($Re \gg 1$) are generally unstable and exhibit turbulence. We will focus on flows with low Reynolds number which correspond to very viscous fluids, very slow flow, or very small length scale.

Although the behavior of fluids has been a focus of research since the mid-1800's, there are still many open questions, including the global existence and smoothness of solutions of the Navier-Stokes equations, one of the Millennium Prize Problems of the Clay Mathematics Institute.

1.1 Thin Films

The applications of thin fluid films range from physical behavior such as rain drops on a window to coating flows to film condensation which is used in refrigerators and air conditioners [57]. The complex behavior of fluids is also exhibited in painting; the paint is not deposited in a uniform layer but rather brush strokes may be present. The fluid then levels due to the surface tension [58, 72].

These thin layers of liquid satisfy the lubrication approximation which simplifies the Navier-Stokes equations. The lubrication approximation is applicable when the characteristic height scale H, the depth of the fluid, is much smaller than the length scale L, of its lateral extent ($\frac{H}{L} \ll 1$). For example, the spreading of a droplet is driven by capillary forces and the height of the free surface of the droplet $h = h(x, t)$ is governed by the generalized lubrication equation

$$h_t + \nabla \cdot (h^3 \nabla \Delta h) = 0. \tag{1.1.1}$$

Tanner's Law [75] uses properties of the contact angle to estimate the spreading of a droplet when capillarity is the main driving force. Brenner and Bertozzi [12] determined a class of similarity solutions and found that the solutions were linearly stable to perturbations away from the *contact line*, the interface between solid, liquid, and gas. Bernoff and Witelski [4] used a spectral analysis to estimate the rate of convergence of a droplet to the similarity solution.

An unresolved issue is the evolution of the contact line of the film. Most commonly the no-slip boundary condition is used at the liquid-solid interface; this relation states that the fluid velocity at the interface is zero. However, a paradox at the contact line is introduced: if the velocity at the liquid-solid interface is zero then the fluid would not be able to advance. Bertozzi [5] discusses this paradox. While this is an interesting obstacle in thin films research, we are not concerned with the behavior of the contact line in this dissertation. Instead, we work on a thin liquid layer and introduce a precursor layer when necessary so that the solid/liquid/air

interface at a contact line is not relevant.

1.2 Driven Thin Fluid Films

The introduction of driving forces creates more interesting dynamics pertaining to the behavior of a thin layer of fluid. The review articles [18, 59] outline the various areas of thin film research, which include the evaporation and condensation of films and films driven by forces such as gravity and a surface tension gradient. Our investigation focuses on the evolution of a thin film driven by surfactant both on a horizontal substrate and on an inclined plane. We only consider the effects of insoluble surfactant; research pertaining to soluble surfactant can be found in [23, 36, 80].

A surfactant lowers the surface tension of a fluid causing the film to be propelled away from the region where the surfactant was introduced. Surfactants perform an array of roles which range from a crucial ingredient in soaps to surfactant replacement therapy, a treatment for premature babies [25, 55]. Another application relevant to thin film research is the tear film on the eye. Break-up of the tear film, which is believed to be a large contributor to dry eye syndrome, is modeled in [11, 30, 50], with comparison to experiments in [43]. The experimental results suggest that there is a lipid layer (thin layer of surfactant) present on the surface of the tear film which is believed to deter the evaporation of the tear film thus reducing film break-up [42].

In this section, we outline the effects of gravity, temperature gradient and surfactant on a thin layer. Combining these effects causes interesting behavior through the competition of forces.

1.2.1 Films Driven by Gravity

A thin layer of fluid traveling down an inclined plane is known to develop a fingering instability [33]. An initially uniform front develops into a series of waves which then propagate at different speeds. Huppert postulated that the wavelength of the fingers at the front of the film was determined by the surface tension [33]. Jerrett and de Bruyn further investigated this behavior by experimentally examining the fingering patterns that developed when the substrate was fixed at different angles of inclination [38]. The corresponding analytical investigation by Bertozzi and Brenner [6] determined that there exists a critical angle below which the film is linearly stable. However, experimental results still exhibited the development of fingers below this critical angle. Bertozzi and Brenner explained the role of transient growth and nonlinearity in generating this instability.

1.2.2 Films Driven by Gravity and a Temperature Gradient

Experiments by Ludviksson and Lightfoot [49] presented surprising results in which a thin fluid climbed out of a heated reservoir of liquid and up a wall due to a temperature gradient which induced a change in surface tension. A *capillary ridge*, a build up of fluid, formed at the leading edge of the film. This observation ignited an interest in the influence of a gradient in the surface tension as a driving force on a film. Not surprisingly, as in the case where fluid travels down an inclined plane, fluid climbing up a plane also develops a fingering instability, as observed in experiments by Cazabat et al. [14].

A natural resulting question was, could the gravity and temperature gradient effects be balanced? Schneemilch and Cazabat [68] searched for this balance and determined that there in fact exists a threshold relating the inclination angle and temperature gradient in which fingering does not occur. Instead of fingering, a more pronounced capillary ridge develops at the leading edge of the film. The development of this ridge is explained mathematically by Bertozzi and Shearer and co-workers in [7, 8, 56] through under-compressive shocks. The main feature of this form of a shock is that characteristics enter the shock from one side and leave from the other. This behavior causes the capillary ridge to widen as more fluid is drawn into it. These concepts and others were then confirmed with experimental results in [74].

These investigations showed that while gravity driven films generally exhibit unstable behavior, the inclusion of a driving force can stabilize the film. In this case, the additional driving force was a surface tension gradient in the form of a temperature gradient. This observation raises numerous questions: Can surface tension gradients be generated in ways other than a temperature gradient? Do all surface tension gradients impose a stabilizing effect? Is stability only achieved when the gravitational and Marangoni forces are in competition?

1.2.3 Films Driven by Gravity and Surfactant

In previous studies, experimental results provided an initial indication for the behavior of the thin film. However, the development of an experiment to explore the evolution of a thin film driven by both gravity and surfactant is difficult. The restricting factor is the deposition and observation of the surfactant on the film. Hence, in this case the main results are achieved through numerical experiments.

Edmonstone, Matar, and Craster initiated a numerical investigation of the stability of a thin film driven by both gravity and surfactant. By varying the angle of inclination of the substrate, they were able to separate the effects of gravity and surfactant on the evolution of the film [24]. The presence of surfactant actually enhances the instabilities inherent to flow on an inclined plane [21, 22, 24]. This result suggests that the stabilizing effect observed as a film climbs up an incline, when both gravity and a temperature gradient are present, is actually from the

competition of the forces. However, when fluid travels down an incline, gravity and surfactant are working in the same direction which causes the fingering instability to be enhanced.

The numerical simulations in [24] exhibit a traveling wave solution with interesting characteristics. The structure of the solution was characterized in [47]. The solution for the height equation is a three step piecewise constant solution which is related to a piecewise linear solution for the surfactant concentration. The structure of the solution is further examined in [48]. In Chapter 6, we perform a stability analysis on this traveling wave solution.

1.2.4 Films Driven by Surfactant

The governing system of partial differential equations (PDE) for the evolution of the film height and surfactant concentration was first derived by Gaver and Grotberg in [29]. The equations include a convective term that is dependent on the local surface tension. This influence is incorporated through an equation of state which connects the surface tension of the film to the surfactant concentration in both the equation for the height of the film and the equation for the surfactant concentration. Additional influences such as gravity and capillarity are also included in the equations. The effect of surface diffusion of the surfactant molecules is incorporated in the equation for the surfactant concentration. We present the derivation of this system in Chapter 2.

Jensen and co-workers considered various geometries for the spreading of surfactant on a thin fluid layer, including a droplet, a planar strip, and a spreading front. In the case where the diffusive, gravitational, and capillary forces are weak, a similarity scaling was determined [35]. Corresponding similarity solutions were found in [34]. We consider only the spreading of a droplet of surfactant. In this context, the similarity scaling and solution are only relevant near the edge of the droplet. In Chapter 4, we numerically investigate the similarity scaling and solution suggested by Jensen in [34] and extend the analysis to determine a solution for the region near the center of the droplet.

The dynamics of the surfactant induced spreading film have been the subject of numerous experiments. Ahmad and Hansen [2] compared a stress balance model to experimental results for spreading of oleic acid on glycerin. The spreading was visualized by the displacement of talc particles that were dusted on the surface. Despite the simplifications implemented in the model, the observed behavior still agreed with the prediction. However, the model derived by Gaver and Grotberg and the analysis by Jensen contradict the spreading behavior predicted in the early investigations of Ahmad and Hansen [2], as well as Joos and Pintens [39]. Gaver and Grotberg tracked the spreading of oleic acid on glycerin using dyed markers. This investigation revealed that the deformation of the free surface occurs ahead of disturbance of the leading edge of the surfactant [28].

Most previous experiments were designed to visualize the disturbance of the underlying film, leaving the location of the surfactant molecules to be inferred. However, Bull et al. [13] developed an experimental procedure to track the location of the surfactant molecules. A layer of glycerin was deposited in a clear glass petri dish with distance markers on the bottom in order to visualize the disturbance of the film. Fluorescent surfactant was deposited in a constraining ring and a less densely packed surfactant outside of the ring. When the ring was lifted, the location of the surfactant molecules was observed by exciting the fluorescence with a laser line. This provided an important advance in the study of spreading of surfactant on thin films, the ability to track the location of the surfactant. We further develop this technique as described in Chapter 5.

The shape of the height profile was obtained by Dussaud et. al. [20], differing from other experiments which only tracked the deformation of the free surface. The profiles were obtained using an optical device known as Moiré topography that tracks the slope of the thin film surface after a droplet of oleic acid is deposited on a layer of glycerin. There was agreement between the experimental height profile and that predicted by the mathematical model if the model included a preexisting layer of surfactant on the film.

These studies and the work we present in this dissertation, consider a thin film with thickness of the order of millimeters. For thinner films, on the order of micrometers, fingering instabilities develop and the film dewets. The stability of the film is directly related to the thickness; thicker films are more stable [7]. The development of fingers is also observed in [53, 78, 77, 37]. We do not address this issue in this dissertation.

1.3   Organization of the Dissertation

This dissertation focuses on thin liquid films driven by insoluble surfactant. In Chapters 3-5, we consider the evolution of a film on a horizontal substrate when surfactant is introduced to the surface. The film will be driven away from the region where the surfactant is deposited due to the change in surface tension. In Chapter 6 we also include the driving force of gravity when the thin film is on an incline.

To lay the foundation for the subsequent chapters, the derivation of the system modeling the evolution of the film height and surfactant concentration is presented in Chapter 2. This system is based on the Navier-Stokes equations using the lubrication approximation and was first developed by Gaver and Grotberg [29]. We will be considering a fluid on both a horizontal substrate and an inclined plane, thus we present the corresponding equations in this chapter.

In Chapter 3, we outline a numerical method used to better understand the basic structure of the modeling equations. If we ignore the effects of gravity, capillarity and surface diffusion, the system is vastly simplified. This simplification allows for analysis of the system which

we would like to compare to numerical results. However, without the smoothing influences of the physical parameters, the solution for the surfactant concentration develops a corner which initiates a shock in the height profile. To capture these singular solutions numerically requires innovative techniques. We present a method in which computations are performed on a fixed domain and use jump conditions as boundary conditions. This tactic reduces computational time and improves the numerical results.

In Chapter 4, we compare the numerical results mentioned above to a similarity scaling and solution discovered by Jensen [35, 36]. However, solutions are only known for the region near the leading edge of the surfactant. Near the center of the droplet, the solution departs from the known solution in order to satisfy the boundary conditions. We show that while a similarity solution exists in this center region, the numerical solution in fact converges to a function that is not self-similar.

In Chapter 5, we examine the extent to which the model captures the behavior observed in an experiment. The novelty of this experiment is that we are able to visualize the disturbance in the height of the film and the location of the surfactant molecules simultaneously. We vary the constitutive information in the model, including the equation of state, the initial conditions and the influence from gravity, capillarity, and surface diffusion in order to align the numerical and experimental results. We find that while the experimental spreading rate of the surfactant can be captured by the model, the model does not accurately represent the distribution of surfactant.

In Chapter 6, we consider the flow of a thin film down an incline driven by both gravity and surfactant. We perform a stability analysis for the traveling wave solution presented in [48]. We use the dispersion relation to determine that the solution of the one dimensional system, without the effects of gravity, capillarity, and surface diffusion, is stable. When considering the system in both one and two-dimensions, we linearize about the traveling wave solution for the height and the trivial solution for the surfactant concentration. We use the Evans function to determine that the solution for the one dimensional system is stable. In two dimensions, the stability is actually independent of the surfactant but depends on the size of the capillary ridge which corresponds to the analysis in [6].

Chapter 2

Thin Film Equations

In this chapter, we derive a system of nonlinear partial differential equations that governs the motion of a thin liquid film with surfactant. The system includes an equation for the height of the film and an equation for the concentration of insoluble surfactant which resides on the free surface of the film. Variations in the surfactant concentration induce surface tension gradients which drive the fluid motion.

The derivation of the equations is based on a series of assumptions. The central assumptions are:

(A) The assumption that the flow is slow. Specifically, the Reynolds number is assumed to be small enough that the inertial effects can be ignored. This results in the Navier-Stokes equations being reduced to the Stokes equations.

(B) The assumption that the fluid layer is thin. Specifically, we assume that the height of the fluid free surface is small compared to the horizontal extent of the fluid. This is the heart of lubrication theory. In this case, the Stokes equations are simplified to such an extent that the system can be analytically integrated. As a result, we obtain an expression for the horizontal velocity that is used to complete the derivation.

2.1   Derivation of the Height Equation

In general, a film can spread in three directions, (x, y, z); thus the three-dimensional velocity vector is

$$\vec{u} = (u(x, y, z, t), v(x, y, z, t), w(x, y, z, t)) \, .$$

For simplification, we derive the system of equations in two dimensions. The derivation in three dimensions is analogous and the resulting equations are written at the end of this chapter. We

8

reduce to two dimensions by assuming the flow is independent of y. Thus the velocity in the y direction is also negligible which reduces the velocity components to

$$u = u(x, z, t), \qquad v = 0, \qquad w = w(x, z, t).$$

2.1.1 Navier-Stokes Equations

With the two dimensional assumptions, the Navier-Stokes equations reduce to a system of two equations and the incompressibility condition

$$\rho(u_t + uu_x + wu_z) = -p_x + \mu(u_{xx} + u_{zz}) + \rho g \sin\alpha \qquad (2.1.1a)$$
$$\rho(w_t + uw_x + ww_z) = -p_z + \mu(w_{xx} + w_{zz}) - \rho g \cos\alpha \qquad (2.1.1b)$$
$$u_x + w_z = 0 \qquad (2.1.1c)$$

where ρ is the density, μ is the viscosity, g is gravity, and α is the angle of incline of the substrate. The effect of gravity is split into two components. The force acting perpendicular to the substrate (in the z direction) is $\rho g_{perp} = \rho g \cos\alpha$ and the force acting tangent to the substrate (in the x direction) is $\rho g_{tan} = \rho g \sin\alpha$. The unknowns in (2.1.1) are velocity (u, w) and pressure $p(x, z, t)$.

In order to determine the leading order terms in (2.1.1), we define the scalings

$$L: \text{length scale in the } x \text{ direction}$$
$$H: \text{length scale in the } z \text{ direction}$$
$$U: \text{velocity scale in the } x \text{ direction}$$
$$W: \text{velocity scale in the } z \text{ direction}$$
$$T: \text{time scale.}$$

2.1.2 Lubrication Approximation

From non-dimensionalization of the Navier-Stokes equations, we know the Reynolds number is $Re = \frac{\rho LU}{\mu}$. Invoking assumption **(A)**, the inertial terms of the Navier-Stokes equations (2.1.1) can be neglected which results in the Stokes equations:

$$-p_x + \mu(u_{xx} + u_{zz}) + \rho g \sin\alpha = 0 \qquad (2.1.2a)$$
$$-p_z + \mu(w_{xx} + w_{zz}) - \rho g \cos\alpha = 0 \qquad (2.1.2b)$$
$$u_x + w_z = 0. \qquad (2.1.2c)$$

Incorporating the scalings

$$x = L\hat{x}, \qquad z = H\hat{z}, \qquad u = U\hat{u}, \qquad t = T\hat{t} \tag{2.1.3}$$

into (2.1.2c) we find

$$\frac{U}{L}\hat{u}_{\hat{x}} + \frac{1}{H}w_{\hat{z}} = 0. \tag{2.1.4}$$

The requirement to be considered a thin film is $\frac{H}{L} \ll 1$ (assumption (**B**)); define $\varepsilon = \frac{H}{L}$ to be a small parameter. Balancing the terms in (2.1.4) and applying the thin film assumption defines

$$w = \frac{HU}{L}\hat{w} = \varepsilon U\hat{w}.$$

Implementing the scalings into (2.1.2a)

$$\mu\left(\frac{U}{L^2}\hat{u}_{\hat{x}\hat{x}} + \frac{U}{H^2}\hat{u}_{\hat{z}\hat{z}}\right) + \rho g \sin\alpha = \frac{1}{L}p_{\hat{x}}$$

and multiplying through by H^2 results in

$$\mu(\varepsilon^2 U\hat{u}_{\hat{x}\hat{x}} + U\hat{u}_{\hat{z}\hat{z}}) + H^2\rho g \sin\alpha = \varepsilon H p_{\hat{x}}. \tag{2.1.5}$$

Similarly for (2.1.2b)

$$\mu(\varepsilon^3 U\hat{w}_{\hat{x}\hat{x}} + \varepsilon U\hat{w}_{\hat{z}\hat{z}}) - H^2\rho g \cos\alpha = H p_{\hat{z}}. \tag{2.1.6}$$

Next, we introduce a scaling for the pressure $p = P_0\hat{p}$. Balancing the leading order terms in (2.1.5) so that $P_0\varepsilon H \sim \mu U \geq H^2\rho g$, determines $P_0 = \frac{\mu U}{\varepsilon H}$. Implementing this scaling into (2.1.6) generates

$$\mu(\varepsilon^3 U\hat{w}_{\hat{x}\hat{x}} + \varepsilon U\hat{w}_{\hat{z}\hat{z}}) - H^2\rho g \cos\alpha = \frac{\mu U}{\varepsilon}\hat{p}_{\hat{z}}. \tag{2.1.7}$$

Thus the first two terms are obviously of higher order than the other terms. We retain the last two terms in order to incorporate the effects of the normal component of gravity. These simplifications result in the reduced Stokes equations, returning to dimensional variables

$$p_x = \mu u_{zz} + \rho g \sin\alpha \tag{2.1.8a}$$
$$p_z = -\rho g \cos\alpha \tag{2.1.8b}$$

in which u, p are the unknowns. Since the location of the surface of the film is also unknown, we have a third variable $z = h(x, t)$ for the height of the free surface.

2.1.3 Boundary Conditions

Normal Stress Boundary Condition

The force on the film from the atmosphere must be balanced with the pressure from the film at the interface $z = h(x, t)$. This balance occurs through surface tension, which is expressed as

$$p - p_{atm} = -\gamma \bar{\kappa}$$

where p_{atm} is the atmospheric pressure, γ is the surface tension of the thin film, and $\bar{\kappa}$ is the curvature of the film,

$$\bar{\kappa} = \frac{h_{xx}}{(1 + h_x^2)^{\frac{3}{2}}} = h_{xx} \left(1 - \frac{3}{2} h_x^2 + \dots \right).$$

Since $h_x \sim \frac{H}{L} \ll 1$ the boundary condition simplifies to (ignoring higher order terms)

$$p - p_{atm} = -\gamma h_{xx} \qquad \text{at } z = h(x, t). \tag{2.1.9}$$

Tangential Stress Boundary Condition

The change in surface tension induced by the insoluble surfactant creates a stress on the surface of the film. The relation of the surface tension σ to the surfactant concentration Γ is modeled through the equation of state, $\sigma = \sigma(\Gamma)$. In this chapter, we will use this general form of the equation of state. In Chapter 4 we use a linear equation of state and in §5.8 we examine the influence of different choices of the equation of state on the solution.

A change in surface tension drives the film with a surface stress acting tangentially to the film. The film moves from areas of high surface tension to low due to the Marangoni forces. In the lubrication approximation, the tangent plane is horizontal to leading order, since $h_x \sim \frac{H}{L} = \varepsilon \ll 1$. Consequently, the unit tangent $\hat{t}$ in the x-direction is $(1, 0, 0)$, and the normal $\hat{n}$ to the free surface is vertical: $\hat{n} = (0, 0, 1)$. Thus, the surface tension gradient is coupled to the shear component of stress through a stress tensor, $\mathcal{T} = \mathcal{T}_{ij} - pI + 2\mu\mathcal{D}$ [17] by

$$\frac{d}{dx}\sigma(\Gamma) = \hat{t}.\mathcal{T}.\hat{n} = \mathcal{T}_{13} = 2\mu\mathcal{D}_{13}$$

where the strain rate tensor, $\mathcal{D}$, is

$$\mathcal{D} \;=\; \begin{pmatrix} \frac{\partial u}{\partial x} & \frac{1}{2}\left(\frac{\partial u}{\partial y} + \frac{\partial v}{\partial x}\right) & \frac{1}{2}\left(\frac{\partial u}{\partial z} + \frac{\partial w}{\partial x}\right) \\[4pt] \frac{1}{2}\left(\frac{\partial v}{\partial x} + \frac{\partial u}{\partial y}\right) & \frac{\partial v}{\partial y} & \frac{1}{2}\left(\frac{\partial v}{\partial z} + \frac{\partial w}{\partial y}\right) \\[4pt] \frac{1}{2}\left(\frac{\partial w}{\partial x} + \frac{\partial u}{\partial z}\right) & \frac{1}{2}\left(\frac{\partial w}{\partial y} + \frac{\partial v}{\partial z}\right) & \frac{\partial w}{\partial z} \end{pmatrix}.$$

For two dimensional flow, $v = 0$ and $u_y = 0$, so $\mathcal{D}$ reduces to

$$\mathcal{D} = \begin{pmatrix} u_x & 0 & \frac{1}{2}(u_z + w_x) \\[4pt] 0 & 0 & 0 \\[4pt] \frac{1}{2}(w_x + u_z) & 0 & w_z \end{pmatrix}.$$

Thus

$$\mathcal{D}_{13} = \tfrac{1}{2}(u_z + w_x) \sim \tfrac{1}{2}u_z$$

since $w_x \sim \frac{\varepsilon U}{L} \ll u_z \sim \frac{U}{H}$. The tangential stress boundary condition is

$$\frac{\partial}{\partial x}\sigma(\Gamma) = \mu u_z \qquad \text{at } z = h(x,t). \tag{2.1.10}$$

No-slip Boundary Condition

We are considering the solid substrate at $z = 0$ to be at rest, so the no-slip boundary condition is simply

$$u = 0 \qquad \text{at } z = 0. \tag{2.1.11}$$

Note in order to recover $w(x,t)$ from the incompressibility condition (2.1.2c), we would also need $w = 0$ at $z = 0$.

2.1.4   Integrating the PDE

Integrating (2.1.8) and applying the boundary conditions (2.1.9-2.1.11) we derive the dimensional thin film equation. First we integrate (2.1.8b) with respect to z over the thickness of the film $0 \le z \le h(x,t)$ and apply the normal stress boundary condition (2.1.9) to determine

$$p = \rho g \cos\alpha(h - z) + p_{atm} - \gamma h_{xx}.$$

12

Differentiating with respect to x,

$$p_x = \rho g h_x \cos\alpha - \gamma h_{xxx}. \tag{2.1.12}$$

But (2.1.8a) is an equation for p_x, ergo we relate (2.1.8a) and (2.1.12)

$$\mu u_{zz} = \rho g h_x \cos\alpha - \gamma h_{xxx} - \rho g \sin\alpha. \tag{2.1.13}$$

Since h is independent of z, we integrate (2.1.13) and apply the tangential stress boundary condition (2.1.10)

$$\mu u_z = (\rho g h_x \cos\alpha - \gamma h_{xxx} - \rho g \sin\alpha)(z - h) + \sigma_x. \tag{2.1.14}$$

Integrating again and applying the no-slip boundary condition (2.1.11) we determine the velocity in the x direction

$$u = \frac{1}{\mu}\left[(\rho g h_x \cos\alpha - \gamma h_{xxx} - \rho g \sin\alpha)(\tfrac{1}{2}z^2 - hz) + \sigma_x z\right]. \tag{2.1.15}$$

Note that the velocity u has a parabolic profile.

2.1.5 Depth-averaged Velocity

We depth-average the velocity u over the thickness of the film. Let $\bar{u}$ denote the average velocity. Then using (2.1.15) we determine

$$
\begin{aligned}
\bar{u} = \frac{1}{h}\int_0^h u\,dz &= \frac{1}{h\mu}\left[(\rho g h_x \cos\alpha - \gamma h_{xxx} - \rho g \sin\alpha)\left(\tfrac{1}{6}z^3 - \tfrac{1}{2}hz^2\right) + \tfrac{1}{2}\sigma_x z^2\right]_0^h \\
&= \frac{1}{h\mu}\left[(\rho g h_x \cos\alpha - \gamma h_{xxx} - \rho g \sin\alpha)\left(\tfrac{1}{6}h^3 - \tfrac{1}{2}h^3\right) + \tfrac{1}{2}\sigma_x h^2\right] \\
&= \frac{1}{h\mu}\left[(\gamma h_{xxx} - \rho g h_x \cos\alpha + \rho g \sin\alpha)\tfrac{1}{3}h^3 + \tfrac{1}{2}\sigma_x h^2\right]. \tag{2.1.16}
\end{aligned}
$$

2.1.6 Conservation of Mass

The change in the height of the film is governed by the flow of the fluid beneath the free surface. Consider an interval (a,b) of fluid. Then

$$\frac{d}{dt}\int_a^b h(x,t)\,dx = F_a - F_b \tag{2.1.17}$$

where F represents the flux at point a and b respectively. Using the depth-averaged velocity we determine the fluxes

$$F_a = h\bar{u}|_{x=a}, \qquad F_b = h\bar{u}|_{x=b}. \tag{2.1.18}$$

Thus the conservation of mass in the region (a, b) is expressed as (since ρ is constant)

$$\int_a^b \frac{\partial h}{\partial t} dx = -\int_a^b \frac{\partial}{\partial x}(h\bar{u}) dx. \tag{2.1.19}$$

Since the interval (a, b) is arbitrary, this equation simplifies to

$$\frac{\partial h}{\partial t} + \frac{\partial}{\partial x}(h\bar{u}) = 0. \tag{2.1.20}$$

Finally, implementing the depth-averaged velocity (2.1.16) in (2.1.20) results in the dimensional thin film equation

$$h_t + \frac{\rho g \sin \alpha}{\mu} \left(\tfrac{1}{3}h^3\right)_x + \frac{1}{\mu}\left(\tfrac{1}{2}\sigma_x h^2\right)_x = \frac{\rho g \cos \alpha}{\mu}\left(\tfrac{1}{3}h^3 h_x\right)_x - \frac{\gamma}{\mu}\left(\tfrac{1}{3}h^3 h_{xxx}\right)_x. \tag{2.1.21}$$

2.1.7 Conservation of Surfactant

The derivation of the equation modeling the evolution of the surfactant concentration Γ also relies on the property of conservation of mass. Consider a slice of the fluid (a, b) then

$$\frac{d}{dt}\int_a^b \Gamma(x, t) dx = F_a^\Gamma - F_b^\Gamma \tag{2.1.22}$$

where F^Γ represents the flux of surfactant at points a and b respectively. Since the surfactant is insoluble, we know it will travel at the surface velocity of the fluid, $u_h = u(h, t)$ given by (2.1.15):

$$u_h = \frac{1}{\mu}\left[\tfrac{1}{2}h^2\left(\gamma h_{xxx} - \rho g h_x \cos \alpha + \rho g \sin \alpha\right) + \sigma_x h\right]. \tag{2.1.23}$$

However, surface diffusion also affects the flux. Fick's Law states that the molecules will move from a region of high concentration to low with a flux proportional to the concentration gradient. The flux is then defined as

$$F_a^\Gamma = \Gamma u_h - D\Gamma_x|_{x=a}, \qquad F_a^\Gamma = \Gamma u_h - D\Gamma_x|_{x=b}$$

where D is a diffusion constant. Since (a, b) is an arbitrary interval, the surfactant equation is

$$\Gamma_t + (\Gamma u_h)_x = D\Gamma_{xx}. \tag{2.1.24}$$

Incorporating u_h from (2.1.23), the dimensional equation for the evolution of the surfactant concentration is

$$\Gamma_t + \frac{\rho g \sin \alpha}{\mu}\left(\tfrac{1}{2}h^2\Gamma\right)_x + \frac{1}{\mu}\left(h\Gamma\sigma_x\right)_x = \frac{\rho g \cos \alpha}{\mu}\left(\tfrac{1}{2}h^2\Gamma h_x\right)_x - \frac{\gamma}{\mu}\left(\tfrac{1}{2}h^2\Gamma h_{xxx}\right)_x + D\Gamma_{xx}. \tag{2.1.25}$$

A full derivation of the advection diffusion equation for surfactant transport can be found in [73].

2.1.8 Non-dimensionalization

In order to non-dimensionalize, we must first stipulate the physical problem we are considering. In Chapters 3-5, we consider a thin film spreading on a horizontal substrate, corresponding to $\alpha = 0$. In Chapter 6, we consider a film traveling down an inclined plane, corresponding to $\alpha > 0$. Below we address the non-dimensionalization of these two cases separately because the resulting non-dimensional parameters are dependent on α.

Horizontal Substrate: $\alpha = 0$

When $\alpha = 0$ the system of equations reduces to

$$h_t + \frac{1}{\mu}\left(\tfrac{1}{2}\sigma_x h^2\right)_x = \frac{\rho g}{\mu}\left(\tfrac{1}{3}h^3 h_x\right)_x - \frac{\gamma}{\mu}\left(\tfrac{1}{3}h^3 h_{xxx}\right)_x \tag{2.1.26a}$$

$$\Gamma_t + \frac{1}{\mu}\left(h\Gamma\sigma_x\right)_x = \frac{\rho g}{\mu}\left(\tfrac{1}{2}h^2\Gamma h_x\right)_x - \frac{\gamma}{\mu}\left(\tfrac{1}{2}h^2\Gamma h_{xxx}\right)_x + D\Gamma_{xx}. \tag{2.1.26b}$$

Consider the scalings

$$x = L\hat{x}, \qquad \Gamma = \Gamma_m\hat{\Gamma}, \qquad t = T\hat{t}, \qquad z = H\hat{z}, \qquad \sigma = S\hat{\sigma} \tag{2.1.27}$$

where Γ_m is the concentration of a saturated monolayer of surfactant and S is the difference in the surface tension of the fluid without surfactant and the minimum surface tension of the underlying fluid. We consider the vertical direction z to represent the height of the film h which transforms the scaling $z = H\hat{z}$, to $h = H\hat{h}$. Implementing these scalings into (2.1.26) results in

$$\frac{H}{T}\hat{h}_{\hat{t}} \quad + \quad \frac{1}{\mu}\frac{SH^2}{L^2}\left(\tfrac{1}{2}\hat{h}^2\hat{\sigma}_{\hat{x}}\right)_{\hat{x}} = \frac{\rho g}{\mu}\frac{H^4}{L^2}\left(\tfrac{1}{3}\hat{h}^3\hat{h}_{\hat{x}}\right)_{\hat{x}} - \frac{\gamma}{\mu}\frac{H^4}{L^4}\left(\tfrac{1}{3}\hat{h}^3\hat{h}_{\hat{x}\hat{x}\hat{x}}\right)_{\hat{x}} \qquad (2.1.28a)$$

$$\frac{\Gamma_m}{T}\hat{\Gamma}_{\hat{t}} \quad + \quad \frac{1}{\mu}\frac{SH\Gamma_m}{L^2}\left(\hat{h}\hat{\Gamma}\hat{\sigma}_{\hat{x}}\right)_{\hat{x}}$$

$$= \quad \frac{\rho g}{\mu}\frac{H^3\Gamma_m}{L^2}\left(\tfrac{1}{2}\hat{h}^2\hat{\Gamma}\hat{h}_{\hat{x}}\right)_{\hat{x}} - \frac{\gamma}{\mu}\frac{H^3\Gamma_m}{L^4}\left(\tfrac{1}{2}\hat{h}^2\hat{\Gamma}\hat{h}_{\hat{x}\hat{x}\hat{x}}\right)_{\hat{x}} + \frac{D\Gamma_m}{L^2}\hat{\Gamma}_{\hat{x}\hat{x}} \qquad (2.1.28b)$$

The time scale T is set by balancing the coefficients of the advective terms of the height equation (2.1.28a)

$$\frac{H}{T} = \frac{1}{\mu}\frac{SH^2}{L^2} \qquad \text{which implies} \qquad T = \frac{\mu L^2}{SH}. \qquad (2.1.29)$$

Note this same balance applies in (2.1.28b). Multiplying (2.1.28) by $\frac{\mu L^2}{SH^2}$ results in the non-dimensional equations, dropping the $\hat{\ }$

$$h_t + \left(\tfrac{1}{2}h^2\sigma_x\right)_x = \beta\left(\tfrac{1}{3}h^3h_x\right)_x - \kappa\left(\tfrac{1}{3}h^3h_{xxx}\right)_x \qquad (2.1.30a)$$

$$\Gamma_t + (h\Gamma\sigma_x)_x = \beta\left(\tfrac{1}{2}h^2\Gamma h_x\right)_x - \kappa\left(\tfrac{1}{2}h^2\Gamma h_{xxx}\right)_x + \delta\Gamma_{xx} \qquad (2.1.30b)$$

where $\beta = \frac{\rho g H^2}{S}$ balances gravity and Marangoni forces, $\kappa = \frac{\gamma H^2}{SL^2}$ is the ratio of capillary driving forces to the forces from the surface-tension gradient, and $\delta = \frac{1}{Pe} = \frac{\mu D}{SH}$, where Pe is the Peclet number. This parameter is the ratio of convection to surface diffusion of the surfactant.

The equation for the height of the film incorporating flow in the y-direction is derived in [19]. Following this derivation, the system of equations for the height of the film and the surfactant concentration in two-dimensions is

$$h_t + \nabla.\left(\tfrac{1}{2}h^2\nabla\sigma(\Gamma)\right) = \beta\nabla.\left(\tfrac{1}{3}h^3\nabla h\right) - \kappa\nabla.\left(\tfrac{1}{3}h^3\nabla\Delta h\right) \qquad (2.1.31a)$$

$$\Gamma_t + \nabla.\left(h\Gamma\nabla\sigma(\Gamma)\right) = \beta\nabla.\left(\tfrac{1}{2}h^2\Gamma\nabla h\right) - \kappa\nabla.\left(\tfrac{1}{2}h^2\Gamma\nabla\Delta h\right) + \delta\Delta\Gamma. \qquad (2.1.31b)$$

In Chapters 3-5, we consider axisymmetric flow. Interpreting (2.1.31) in plane polar coordinates (r,θ), with axisymmetry (i.e., no dependance on θ), the equations are

$$h_t + \frac{1}{r}\left(\tfrac{1}{2}rh^2\sigma_r\right)_r = \beta\frac{1}{r}\left(\tfrac{1}{3}rh^3h_r\right)_r - \kappa\frac{1}{r}\left(\tfrac{1}{3}rh^3\left(h_{rr} + \tfrac{1}{r}h_r\right)_r\right)_r \qquad (2.1.32a)$$

$$\Gamma_t + \frac{1}{r}\left(rh\Gamma\sigma_r\right)_r = \beta\frac{1}{r}\left(\tfrac{1}{2}rh^2\Gamma h_r\right)_r - \kappa\frac{1}{r}\left(\tfrac{1}{2}rh^2\Gamma\left(h_{rr} + \tfrac{1}{r}h_r\right)_r\right)_r + \delta\frac{1}{r}\left(r\Gamma_r\right)_r. \qquad (2.1.32b)$$

The axisymmetric equations are derived in [29].

Inclined Plane: $\alpha > 0$

In Chapter 6, we consider flow traveling down an inclined plane which corresponds to $\alpha > 0$. Consider the scalings (2.1.27) in the equations (2.1.21),(2.1.25),

$$\frac{H}{T}\hat{h}_{\hat{t}} \;+\; \frac{\rho g\sin\alpha}{\mu}\frac{H^3}{L}\left(\tfrac{1}{3}\hat{h}^3\right)_x + \frac{1}{\mu}\frac{SH^2}{L^2}\left(\tfrac{1}{2}\hat{h}^2\hat{\sigma}_{\hat{x}}\right)_{\hat{x}}$$

$$= \;\frac{\rho g\cos\alpha}{\mu}\frac{H^4}{L^2}\left(\tfrac{1}{3}\hat{h}^3\hat{h}_{\hat{x}}\right)_{\hat{x}} - \frac{\gamma}{\mu}\frac{H^4}{L^4}\left(\tfrac{1}{3}\hat{h}^3\hat{h}_{\hat{x}\hat{x}\hat{x}}\right)_{\hat{x}} \tag{2.1.33a}$$

$$\frac{\Gamma_m}{T}\hat{\Gamma}_{\hat{t}} \;+\; \frac{\rho g\sin\alpha}{\mu}\frac{H^2\Gamma_m}{L}\left(\tfrac{1}{2}\hat{h}^2\hat{\Gamma}\right)_x + \frac{1}{\mu}\frac{SH\Gamma_m}{L^2}\left(\hat{h}\hat{\Gamma}\hat{\sigma}_{\hat{x}}\right)_{\hat{x}}$$

$$= \;\frac{\rho g\cos\alpha}{\mu}\frac{H^3\Gamma_m}{L^2}\left(\tfrac{1}{2}\hat{h}^2\hat{\Gamma}\hat{h}_{\hat{x}}\right)_{\hat{x}} - \frac{\gamma}{\mu}\frac{H^3\Gamma_m}{L^4}\left(\tfrac{1}{2}\hat{h}^2\hat{\Gamma}\hat{h}_{\hat{x}\hat{x}\hat{x}}\right)_{\hat{x}} + \frac{D\Gamma_m}{L^2}\hat{\Gamma}_{\hat{x}\hat{x}}. \tag{2.1.33b}$$

First, we balance the coefficients of the tangential gravity and Marangoni terms in (2.1.33a) to define S:

$$\frac{\rho g\sin\alpha}{\mu}\frac{H^3}{L} = \frac{H^2S}{\mu L^2} \qquad \text{which implies} \qquad S = LH\rho g\sin\alpha. \tag{2.1.34}$$

Next we determine the time scale

$$\frac{H}{T} = \frac{H^2S}{\mu L^2} = \frac{H^3\rho g\sin\alpha}{\mu L} \qquad \text{which implies} \qquad T = \frac{\mu L}{H^2\rho g\sin\alpha}. \tag{2.1.35}$$

Note balancing the equivalent terms in (2.1.33b) results in the same relation. Multiplying (2.1.33) by $\frac{\mu L}{H^3\rho g\sin\alpha}$ produces the non-dimensional system, dropping the ˆ

$$h_t + \left(\tfrac{1}{3}h^3\right)_x + \left(\tfrac{1}{2}h^2\sigma_x\right)_x \;=\; \beta\left(\tfrac{1}{3}h^3 h_x\right)_x - \kappa\left(\tfrac{1}{3}h^3 h_{xxx}\right)_x \tag{2.1.36a}$$

$$\Gamma_t + \left(\tfrac{1}{2}h^2\Gamma_x\right)_x + \left(h\Gamma\sigma_x\right)_x \;=\; \beta\left(\tfrac{1}{2}h^2\Gamma h_x\right)_x - \kappa\left(\tfrac{1}{2}h^2\Gamma h_{xxx}\right)_x + \delta\Gamma_{xx} \tag{2.1.36b}$$

where

$$\beta = \cot\alpha\frac{H}{L}, \qquad \kappa = \frac{\gamma H}{L^3\rho g\sin\alpha}, \qquad \delta = \frac{D\mu}{LH^2\rho g\sin\alpha}. \tag{2.1.37}$$

The system of equations which incorporate flow in the y-direction on the inclined plane is derived in [24]

$$h_t + \left(\tfrac{1}{3}h^3\right)_x + \nabla\cdot\left(\tfrac{1}{2}h^2\nabla\sigma(\Gamma)\right) \;=\; \beta\nabla\cdot\left(\tfrac{1}{3}h^3\nabla h\right) - \kappa\nabla\cdot\left(\tfrac{1}{3}h^3\nabla\Delta h\right) \tag{2.1.38a}$$

$$\Gamma_t + \left(\tfrac{1}{2}h^2\Gamma\right)_x + \nabla\cdot\left(h\Gamma\nabla\sigma(\Gamma)\right) \;=\; \beta\nabla\cdot\left(\tfrac{1}{2}h^2\Gamma\nabla h\right) - \kappa\nabla\cdot\left(\tfrac{1}{2}h^2\Gamma\nabla\Delta h\right) + \delta\Delta\Gamma. \tag{2.1.38b}$$

Remark: When $\alpha = 0$, the scaling for the surface tension σ is not explicitly defined. However, when $\alpha > 0$ the scaling assumes the driving forces are comparable. The relation (2.1.34)

gives the balance $\frac{S}{LH\rho g} = O(1)$. In both cases, the ratio $\frac{\beta}{\kappa} = \frac{\rho g L^2}{\gamma}$ expresses the relative strength of the dissipative terms.

Chapter 3

Numerical Method: $\beta = \kappa = \delta = 0$

In this chapter, we develop a numerical method for the simplified system in which the coefficients of the higher order derivatives in (2.1.30), β, κ, δ, are all set to zero. In §3.1 we classify the type of PDE, determine jump conditions, and show the surfactant concentration has compact support. We develop a numerical method for the system in §3.2 and examine the numerical results in §3.3. The property of conservation of mass is investigated in §3.4 along with convergence in §3.5. The numerical results are verified by developing a different numerical method and comparing the results from the two schemes in §3.6. A numerical method for the full system (2.1.30) is developed in §5.2.1.

The system (2.1.30) is simplified by setting $\beta = \kappa = \delta = 0$ which reduces the system from a fourth order nonlinear PDE coupled to a second order nonlinear PDE to a nonlinear system which is first order in h and second order in Γ. The simplified system is

$$h_t = -\left(\tfrac{1}{2}h^2\sigma(\Gamma)_x\right)_x \tag{3.0.1a}$$

$$\Gamma_t = -\left(h\Gamma\sigma(\Gamma)_x\right)_x. \tag{3.0.1b}$$

In §3.1 we discuss the implications of simplifying this system and show that the system is mixed hyperbolic-parabolic.

When determining an accurate and efficient numerical method to implement for numerical simulations, we must consider the type of PDE. Equations (3.0.1) are nonlinear conservation laws. If $\sigma(\Gamma)$ is regarded as a given function, then (3.0.1a) is a scalar first order conservation law. Therefore, discontinuities (shocks) may develop in finite time from smooth initial data. (For example, if $\sigma(\Gamma)_x = 1$, then (3.0.1a) is the inviscid Burgers' equation.) A good numerical scheme must capture this behavior and avoid instabilities, which often appear in the form of numerical oscillations near discontinuities in the solution. On the other hand, equation (3.0.1b) is a second order parabolic equation for Γ, if h is regarded as a given function. Consequently,

this equation tends to smooth solutions, except where h jumps or $\Gamma = 0$, where the PDE is degenerate. However, numerical methods for parabolic equations often present stability issues which may be overcome by the use of an implicit method. Also, if the edge of the support is not treated carefully the degeneracy of (3.0.1b) leads to artificial smoothing of the solution. We seek a numerical method which handles these issues simultaneously.

We further investigate the properties of the system (3.0.1) in order to determine a suitable method. Since we are ignoring all smoothing effects of the equations by setting $\beta = \kappa = \delta = 0$, we must be very sensitive to the introduction of artificial smoothing from the numerical method. We notice that if the initial condition for the surfactant concentration profile has compact support then the profile will maintain compact support, shown below in Lemma 1. The numerical simulations must also capture this property accurately. Artificial smoothing may occur due to the edge of the support (i.e., leading edge) of the surfactant falling between two gridpoints. This smoothed behavior would then propagate to future profiles. In order to avoid this artificial behavior, in §3.2 we formulate a numerical method based on tracking the edge to ensure that the leading edge occurs at a gridpoint. In this procedure, we scale the spatial variable by the location of the free boundary and formulate the equations on the resulting fixed domain, together with an ODE for the free boundary location as a function of time. We then discretize this system in space and time. The choice of discretization in the finite difference method presented in §3.3 affects the accuracy and stability of the solution, as discussed in [46]. In §3.4 and §3.5 we investigate the desired properties of conservation of mass and convergence of the numerical scheme.

In §3.6, we implement a different numerical scheme on the physical domain in order to verify the results in §3.3. In this scheme, the edge is captured rather than tracked. We work with the equations (3.0.1a) and (3.0.1b) separately which allows for tailored discretization for each type of equation. First we update the height h from equation (3.0.1a) explicitly using the Godunov finite volume method. Then we solve the surfactant equation using an implicit parabolic solver with the height profile determined in the previous step. In these simulations, the height profile jumps when $\Gamma = 0$ due to the discontinuity in Γ_x. We compare the solutions from the methods on the fixed and physical domain to better understand the behavior of the system of equations.

3.1 Simplified System

In Chapter 5 we consider an axisymmetric droplet of surfactant spreading on a thin layer of fluid. We investigate the simplified axisymmetric system and develop a numerical method in §3.7. However, we first simplify the problem by working in planar geometry. In anticipation of the axisymmetric problem, we assume that h, Γ are even functions of x and consider the

simplified system (3.0.1) on the domain $x \geq 0$ with initial and boundary conditions

$$h(x,0) = h_0(x) > 0, \qquad \Gamma(x,0) = \Gamma_0(x) \tag{3.1.1a}$$

$$h_x(0,t) = 0, \qquad \Gamma_x(0,t) = 0. \tag{3.1.1b}$$

The wave-like propagation of solutions of the full system (2.1.30) is largely determined by the simplified equations (3.0.1). These solutions ignore the physical effects incorporated through the higher order terms which smooth the solutions. The higher order terms (terms with the coefficients β, κ, δ) affect the transport speed in the equations as well as smooth the solution. Nonetheless ignoring these terms, we can determine the basic behavior of the solutions of the full system (2.1.30) from equations (3.0.1).

The surface tension, σ, of the fluid is related to the surfactant concentration, Γ, through an equation of state $\sigma = \sigma(\Gamma)$. We consider a smooth function about the base surface tension with the property $\sigma'(\Gamma) < 0$, since the surface tension decreases as the surfactant concentration increases. Including only leading order terms, the linearization of such a relation about $\Gamma = 0$ is

$$\sigma(\Gamma) = \sigma_0 - \sigma_m \Gamma \tag{3.1.2}$$

where σ_0 is the surface tension of the clean underlying fluid and $\sigma_m = -\sigma'(0)$. The coefficients σ_0, σ_m are generally absorbed into the non-dimensional coefficients during non-dimensionalization of the equations. The equation of state is then

$$\sigma(\Gamma) = 1 - \Gamma, \tag{3.1.3}$$

which results in the system

$$h_t = \left(\tfrac{1}{2} h^2 \Gamma_x \right)_x \tag{3.1.4a}$$

$$\Gamma_t = \left(h \Gamma \Gamma_x \right)_x . \tag{3.1.4b}$$

Classification of PDE

To better understand the behavior of the system (3.1.4), we classify the type of equations. Let $h = H$ and $\Gamma = G$ be solutions of (3.1.4). Linearizing about this solution, we set $h = H + \bar{h}$, $\Gamma = G + \bar{\Gamma}$ and obtain the linearized equations

$$\bar{h}_t - \left(\tfrac{1}{2} H^2 \bar{\Gamma}_x + H \bar{h} G_x \right)_x = 0 \tag{3.1.5a}$$

$$\bar{\Gamma}_t - \left(H G_x \bar{\Gamma} + H G \bar{\Gamma}_x + G G_x \bar{h} \right)_x = 0. \tag{3.1.5b}$$

Written in matrix form, this system is

$$
\begin{pmatrix} \bar{h} \\ \bar{\Gamma} \end{pmatrix}_t - \begin{pmatrix} (HG_x)_x + HG_x\partial_x & \frac{1}{2}H^2\partial_x^2 + HH_x\partial_x \\ (GG_x)_x + GG_x\partial_x & (HG_x)_x + (HG_x + (HG)_x)\partial_x + HG\partial_x^2 \end{pmatrix} \begin{pmatrix} \bar{h} \\ \bar{\Gamma} \end{pmatrix} = 0 \qquad (3.1.6)
$$

Following the techniques outlined in [65], we freeze coefficients and consider the solutions $\bar{h} = ae^{i\zeta x}e^{i\lambda t}$, $\bar{\Gamma} = be^{i\zeta x}e^{i\lambda t}$. Then the leading order terms of (3.1.6), for $\zeta \to \infty$ are

$$
i\lambda \begin{pmatrix} a \\ b \end{pmatrix} = \begin{pmatrix} iHG_x\zeta & -\frac{1}{2}H^2\zeta^2 \\ iGG_x\zeta & -HG\zeta^2 \end{pmatrix} \begin{pmatrix} a \\ b \end{pmatrix} = 0. \qquad (3.1.7)
$$

We now confirm that (3.1.7) is the principal symbol by weighting the equations in (3.1.7) by s_1 for the h equation and s_2 for the Γ equation and the variables $\bar{h}$ by t_1 and $\bar{\Gamma}$ by t_2. The relation of these weights is

$$
s_1 + t_1 = 1 \qquad s_1 + t_2 \geq 2 \qquad\qquad (3.1.8)
$$

$$
s_2 + t_1 \geq 1 \qquad s_2 + t_2 = 2. \qquad\qquad (3.1.9)
$$

But these equations are only satisfied when $s_1 + t_2 = 2$ and $s_2 + t_1 = 1$. It follows that (3.1.7) is the principal symbol, since $s_i + t_j$ is then precisely the power of ζ in the (i, j) entry of the matrix.

In order to classify the equations, we seek the eigenvalues of the matrix in (3.1.7),

$$
det \begin{pmatrix} iHG_x\zeta - i\lambda & -\frac{1}{2}H^2\zeta^2 \\ iGG_x\zeta & -HG\zeta^2 - i\lambda \end{pmatrix} = -\lambda^2 + \lambda(HG_x\zeta + iHG\zeta^2) - \frac{1}{2}iH^2GG_x\zeta^3 = 0. \qquad (3.1.10)
$$

Retaining only leading order terms,

$$
\lambda = \tfrac{1}{2}(HG_x\zeta + iHG\zeta^2 \pm iHG\zeta^2). \qquad (3.1.11)
$$

The eigenvalue

$$
\lambda = \tfrac{1}{2}HG_x\zeta \qquad (3.1.12)
$$

corresponds to (3.1.4a) being hyperbolic and

$$
\lambda = \tfrac{1}{2}(HG_x\zeta + 2iHG\zeta^2) \qquad (3.1.13)
$$

corresponds to (3.1.4b) being parabolic. Note (3.1.4b) is actually degenerate parabolic since the equation is trivial when $\Gamma \equiv 0$, which also reduces (3.1.4a) to $h_t = 0$.

3.1.1 Jump Conditions

We consider solutions of the PDE (3.1.4) with conditions (3.1.1) for smooth h_0. We also consider Γ_0 to have compact support, with $supp(\Gamma_0) = [0,1]$ and assume Γ_0 is smooth on $[0,1]$. The point, $x = x_0(t)$, where $\Gamma(x,t)$ goes to zero we call the **leading edge** of the surfactant. We consider a surfactant profile with non-zero slope at $x = x_0(t)$. Thus there is a jump in Γ_x, at $x = x_0(t)$, which causes a corresponding jump in the height. In this section we determine the jump condition inherent to the system (3.1.4).

Consider a solution of (3.1.4) in which Γ has compact support such that the profile goes to zero at the leading edge with non-zero slope. We determine the spreading speed $s = \dot{x}_0(t)$ of the surfactant by observing

$$\frac{d}{dt}\Gamma(x_0(t),t) = 0 \tag{3.1.14}$$

then

$$\dot{x}_0\Gamma_x + \Gamma_t = 0. \tag{3.1.15}$$

Substituting in (3.1.4b)

$$\dot{x}_0\Gamma_x - (h\Gamma\Gamma_x)_x = -h\Gamma_x^2 \tag{3.1.16}$$

and applying the property that $\Gamma(x_0(t),t) = 0$ implies $\dot{x}_0 = -h\Gamma_x$. Thus the transport speed is $s = -h\Gamma_x$. Define

$$h^- = \lim_{x\to st^-} h, \qquad h^+ = \lim_{x\to st^+} h \tag{3.1.17}$$

$$\Gamma^- = \lim_{x\to st^-} \Gamma < 0, \qquad \Gamma^+ = \lim_{x\to st^+} \Gamma = 0. \tag{3.1.18}$$

We observe that the velocity of the surfactant leading edge is also the surface velocity of the film which makes sense since the surfactant is insoluble; the transport speed is $s = -h^-\Gamma_x^-$. We are then able to determine the jump in the height of the film from the jump conditions of the height PDE,

$$-s\,[h] \;=\; \left[\tfrac{1}{2}h^2\Gamma_x\right]. \tag{3.1.19}$$

Thus,

$$h^-\Gamma_x^-(h^+ - h^-) \;=\; \tfrac{1}{2}((h^+)^2\Gamma_x^+ - (h^-)^2\Gamma_x^-).$$

But $\Gamma_x^+ = 0$ and dividing by $h^-\Gamma_x^-$, since $h^-\Gamma_x^- \neq 0$ we obtain

$$(h^+ - h^-) \;=\; -\tfrac{1}{2}h^-$$

Consequently,

$$h^- \;=\; 2h^+ \tag{3.1.20}$$

is the jump condition. Accordingly, the jump in the derivative of the surfactant concentration causes the height profile to jump to twice the initial height, at the leading edge. Note that this jump is independent of the magnitude of the jump in Γ_x, which only affects the speed.

The shock in the height profile results from the discontinuity in Γ_x in equation (3.1.4a). The characteristic speed for the height of the film in the presence of surfactant, $\lambda = -\tfrac{1}{2}h^-\Gamma_x^-$ is half the shock speed $s = -h^-\Gamma_x^-$. However, to the right of the leading edge where there is no surfactant, the characteristic speed is zero. Hence the flux is discontinuous due to the discontinuity in Γ_x at the leading edge. This discontinuity creates and drives the shock in the height profile. Kruzkov developed an existence theory for Lipschitz continuous flux functions [44]. Existence and uniqueness results for discontinuous fluxes were addressed recently in [15, 40, 41].

3.1.2 Compact Support

The porous medium equation, $\Gamma_t = \nabla.(\Gamma\nabla\Gamma)$ has a finite speed of propagation, shown in [79]. An important characteristic used to establish this property is that the equation degenerates at $\Gamma = 0$. The surfactant equation (3.1.4b) also has this degeneracy. Consequently a similar argument shows that the surfactant and film disturbance spread with a finite speed.

We consider weak solutions of (3.1.4), in which h necessarily jumps at the leading edge of the spreading surfactant, as stipulated by the jump condition (3.1.20). In the following lemma we establish that the surfactant maintains compact support, assuming that solutions are unique and piecewise smooth. Existence and uniqueness of solutions of system (3.1.4) are considered by Renardy [62, 63, 64]. Let $w(x,t) = -h\Gamma_x$ be the surface fluid velocity. In anticipation of this result, let $x = x_0(t)$ denote the location of the leading edge of the support of $\Gamma(x,t)$ at time $t \geq 0$.

Lemma 1 *Let $(h(x,t), \Gamma(x,t))$ be a piecewise smooth solution of (3.1.4), and (3.1.1), with $\Gamma(x,t)$ continuous. Then the support of $\Gamma(\cdot,t)$ remains bounded for each $t > 0$. Moreover,*

$$\dot{x}_0(t) = w(x_0(t)-, t). \tag{3.1.21}$$

Proof: Let h, Γ be the solution. Then the surface velocity speed $w(x,t) = -h(x,t)\Gamma_x(x,t)$ is well defined as a piecewise continuous function, since it involves spatial derivatives of h and Γ one order below the highest order of those appearing in the PDE, (3.1.4). The only jump in $w(x,t)$ is at the interface $x = x_0(t)$ defined by (3.1.21) with initial condition $x_0(0) = 1$.

For each $x_1 > 0$, define the characteristic curve $\hat{x}(t), t > 0$ by

$$\frac{d\hat{x}(t)}{dt} = w(\hat{x}(t)-, t), \quad \hat{x}(0) = x_1.$$

The PDE (3.1.4b) in terms of $w(x,t)$ is

$$\Gamma_t + (w\Gamma)_x = 0,$$

i.e.,

$$\Gamma_t + w\Gamma_x = -w_x\Gamma$$

Then on the characteristic $\hat{x}(t)$ through x_1,

$$\frac{d\Gamma}{dt} = -w_x\Gamma, \quad \Gamma(0) = \Gamma_0(x_1).$$

Therefore,

$$\Gamma(t) = \Gamma_0(x_1)\exp\left(-\int_0^t w(x,s)_x\Big|_{x=\hat{x}(s)} ds\right). \tag{3.1.22}$$

It follows that if $x_1 > 1$, where $\Gamma_0(x_1) = 0$, then $\Gamma(t) = 0$, at least for short time, until w encounters a singularity where Γ is first non-zero, i.e., along $x = x_0(t)$.

Now let $x_0(t)$ be defined by (3.1.21). Then on $x = x_0(t)$ we have $\Gamma(t)$ defined by (3.1.22), with $x_1 = 1$ and $\hat{x} = x_0$, so that $\Gamma(t) = 0$ along $x_0(t)$. However, if $x_1 < 1$, then $\Gamma_0(x_1) > 0$, so that $\Gamma(t) > 0$ on the characteristic originating at $x = x_1$. ∎

Thus the surfactant profile $\Gamma(x,t)$ maintains compact support. If the height is initially constant, e.g. $h_0(x) = 1$, then the height profile remains unchanged in the absence of surfactant. If there is no surfactant, $\Gamma_x = 0$ reduces (3.1.4a) to $h_t = 0$; h remains constant. Therefore, if $x > x_0(t)$ then $\Gamma = 0$ and $h(x,t) = h_0(x) = 1$.

3.2 Numerical Method

The property that the surfactant maintains compact support allows the support to be transformed to a fixed domain. A change of variables mapping two free boundaries to a fixed domain

is described in [3]. However, we consider the solution to be symmetric and only consider one free boundary. Using the location of the leading edge of the surfactant profile $x_0(t)$ as a scaling factor, we define $\xi = \frac{x}{x_0(t)}$. Consider the transformed variables

$$h(x,t) = \bar{h}(\xi,t), \qquad \Gamma(x,t) = \bar{\Gamma}(\xi,t), \qquad \xi = \frac{x}{x_0(t)}. \tag{3.2.1}$$

Then (3.1.4) becomes, dropping the $^-$,

$$h_t - \frac{\dot{x}_0}{x_0}\xi h_\xi = \frac{1}{x_0^2}\left(\tfrac{1}{2}h^2\Gamma_\xi\right)_\xi \tag{3.2.2a}$$

$$\Gamma_t - \frac{\dot{x}_0}{x_0}\xi\Gamma_\xi = \frac{1}{x_0^2}\left(h\Gamma\Gamma_\xi\right)_\xi \tag{3.2.2b}$$

on $0 \leq \xi \leq 1$. Consider an initially uniform film in order to examine the deformation caused by the presence of a finite layer of surfactant. Typical choices of initial data for (3.2.2) are

$$h_0(x) = h_0(\xi) = 1, \qquad \Gamma_0(x) = \Gamma_0(\xi) = \begin{cases} 1 - \xi^{10} & \xi < 1 \\ 0 & \xi \geq 1 \end{cases}, \qquad x_0(0) = 1. \tag{3.2.3}$$

Note at $t = 0$, $\xi = x$ since $x_0(0) = 1$. The conditions of the free boundary located at $\xi = 1$, are stipulated by the compact support of the surfactant and the jump condition (3.1.20) of the PDE. Combining these with the boundary conditions at $x = 0$ given by (3.1.1b), the boundary conditions of the system (3.2.2) are

$$h_\xi(0,t) = 0, \qquad \Gamma_\xi(0,t) = 0 \tag{3.2.4a}$$

$$h(1,t) = 2h(1^+,t) = 2, \qquad \Gamma(1,t) = 0. \tag{3.2.4b}$$

The speed of the leading edge of the surfactant, $\dot{x}_0(t)$, is determined from (3.2.2b) evaluated at $\xi = 1$, noting that $\Gamma_t(1,t) = 0$,

$$-\frac{\dot{x}_0}{x_0}\Gamma_\xi\big|_{\xi=1^-} = \frac{1}{x_0^2}\left(h_\xi\Gamma\Gamma_\xi + h\Gamma_\xi^2 + h\Gamma\Gamma_{\xi\xi}\right)\big|_{\xi=1^-}.$$

However $\Gamma(1,t) = 0$, so that

$$-\frac{\dot{x}_0}{x_0}\Gamma_\xi\big|_{\xi=1^-} = \frac{1}{x_0^2}h\Gamma_\xi^2\big|_{\xi=1^-}.$$

Dividing through by $\Gamma_\xi \neq 0$, we find

$$\dot{x}_0 = -\frac{1}{x_0}h(1^-,t)\Gamma_\xi(1^-,t). \tag{3.2.5}$$

26

Note that (3.2.5) expresses the fact that the leading edge $x = x_0(t)$ of the surfactant moves with the surface velocity $s = -h\Gamma_x$.

3.3   Numerical Scheme

In this section we outline the finite difference method used to generate numerical results for system (3.2.2)–(3.2.5). In this method, the spatial derivatives of the linear terms are upwinded and the nonlinear terms are center differenced. The temporal step is implicit. We solve the system of equations (3.2.2) simultaneously for h and Γ. Though the PDE is not written in conservation form, in §3.4 we show that both the equations and the discretization conserve mass.

Let $h_j^n \approx h(j\Delta\xi, n\Delta t)$ and $\Gamma_j^n \approx \Gamma(j\Delta\xi, n\Delta t)$ where $\Delta\xi = \frac{1}{N}$, N is the number of gridpoints. We use the standard notation for spatial averages of $u_j^n \approx u(j\Delta\xi, n\Delta t)$,

$$\bar{u}_{j+\frac{1}{2}}^n \equiv \frac{u_{j+1}^n + u_j^n}{2}. \tag{3.3.1}$$

The discretized equations are

$$h_j^{n+1} = h_j^n + \Delta t \xi_j \frac{x_0^{n+1} - x_0^n}{x_0^n \Delta t} \left(\frac{h_{j+1}^{n+1} - h_j^{n+1}}{\Delta\xi} \right) + \frac{\Delta t}{(x_0^n)^2 \Delta\xi} \left(\mathcal{F}_{j+\frac{1}{2}}^{n+1} - \mathcal{F}_{j-\frac{1}{2}}^{n+1} \right) \tag{3.3.2a}$$

$$\Gamma_j^{n+1} = \Gamma_j^n + \Delta t \xi_j \frac{x_0^{n+1} - x_0^n}{x_0^n \Delta t} \left(\frac{\Gamma_{j+1}^{n+1} - \Gamma_j^{n+1}}{\Delta\xi} \right) + \frac{\Delta t}{(x_0^n)^2 \Delta\xi} \left(\mathcal{G}_{j+\frac{1}{2}}^{n+1} - \mathcal{G}_{j-\frac{1}{2}}^{n+1} \right) \tag{3.3.2b}$$

where $1 \leq j \leq N - 1$ and $n \geq 0$. The flux functions (dropping the superscript $n + 1$) are represented by

$$\mathcal{F}_{j+\frac{1}{2}} = \frac{1}{2} \left(\bar{h}_{j+\frac{1}{2}} \right)^2 \frac{\Gamma_{j+1} - \Gamma_j}{\Delta\xi}, \qquad \mathcal{G}_{j+\frac{1}{2}} = \bar{h}_{j+\frac{1}{2}} \bar{\Gamma}_{j+\frac{1}{2}} \frac{\Gamma_{j+1} - \Gamma_j}{\Delta\xi}. \tag{3.3.3a}$$

The leading edge of the surfactant is updated explicitly, based on (3.2.5) and $\Gamma_N^n = 0$:

$$x_0^{n+1} = x_0^n + \Delta t \frac{2}{x_0^n} \frac{\Gamma_{N-1}^n}{\Delta\xi}. \tag{3.3.4}$$

The initial and boundary conditions are

$$h_j^0 = 1, \qquad \Gamma_j^0 = 1 - \xi_j^{10} \tag{3.3.5a}$$

$$h_0^n = h_1^n, \qquad h_N^n = 2 \tag{3.3.5b}$$

$$\Gamma_0^n = \Gamma_1^n, \qquad \Gamma_N^n = 0. \tag{3.3.5c}$$

27

The linear terms are upwinded in (3.3.2), using forward differences, because the contribution to the characteristic speed, $\frac{-\xi \dot{x}_0}{x_0}$ is negative. Implementation at each time step includes Newton's method with exact Jacobian. The time step Δt is chosen small enough to ensure convergence of Newton's method.

When the height and surfactant profiles are plotted in the physical variable $x = x_0(t)\xi$, the domain increases as a function of time, as seen in Figure 3.1. These plots are generated from the numerical data generated on the fixed domain and translated to the physical domain; the spatial step $\Delta x = x_0(t)\Delta \xi$ is time dependent. Figure 3.2 shows the solution in the scaled variable ξ, for which the computational domain remains fixed. This property allows for use of fewer grid points since the domain is stationary at $[0, 1]$ rather than growing with time to a size of $[0, 50]$ or larger. This simplification greatly increases the speed of the computation.
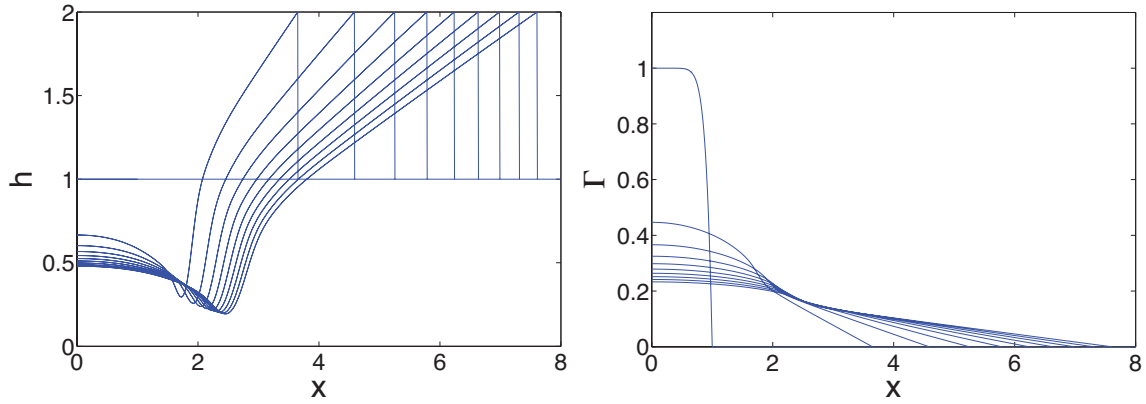
Figure 3.1: The height (left) and surfactant concentration (right) profiles in the physical variable x at $t = 0$, 5, 10, 20, ..., 45 and $\Delta x = 0.001 x_0(t)$.

3.4 Conservation of Mass

The PDE (3.2.2-3.2.4) is not written in conservative form, however, it in fact does conserve mass. The mass of fluid between $x = 0$ and the free boundary $x = x_0$ is

$$m_h(t) = \int_0^{x_0(t)} h \ dx = \int_0^1 x_0 h \ d\xi. \tag{3.4.1}$$
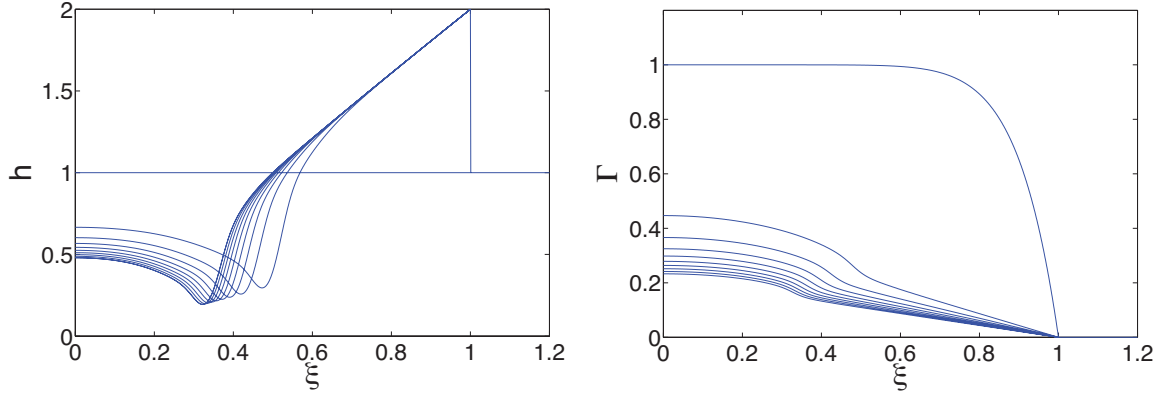
Figure 3.2: The height (left) and surfactant concentration (right) profiles in the scaled variable ξ at $t = 0,\ 5,\ 10,\ 20,\ ...,45$ and $\Delta\xi = 0.001$.

If the height of the film is initially uniform, as the film spreads more fluid is incorporated into the profile. Since there is no deformation ahead of $x = x_0(t)$ if the initial height is constant (e.g., h=1), conservation of mass requires $m_h(t) = x_0(t)$, the area of the fluid for $0 < x < x_0(t)$. Define the excess mass for the fluid by

$$M_h(t) = \int_0^1 x_0 h \; d\xi - x_0. \tag{3.4.2}$$

Observe that $M_h(0) = 0$ since $x_0(0) = 1$ and $h(\xi, 0) = 1$. To check conservation of mass, we verify $M_h'(t) = 0$ for $t > 0$:

$$M_h'(t) = \int_0^1 (\dot{x}_0 h + x_0 h_t) \; d\xi - \dot{x}_0.$$

From (3.2.5) and (3.2.2a),

$$M_h'(t) = \frac{1}{x_0} \left[\int_0^1 \left(-h(1,t)\Gamma_\xi(1,t)h - h(1,t)\Gamma_\xi(1,t)\xi h_\xi + \left(\tfrac{1}{2}h^2\Gamma_\xi\right)_\xi \right) d\xi + h(1,t)\Gamma_\xi(1,t) \right].$$

Combining the first two terms

$$M_h'(t) = \frac{1}{x_0} \left[\int_0^1 \left(-h(1,t)\Gamma_\xi(1,t)\,(\xi h)_\xi + \left(\tfrac{1}{2}h^2\Gamma_\xi\right)_\xi \right) d\xi + h(1,t)\Gamma_\xi(1,t) \right].$$

29

Implementing the boundary conditions (3.2.4) and $h(1,t) = 2$

$$
\begin{aligned}
M_h'(t) &= \frac{1}{x_0}\left[-h(1,t)^2\Gamma_\xi(1,t) + \tfrac{1}{2}h(1,t)^2\Gamma_\xi(1,t) + h(1,t)\Gamma_\xi(1,t)\right] \\
&= 0
\end{aligned}
\tag{3.4.3}
$$

The argument for conservation of surfactant is similar. However, the surfactant mass does not change with time; thus we define the excess mass function

$$
M_g(t) = \int_0^1 x_0\Gamma(\xi,t)d\xi - \int_0^1 \Gamma(\xi,0)d\xi
\tag{3.4.4}
$$

and observe $M_g(0) = 0$ and $M_g'(t) = 0$ for $t > 0$.

Since the PDE conserves mass we check that the numerical scheme also has this property. We define the excess mass function (3.4.2) in discrete form

$$
M_h^n = \sum_{j=1}^{N-1} x_0 h_j^n \Delta\xi - x_0.
\tag{3.4.5}
$$

The calculation below requires the use of summation by parts which states

$$
\sum_{k=m}^{n} f_k(g_{k+1} - g_k) = f_{n+1}g_{n+1} - f_m g_m - \sum_{k=m}^{n} g_{k+1}\left(f_{k+1} - f_k\right).
\tag{3.4.6}
$$

Also the flux defined in (3.3.3a) and properties of the boundary are used; specifically we observe that

$$
\mathcal{F}_{\frac{1}{2}} = 0, \qquad \frac{1}{x_0}\mathcal{F}_{N-\frac{1}{2}} = -\dot{x}_0 + O(\Delta\xi).
\tag{3.4.7}
$$

Then

$$
\begin{aligned}
\frac{M_h^{n+1} - M_h^n}{\Delta t} &= \sum_{j=1}^{N-1}\frac{x_0^{n+1}h_j^{n+1} - x_0^n h_j^n}{\Delta t}\Delta\xi - \sum_{j=1}^{N-1}\frac{x_0^{n+1} - x_0^n}{\Delta t} \\
&= \sum_{j=1}^{N-1}\frac{x_0^{n+1}h_j^{n+1} - x_0^n h_j^{n+1}}{\Delta t}\Delta\xi + \sum_{j=1}^{N-1}\frac{x_0^n h_j^{n+1} - x_0^n h_j^n}{\Delta t}\Delta\xi - \sum_{j=1}^{N-1}\frac{x_0^{n+1} - x_0^n}{\Delta t} \\
&= \sum_{j=1}^{N-1}\dot{x}_0 h_j^{n+1}\Delta\xi + \sum_{j=1}^{N-1}x_0^n\frac{h_j^{n+1} - h_j^n}{\Delta t}\Delta\xi - \dot{x}_0.
\end{aligned}
\tag{3.4.8}
$$

Using (3.3.2a)

$$\frac{M_h^{n+1} - M_h^n}{\Delta t} = \sum_{j=1}^{N-1} \dot{x}_0 h_j^{n+1} \Delta \xi + \sum_{j=1}^{N-1} \xi_j \dot{x}_0 \left(h_{j+1}^{n+1} - h_j^{n+1} \right) + \sum_{j=1}^{N-1} \frac{1}{x_0} \left(\mathcal{F}_{j+\frac{1}{2}} - \mathcal{F}_{j-\frac{1}{2}} \right) - \dot{x}_0.$$

From summation by parts

$$\frac{M_h^{n+1} - M_h^n}{\Delta t} = \sum_{j=1}^{N-1} \dot{x}_0 h_j^{n+1} \Delta \xi + \left(\xi_N h_N^{n+1} - \xi_1 h_1^{n+1} - \sum_{j=1}^{N-1} h_{j+1}^{n+1} \Delta \xi \right) \dot{x}_0 + \frac{1}{x_0} \left(\mathcal{F}_{N-\frac{1}{2}} - \mathcal{F}_{\frac{1}{2}} \right) - \dot{x}_0$$

$$= \left(\xi_N h_N^{n+1} - \xi_1 h_1^{n+1} + h_1^{n+1} \Delta \xi - h_N^{n+1} \Delta \xi \right) \dot{x}_0 + \frac{1}{x_0} \mathcal{F}_{N-\frac{1}{2}} - \dot{x}_0.$$

Since $\xi_1 = \Delta \xi$, $\xi_N = 1$, $h_N = 2$ we find,

$$\begin{aligned}\frac{M_h^{n+1} - M_h^n}{\Delta t} &= (2 - 2\Delta \xi) \dot{x}_0 - \dot{x}_0 + O(\Delta \xi) - \dot{x}_0 \\ &= O(\Delta \xi).\end{aligned}$$

Thus each time step introduces an error of $O(\Delta \xi)$ in the mass. If we consider K time steps then the excess mass is

$$M_h^k - M_h^0 = \sum_{k=0}^{K-1} M_h^{k+1} - M_h^k = K\Delta t \cdot O(\Delta \xi) = O(T\Delta \xi), \qquad \text{where } T = K\Delta t. \quad (3.4.9)$$

Therefore the numerical scheme conserves mass over any finite time interval, as $\Delta \xi \to 0$. The calculation to show conservation of surfactant is similar; the numerical excess mass function is

$$M_g^n = \sum_{j=1}^{N-1} x_0 \Gamma_j^n \Delta \xi - \sum_{j=1}^{N-1} \Gamma_j^0 \Delta \xi. \quad (3.4.10)$$

The numerical results also demonstrate that mass is conserved up to $O(\Delta \xi)$. As the number of grid points N is doubled, the error in the mass is cut in half as seen in Table 3.1.

3.5 Convergence

We perform a grid refinement to investigate the convergence of the solutions. Figure 3.3 shows the solutions of (3.3.2)-(3.3.5) at time $t = 0.1$ with $N = 250$, 500, 1000, 2000 grid points. Table 3.2 demonstrates the rate of convergence of the solutions using the ∞-norm. Note that while the surfactant profile converges, the height profile in fact does not converge under grid refinement.

There are three pieces to the solution (as labeled in Figure 3.4), defined as Region I: the

Table 3.1: The error in the conservation of mass at $t = .1$, with $\Delta x = \frac{1}{N}$, M_h defined by (3.4.5) and M_g defined by (3.4.10).

N	M_h	$\frac{M_h(N+1)}{M_h(N)}$	M_g	$\frac{M_g(N+1)}{M_g(N)}$
250	0.0127	-	-4.875×10^{-4}	-
500	0.0064	0.5039	-2.329×10^{-4}	0.4777
1000	0.0032	0.5	-1.1217×10^{-4}	0.4816
2000	0.0016	0.5	-5.4362×10^{-5}	0.4846
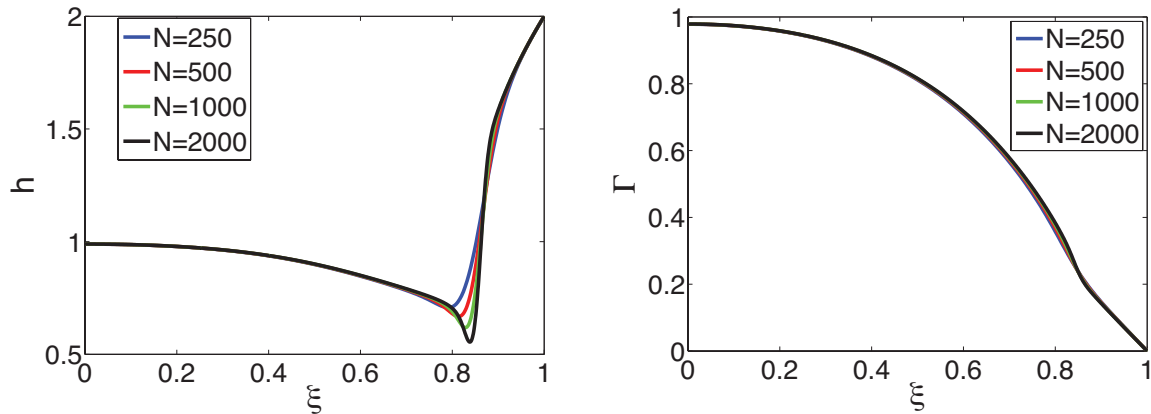
Figure 3.3: The height (left) and surfactant concentration (right) at $t = 0.1$ with $N = 250, 500, 1000, 2000$.

inner solution near $\xi = 0$, Region II: the region connecting Regions I and III and Region III: the outer solution near $\xi = 1$. The solutions corresponding to the height profiles of Figure 3.3(left) in Region I and Region III appear to converge. In Region II, the height exhibits interesting behavior which we do not expect from the analysis of the PDE. The profile develops a cavity in this region and the minimum continues to decrease under grid refinement. Thus in order to verify that this behavior is not an effect of the numerical scheme or change of variables, we implement a different method in §3.6 which includes a hyperbolic solver to simulate the height equation. This method discretizes the system (3.1.4) directly by eliminating the change of variables which transforms the domain to a fixed interval. Moreover, it does not require boundary conditions at the free boundary.
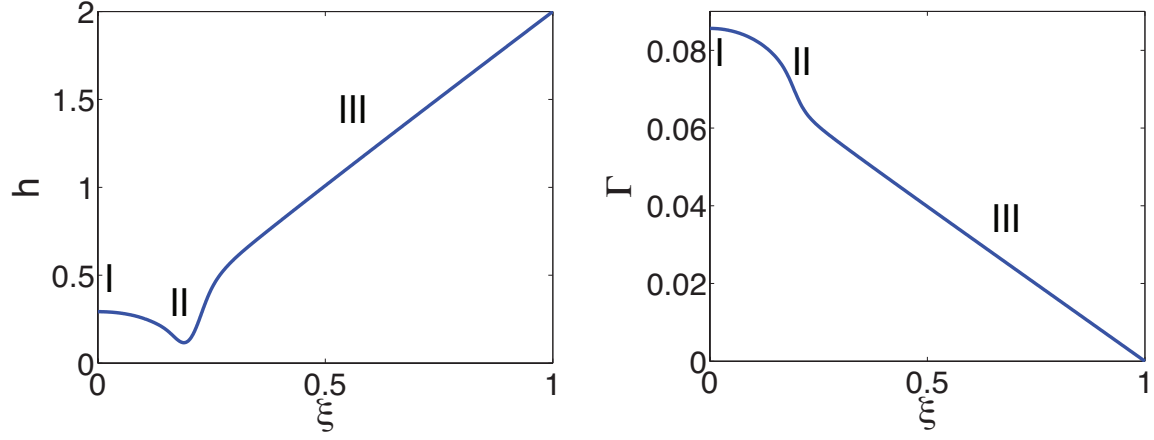
Figure 3.4: The regions of the height and surfactant concentration profiles at $t = 1000$. Region I corresponds to the inner solution, Region II to the intermediate solution, and Region III to the outer solution.

Table 3.2: Error in the height and surfactant profiles at $t = 0.1$ with $N = 250$, 500, 1000, 2000 using the ∞-norm.

N_1	N_2	$\|h_{N_2} - h_{N_1}\|_\infty$	$\|\Gamma_{N_2} - \Gamma_{N_1}\|_\infty$
250	500	0.1145	0.0109
500	1000	0.1165	0.0093
1000	2000	0.1231	0.0087

3.6 Godunov's Method

Finite volume methods are widely used for simulating hyperbolic conservation laws [45]. These methods are derived from the integral form of the conservation law. Rather than working with grid points, as done with finite difference schemes, the domain is split into cells and cell averages are obtained. The flux at the cell boundary is then used to update the cell average at the next time step. The choice of the piecewise polynomial approximation used in reconstructing the solutions from cell averages and the choice of numerical flux affect the accuracy and stability of the solution as discussed in [45]. The use of the flux in finite volume methods is inherent to properties of conservation of mass:

change in mass = entering mass - leaving mass.

Consider the hyperbolic conservation law

$$u_t + f(u)_x = 0 \tag{3.6.1}$$

where $f(u)$ is a flux function. The finite volume discretization for this equation is

$$u_j^{n+1} = u_j^n - \frac{\Delta t}{\Delta x} \left(\mathcal{F}_{j+\frac{1}{2}}^n - \mathcal{F}_{j-\frac{1}{2}}^n \right) \tag{3.6.2}$$

in which u_j^n is an approximation to the cell average centered at x_j at time n. In Godunov's method the numerical flux depends on whether the solution is increasing or decreasing within the cell. In this scheme, the numerical flux is defined by

$$\mathcal{F}(u_R, u_L) = \begin{cases} \min_{u_L \leq u \leq u_R} f(u) & \text{if } u_L < u_R \\ \max_{u_R \leq u \leq u_L} f(u) & \text{if } u_R < u_L. \end{cases} \tag{3.6.3}$$

As discussed in §3.1, the height equation (3.1.4a) is a hyperbolic conservation law. Accordingly, we use Godunov's method to update cell averages of the height. On the other hand the surfactant equation (3.1.4b) is a parabolic equation so it is updated using a second order implicit method for (3.2.2b) with centered difference for the spatial discretization. In summary, the algorithm we implement for solving the system (3.2.2) in two steps is:

- Step 1: Update h^n to h^{n+1} using Godunov's method and the data h^n, Γ^n

- Step 2: Update Γ^n to Γ^{n+1} using a centered difference implicit method and the data h^{n+1}

In the update of h^n we take Γ^n as constant in time which means the method will be first order accurate in time. Accordingly, we only use a first order time update for the height profile. In space we also use a first order method in the form of the basic Godunov method as described

above with piecewise constant reconstruction of the solution. This choice is made to simplify the calculation. However, we still choose to use an implicit method that is second order accurate for the surfactant equation in order to reduce the restriction on the step size.

We enforce the CFL condition in order to achieve stability in the hyperbolic h equation, $\Delta t < \frac{1}{\lambda_{max}} \Delta x.$, The largest absolute characteristic speed λ_{max} is

$$\lambda_{\max} = \max_{x,\, t} \left| -h(x,t)\Gamma_x(x,t) \right|. \tag{3.6.4}$$

which occurs at $t = 0$ because Γ_x is largest initially. Note we are not concerned with stability constraints from the Γ equation since it is a parabolic equation and we update it implicitly.

More sophisticated methods may also be used by incorporating flux limiting in the approximation. Flux limiting weights the choice of discretization for the flux depending on the direction the information is coming from. Such methods are potentially higher order accurate.

This scheme captures the shock in the height profile instead of tracking it, as in the method described in §3.2 and §3.3. Boundary conditions are not enforced at the free boundary. We work on the full domain $-a < x < a$ with $a > 1$, which eliminates the necessity to define a boundary condition at $x = 0$. We consider the same initial conditions as previously:

$$h_0(x) = 1 \tag{3.6.5}$$

$$\Gamma_0(x) = \begin{cases} 1 - x^{10}, & |x| < 1 \\ 0, & \text{otherwise} \end{cases} \tag{3.6.6}$$

and boundary conditions

$$h(-a,t) = h(a,t) = 1 \tag{3.6.7}$$

$$\Gamma(-a,t) = \Gamma(a,t) = 0. \tag{3.6.8}$$

The numerical scheme is

$$h_j^{n+1} = h_j^n + \frac{\Delta t}{\Delta x} \left(\mathcal{F}(h_{j+1}^n, h_j^n, \Gamma_{j+1}^n, \Gamma_j^n) - \mathcal{F}(h_j^n, h_{j-1}^n, \Gamma_j^n, \Gamma_{j-1}^n) \right) \tag{3.6.9a}$$

$$\Gamma_j^{n+1} = \Gamma_j^n + \frac{\Delta t}{\Delta x} \left(\mathcal{G}_{j+\frac{1}{2}}^{n+1} - \mathcal{G}_{j-\frac{1}{2}}^{n+1} \right) \tag{3.6.9b}$$

where $-N < j < N$, $n > 0$. The flux for (3.6.9a) is defined by (3.6.3) where

$$f(h) = \tfrac{1}{2}h^2 \Gamma_x \tag{3.6.10}$$

which results in

$$
\mathcal{F}(h_{j+1}^n, h_j^n, \Gamma_{j+1}^n, \Gamma_j^n) = \begin{cases} \min_{h_j^n \le h \le h_{j+1}^n} \frac{1}{2} h^2 \frac{\Gamma_{j+1}^n - \Gamma_j^n}{\Delta x} & \text{if } h_j^n < h_{j+1}^n \\ \max_{h_{j+1}^n \le h \le h_j^n} \frac{1}{2} h^2 \frac{\Gamma_{j+1}^n - \Gamma_j^n}{\Delta x} & \text{if } h_{j+1}^n < h_j^n \end{cases}
$$

and the flux for (3.6.9b) is

$$
\mathcal{G}_{j+\frac{1}{2}}^{n+1} = \bar{h}_{j+\frac{1}{2}}^{n+1} \bar{\Gamma}_{j+\frac{1}{2}}^{n+1} \frac{\Gamma_{j+1}^{n+1} - \Gamma_j^{n+1}}{\Delta \xi}. \tag{3.6.11}
$$

Figure 3.5 and Figure 3.6 demonstrate the convergence of the scheme (3.6.9) for the height and surfactant profiles, respectively. As for the scheme (3.3.2), the solutions converge in Regions I, III but not in Region II. Also, as the grid is refined the solutions develop a jump as expected from the jump condition (3.1.20). We compare profiles created with the numerical scheme (3.3.2) to the profiles created with the scheme (3.6.9), in Figure 3.7. We observe that the profiles agree. Therefore the scheme (3.3.2) is acceptable for examination of the behavior in Regions I,III which are the areas of the solution we consider in Chapter 4.
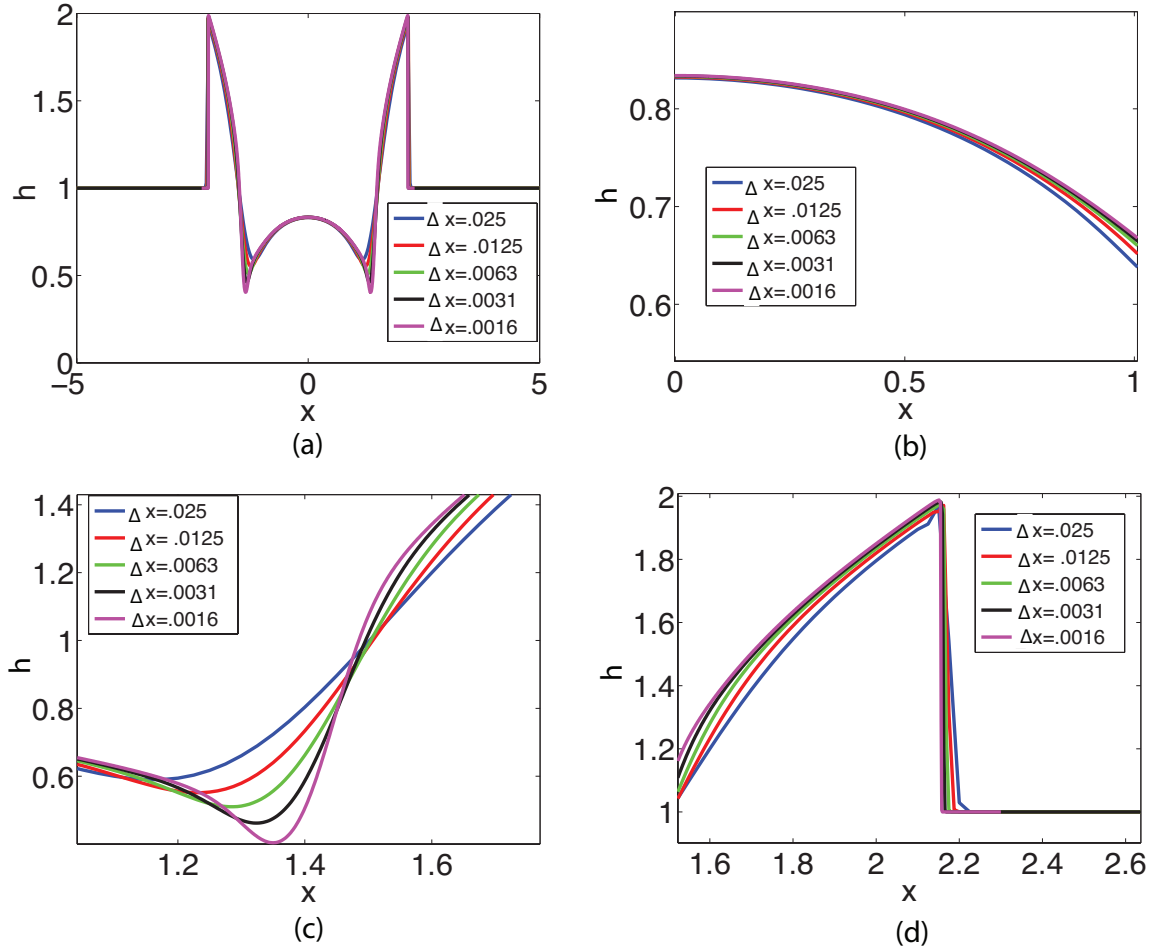
Figure 3.5: Numerical solutions of the height using the scheme (3.6.9) at $t = 1$ with $\Delta x =$ .025, .0125, .0063, .0031, .0016. (a) The full solution in physical variable x. (b) Region I. (c) Region II. (d) Region III.
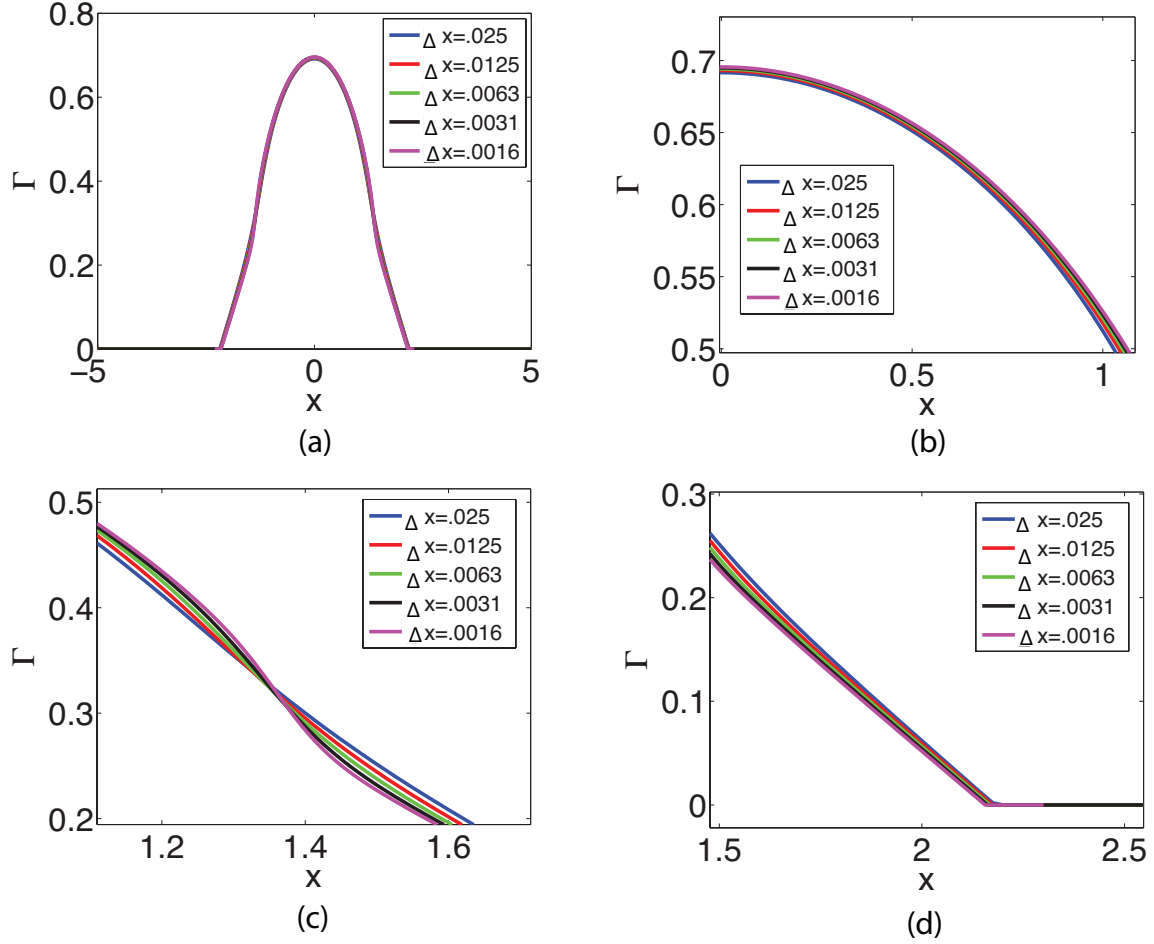
Figure 3.6: Numerical solutions of the surfactant using the scheme (3.6.9) at $t = 1$ with $\Delta x = .025, .0125, .0063, .0031, .0016$. (a) The full solution in physical variable x. (b) Region I. (c) Region II. (d) Region III.
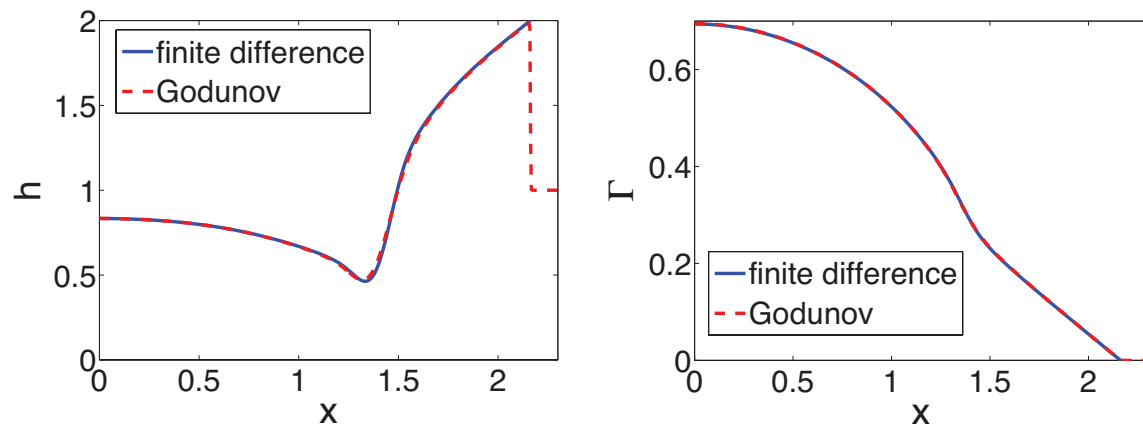
Figure 3.7: Comparison of the schemes (3.3.2) and (3.6.9) with $\Delta x = 0.0035$ at $t = 0.9$. Left: height h; Right: Surfactant Concentration Γ.

3.7 Axisymmetric Flow

We also consider the spreading of an axisymmetric droplet. Here we are working in cylindrical coordinates (r, θ, z) but assume the solutions are independent of θ due to axisymmetry and define $z = h$. The equations are

$$h_t = \frac{1}{r} \left(r \tfrac{1}{2} h^2 \Gamma_r \right)_r \tag{3.7.1a}$$

$$\Gamma_t = \frac{1}{r} \left(r h \Gamma \Gamma_r \right)_r \tag{3.7.1b}$$

with boundary and initial conditions equivalent to (3.1.1).

The axisymmetric equations have similar properties to the planar case. Chertock [16] extended the numerical method developed by Barenblatt et. al. [3] to the axisymmetric case. We follow a similar procedure by again introducing a scaled variable $\hat{\xi} = \frac{r}{r_0(t)}$ so that (3.7.1) becomes, dropping the $\hat{}$,

$$h_t = \frac{\xi \dot{r}_0(t)}{r_0(t)} h_\xi + \frac{1}{\xi r_0(t)^2} \left(\tfrac{1}{2} \xi h^2 \Gamma_\xi \right)_\xi \tag{3.7.2a}$$

$$\Gamma_t = \frac{\xi \dot{r}_0(t)}{r_0(t)} \Gamma_\xi + \frac{1}{\xi r_0(t)^2} \left(\xi h \Gamma \Gamma_\xi \right)_\xi \tag{3.7.2b}$$

$$\dot{r}_0(t) = -\frac{1}{r_0(t)} h(1,t) \Gamma_\xi(1,t) \tag{3.7.2c}$$

where $0 \leq \xi \leq 1$.
The resulting numerical scheme is

$$h_j^{n+1} = h_j^n + \Delta t \xi_j \frac{r_0^{n+1} - r_0^n}{r_0^n \Delta t} \left(\frac{h_{j+1}^{n+1} - h_j^{n+1}}{\Delta \xi} \right) + \frac{\Delta t}{\xi_j (r_0^n)^2 \Delta \xi} \left(\mathcal{F}_{j+\frac{1}{2}}^{n+1} - \mathcal{F}_{j-\frac{1}{2}}^{n+1} \right) \tag{3.7.3a}$$

$$\Gamma_j^{n+1} = \Gamma_j^n + \Delta t \xi_j \frac{r_0^{n+1} - r_0^n}{r_0^n \Delta t} \left(\frac{\Gamma_{j+1}^{n+1} - \Gamma_j^{n+1}}{\Delta \xi} \right) + \frac{\Delta t}{\xi_j (r_0^n)^2 \Delta \xi} \left(\mathcal{G}_{j+\frac{1}{2}}^{n+1} - \mathcal{G}_{j-\frac{1}{2}}^{n+1} \right) \tag{3.7.3b}$$

with flux functions

$$\mathcal{F}_{j+\frac{1}{2}} = \tfrac{1}{2} \bar{\xi}_{j+\frac{1}{2}} \left(\bar{h}_{j+\frac{1}{2}} \right)^2 \frac{\Gamma_{j+1} - \Gamma_j}{\Delta \xi}, \qquad \mathcal{G}_{j+\frac{1}{2}} = \bar{\xi}_{j+\frac{1}{2}} \bar{h}_{j+\frac{1}{2}} \bar{\Gamma}_{j+\frac{1}{2}} \frac{\Gamma_{j+1} - \Gamma_j}{\Delta \xi} \tag{3.7.4a}$$

and

$$r_0^{n+1} = r_0^n + \Delta t \frac{2}{r_0^n} \frac{\Gamma_{N-1}^n}{\Delta \xi}. \tag{3.7.5}$$

Figure 3.8 shows the numerical solutions on the fixed domain. Note the solutions have a similar structure as in planar coordinates, shown in Figure 3.2.
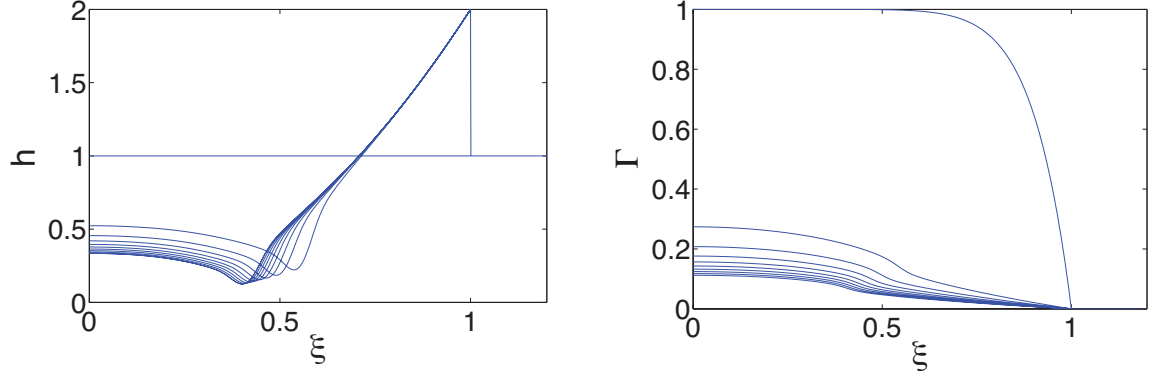
Figure 3.8: The height (left) and surfactant concentration (right) profiles (axisymmetric case) in the scaled variable $\xi = \frac{r}{r_0(t)}$ with $t = 0, 5, 10\ 20, ...45$ and $\Delta\xi = 0.001$.

In axisymmetric coordinates the mass of the fluid and surfactant between $r = 0$ and the free boundary $r = r_0$ is

$$m_h^r = \int_0^{r_0(t)} hr\ dr = \int_0^1 r_0^2 h\xi\ d\xi \tag{3.7.6}$$

$$m_g^r = \int_0^{r_0(t)} \Gamma r\ dr = \int_0^1 r_0^2 \Gamma\xi\ d\xi. \tag{3.7.7}$$

Thus the excess mass functions are

$$M_h^r(t) = \int_0^1 r_0^2 h(\xi, t)\xi\ d\xi - \tfrac{1}{2}r_0^2 \tag{3.7.8}$$

$$M_g^r(t) = \int_0^1 r_0^2 \Gamma(\xi, t)\xi\ d\xi - \int_0^1 \Gamma(\xi, 0)\xi\ d\xi. \tag{3.7.9}$$

Following the same procedure as in §3.4, we can show that the mass is conserved in the numerical scheme up to $O(\Delta\xi)$ over finite time intervals.

Chapter 4

Similarity Solutions

In this chapter, we examine the existence of a similarity solution for the simplified system, $\beta = \kappa = \delta = 0$. In §4.1, we analyze the solutions for the system in planar coordinates. Then in §4.2 we show the corresponding analysis for the system in axisymmetric coordinates.

4.1 Planar Coordinates

Recall from Chapter 3, in the planar case we consider a strip of surfactant deposited on a flat thin liquid film. We assume that along the strip the surfactant spreads uniformly which reduces the problem to one spatial dimension. Using the numerical method described in §3.2, numerical solutions of the system (3.2.2-3.2.5) are generated. Figure 3.2 is the numerical solution for the height (3.2.2a) and surfactant (3.2.2b) profiles. There are three regions to consider for the solution as labeled in Figure 3.4. We will only consider Region I, which we refer to as the inner solution, and Region III, which we refer to as the outer solution. In §4.1.1 we investigate the outer solution through a similarity scaling analysis, phase plot, and show the equations (3.1.4) are scale invariant. Then in §4.1.2 we perform a similar analysis for the inner solution but show in fact the solutions are not self similar. We do not investigate the structure of the solution in Region II.

4.1.1 Outer Solution

We seek a similarity solution for the outer solution of the height and surfactant concentration profiles. Jensen and Grotberg [35] determined a scaling for this region and Jensen [34] investigated the existence of a solution through a phase plane analysis. Using these as a guide, we explore the existence of a similarity solution.

Similarity Scaling

While Jensen and Grotberg [35] determined a similarity scaling for the outer solution, the solutions were compared to numerical simulations including the smoothing effects from β, κ, δ. In this section, we derive those scalings for the height and surfactant profiles but then are able to use the numerical simulations generated from the simplified system to confirm the scalings. We must incorporate a scaling parameter a in order to include the effects of the mass of surfactant. The analogous scaling parameter for the height is taken to be $a_h = 1$ since the initial height of the film is normalized to $h = 1$. Scaling Γ by a requires time to also be scaled by a, thus we consider solutions of the form

$$h_a(x, at) = h_1(x, at), \qquad \Gamma_a(x, t) = a\Gamma_1(x, at) \tag{4.1.1}$$

This balance is shown below in the discussion of Scale Invariant Solutions. For now, we take $a = 1$ but when matching to numerical simulations we determine a from the initial mass of the surfactant.

We begin with the equations on the physical domain (3.1.4). Let

$$h_1(x, t) = t^\mu H(\rho), \qquad \Gamma_1(x, t) = t^\nu G(\rho), \qquad \rho = \frac{x}{t^\lambda}. \tag{4.1.2}$$

Note with this scaling, $0 \leq \rho \leq 1$ since the leading edge of the surfactant is located at $x = t^\lambda$. Also $G(1) = 0$. The boundary conditions are equivalent to (3.2.4) with initial conditions (3.2.3). Substituting into (3.1.4) we obtain

$$\mu t^{\mu-1} H - \lambda t^{\mu-1} \rho H' - t^{2\mu+\nu-2\lambda} \left(\tfrac{1}{2} H^2 G'\right)' = 0 \tag{4.1.3a}$$

$$\nu t^{\nu-1} G - \lambda t^{\nu-1} \rho G' - t^{\mu+2\nu-2\lambda} \left(HGG'\right)' = 0 \tag{4.1.3b}$$

in which $' = \frac{d}{d\rho}$. Balancing powers of t we find

$$\mu + \nu - 2\lambda + 1 = 0. \tag{4.1.4}$$

Utilizing this relation (4.1.3) reduces to

$$\mu H - \lambda \rho H' - \left(\tfrac{1}{2} H^2 G'\right)' = 0 \tag{4.1.5a}$$

$$\nu G - \lambda \rho G' - (HGG')' = 0 \tag{4.1.5b}$$

which may be written as a non-autonomous system of three equations for $(H, G, G')(\rho)$.

A two parameter family of solutions exist for (4.1.4); we seek further equations to restrict

the solutions. Conservation of the total mass of the surfactant,

$$\int_0^{t^\lambda} \Gamma \, dx = \int_0^1 t^{\nu+\lambda} G(\rho) \, d\rho$$

implies

$$\nu + \lambda = 0. \tag{4.1.6}$$

Finally, the boundary condition $h = 2$ at $\rho = 1$, which doesn't change with time, implies

$$\mu = 0. \tag{4.1.7}$$

Combining (4.1.4), (4.1.6), and (4.1.7), we find the scaling exponents

$$\mu = 0, \qquad \nu = -\frac{1}{3}, \qquad \lambda = \frac{1}{3}. \tag{4.1.8}$$

Figure 4.1 shows this similarity scaling with the numerical solutions for $1000 < t < 10000$ using the spatial variable $\xi = \frac{x}{x_0(t)}$. With these scalings, the plots form a single line in the region around $\rho = 1$. Therefore we can deduce that (4.1.8) is an accurate similarity scaling.

We compare the spatial variable $\rho = \frac{x}{(at)^\lambda}$ to the spatial variable $\xi = \frac{x}{x_0(t)}$ used in §3.2. Specifically we examine the dependence of $x_0(t)$ on t. In Figure 4.2 we plot $x_0(t)$ against t on a log-log plot. The graph is a straight line with slope $\frac{1}{3}$, for comparison a straight line with this slope is also plotted. Thus, Figure 4.2 shows that $x_0(t) \sim t^{\frac{1}{3}}$. Therefore the numerical simulations support the determined scaling of the spatial variable with respect to time. Figure 4.3 shows $x_0(t) \approx (Dt)^{\frac{1}{3}}$ where $D = \frac{120}{11}$ is a scaling which incorporates the initial surfactant mass and is determined below by the scale invariance of the equations. Notice there is a slight discrepancy between $x = x_0$ and $x = (Dt)^{\frac{1}{3}}$ which is due to the difference between the numerical solutions and the similarity solution. This comparison is made below and exhibited in Figure 4.5. Notice the numerical simulations near $x = 0$ are larger than the expected similarity solution for the surfactant concentration. In order to account for this disparity the numerical simulations are smaller than the similarity solution away from this region in order to conserve mass. Thus the slope of the surfactant profile at the leading edge is smaller than the predicted slope in the similarity solution which causes the spreading to occur at a slightly slower rate.

Phase Plane

Jensen [34] investigated the phase plane associated with the system of equations (4.1.5). In this section we outline Jensen's procedure that reduces the system to an autonomous vector field
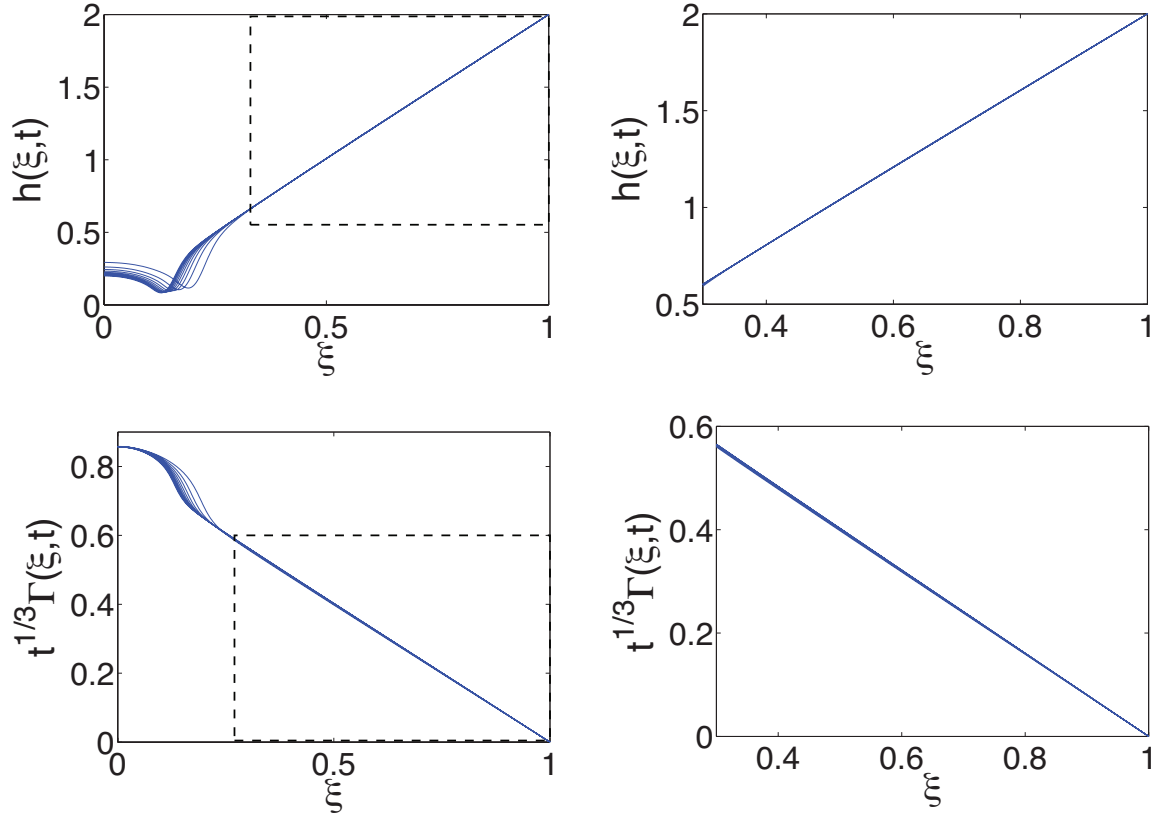
Figure 4.1: The height profile $h(\xi, t)$ (top left) with zoomed in similarity scaled region (top right). The scaled surfactant profile $t^{\frac{1}{3}}\Gamma(\xi, t)$ (bottom left) with zoomed in similarity scaled region (bottom left) for $1000 \leq t \leq 10000$.

in $\mathbb{R}^2$. The phase plane is then interpreted to better understand the solutions. We begin by writing the PDE system (3.1.4) in the form

$$h_t + \left(\tfrac{1}{2}hv\right)_x = 0 \tag{4.1.9a}$$

$$\Gamma_t + (\Gamma v)_x = 0 \tag{4.1.9b}$$

$$v + h\Gamma_x = 0 \tag{4.1.9c}$$

where $v(x, t)$ is the surface velocity. Recognizing that $v(x, t)$ scales like $\frac{x}{t}$ we scale $h\Gamma$ by $\frac{x^2}{t}$. We now define a change of variables

$$h(x, t) = \left(\frac{x^2}{t}\right)^{\alpha} \hat{h}(x, t), \qquad \Gamma(x, t) = \left(\frac{x^2}{t}\right)^{1-\alpha} \hat{\Gamma}(x, t), \qquad v(x, t) = \left(\frac{x}{t}\right) \hat{v}(x, t) \tag{4.1.10}$$
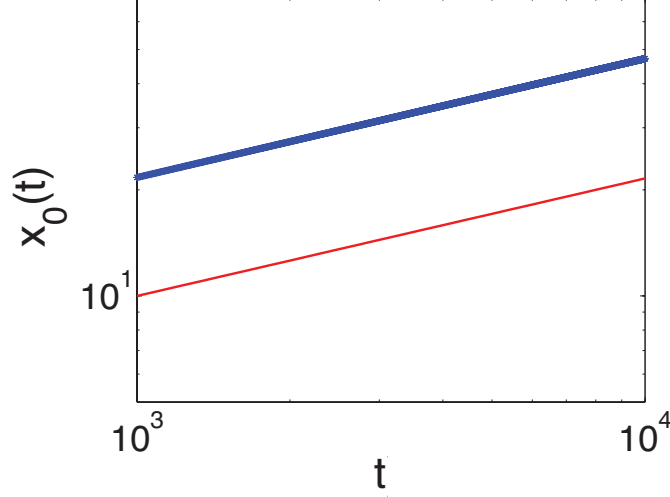
Figure 4.2: Log-log plot of the location of the leading edge of surfactant $x_0(t)$ vs. t. The comparison line (thin, red) has slope $\frac{1}{3}$.

where $\alpha \geq 0$ is constant and $t > 0$. We want to investigate the phase plane which corresponds to the similarity scaling above. Since $h(x_0(t), t) = 2$, the height profile is not scaled by time, so that $\alpha = 0$. The system (4.1.9) is then transformed to

$$2t\hat{h}_t + x\left(\hat{h}\hat{v}\right)_x + \hat{h}\hat{v} = 0 \tag{4.1.11a}$$

$$t\hat{\Gamma}_t - \hat{\Gamma} + x\left(\hat{\Gamma}\hat{v}\right)_x + 3\hat{\Gamma}\hat{v} = 0 \tag{4.1.11b}$$

$$\hat{v} + 2\hat{h}\hat{\Gamma} + x\hat{h}\hat{\Gamma}_x = 0. \tag{4.1.11c}$$

We seek similarity solutions that are functions of the single variable $\rho = \frac{x}{t^\lambda}$. In this section, we consider $\lambda = \frac{1}{3}$ from (4.1.8) which is also in agreement with Figure 4.2. In order to make (4.1.11) autonomous we define $\varphi = \log|\rho|$ and write solutions of (4.1.11) in the form

$$\hat{h}(x, t) = H(\varphi), \qquad \hat{\Gamma}(x, t) = G(\varphi), \qquad \hat{v}(x, t) = V(\varphi). \tag{4.1.12}$$

Then

$$H_\varphi\left(V - \frac{2}{3}\right) + HV_\varphi + HV = 0 \tag{4.1.13a}$$

$$G_\varphi\left(V - \frac{1}{3}\right) + GV_\varphi - G + 3GV = 0 \tag{4.1.13b}$$

$$V + 2HG + HG_\varphi = 0. \tag{4.1.13c}$$

46
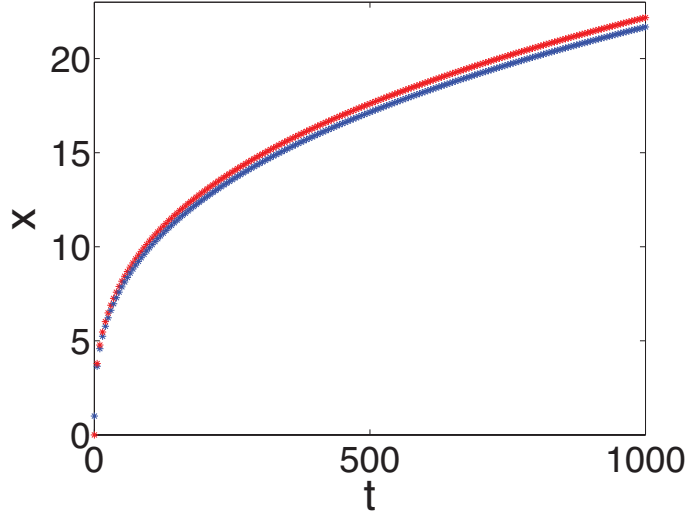
Figure 4.3: The location of the leading edge of the surfactant $x = x_0(t)$ in blue compared to $x = (Dt)^{\frac{1}{3}}$ where $D = \frac{120}{11}$ in red.

Next we reduce this 3×3 system to a 2×2 system by eliminating H through another change of variables $U(\varphi) = HG$ and substituting in for $H = \frac{U}{G}$. But then G is only present in the combination $\frac{G_\varphi}{G}$ which suggests a change of variable $\psi = \log|G|$. By eliminating ψ_φ from resulting equation from (4.1.13c) and substituting into (4.1.13a-4.1.13b) we find

$$\frac{dU}{d\varphi} = -\frac{2V - 1}{V - \frac{2}{3}} (U + V) \tag{4.1.14a}$$

$$\frac{dV}{d\varphi} = -\frac{V - \frac{1}{3}}{U} (U - V). \tag{4.1.14b}$$

In Figure 4.4 we show the phase plane for the system of equations (4.1.14), generated using the pplane8 program in MATLAB. Recall we are considering the domain $0 \leq \rho \leq 1$. In the transformed variables, $\rho = 0$ corresponds to $\varphi = -\infty$ and $\rho = 1$ to $\varphi = 0$. Since $h(x,t) > 0$, $\Gamma(x,t) > 0$ for all x and t, $U(\varphi) = H(\varphi)G(\varphi) > 0$. From (4.1.9c),(4.1.10), and (4.1.12) the velocity can be written as $V(\phi) = -\frac{t}{x}h\Gamma_x > 0$ since $\Gamma_x < 0$. Thus we expect the trajectory which corresponds to the similarity solution to be in quadrant I of the phase plane. Specifically we consider the trajectory which corresponds to $V = \frac{1}{3}$; for which $\frac{dV}{d\varphi} = 0$. And we seek the $U(\varphi)$ that corresponds to $V = \frac{1}{3}$,

$$\frac{dU}{d\varphi} = -U - \frac{1}{3}.$$

47

Integrating gives

$$U = ae^{-\varphi} - \tfrac{1}{3}.$$

We let $a = \tfrac{1}{3}$ so that $U \to 0$ as $\varphi \to 0$. Note also that $U \to \infty$ as $\varphi \to -\infty$.
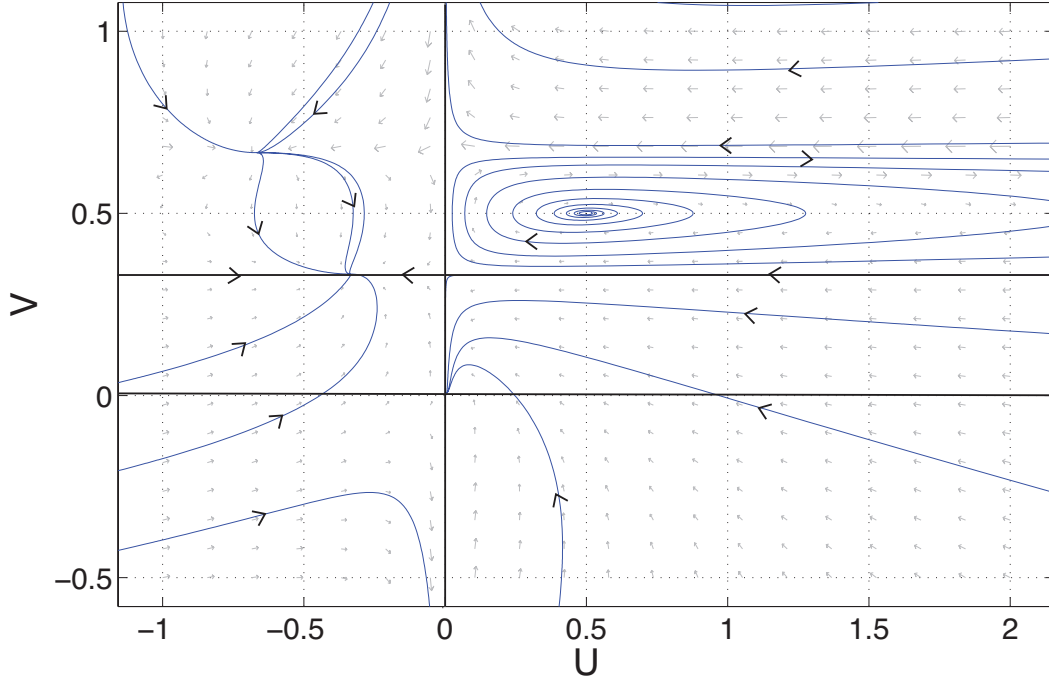
Figure 4.4: Phase plot of (4.1.9)

Using the definition $\varphi = \log |\rho|$ we find

$$U = HG = \tfrac{1}{3}\left(\frac{1-\rho}{\rho}\right). \qquad (4.1.15)$$

We now write $V(\varphi) = -\tfrac{t}{x}h\Gamma_x$ in terms of H, G using (4.1.12)

$$V = -\frac{1}{\rho}H\left(\rho^2 G\right)_\rho = \tfrac{1}{3}. \qquad (4.1.16)$$

48

Solving (4.1.15) for H, we then use (4.1.16) to determine a formula for G

$$G(\rho) = A\frac{1-\rho}{\rho^2}.$$

and implementing this definition in (4.1.15) we find

$$\begin{aligned} H &= \frac{1}{3G\rho}(1-\rho) \\ &= \frac{\rho^2}{3\rho A(1-\rho)}(1-\rho) \\ &= \frac{\rho}{3A}. \end{aligned}$$

The boundary condition $H(1,t) = 2$ implies the constant $A = \frac{1}{6}$. Thus the solutions in terms of $h(\rho,t)$, $\Gamma(\rho,t)$ are

$$\begin{aligned} h &= 2\rho && \text{(4.1.17a)} \\ \Gamma &= \frac{1}{6t^{\frac{1}{3}}}(1-\rho). && \text{(4.1.17b)} \end{aligned}$$

Note that the explicit solutions (4.1.17) can be achieved in an easier manner by observing that (4.1.5) is integrable.

In order to compare the explicit solutions to the numerical solutions of (3.2.2) we must incorporate the initial surfactant mass through the scaling of Γ (4.1.1). Below we show the simplified system is scale invariant. Figure 4.5 shows the numerical solutions of (3.2.2) and the scaled similarity solutions (4.1.17) at $t = 10000$.

Scale Invariant Solutions

In this section we show that the equations (3.1.4) are scale invariant and connect that property to the similarity solutions discussed above. Consider the scalings

$$h(x,t) = a\hat{h}(x,t), \qquad \Gamma(x,t) = b\hat{\Gamma}(x,t), \qquad x = c\hat{x}, \qquad t = d\hat{t}. \qquad \text{(4.1.18)}$$

Then (3.1.4) becomes

$$\begin{aligned} \frac{a}{d}\hat{h}_t &= \frac{a^2 b}{c^2}(\tfrac{1}{2}\hat{h}^2\hat{\Gamma}_{\hat{x}})_{\hat{x}} \\ \frac{b}{d}\hat{\Gamma}_t &= \frac{ab^2}{c^2}(\hat{h}\hat{\Gamma}\hat{\Gamma}_{\hat{x}})_{\hat{x}}. \end{aligned}$$
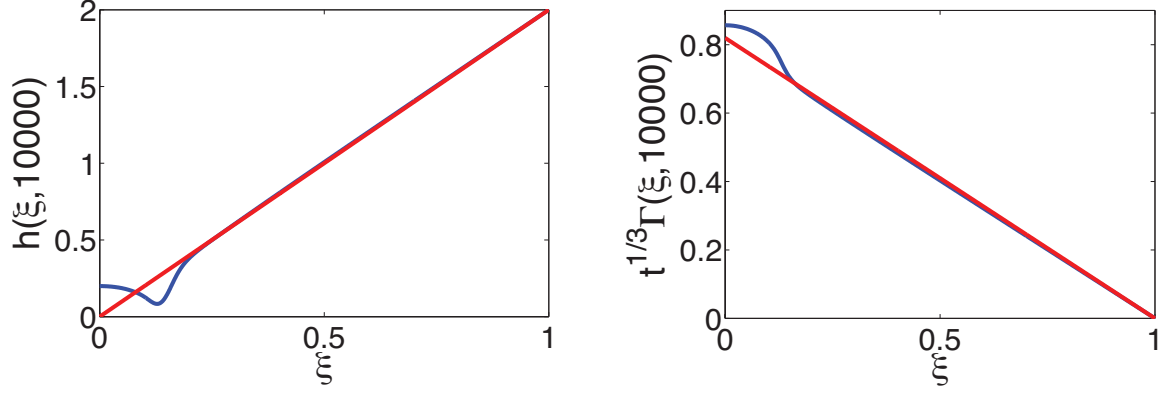
Figure 4.5: The height h (left) and surfactant concentration Γ (right) profiles at $t = 10000$, in blue, plotted against the similarity solutions (4.1.17), in red.

Balancing the coefficients we determine

$$b = \frac{c^2}{ad}. \tag{4.1.19}$$

Exploiting the relations determined by the invariant scaling we search for self-similar solutions. We consider the spatial variables to be scaled by time

$$\hat{h}(x,t) = t^\mu H(\rho), \quad \hat{\Gamma}(x,t) = t^\nu G(\rho), \quad \rho = \frac{x}{t^\lambda}. \tag{4.1.20}$$

Implementing the scalings from (4.1.18) we determine a the spatial variable ρ to be of the form

$$\rho = \frac{x}{t^\lambda} = \frac{c\hat{x}}{(d\hat{t})^\lambda}.$$

We take the spatial scale to be independent of the scaling parameters chosen which requires the relation

$$c = d^\lambda. \tag{4.1.21}$$

Equating (4.1.19) and (4.1.21) results in

$$c = (abd)^{\frac{1}{2}} \quad = \quad d^\lambda$$

$$\tag{4.1.22}$$

which implies

$$(ab)^{\frac{1}{2}} = d^{\lambda - \frac{1}{2}} \qquad (4.1.23)$$

and suggests

$$a = d^{\mu}, \qquad b = d^{\nu}. \qquad (4.1.24)$$

Using (4.1.23) and (4.1.24) we find a relation for the scaling exponents μ, ν, λ

$$\frac{\mu}{2} + \frac{\nu}{2} = \lambda - \frac{1}{2} \qquad (4.1.25)$$

which is the same scaling as (4.1.4) found from the similarity scaling

$$2\lambda = \mu + \nu + 1. \qquad (4.1.26)$$

From the restrictions stipulated by the conservation of mass of surfactant (4.1.6), the boundary condition (4.1.7), and (4.1.26) we find

$$\mu = 0, \qquad \nu = -\tfrac{1}{3}, \qquad \lambda = \tfrac{1}{3}. \qquad (4.1.27)$$

$$(4.1.28)$$

Absorbing the scaling of ρ into the time variable, we consider

$$h(x,t) = aH(\rho), \qquad \Gamma(x,t) = bt^{-\frac{1}{3}}G(\rho), \qquad \rho = \frac{x}{(Dt)^{\frac{1}{3}}}. \qquad (4.1.29)$$

and substitute into (3.1.4) which results in the ODE

$$-\tfrac{1}{3}a\rho H' - \frac{a^2 b}{D^{\frac{2}{3}}}\left(\tfrac{1}{2}H^2 G'\right)' = 0 \qquad (4.1.30a)$$

$$-\tfrac{1}{3}bG - \tfrac{1}{3}b\rho G' - \frac{ab^2}{D^{\frac{2}{3}}}\left(HGG'\right)' = 0. \qquad (4.1.30b)$$

We can then further relate the scaling coefficients to find

$$b = \frac{D^{\frac{2}{3}}}{a}.$$

Then (6.2.9) becomes (4.1.5) with the use of (4.1.27). We consider the initial condition $h(\rho, 0) =$

1 which represents a normalized height and suggests $a = 1$. The resulting balance is $b = D^{\frac{2}{3}}$ where D is determined by relating the initial surfactant mass to the explicit solution (4.1.17b)

$$\int_0^1 \frac{D}{6}(1 - \rho)d\rho = \int_0^1 \Gamma_0 dx.$$

The initial conditions (3.2.3) require that $D = \frac{120}{11}$. The corresponding explicit solutions

$$h(\rho, t) = 2\rho$$
$$\Gamma(\rho, t) = \frac{\left(\frac{120}{11}\right)^{\frac{2}{3}}}{6t^{\frac{1}{3}}}(1 - \rho).$$

are plotted in Figure 4.5.

4.1.2 Inner Solution

We now investigate the inner solution of (3.1.4) which is labeled Region I in Figure 3.4. In [35], Jensen and Grotberg performed an initial investigation of the scaling exponent for the height and surfactant profiles near $x = 0$. In the planar case, the following analysis is different than Jensen and Grotberg's approach but the results agree. We begin with a numerical investigation to determine the approximate scaling exponents for a similarity solution. Then we show that a similarity solution exists through a phase plane analysis. However, the similarity solution does not agree with the numerical solutions. Subsequently we explore the existence of non-self-similar solutions through an asymptotic analysis.

Numerical Investigation

We consider a regular expansion in the variable $\eta = \frac{x}{t^\lambda}$ for the height and surfactant variables. Due to the boundary conditions $h_\eta(\eta, t) = \Gamma_\eta(\eta, t) = 0$ and the form of the solutions being even functions of η, we consider an expansion of the form

$$h(x, t) = t^\mu \left(H_0(t) + \tfrac{1}{2}H_1(t)\eta^2 + \dots \right) \tag{4.1.31a}$$
$$\Gamma(x, t) = t^\nu \left(G_0(t) + \tfrac{1}{2}G_1(t)\eta^2 + \dots \right). \tag{4.1.31b}$$

Using the numerical simulations discussed in §3.3 we have simulations for $0 \leq t \leq 10000$. First we determine the scaling exponents μ and ν. Figure 4.6 is a log-log plot of the values of $h(0, t)$ and $\Gamma(0, t)$. Notice that the points create a straight line, the slopes of these lines give $\mu \approx -\frac{1}{6}$ and $\nu \approx -\frac{1}{3}$. Using these scaling exponents μ and ν in the relation (4.1.4) we find $\lambda \approx \frac{1}{4}$. In Figure 4.7 we implement these scaling exponents near $\eta = 0$ and observe the plots sit on top of each other.
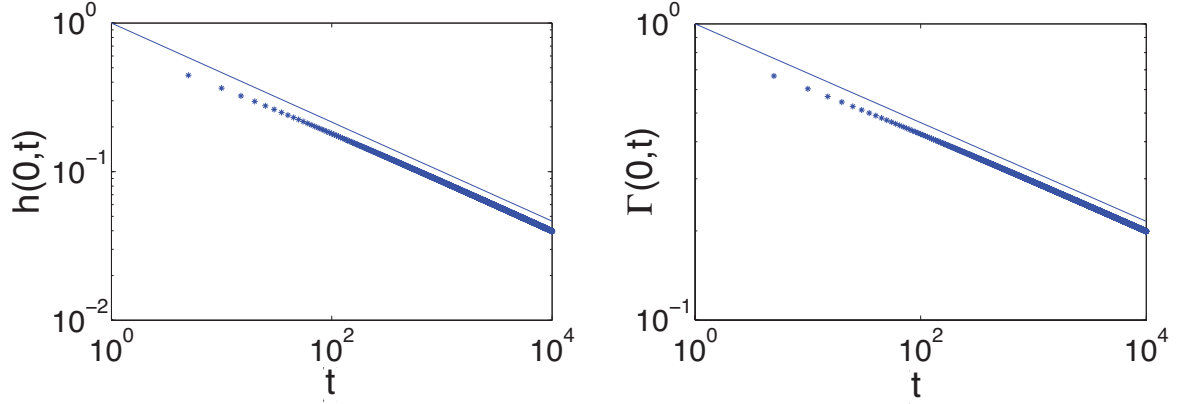
Figure 4.6: Log-log plot of $h(0,t)$ (left) and $\Gamma(0,t)$(right) against t where $0 < t < 10000$, each $*$ is an increment of $t = 5$. The thin comparison line on the height plot (left) has slope $-\frac{1}{6}$ and in the surfactant plot (right) the line has slope $-\frac{1}{3}$.

Note $\nu = 2\mu$ which we prove is inherent to the system in the following lemma:

Lemma 2 *Consider the system of equations (3.1.4). If $h_x(0,t) = \Gamma_x(0,t) = 0$ then $h^2(0,t) = \Gamma(0,t)$.*

Proof: Let h, Γ be solutions of (3.1.4). Consider the equations evaluated at $x = 0$. Then

$$h_t = (\tfrac{1}{2}h^2\Gamma_x)_x = hh_x\Gamma_x + \tfrac{1}{2}h^2\Gamma_{xx} = \tfrac{1}{2}h^2\Gamma_{xx}$$

since $h_x(0,t) = \Gamma_x(0,t) = 0$. Similarly,

$$\Gamma_t = (h\Gamma\Gamma_x)_x = h_x\Gamma\Gamma_x + h\Gamma_x^2 + h\Gamma\Gamma_{xx} = h\Gamma\Gamma_{xx}.$$

Thus

$$2\frac{h_t}{h} = \frac{\Gamma_t}{\Gamma}$$

which implies $h^2 = A\Gamma$ but from the initial conditions $h(0,0) = \Gamma(0,0) = 1$, therefore $A = 1$. This produces the result

$$h^2(0,t) = \Gamma(0,t). \qquad \blacksquare$$

Thus when h and Γ are scaled by time, the scaling exponent of Γ must be twice the scaling exponent of h.
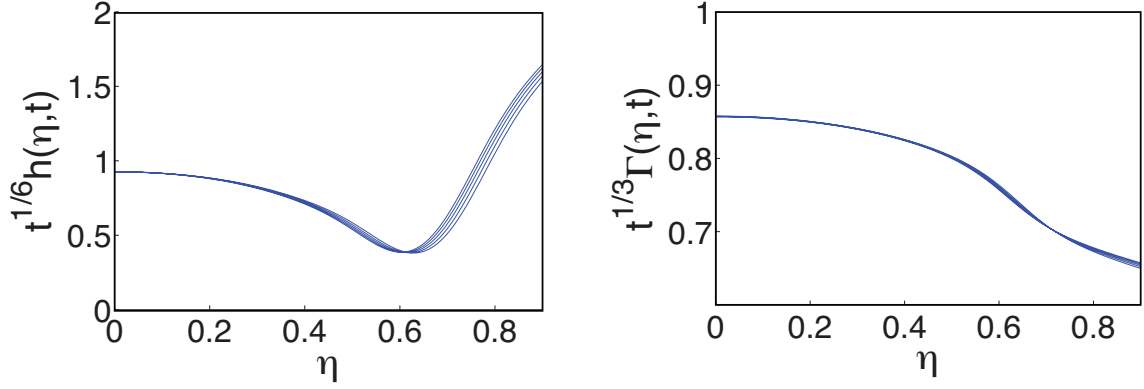
Figure 4.7: The scaled height profile $t^{\frac{1}{6}}h(\eta,t)$ (left) and the scaled surfactant profile $t^{\frac{1}{3}}\Gamma(\eta,t)$ (right) where $\eta = \frac{x}{t^{\frac{1}{4}}}$.

Next we investigate the leading order terms, $H_0(t)$ and $G_0(t)$, in the expansion (4.1.31). Figure 4.8 is a plot of $H_0(t) = t^{\frac{1}{6}}h(0,t)$ and $G_0(t) = t^{\frac{1}{3}}\Gamma(0,t)$. This figure demonstrates that these values are approximately constant with respect to time with $H_0 \approx 0.926$ and $G_0 \approx 0.8575$. Also, note $G_0 \approx H_0^2$ as expected from Lemma 2.
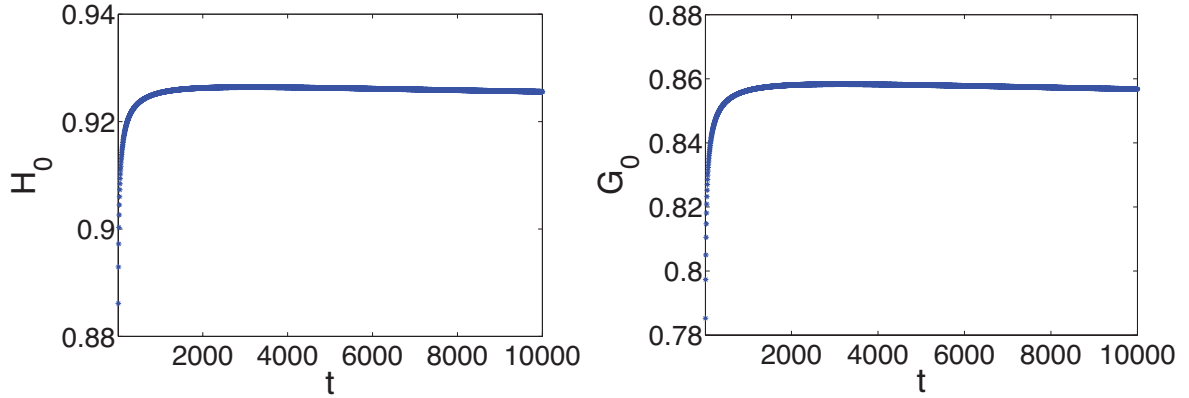
Figure 4.8: $H_0 = t^{\frac{1}{6}}h(0,t)$ vs. t (left) and $G_0 = t^{\frac{1}{3}}\Gamma(0,t)$ vs. t (right).

The values $H_1(t)$ and $G_1(t)$ can be determined by setting $h(\eta,t) = t^{\frac{1}{6}}H(\eta,t)$, $\Gamma(\eta,t) =$
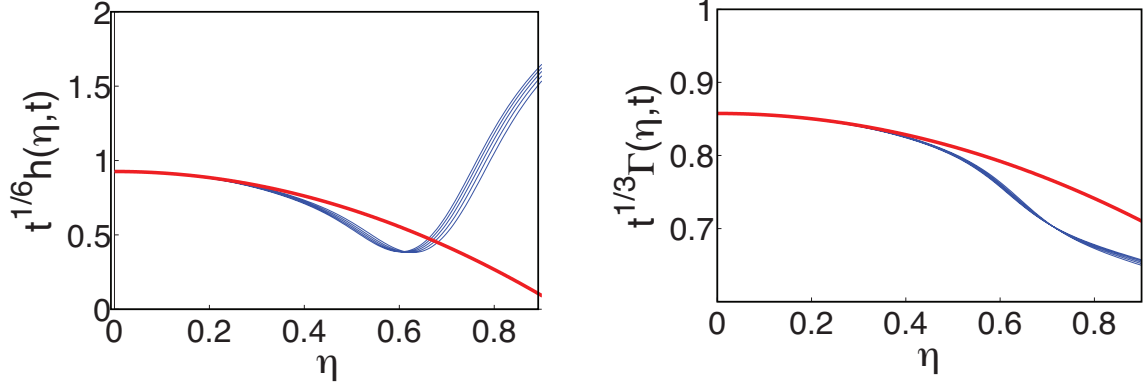
Figure 4.9: The scaled solutions and numerical expansion for $5000 \leq t \leq 10000$. Left: The scaled solutions $t^{\frac{1}{6}} h(\eta, t)$ in blue and the expansion $H = .926 - \frac{2.06}{2}\eta^2$ in red. Right: The scaled solutions $t^{\frac{1}{3}} \Gamma(\eta, t)$ in blue and the expansion $G = .8575 - \frac{.3634}{2}\eta^2$ in red.

$t^{\frac{1}{3}} G(\eta, t)$ and using the Taylor series expansion of the form

$$H(\eta, t) = H_0 + \tfrac{1}{2} H_{\eta\eta}(0, t)\eta^2 + \dots \tag{4.1.32}$$

$$G(\eta, t) = G_0 + \tfrac{1}{2} G_{\eta\eta}(0, t)\eta^2 + \dots. \tag{4.1.33}$$

Comparing (4.1.31) and (4.1.32) we see that $H_1(t) = H_{\eta\eta}(0, t)$ and $G_1(t) = G_{\eta\eta}(0, t)$. Using a finite difference operator on the numerical data,

$$H_1 \approx \frac{H_3^n - 2H_2^n + H_1^n}{\Delta\eta^2} \approx -2.06$$

$$G_1 \approx \frac{G_3^n - 2G_2^n + G_1^n}{\Delta\eta^2} \approx -0.3634.$$

Note the finite difference is centered at the second grid points from the origin to avoid an inaccurate approximation due to the Neumann boundary conditions. In Figure 4.9, we plot the expansions $H = .926 - \frac{2.06}{2}\eta^2$ and $G = .8575 - \frac{0.3634}{2}\eta^2$ against the scaled numerical solutions, $t^{\frac{1}{6}} h(\eta, t)$ and $t^{\frac{1}{3}} \Gamma(\eta, t)$. We observe that the expansion fits the numerical simulations in the region near $\eta = 0$.

Phase Plane

The phase plane analysis outlined in §4.1.1 and [34] is relevant for the outer solution. However, we now want to seek a solution in which $x \to 0$. The analysis is not as straight-forward in this region, since two changes of variables introduce complications: (i) the change of variable

(4.1.10) appears to degenerate as $x \to 0$, (ii) the change of variables $\varphi = \log \left| \frac{x}{t^\lambda} \right|$ is used but now we are seeking solutions in which $\varphi \to -\infty$ as $x \to 0$. In this section, we handle both of these issues in order to create the phase plane.

Consider the system of equations (4.1.9) with the change of variables (4.1.10). We write (4.1.10) in the spatial variable $\eta = \frac{x}{t^\lambda}$

$$h(x,t) = \left(\frac{(t^\lambda \eta)^2}{t} \right)^\alpha \tilde{h}(\eta), \quad \Gamma(x,t) = \left(\frac{(t^\lambda \eta)^2}{t} \right)^{1-\alpha} \tilde{\Gamma}(\eta), \quad v(x,t) = \left(\frac{t^\lambda \eta}{t} \right) V(\eta) \qquad (4.1.34)$$

and relate to the scaling

$$h(x,t) = t^\mu Y(\eta), \quad \Gamma(x,t) = t^{2\mu} Z(\eta). \qquad (4.1.35)$$

Balancing the powers of t, the height variable defines

$$\alpha = \frac{\mu}{2\lambda - 1} \qquad (4.1.36)$$

and from the surfactant variable

$$\alpha = \frac{1 + 2\mu - 2\lambda}{1 - 2\lambda}.$$

Eliminating α, we solve for λ,

$$\lambda = \frac{3\mu + 1}{2}.$$

Note that the scalings determined in the numerical investigation $\mu = -\frac{1}{6}$, $\nu = -\frac{1}{3}$, $\lambda = \frac{1}{4}$ satisfy this relation. Using these scalings and (4.1.36) we find $\alpha = \frac{1}{3}$. The change of variables (4.1.10) with $\alpha = \frac{1}{3}$ in (4.1.9) results in a system of similar form to (4.1.11)

$$2t\hat{h}_t - \frac{2}{3}\hat{h} + x\left(\hat{h}\hat{v} \right)_x + \frac{5}{3}\hat{h}\hat{v} = 0 \qquad (4.1.37a)$$

$$t\hat{\Gamma}_t - \frac{2}{3}\hat{\Gamma} + x\left(\hat{\Gamma}\hat{v} \right)_x + \frac{7}{3}\hat{\Gamma}\hat{v} = 0 \qquad (4.1.37b)$$

$$\hat{v} + \frac{4}{3}\hat{h}\hat{\Gamma} + x\hat{h}\hat{\Gamma}_x = 0. \qquad (4.1.37c)$$

The scaling $\varphi = \log \eta$ transforms (4.1.34) to

$$h(x,t) = t^{-\frac{1}{6}} e^{\frac{2}{3}\varphi} H(\varphi), \qquad \Gamma(x,t) = t^{-\frac{1}{3}} e^{\frac{4}{3}\varphi} G(\varphi), \qquad v(x,t) = t^{-\frac{3}{4}} e^\varphi V(\varphi). \qquad (4.1.38)$$

Note we are interested in $\eta \to 0^+$ which corresponds to $\varphi \to -\infty$. Since $h(0,t) \sim t^{-\frac{1}{6}} H_0$ and

$$\Gamma(0,t) \sim t^{-\frac{1}{3}} G_0,$$

$$H(\varphi) = H_0 e^{-\frac{2}{3}\varphi} \to \infty, \qquad \text{as } \varphi \to -\infty$$

$$G(\varphi) = G_0 e^{-\frac{4}{3}\varphi} \to \infty, \qquad \text{as } \varphi \to -\infty.$$

Also $\Gamma_x(0,t) = 0$ stipulates that

$$e^\varphi V(\varphi) \to 0, \qquad \text{as } \varphi \to -\infty \tag{4.1.39}$$

which suggests $V(\varphi)$ is bounded. With the change of variables (4.1.38), (4.1.37) becomes

$$H_\varphi(V - \tfrac{1}{2}) + HV_\varphi - \frac{2}{3}H + \frac{5}{3}HV = 0 \tag{4.1.40a}$$

$$G_\varphi(V - \tfrac{1}{4}) + GV_\varphi - \frac{2}{3}G + \frac{7}{3}GV = 0 \tag{4.1.40b}$$

$$V + \frac{4}{3}HG + HG_\varphi = 0. \tag{4.1.40c}$$

Again we introduce another change of variable $U(\varphi) = HG$ and $\psi = \log\ G$ thus (4.1.40a), (4.1.40b) become

$$\frac{dU}{d\varphi} = -\left(2U + \frac{V(2V - \frac{3}{4})}{V - \frac{1}{2}}\right) \tag{4.1.41a}$$

$$\frac{dV}{d\varphi} = -\left(\frac{U(V - \frac{1}{3}) + V(\frac{1}{4} - V)}{U}\right). \tag{4.1.41b}$$

From (4.1.40c),

$$V + \frac{4}{3}U + U\frac{d\psi}{d\varphi} = 0$$

and solving for $\frac{d\psi}{d\varphi} = \frac{G'}{G}$,

$$\frac{d\psi}{d\varphi} = \frac{G'}{G} = \frac{-(V + \frac{4}{3}U)}{U}. \tag{4.1.42}$$

But $U = HG \to \infty$ as $\varphi \to -\infty$. Therefore, in order to work in a finite domain let $W = \frac{1}{U}$ so

that we are considering $W \to 0$ as $\varphi \to -\infty$. Then (4.1.41) becomes

$$\frac{dW}{d\varphi} = 2W + \frac{VW^2(2V - \frac{3}{4})}{V - \frac{1}{2}} \tag{4.1.43a}$$

$$\frac{dV}{d\varphi} = -\left((V - \frac{1}{3}) + VW(\frac{1}{4} - V)\right). \tag{4.1.43b}$$

Figure 4.10 is the phase portrait for (4.1.43). We consider solutions where V remains bounded as $\varphi \to -\infty$. From the phase portrait, Figure 4.10 we observe that trajectories that correspond to V being bounded approach the equilibrium $(W, V) = (0, \frac{1}{3})$ as $\varphi \to -\infty$. The eigenvalues and eigenvectors of (4.1.43) at this equilibrium point are

$$\lambda_1 = -1, \qquad \begin{pmatrix} w_{\lambda_1} \\ v_{\lambda_1} \end{pmatrix} = \begin{pmatrix} 0 \\ 1 \end{pmatrix} \tag{4.1.44a}$$

$$\lambda_2 = 2, \qquad \begin{pmatrix} w_{\lambda_2} \\ v_{\lambda_2} \end{pmatrix} = \begin{pmatrix} 1 \\ \frac{1}{3 \cdot 36} \end{pmatrix}. \tag{4.1.44b}$$

Since (4.1.44a) corresponds to a stable manifold, we are interested in the behavior of (4.1.44b). To determine the dynamics on the unstable manifold tangent to the eigenvector (4.1.44b) we expand about the equilibrium point $(0, \frac{1}{3})$

$$W = w_1 e^{2\varphi} + w_2 e^{4\varphi} + \cdots = w_1 \eta^2 + w_2 \eta^4 + \ldots \tag{4.1.45a}$$

$$V = \frac{1}{3} + v_1 e^{2\varphi} + \cdots = \frac{1}{3} + v_1 \eta^2 + \ldots. \tag{4.1.45b}$$

where the expansion is in terms of $\lambda_2 \varphi = 2\varphi$. From (4.1.44b) we know $v_1 = \frac{1}{3 \cdot 36} w_1$. Since $W = \frac{1}{U} = \frac{1}{HG}$ and $HG \sim H_0 G_0 e^{-2\varphi}$ as $\varphi \to -\infty$, we obtain $w_1 = \frac{1}{H_0 G_0}$. Thus $v_1 = \frac{1}{3 \cdot 36 H_0 G_0}$. We still seek w_2. Integrating and including up to the second order terms of (4.1.42), we find

$$G = \eta^{-\frac{4}{3}} \left(G_0 - \frac{1}{6H_0} \eta^2 + O(\eta^4) \right). \tag{4.1.46}$$

Since $H = \frac{1}{WG}$, using (4.1.45a) with $w_1 = \frac{1}{H_0 G_0}$ and (4.1.46) we find

$$\begin{aligned} WG &= \left(\frac{1}{H_0 G_0} \eta^2 + w_2 \eta^4 + \ldots \right) \left[\eta^{-\frac{4}{3}} \left(G_0 - \frac{1}{6H_0} \eta^2 + O(\eta^4) \right) \right] \\ &= \frac{1}{H_0} \eta^{\frac{2}{3}} \left(1 + w_2 H_0 G_0 \eta^2 \right) \left(1 - \frac{1}{6H_0 G_0} \eta^2 + O(\eta^4) \right) \end{aligned}$$
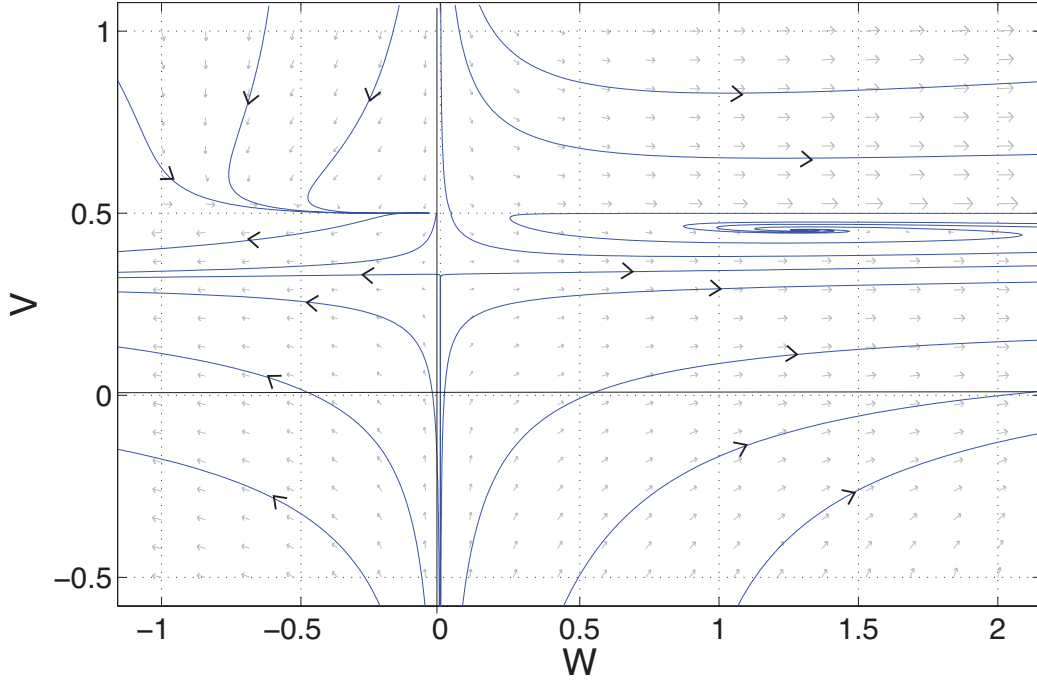
Figure 4.10: Phase plot of (4.1.43)

which implies

$$H = \frac{1}{WG} = H_0 \eta^{-\frac{2}{3}} \left(1 + \left(\frac{1}{6H_0 G_0} - w_2 H_0 G_0 \right) \eta^2 \right) + O(\eta^4). \qquad (4.1.47)$$

Consider the expression of the unstable manifold W as a function of $V - \frac{1}{3}$,

$$
\begin{aligned}
W &= W_m (V - \tfrac{1}{3}) \\
&= a(V - \tfrac{1}{3}) + b(V - \tfrac{1}{3})^2 + \dots, \qquad (4.1.48)
\end{aligned}
$$

where $a = 3 \cdot 36$, so that the curve (4.1.48) is tangent to the eigenvector in (4.1.44b). We still need to determine b. Differentiating (4.1.48) with respect to V

$$\frac{dW}{dV} = 3 \cdot 36 + 2b(V - \tfrac{1}{3}). \qquad (4.1.49)$$

But from (4.1.43) we also know

$$F(W,V) = \frac{dW}{dV} = \frac{2W + W^2 \frac{V(2V - \frac{3}{4})}{V - \frac{1}{2}}}{-((V - \frac{1}{3}) + VW(\frac{1}{4} - V))}. \tag{4.1.50}$$

Define $u = V - \frac{1}{3}$ then (4.1.48) becomes $W = au + bu^2$, substituting into (4.1.50), canceling a factor of u, and retaining leading order terms, we find

$$F(W,V) = \frac{2a + 2bu + \frac{1}{6}a^2 u}{\left(-1 + \frac{1}{36}a\right)\left(1 + \frac{\frac{5}{12}a + \frac{1}{36}b}{-1 + \frac{1}{36}a}u\right)} \tag{4.1.51}$$

Note that when $u = 0$, $a = 3 \cdot 36$ which corresponds to the relation from the eigenvector (4.1.44b). Equating $O(u)$ terms from (4.1.49) and (4.1.51)

$$2b = \frac{1}{2}\left(2b + \frac{1}{6}a^2\right) - \frac{1}{2}a\left(\frac{1}{36}b + \frac{5}{12}a\right)$$

since $a = 3 \cdot 36$ we find

$$b = -\frac{4 \cdot 9^3}{5}. \tag{4.1.52}$$

Now we must solve for u. Since $u = V - \frac{1}{3}$ then $u' = V'$. Using (4.1.43b) and substituting $W = au + bu^2$ and $V = u + \frac{1}{3}$ we find

$$u' = 2u + \frac{3^2 \cdot 4^2}{5}u^2.$$

Define $c = \frac{3^2 \cdot 4^2}{5}$ and integrate to determine

$$u = 2k\eta^2(1 + ck\eta^2)$$

where k is a constant of integration. Therefore, from (4.1.48)

$$W = 2ak\eta^2 + (2ack^2 + 4bk^2)\eta^4.$$

But we know $w_1 = \frac{1}{H_0 G_0} = 2ak$, thus $k = \frac{1}{2aH_0 G_0}$. Substituting in the definitions of the parameters a, b, c, k we find

$$w_2 = 2ack^2 + 4bk^2 = \frac{1}{12H_0^2 G_0^2}.$$

60

Finally, using (4.1.47) the expansion for H is

$$H = \eta^{-\frac{2}{3}} \left(H_0 + \frac{1}{12G_0}\eta^2 + \dots \right). \tag{4.1.53}$$

Therefore, a similarity solution corresponding to the scalings $\mu = -\frac{1}{6}$, $\nu = -\frac{1}{3}$, $\lambda = \frac{1}{4}$ exists. The form of the solution (4.1.53) suggests that the solution should be concave up near $\eta = 0$ since $G_0 > 0$. However, from the numerical simulations, we know that near $\eta = 0$, the solution is concave down. We further investigate this contradiction through an asymptotic analysis. We find that the solution illustrated by the numerical simulations is in fact not a similarity solution.

Asymptotic Analysis

The inner solution does not have the same constraints as the outer solution in the sense that in this region, surfactant mass does not have to be conserved since it may move to a different region of the solution. Also the boundary values are allowed to evolve with time since they are Neumann conditions. However, we can still use asymptotic techniques in order to examine the similarity solution. Consider the system of equations (3.1.4) and the change of variables

$$h(x,t) = t^{\mu} H(\eta, t), \qquad \Gamma(x,t) = t^{\nu} G(\eta, t), \qquad \eta = \frac{x}{t^{\lambda}} \tag{4.1.54}$$

which results in the system

$$\mu t^{\mu-1} H - \lambda t^{\mu-1}\eta H_\eta + t^{\mu} H_t = t^{2\mu-2\lambda+\nu} \left(\tfrac{1}{2}H^2 G_\eta\right)_\eta \tag{4.1.55a}$$

$$\nu t^{\nu-1} G - \lambda t^{\nu-1}\eta G_\eta + t^{\nu} G_t = t^{\mu-2\lambda+2\nu} \left(HGG_\eta\right)_\eta. \tag{4.1.55b}$$

By relating the powers of t, we obtain the same relation for the exponents as the outer solution (4.1.4), $\lambda = \frac{1}{2}(\mu + \nu + 1)$. Implementing this relation we have the equations

$$tH_t + \mu H - \lambda\eta H_\eta = \left(\tfrac{1}{2}H^2 G_\eta\right)_\eta$$

$$tG_t + \nu G - \lambda\eta G_\eta = \left(HGG_\eta\right)_\eta.$$

Notice that tH_t corresponds to a logarithmic derivative, thus we use a change of variables $\tau = \log t$ which simplifies the equations to

$$H_\tau + \mu H - \lambda\eta H_\eta = \left(\tfrac{1}{2}H^2 G_\eta\right)_\eta \tag{4.1.57a}$$

$$G_\tau + \nu G - \lambda\eta G_\eta = \left(HGG_\eta\right)_\eta. \tag{4.1.57b}$$

61

Consider the Taylor series expansion of H, G about $\eta = 0$

$$H(\eta, \tau) \;=\; H_0(\tau) + \tfrac{1}{2}H_1(\tau)\eta^2 + \dots \tag{4.1.58a}$$

$$G(\eta, \tau) \;=\; G_0(\tau) + \tfrac{1}{2}G_1(\tau)\eta^2 + \frac{1}{24}G_2(\tau)\eta^4 \dots. \tag{4.1.58b}$$

The expansion (4.1.58) in the system (4.1.57) is

$$(H_0' \;+\; \tfrac{1}{2}H_1'\eta^2 + \dots) + \mu(H_0 + \tfrac{1}{2}H_1\eta^2 + \dots) - \lambda\eta(H_1\eta + \dots)$$
$$= \left(\tfrac{1}{2}(H_0 + \tfrac{1}{2}H_1\eta^2 + \dots)^2(G_1\eta + \frac{1}{6}G_2\eta^3 + \dots) \right)_\eta \tag{4.1.59a}$$

$$(G_0' \;+\; \tfrac{1}{2}G_1'\eta^2 + \dots) + \nu(G_0 + \tfrac{1}{2}G_1\eta^2 + \dots) - \lambda\eta(G_1\eta + \dots)$$
$$= \left((H_0 + \tfrac{1}{2}H_1\eta^2 + \dots)(G_0 + \tfrac{1}{2}G_1\eta^2 + \dots)(G_1\eta + \frac{1}{6}G_2\eta^3 + \dots) \right)_\eta ..\tag{4.1.59b}$$

The $O(1)$ terms give the relations

$$H_0' \;=\; -\mu H_0 + \tfrac{1}{2}H_0^2 G_1 \tag{4.1.60a}$$

$$G_0' \;=\; -\nu G_0 + H_0 G_0 G_1. \tag{4.1.60b}$$

From the numerical investigation we know that it is a reasonable assumption to take H_0 and G_0 constant (see Figure 4.8). The system (4.1.60) stipulates a single relation

$$2\mu = \nu \tag{4.1.61}$$

which also satisfies the property in Lemma 2. We find the values of the constant terms H_0 and G_0 and the scaling exponent μ from the numerical simulations. Then using the relations (4.1.4) and (4.1.61), the solution is determined from the expansion (4.1.58).

Now, consider the $O(\eta^2)$ terms

$$\tfrac{1}{2}H_1' \;=\; -\tfrac{1}{2}\mu H_1 + \lambda H_1 + \tfrac{1}{2}(3H_0 H_1 G_1 + \tfrac{1}{2}H_0^2 G_2) \tag{4.1.62a}$$

$$\tfrac{1}{2}G_1' \;=\; -\tfrac{1}{2}\nu G_1 + \lambda G_1 + \tfrac{1}{2}H_0 G_0 G_2 + \frac{3}{2}H_1 G_0 G_1 + \frac{3}{2}H_0 G_1^2. \tag{4.1.62b}$$

From (4.1.60a), $H_0 G_1 = 2\mu$ and since H_0 is constant, G_1 must be constant and $G_1 = \frac{2\mu}{H_0}$.

While G_1 is set without using (4.1.62b), we must use this equation to determine H_1. Multiplying (4.1.62b) by $2H_0$ and letting $G_1' = 0$,

$$0 = -\nu H_0 G_1 + 2\lambda H_0 G_1 + 3H_0^2 G_1^2 + H_0^2 G_0 G_2 + 3H_0 H_1 G_0 G_1.$$

62

Implementing the relations $2\mu = H_0 G_1$

$$0 = (-\nu + 2\lambda + 6\mu + 3H_1 G_0)2\mu + H_0^2 G_0 G_2$$

and $\nu = 2\mu$

$$0 = (4\mu + 2\lambda + 3H_1 G_0)2\mu + H_0^2 G_0 G_2.$$

Therefore

$$H_0^2 G_2 = -\frac{2\mu}{G_0}(4\mu + 2\lambda + 3H_1 G_0). \tag{4.1.63}$$

While the numerical investigations support that H_0, G_0 are constant which implies G_1 is constant due to the relations $H_0 G_1 = 2\mu$, H_1 may depend on time. We consider the two cases: H_1 constant and $H_1(\tau)$ a function of time, separately.

Case 1: H_1 constant
Substituting (4.1.63) and $H_1' = 0$ into (4.1.62a) results in

$$0 = (2\mu + 2\lambda)H_1 - \frac{\mu}{G_0}(4\mu + 2\lambda)$$

we solve for H_1

$$H_1 = \frac{\frac{\mu}{G_0}(4\mu + 2\lambda)}{2\mu + 2\lambda}.$$

Consider the values $\mu = -\frac{1}{6}$, $\nu = -\frac{1}{3}$, $\lambda = \frac{1}{4}$ which were determined from the numerical investigations. While these values are numerical approximations, Figure 4.7 is convincing that the actual values are approximately those chosen. Thus we can expect results similar to those obtained with these values. Then using the relation for G_1 we find $G_1 = \frac{2\mu}{H_0} \approx -0.36$ which approximately agrees with the value found from the numerical investigation. However, $H_1 = \frac{1}{6G_0} > 0$ since $G_0 > 0$ which suggests that the inner solution of the height profile is concave up. This result corresponds to the phase plane analysis but contradicts the numerical simulations. Consequently, H_1 must not be constant.

Case 2: $H_1(\tau)$
Assuming H_1 is a function of τ and using (4.1.62a), (4.1.63), we know

$$H_1' = (2\mu + 2\lambda)H_1 - \frac{\mu}{G_0}(4\mu + 2\lambda).$$

Thus

$$
\begin{aligned}
H_1(\tau) &= Ae^{\frac{\tau}{6}} + \frac{1}{6G_0} \\
&= At^{\frac{1}{6}} + \frac{1}{6G_0}.
\end{aligned}
\tag{4.1.64}
$$

The Taylor series expansion (4.1.58) in terms of x, t is

$$
H(x,t) = H_0 + \tfrac{1}{2}\left(A\left(\frac{x}{t^{\frac{1}{6}}}\right)^2 + \frac{1}{6G_0}\left(\frac{x}{t^{\frac{1}{4}}}\right)^2\right) + O(x^4) \qquad \text{as } t \to \infty, x \to 0. \tag{4.1.65}
$$

We use the numerical simulations to solve for A by transforming this equation to the variables η, t and find $A \approx -0.53$ at $t = 10000$, $\eta = 2\Delta\eta$. Recall $H_0 \approx 0.926$ and $G_0 \approx 0.8575$. Figure 4.11 is a plot of (4.1.65) against the numerical solutions at $t = 6000, 7000, 8000, 9000, 10000$. We see this approximation is a good fit near $\eta = 0$. From this asymptotic investigation we determine, while the simulations appear to have a similarity form, in fact the leading order behavior depends on the variables $\eta = \frac{x}{t^{\frac{1}{4}}}$ and t.
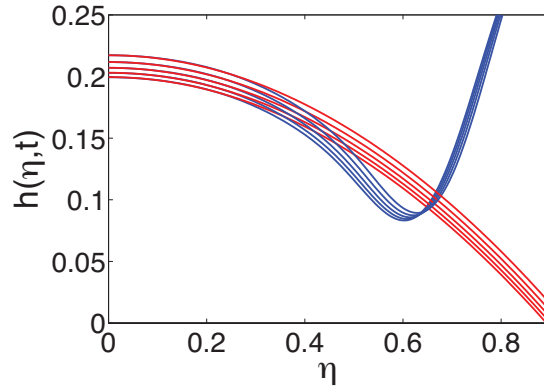
Figure 4.11: The numerical solutions $h(\eta, t)$ in blue and the expansion (4.1.65) at $t = 6000, 7000, 8000, 9000, 10000$ in red.

4.2 Axisymmetric Coordinates

Following a similar procedure as in the planar coordinate analysis, we examine the structure of the solutions in Region I and Region III of the system (3.7.1). In §4.2.1, we investigate the similarity scaling and phase plot of the outer solution (Region III). In §4.2.2, we examine the

behavior of the inner solution (Region I).

4.2.1 Outer Solution

Similarity Scaling

Consider the scalings

$$h(r,t) = t^\mu H(\rho), \qquad \Gamma(r,t) = t^\nu G(\rho), \qquad \rho = \frac{r}{t^\lambda}. \tag{4.2.1}$$

Then the axisymmetric system (3.7.1) is

$$\mu t^{\mu-1} H - \lambda t^{\mu-1} \rho H' - t^{2\mu+\nu-2\lambda} \frac{1}{\rho} \left(\tfrac{1}{2} \rho H^2 G' \right)' = 0 \tag{4.2.2a}$$

$$\nu t^{\nu-1} G - \lambda t^{\nu-1} \rho G' - t^{\mu+2\nu-2\lambda} \frac{1}{\rho} \left(\rho H G G' \right)' = 0. \tag{4.2.2b}$$

Balancing the powers of t results in the same relation as the planar case $\mu + \nu - 2\lambda + 1 = 0$. From conservation of mass,

$$\int_0^{at^\lambda} \Gamma r \, dr = \int_0^1 t^{\nu+2\lambda} G(\rho) \rho \, d\rho$$

we find

$$\nu + 2\lambda = 0.$$

The boundary condition $h = 2$ at $\rho = 1$ again stipulates $\mu = 0$. Thus the scaling exponents are

$$\mu = 0, \qquad \nu = -\tfrac{1}{2}, \qquad \lambda = \tfrac{1}{4}. \tag{4.2.3}$$

In Figure 4.12 we confirm this similarity scaling since the numerical simulations form a single line for $1000 < t < 10000$ using the spatial variable $\hat{\xi} = \frac{r}{r_0(t)}$. We also compare the spatial variable $\hat{\rho} = \frac{r}{(Dt)^{\frac{1}{4}}}$ (where D incorporates the initial mass of the surfactant) to the spatial variable $\hat{\xi} = \frac{r}{r_0(t)}$ used in §3.7. In Figure 4.13 we plot $r_0(t)$ against t on a log-log plot. The data forms a straight line with slope $\frac{1}{4}$ which implies that $r_0(t) \sim t^{\frac{1}{4}}$. Figure 4.14 shows $r_0(t) \approx (Dt)^{\frac{1}{4}}$ where $D = \frac{40}{3}$ is a scaling which incorporates the initial surfactant mass and is determined below by the scale invariance of the equations. Notice the curves $r = r_0$ and $r = (Dt)^{\frac{1}{4}}$ are in much better agreement than the comparison in the planar case. When investigating the property of conservation of mass the discrepancy near the origin is damped out due to the small size of the radius in this region. Thus conservation of mass does not have as influential of an effect at the

leading edge as was seen in the planar case.
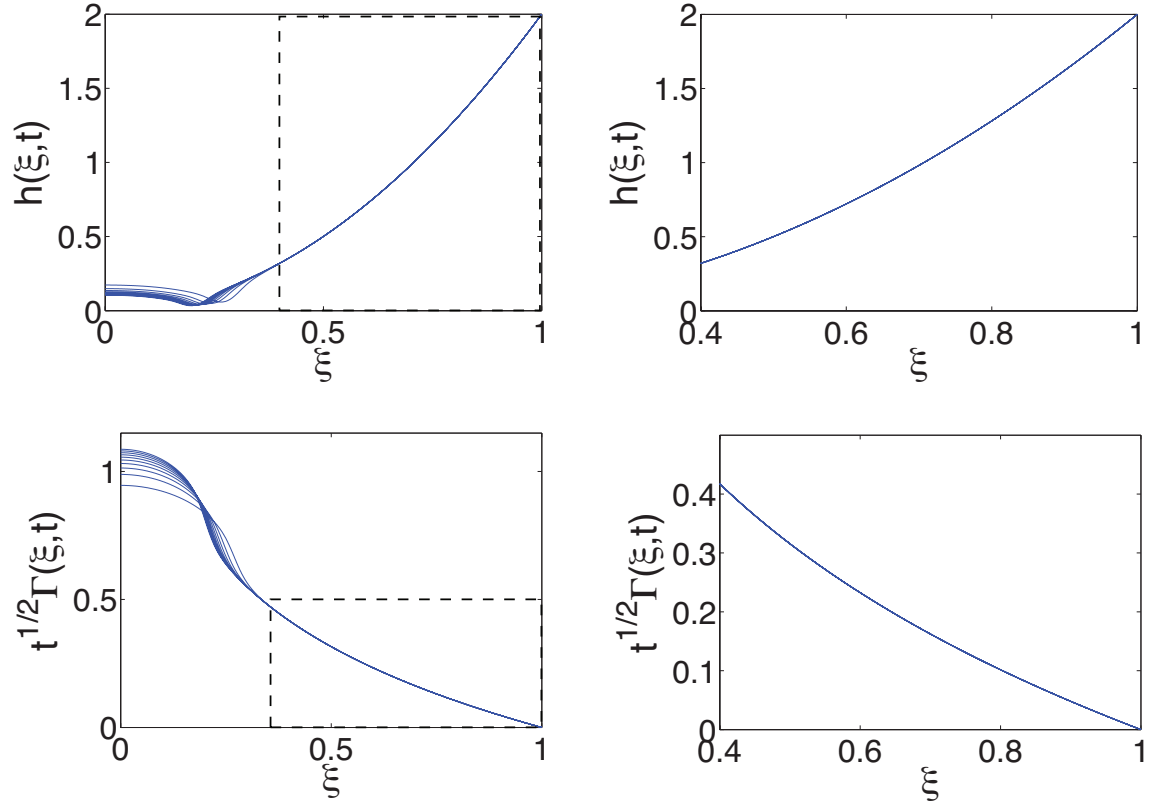
Figure 4.12: The height profile $h(\xi, t)$ (top left) with zoomed in scaled region (top right). The scaled surfactant profile $t^{\frac{1}{2}}\Gamma(\xi, t)$ (bottom left) with zoomed in scaled region (bottom left), at $1000 \leq t \leq 10000$.

Phase Plane

We outline Jensen's phase plane analysis [34] for the axisymmetric equations

$$h_t + \frac{1}{r}\left(\tfrac{1}{2}rhv\right)_r = 0 \tag{4.2.4a}$$

$$\Gamma_t + \frac{1}{r}\left(r\Gamma v\right)_r = 0 \tag{4.2.4b}$$

$$v + h\Gamma_r = 0. \tag{4.2.4c}$$
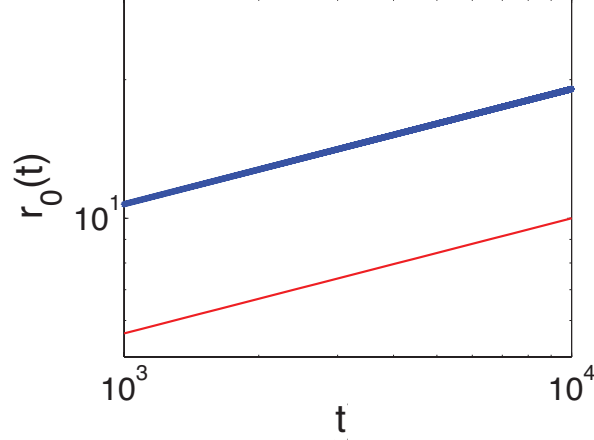
Figure 4.13: Log-log plot of the leading edge of the surfactant $r_0(t)$ (thick, blue) vs. t. The slope of the comparison line (thin, red) is $\frac{1}{4}$.

We use the same scalings as in the planar argument (4.1.10) with $\alpha = 0$ due to the height boundary condition at $\rho = 1$. Implementing the same change of variables results in the system of autonomous ODE

$$\frac{dU}{d\varphi} = -\left(\frac{U(2V - \frac{1}{2}) + V(2V - \frac{3}{4})}{V - \frac{1}{2}}\right) \tag{4.2.5a}$$

$$\frac{dV}{d\varphi} = -\left(\frac{U(2V - \frac{1}{2}) + V(\frac{1}{4} - V)}{U}\right). \tag{4.2.5b}$$

Figure 4.15 shows the phase plane for (4.2.5). We consider the trajectory $V = \frac{1}{4}$ and determine the corresponding $U(\varphi)$. Solving (4.2.5a), we find $U = -\frac{1}{4}\varphi$. From the change of variables of the velocity equation we know $V = -2HG - HG_\varphi$. Thus we determine

$$\Gamma(r,t) = -\frac{1}{8t^{\frac{1}{2}}} \log\left(\frac{r}{t^{\frac{1}{4}}}\right) \tag{4.2.6a}$$

$$h(r,t) = 2\left(\frac{r}{t^{\frac{1}{4}}}\right)^2. \tag{4.2.6b}$$

Notice these solutions differ from the planar case: h is quadratic and Γ is unbounded. In plotting the explicit solutions against the scaled solutions, we must incorporate the initial mass of the surfactant. Consider the scalings

$$h(r,t) = aH(\rho), \qquad \Gamma(r,t) = bt^{-\frac{1}{2}}G(\rho), \qquad \rho = \frac{r}{(Dt)^{\frac{1}{4}}}. \tag{4.2.7}$$

67
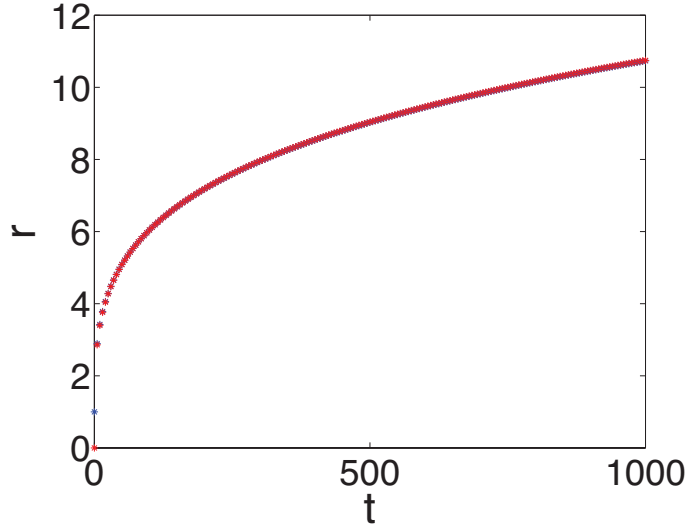
Figure 4.14: The location of the leading edge of the surfactant $r = r_0(t)$ in blue compared to $r = (Dt)^{\frac{1}{4}}$ where $D = \frac{40}{3}$ in red.

to determine the relation of coefficients which make (3.7.1) invariant. Incorporating these scalings into (3.7.1) we find $b = \frac{D^{\frac{1}{2}}}{a}$. Since the height of the film is normalized to $h(r, 0) = 1$ we take $a = 1$. We relate the initial surfactant mass and the mass of the similarity solution

$$\int_0^1 -\frac{D}{8} \log \eta \; \eta \; d\eta = \int_0^1 (1 - r^{10}) r \; dr \tag{4.2.8}$$

to define $D = \frac{40}{3}$. In Figure 4.16 we plot the explicit solution and the scaled numerical solutions.

4.2.2 Inner Solution

Jensen and Grotberg do an initial investigation for the scaling exponent of the height profile for the inner solution in [35]. However, their argument is not convincing. They track the height of the film at $r = 0$ and plot the location versus time on a log-log plot as we do below. However, in their analysis the line chosen does not clearly connect the data which suggests an incorrect choice for scaling exponent. We investigate the inner solution of (3.7.1) through numerics, phase plane analysis, and asymptotics analysis to determine a different scaling exponent than that suggested by Jensen and Grotberg.
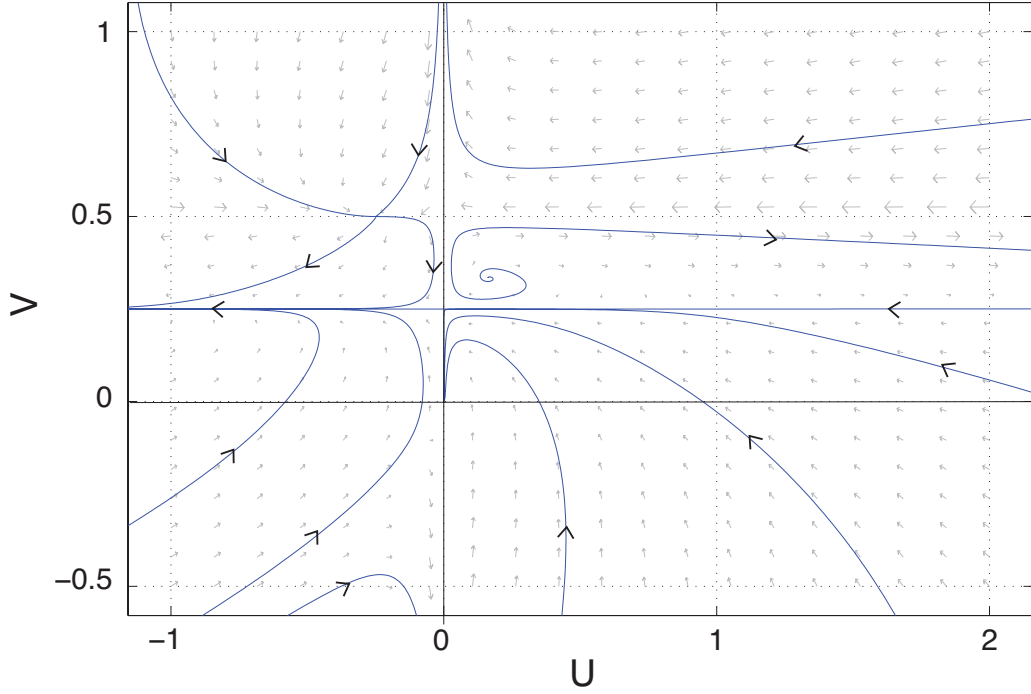
Figure 4.15: Phase plot of (4.2.5).

Numerical Investigation

Consider an expansion of the same form as the planar case, (4.1.58) where $\eta = \frac{r}{t^\lambda}$. First we determine the scaling exponents μ, ν from Figure 4.17 which is a log-log plot of $h(0,t)$ and $\Gamma(0,t)$. The slope of the lines formed by these points specify that $\mu \approx -\frac{2}{9}$ and $\nu \approx -\frac{4}{9}$. From the relation (4.1.4) we find $\lambda = \frac{1}{6}$. Figure 4.18 shows the scaled numerical solutions form a single solution in the region $\eta = 0$ in support of the choice of these exponents.

Notice that again $\nu = 2\mu$. We find that an analogous argument as that in Lemma 2 holds for the system (3.7.1). Differentiating, evaluating at $r = 0$, and using the boundary conditions $h_r(0,t) = 0$ and $\Gamma_r(0,t) = 0$ we find

$$h_t = \frac{1}{r}\tfrac{1}{2}h^2\Gamma_r + hh_r\Gamma_r + \tfrac{1}{2}h^2\Gamma_{rr} = h^2\Gamma_{rr}$$

$$\Gamma_t = \frac{1}{r}h\Gamma\Gamma_r + h_r\Gamma\Gamma_r + h\Gamma_r^2 + h\Gamma\Gamma_{rr} = 2h\Gamma\Gamma_{rr}.$$

69
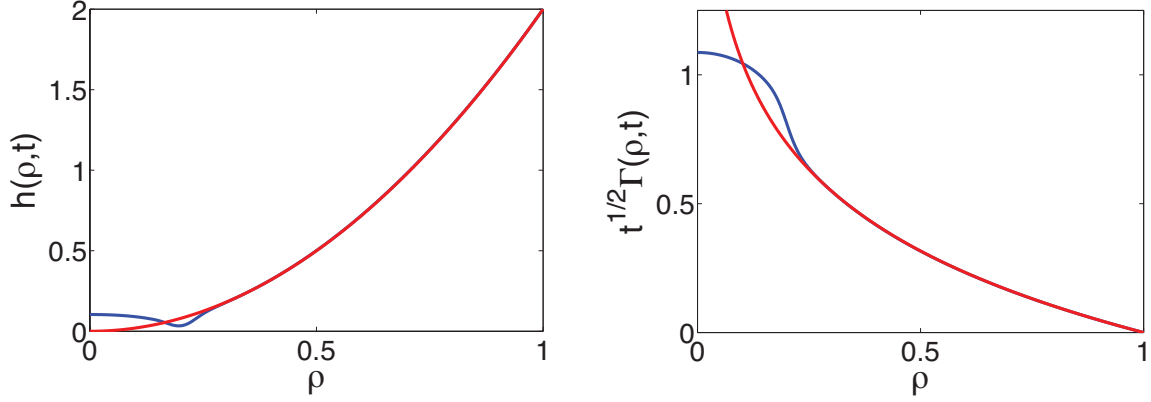
Figure 4.16: The height h (left) and the surfactant concentration Γ (right) profiles at $t = 10000$, in blue and the explicit solution (4.16) in red.

Thus,

$$\frac{h_t}{h} = \frac{1}{2}\frac{\Gamma_t}{\Gamma}$$

which implies $h^2 = A\Gamma$ and from the initial conditions $A = 1$ so

$$h^2(0, t) = \Gamma(0, t). \tag{4.2.9}$$

In Figure 4.19 we determine the values $H_0 \approx 0.807$ and $G_0 \approx 0.651$. Note that $G_0 \approx H_0^2$. We numerically find the second derivatives using finite differences at $t = 10000$, $H_1 \approx -1.05$ and $G_1 \approx -0.279$. In Figure 4.20, we plot the expansions $H = 0.807 - \frac{1.04}{2}\eta^2$ and $G = 0.651 - \frac{0.279}{2}\eta^2$ against the scaled numerical solutions $t^{-\frac{2}{9}}h(\eta, t)$ and $t^{-\frac{4}{9}}\Gamma(\eta, t)$.

Phase Plane

We consider the system (4.2.4) and the change of variables (4.1.34). Relating (4.1.34) to the scaled variables (4.1.35) we determine $\alpha = \frac{1}{3}$. Following a similar procedure to the inner solution phase plane analysis in §4.1.2 we derive the autonomous system

$$\frac{dU}{d\varphi} = -\left(\frac{U\left(2V - \frac{2}{3}\right) + V\left(2V - \frac{1}{2}\right)}{V - \frac{1}{3}}\right) \tag{4.2.10a}$$

$$\frac{dV}{d\varphi} = -\left(\frac{U\left(2V - \frac{4}{9}\right) + \left(V(\frac{1}{6} - V)\right)}{U}\right). \tag{4.2.10b}$$
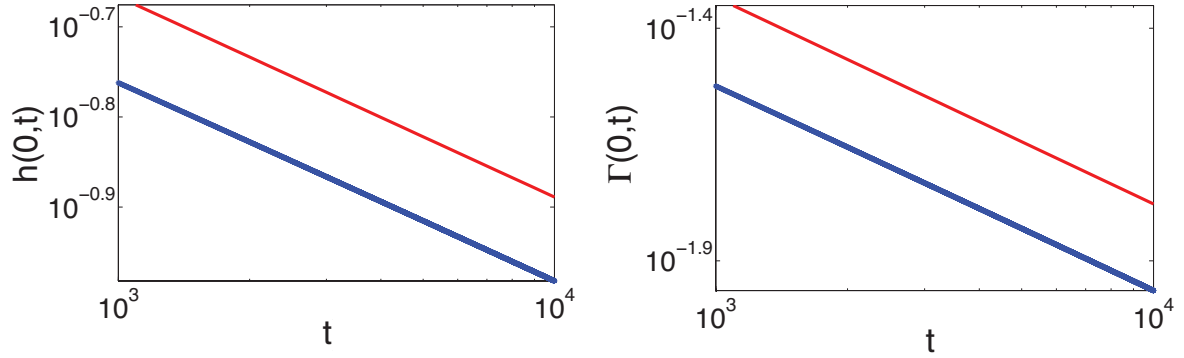
Figure 4.17: Log-log plot of $h(0,t)$ (left) and $\Gamma(0,t)$ (right) against t where $1000 < t < 10000$. The thin red line on the height plot has slope $-\frac{2}{9}$ and the surfactant plot $-\frac{4}{9}$.

Also from the V equation,

$$V + \frac{4}{3}U + U\frac{G'}{G} = 0. \tag{4.2.11}$$

Since we want to examine the solutions as $\eta \to 0$ and $U \to \infty$ as $\varphi \to -\infty$, we implement the change of variable $W = \frac{1}{U}$ which transforms (4.2.10) to

$$\frac{dW}{d\varphi} = 2W + W^2\frac{V(2V - \frac{1}{2})}{V - \frac{1}{3}} \tag{4.2.12a}$$

$$\frac{dV}{d\varphi} = \frac{4}{9} - 2V - WV\left(\frac{1}{6} - V\right). \tag{4.2.12b}$$

Figure 4.21 is the phase plane of (4.2.12) generated using pplane8 in MATLAB. From the phase portrait we observe that the only trajectories where V remains bounded as $\varphi \to -\infty$ approach the equilibrium point $(W,V) = (0, \frac{2}{9})$. The eigenvalues and eigenvectors associated with this point are

$$\lambda_1 = -2, \qquad \begin{pmatrix} w_{\lambda_1} \\ v_{\lambda_1} \end{pmatrix} = \begin{pmatrix} 0 \\ 1 \end{pmatrix} \tag{4.2.13a}$$

$$\lambda_1 = 2, \qquad \begin{pmatrix} w_{\lambda_2} \\ v_{\lambda_2} \end{pmatrix} = \begin{pmatrix} 1 \\ (\frac{1}{18})^2 \end{pmatrix}. \tag{4.2.13b}$$

71
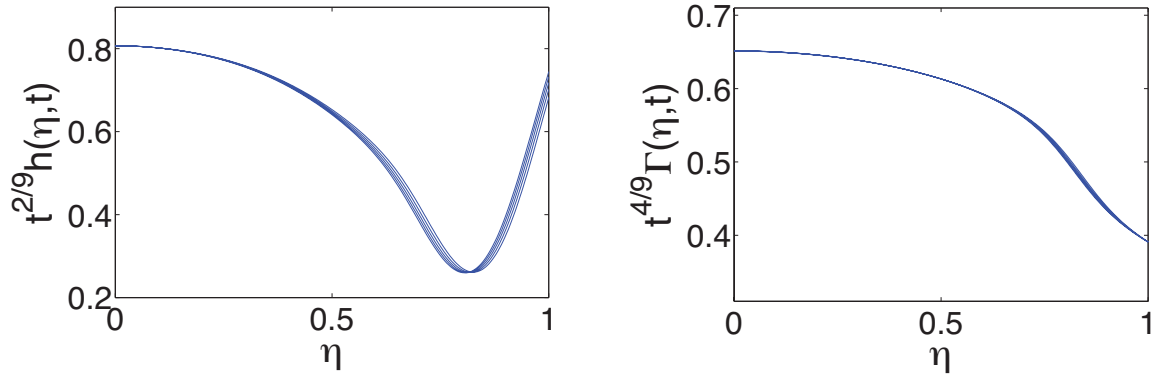
Figure 4.18: The scaled height profile $t^{\frac{2}{9}}h(\eta,t)$ (left) and the scaled surfactant profile $t^{\frac{4}{9}}\Gamma(\eta,t)$ where $\eta = \frac{r}{t^{\frac{1}{6}}}$, $5000 < t < 10000$.
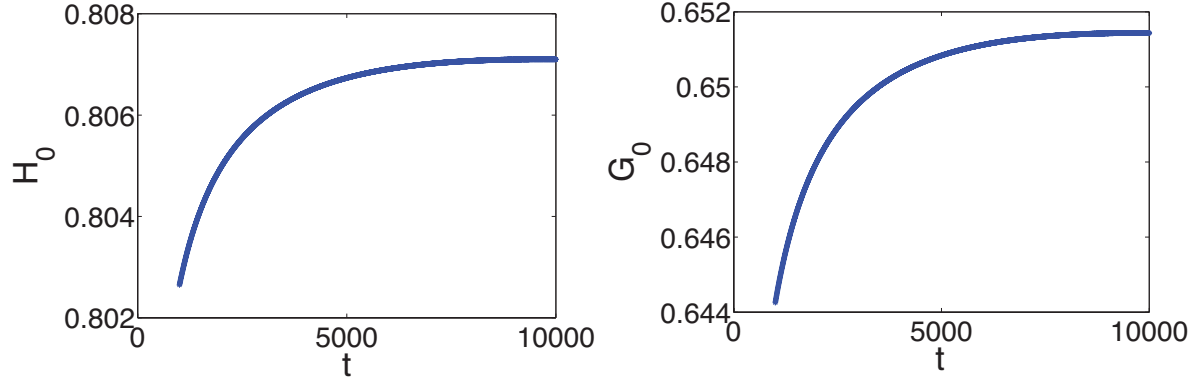
Figure 4.19: $H_0 = t^{\frac{2}{9}}h(0,t)$ vs. t (left) and $G_0 = t^{\frac{4}{9}}\Gamma(0,t)$ vs. t (right).

The eigenvector (4.2.13a) is associated with a stable manifold. We examine the unstable manifold associated with (4.2.13b) by expanding about the equilibrium point $(0, \frac{2}{9})$

$$W = w_1 e^{2\varphi} + w_2 e^{4\varphi} + \cdots = w_1 \eta^2 + w_2 \eta^4 + \ldots \qquad (4.2.14\text{a})$$

$$V = \frac{2}{9} + v_1 e^{2\varphi} + v_2 e^{4\varphi} + \cdots = \frac{2}{9} + v_1 \eta^2 + v_2 \eta^4 + \ldots \qquad (4.2.14\text{b})$$

where the expansion is in terms of $\lambda_2 \varphi = 2\varphi$. Thus from (4.2.13b), $v_1 = \left(\frac{1}{18}\right)^2 w_1 = \left(\frac{1}{18}\right)^2 \frac{1}{H_0 G_0}$ since $W = \frac{1}{HG} \to \frac{1}{H_0 G_0}$ as $\eta \to 0$.
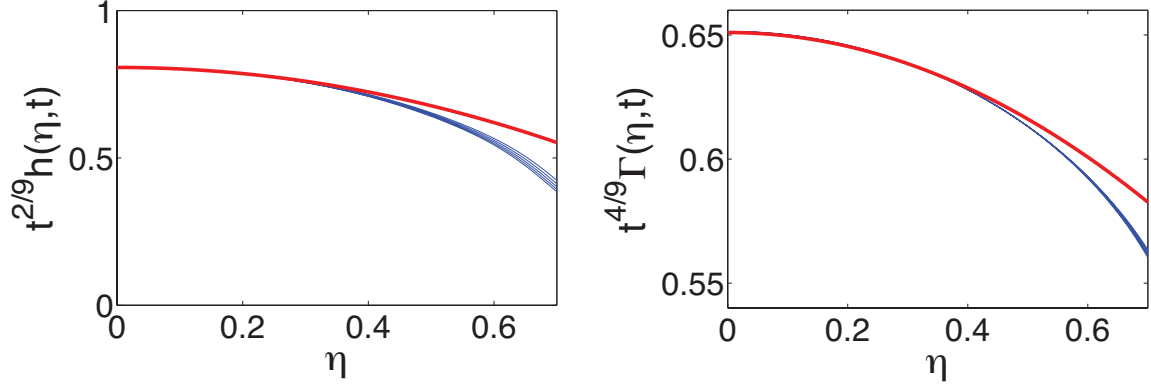
Figure 4.20: The scaled solutions and numerical expansion for $5000 \leq t \leq 10000$. Left: The scaled solutions $t^{\frac{2}{9}} h(\eta, t)$ in blue and the expansion $H = 0.807 - \frac{1.04}{2}\eta^2$ in red. Right: The scaled solutions $t^{\frac{4}{9}} \Gamma(\eta, t)$ in blue and the expansion $G = 0.651 - \frac{0.279}{2}\eta^2$.

From (4.2.11) we know

$$
\begin{aligned}
\frac{G'}{G} &= -\frac{4}{3} - VW \\
&= -\frac{4}{3} - \frac{2}{9}\frac{1}{H_0 G_0}e^{2\varphi} + O(e^{4\varphi})
\end{aligned}
$$

which we can solve to determine

$$
\begin{aligned}
G &= A\eta^{-\frac{4}{3}} e^{-\frac{1}{9H_0 G_0}\eta^2} \\
&= \eta^{-\frac{4}{3}}\left(G_0 - \frac{1}{9H_0}\eta^2 + O(\eta^4)\right).
\end{aligned} \tag{4.2.15}
$$

Since $H = \frac{1}{WG}$, using (4.2.14a) and (4.2.15) we find

$$
H = H_0 \eta^{-\frac{2}{3}}\left(1 + \left(\frac{1}{9H_0 G_0} - w_2 H_0 G_0 \right)\eta^2 + O(\eta^4)\right) \tag{4.2.16}
$$

but we still need to determine a value for w_2. We now investigate

$$
W = a\left(V - \frac{2}{9}\right) + b\left(V - \frac{2}{9}\right)^2 + \dots \tag{4.2.17}
$$

Thus

$$
\frac{dW}{dV} = a + 2b\left(V - \frac{2}{9}\right) \tag{4.2.18}
$$

73
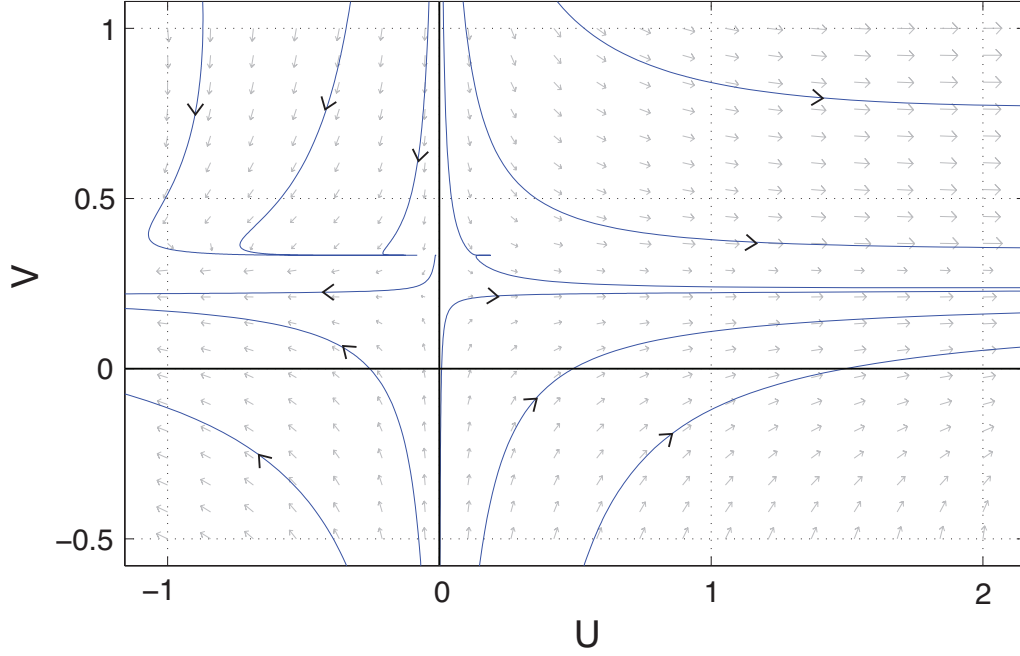
Figure 4.21: Phase portrait of (4.2.12).

but from (4.2.12)

$$\frac{dW}{dV} = F(W, V) = \frac{2W + W^2 \frac{V\left(2V - \frac{1}{2}\right)}{V - \frac{1}{3}}}{\frac{4}{9} - 2V - WV\left(\frac{1}{6} - V\right)}. \tag{4.2.19}$$

We write $u = V - \frac{2}{9}$ then (4.2.17) becomes $W = au + bu^2$, substituting into (4.2.19), canceling a factor of u, and retaining leading order terms, we find

$$F(W, V) = \frac{2a + \left(2b + \frac{a^2}{9}\right)u}{\left(-2 + \frac{1}{9^2}a\right)\left(1 + \frac{\frac{b}{9^2} + \frac{5}{18}a}{-2 + \frac{a}{9^2}}u\right)}. \tag{4.2.20}$$

Notice that if $u = 0$ then $a = 18^2$ which corresponds to the eigenvalue analysis. From the $O(u)$

terms,

$$2b = \frac{1}{2}\left(2b + \frac{a^2}{9}\right) - \frac{1}{2}a\left(\frac{b}{9^2} + \frac{5}{18}a\right) \tag{4.2.21}$$

which implies $b = -\frac{1}{2} \cdot 18^3$. Since $u' = V'$, using (4.2.12b) and substituting $W = au + bu^2$ and $V = u + \frac{2}{9}$ we find

$$u' = 2u + (3 \cdot 18)u^2$$

which implies

$$u = \frac{2k\eta^2}{1 - ck\eta^2} = 2k\eta^2\left(1 + ck\eta^2\right) \tag{4.2.22}$$

where k is a constant of integration and $c = 3 \cdot 18$. Since $W = au + bu^2$

$$W = 2ak\eta^2 + \left(2ack^2 + 4bk^2\right)\eta^4. \tag{4.2.23}$$

But we know $w_1 = \frac{1}{H_0 G_0}$ which implies $k = \frac{1}{2aH_0 G_0}$. Using the values determined above for a, b, c, k we find

$$w_2 = \frac{1}{18(H_0 G_0)^2}. \tag{4.2.24}$$

Therefore, using (4.2.16) the expansion for H is

$$H = \eta^{-\frac{2}{3}}\left(H_0 + \frac{1}{18G_0}\eta^2 + O(\eta^4)\right). \tag{4.2.25}$$

This analysis proves that a similarity solution corresponding to $\mu = -\frac{2}{9}, \nu = -\frac{4}{9}, \lambda = \frac{1}{6}$ exists. But as for the planar case, the similarity solution is concave up near $\eta = 0$ which contradicts the numerical simulations. Thus we investigate the system further through an asymptotic analysis and determine in fact the solutions illustrated by the numerical simulations are not similarity solutions.

Asymptotic Analysis

We consider scalings of the form (4.1.54) in (3.7.1), scale time, and define $\tau = \log t$ to produce the system of ODE

$$H_\tau + \mu H - \lambda \eta H_\eta = \frac{1}{\eta} \left(\tfrac{1}{2} \eta H^2 G_\eta \right)_\eta \tag{4.2.26a}$$

$$G_\tau + \nu G - \lambda \eta G_\eta = \frac{1}{\eta} \left(\eta H G G_\eta \right)_\eta . \tag{4.2.26b}$$

Implementing the expansion (4.1.58) in (4.2.26), the $O(1)$ terms are

$$H_0' = -\mu H_0 + H_0^2 G_1 \tag{4.2.27a}$$

$$G_0' = -\nu G_0 + 2H_0 G_0 G_1. \tag{4.2.27b}$$

Taking H_0 and G_0 to be constant which is supported by the numerical investigation results in $\nu = 2\mu$, which is expected due to Lemma 2. From (4.2.27a) we also find

$$\mu = H_0 G_1. \tag{4.2.28}$$

Thus G_1 is constant and $G_1 = \frac{\mu}{H_0} \approx -0.275$, which agrees with the value determined numerically. From the $O(\eta^2)$ terms, we know

$$\tfrac{1}{2} H_1' = -\tfrac{1}{2} \mu H_1 + \lambda H_1 + \tfrac{1}{3} H_0^2 G_2 + 2H_0 H_1 G_1 \tag{4.2.29a}$$

$$\tfrac{1}{2} G_1' = -\tfrac{1}{2} \nu G_1 + \lambda G_1 + \frac{2}{3} H_0 G_0 G_2 + 2H_1 G_0 G_1 + 2H_0 G_1^2. \tag{4.2.29b}$$

Setting $G_1' = 0$ since G_1 is constant, multiplying (4.2.29b) by H_0, and using (4.2.28) we solve for $H_0^2 G_2$ and substitute into (4.2.29a)

$$H_1' = \frac{1}{9} H_1 - \frac{1}{G_0} \frac{1}{9^2}. \tag{4.2.30}$$

We consider two cases: H_1 constant and H_1 a function of τ.

Case 1: H_1 constant
If H_1 is constant then (4.2.30) determines

$$H_1 = \frac{1}{9G_0} > 0. \tag{4.2.31}$$

Note this case agrees with the phase plane analysis but contradicts the numerical simulations, since the simulations are concave down near $\eta = 0$.

Case 1: $H_1(\tau)$

If $H_1(\tau)$ is a function of τ, and we use the values $\mu = -\frac{2}{9}$, $\nu = -\frac{4}{9}$, $\lambda = \frac{1}{6}$, we find

$$H_1' = \frac{1}{9}H_1 - \frac{1}{G_0}\frac{1}{9^2}. \tag{4.2.32}$$

Integrating we determine

$$H_1 = Ae^{\frac{\tau}{9}} + \frac{1}{9G_0} \tag{4.2.33}$$

$$= At^{\frac{1}{9}} + \frac{1}{9G_0}. \tag{4.2.34}$$

We numerically determine $A \approx -0.447$. Figure 4.22 is the numerical simulations plotted against the expansion $h(\eta, t) = t^{-\frac{2}{9}}\left(.807 + \frac{1}{18 \cdot .651}\eta^2 - \frac{0.447}{2}t^{\frac{1}{9}}\eta^2\right)$ at $t = 6000,\ 7000,\ 8000,\ 9000,\ 10000$.
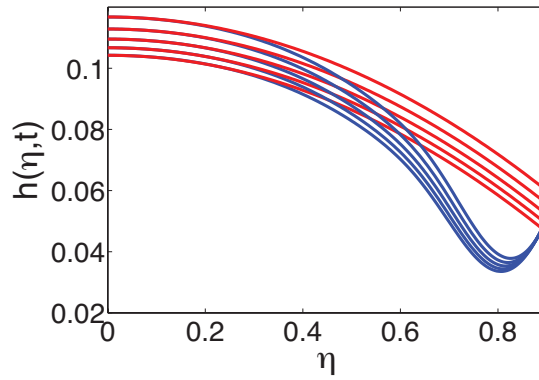
Figure 4.22: The scaled solutions $h(\eta, t)$ in blue and the expansion (4.1.65) at $t = 6000,\ 7000,\ 8000,\ 9000,\ 10000$ in red.

4.3 Discussion

In this chapter, we expanded on the analysis of Jensen and Grotberg [35] and Jensen [34]. We confirmed their results for the scaling of the outer solution through the use of the numerical method presented in §3.2, 3.3. This method was derived for the simplified system of equations (3.2.2) in planar coordinates and (3.7.2) in axisymmetric coordinates. We showed that the surfactant profile maintains compact support and the height profile remains unchanged in the

77

absence of surfactant, if initially h is constant. Using this method we were able to track the location of the shock that forms in the height profile. Due to the boundary condition stipulated by the shock, the height profile is not scaled by time. However, scaling the surfactant and spatial variable by a power of t transforms the solutions to a single curve. Previously in [35], the results were compared to numerical simulations in which the higher order terms β, κ, δ were included. However, we were able to compare the scalings which are for the simplified system to the numerical results of the same system with $\beta = \kappa = \delta = 0$.

We then extended the analysis to the inner solution. Jensen and Grotberg did a preliminary investigation of this region. Through a numerical investigation we are able to determine a possible scaling for a similarity solution. A phase portrait analysis confirms the existence of a similarity solution with the determined scaling parameters. However, the similarity solution predicts that the height profile is concave up near $x = 0$ which contradicts the numerical simulations. We determine, through an asymptotic analysis, that the solutions for the height h and surfactant concentration Γ are in fact not similarity solutions, for both the planar and axisymmetric cases and the determined expansion agrees with the numerics.

Chapter 5

Connecting the Model to the Experiment

The dynamics of surfactant spreading on a thin liquid layer have been of interest for over three decades. Experiments have either focused on the displacement of the thin film or the location of the surfactant. In 1972, Ahmad and Hansen performed experiments to capture the spreading rate of the surfactant [2]. More recently, Bull et al. [13] and Dussaud, Matar, and Troian [20] performed experiments to examine the spreading of surfactant and deformation of the underlying film surface, respectively. The purpose of Bull's experiment was to track the leading edge of the surfactant which was achieved through the use of fluorescence [13]. The goal of Dussaud's experiment was to visualize the disturbance of the film which was observed using Moiré topography; the location of the surfactant was also inferred [20]. Up to this point, there have been no experiments equipped to collect quantitative measurements for both the free surface of the film and the surfactant concentration. In the experiment described in this chapter we produce similar results to those achieved in [13] and [20] but simultaneously measure both the location of the free surface of the film and the surfactant concentration.

We make a comparison between the long accepted lubrication model [29] for the evolution of the height of a thin film driven by surfactant (2.1.32) to the physical behavior observed in the experiment. In §5.1 we outline the experimental set-up, procedure, and results from an experiment performed by David Fallest and Adele Lichtenberger in Karen Daniels' lab, reported in [26]. In §5.2 we discuss the model and numerical method we use to simulate the evolution of the height of the film and surfactant concentration. We also estimate realistic values for various modeling parameters that appear in the model (2.1.32), including the values of β, κ, δ and the form of the equation of state. In §5.3 we connect the experiment to the numerical model by comparing the spreading of the film and the surfactant and also the shape of the profiles. We investigate various initial conditions for the surfactant profile and find that the evolution of

both the film and the surfactant is fairly robust to the choice of the surfactant initial condition. To further investigate this observation, we implement a numerical method that replaces the surfactant equation by the surfactant profiles obtained from the experimental data.

5.1 Experiment

In this section we discuss the thin film experiment in Karen Daniels' lab [26]. The goal of the experiment is to visualize the height of the thin film and the location of the surfactant molecules simultaneously. In §5.1.1 we describe the set-up of the experiment and in §5.1.2 we outline the experimental procedure. The collected data must then be processed and analyzed, which is explained in §5.1.3.

5.1.1 Apparatus

The base of the experiment is an aluminum well with radius $L = 111\ mm$. We deposit a layer of 99.5% anyhydrous glycerin into the well to serve as the thin film in the experiment; the height of the film is $H \approx 1\ mm$. Glycerin has high viscosity, which slows down the experiment to an extent that the movement of the film can be captured in detail using a camera. The glycerin is maintained at a constant temperature of $25 \pm 0.5°C$ by water circulating through the aluminum base from a temperature controlled bath. A camera positioned above the experiment records images of the experiment. The experiment is built on an optical table with dampers in order to minimize vibrations.

Laser profilometry is used to visualize the height of the film. A laser passes through a slit, is refracted by the glycerin, and reflects off the bottom of the aluminum basin. The red channel of the camera captures the red laser.

We visualize the location of the surfactant molecules through the use of fluorescence. The surfactant is a fluorescently tagged lipid, [1-palmitoyl-2-12-[(7-nitro-2-1,3-benzoxadiazol-4-yl)amino]lauroyl-sn-glycero-3-phosphocholine (abbreviated NBD-PC)] which was purchased from Avanti Polar Lipids. A NBD-PC surfactant molecule is insoluble in glycerin. Each molecule has a hydrophilic head and two hydrophobic tails; one tail has a fluorescent tag attached. A black light excites this fluorescent tag allowing the concentration of the surfactant to be determined from images that are captured in the green channel of the camera. For storage and delivery purposes, the surfactant molecules are dissolved in chloroform. This solution is deposited into a ring with radius $8\ mm$ situated in the center of the basin. We allow time for the the chloroform to evaporate before lifting the ring. Figure 5.1 is a schematic of the experimental set-up.
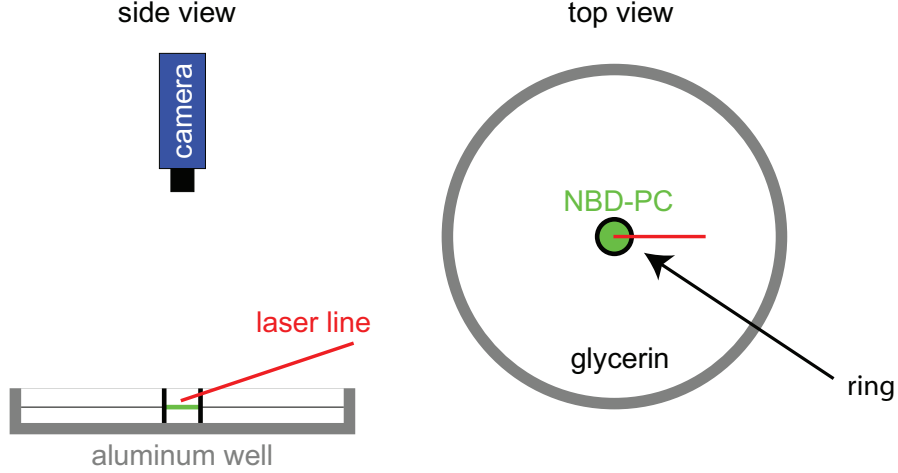
Figure 5.1: Schematic of the initial configuration of the experimental apparatus, side and top view image, from [26].

5.1.2 Experimental Procedure

In order to create the thin film, we deposit 38 mL of glycerin in the aluminum well and allow the film to level. This volume of glycerin creates a fluid with height 0.98 ± 0.03 mm which is of a comparable height to experiments presented in [28, 13]. The constraining ring is placed in the center of the basin and $18\mu L$ of the chloroform and surfactant solution are deposited into the ring. Since the surfactant is in chloroform, we allow approximately 6 minutes per microliter for the chloroform to evaporate.

A monofilament line connected to an overhead pulley run by a slow motor lifts the ring. We use this device to remove the ring in order to minimize the formation of bubbles as the ring is lifted and also to allow for the repeatability of the experiment.

We collect images of the laser line alone or both the laser line and surfactant fluorescence together. When recording only the laser line, the camera is set to take a picture every 0.1 second; we refer to this case as *short exposure time*. For the purpose of simultaneously recording the height and surfactant data, the camera is set to take a picture every second, which we refer to as *long exposure time*. The longer exposure allows for more photons emitted from each fluorescent tag to be captured by the camera thus producing better spatial resolution of the location of the surfactant. Figure 5.2 is an image of the experiment at $t = 1, 3, 5, 7$ *sec*. The areas with brighter green correspond to higher surfactant concentration.

t=1 sec   t=3 sec   t=5 sec   t=7 sec
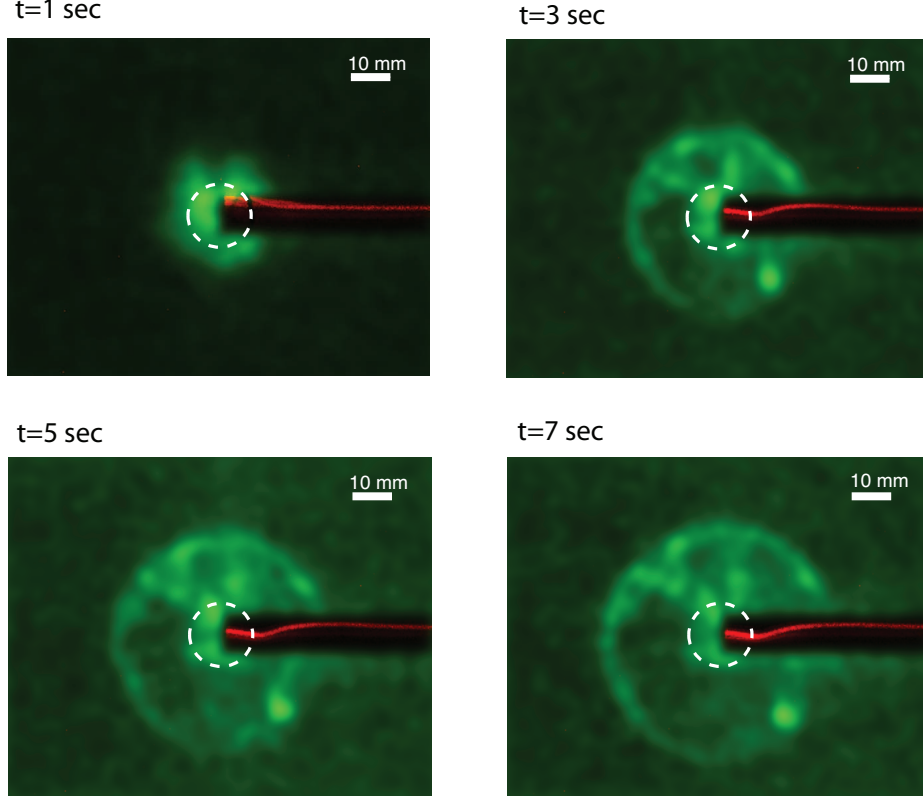
Figure 5.2: Image of red laser profile of film height and green fluorescent intensity at $t = 1, 3, 5, 7$ sec, from [26]. Each image has been processed as described in §5.1.3. The white dashed circle marks the initial location of the confining ring.

5.1.3   Experimental Results

A sequence of images records the dynamics of the spreading film. We then extract and calibrate the height of the film and surfactant concentration of the surfactant from each image. In order to calibrate the height of the film, images are taken of the laser line reflecting off the basin plate, before glycerin is introduced to the basin. Images are then taken of the laser line during the experiment. The height of the film is determined by the change in the location of the laser line through comparison of these images with and without glycerin.

In order to obtain experimental data for the surfactant concentration, the images are processed in a series of steps. One difficulty is that the high intensity of the laser signal obstructs the fluorescent measurement for the surfactant in its vicinity. The region in which the laser line is present is discarded from the picture to eliminate the contamination of the fluorescent measurement from the laser line, as shown in Figure 5.2. Another issue is that the images of the surfactant exhibit a considerable amount of noise. To resolve this, we implement a procedure

known as image division and median filtering to eliminate the noisiest pixels. However, as can be seen outside the brighter ring in Figure 5.2 some background noise remains. After this processing, the fluorescence of the surfactant is radially averaged (excluding the region discarded due to contamination from the laser line) to obtain the experimental values of $\Gamma(r,t)$ from the experimental image.

The processed experimental data are shown in Figure 5.3; the location of the maximum of the height and leading edge of surfactant are marked on these plots with the symbol •. There are some interesting features to observe which were not initially expected:

1. The capillary ridge initially appears to be slightly behind the leading edge of the surfactant but catches up so that these points are at approximately the same location. This can be seen by comparing the location of the • in the height and surfactant profiles at a given time.

2. A monolayer Γ_C of surfactant spreads from the bulk. Once the bulk and the layer are uniform, the surfactant spreads uniformly.

3. In Figure 5.2, the surfactant concentration does not appear to be uniform but rather there are spots which are brighter. We believe that these brighter areas are due to attraction between the surfactant molecules [54], which we refer to as *clumping*.

4. Immediately behind the leading edge of the surfactant, an unexpected peak of surfactant develops. This may be an artifact of clumping of the surfactant.

We note that the shape of the experimental height profiles are in agreement with to those generated in [20]. Only the location of the leading edge of the surfactant is reported in [13].

When the goal of the experiment is to capture only the evolution of the height of the film, we collect the height profiles at a greater frequency through the use of a short exposure time. It turns out that matching the experimental and numerical height profiles is easier since there is more data in time. When images are captured every second (so that surfactant concentration can also be collected), the exposure time on the camera is longer which causes the laser line to be more smeared.

We compare the height profiles taken at short and long exposure times in two different ways. In each frame of Figure 5.4, we show a thick black line for the height from an experimental run with long exposure time and thin lines for the short exposure profiles at the same time, for several different experimental runs. We observe that the longer time exposure (thick black line) is a reasonable representation of the short exposure runs. In Figure 5.5 we compare longer time exposure to shorter in a different way. In that figure we use the same black line at $t = 4$ as in Figure 5.4, but also show short time exposures around $t = 4$ ($t = 3.5, 3.6, 3.7, \ldots, 4.5$),

83
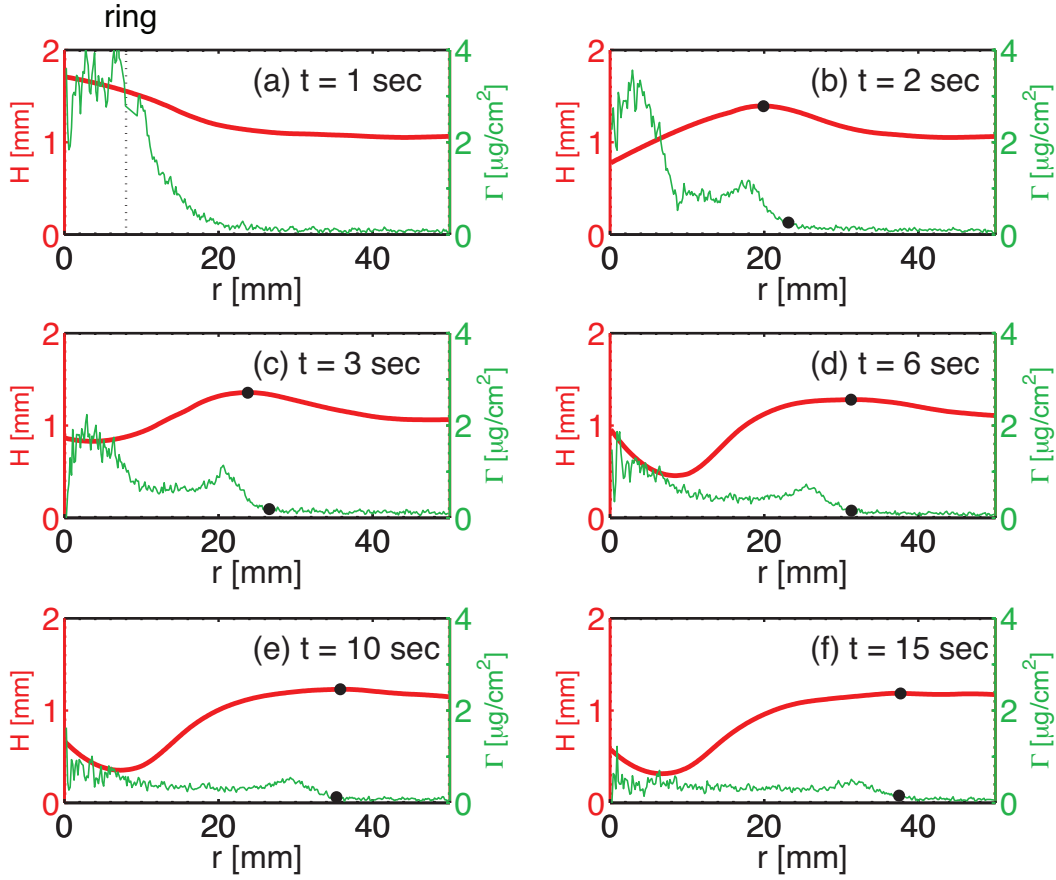
Figure 5.3: Comparison of fluorescence intensity ($\Gamma(r,t)$, thin green, right axis) and height ($H(r,t)$, thick red, left axis) profiles. The location of the capillary ridge and surfactant leading edge are marked with a •, from [26].

from two separate runs. The two runs we compare to are: (i) a run that has the closest fit to the long exposure run and (ii) a run that exhibits the typical behavior of the short exposure time runs over the entire time interval of the experiment. The latter is the run that we use in §5.3 when fitting the model to the experiment.
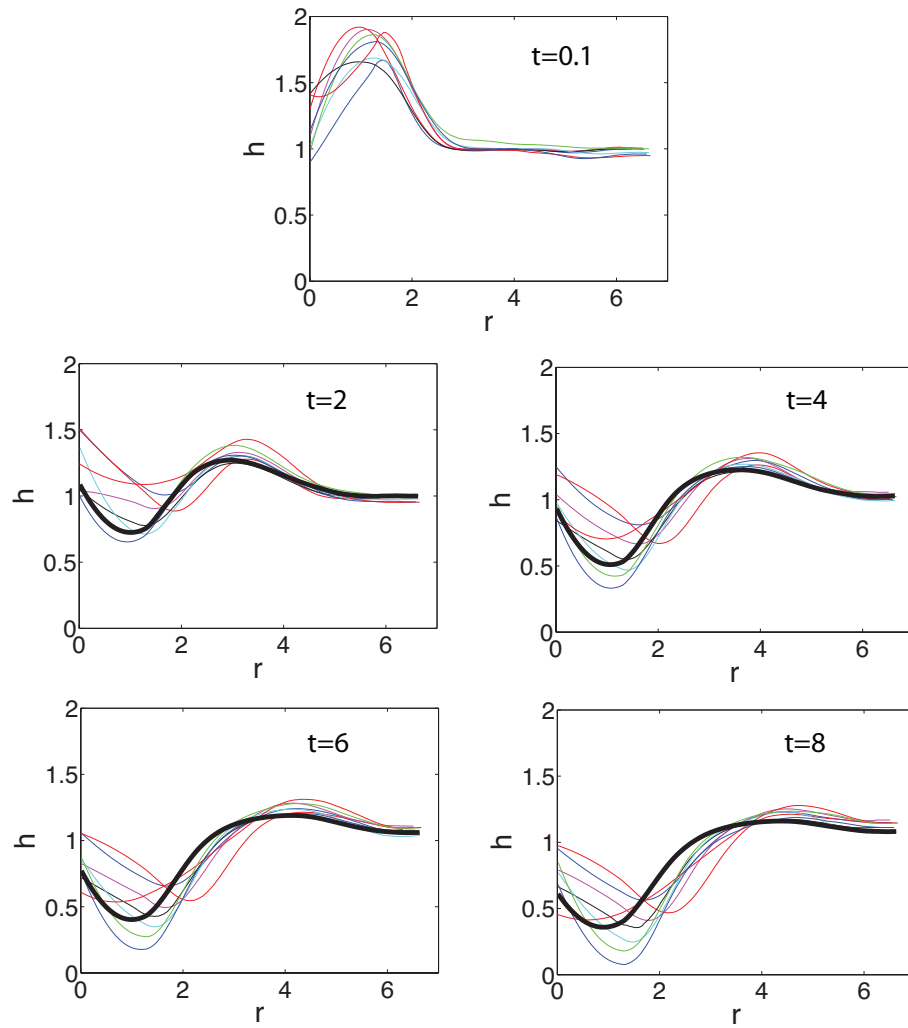
Figure 5.4: Experimental height data collected at short exposure time (0.1 second intervals), shown at $t = 0.1, 2, 4, 6, 8$ *sec*. Each thin line represents a different experimental run. The thick black line is derived fom data collected at a long exposure time (1 second interval).
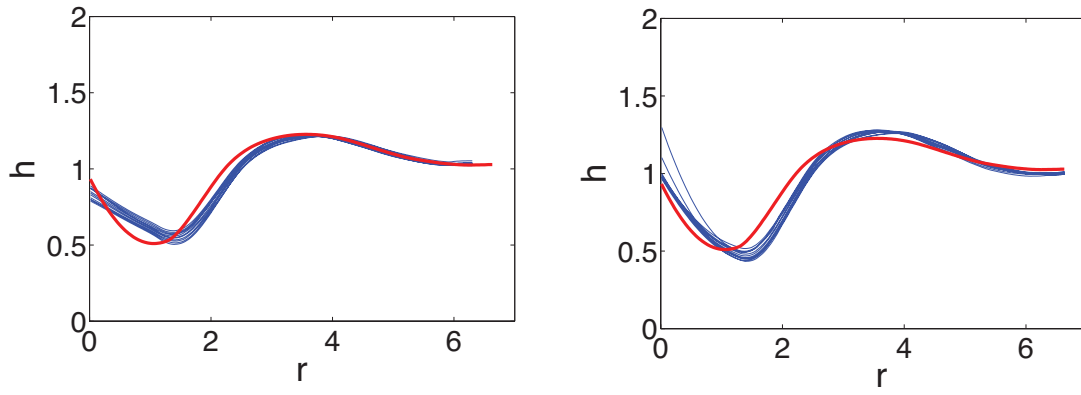
Figure 5.5: Experimental height profile collected with long exposure time (data collected at one second intervals) in red, shown at $t = 4\ sec$ (on both figures). Experimental height profile (two different experimental runs) collected with short exposure time (0.1 second intervals) in blue, shown at $t = 3.5, 3.6, 3.7, \dots 4.5$. Left: Short exposure time experimental run which most closely fits long exposure time height profile. Right: Short exposure time experimental run which exhibits the typical behavior of all the runs.

86

5.2 Theoretical Model

Since the experimental set-up consists of a circular basin holding the thin film, the surfactant is deposited in a circular ring, and the film spreads in a circular manner as seen in Figure 5.2, we consider axisymmetric spreading. The corresponding model is in plane polar coordinates (r, θ) but we assume that (h, Γ) are independent of θ: (2.1.32) in §2.1.8,

$$h_t + \frac{1}{r}\left(\tfrac{1}{2}rh^2\sigma_r\right)_r = \beta\frac{1}{r}\left(\tfrac{1}{3}rh^3h_r\right)_r - \kappa\frac{1}{r}\left(\tfrac{1}{3}rh^3\left(h_{rr} + \frac{1}{r}h_r\right)_r\right)_r \tag{5.2.1a}$$

$$\Gamma_t + \frac{1}{r}\left(rh\Gamma\sigma_r\right)_r = \beta\frac{1}{r}\left(\tfrac{1}{2}rh^2\Gamma h_r\right)_r - \kappa\frac{1}{r}\left(\tfrac{1}{2}rh^2\Gamma\left(h_{rr} + \frac{1}{r}h_r\right)_r\right)_r + \delta\frac{1}{r}\left(r\Gamma_r\right)_r. \tag{5.2.1b}$$

The boundary conditions at $r = 0$ are set utilizing the property that h is an even function which causes the odd derivatives to be zero; for large r, we expect the free surface to be undisturbed, and the surfactant concentration to be identically zero. Consequently,

$$h_r(0, t) = \Gamma_r(0, t) = 0, \qquad \kappa h_{rrr}(0, t) = 0, \qquad \lim_{r\to\infty} h(r, t) = 1, \qquad \lim_{r\to\infty} \Gamma(r, t) = 0. \tag{5.2.2}$$

5.2.1 Numerical Method

In this section we outline the finite difference method used to generate numerical results for system (5.2.1). We treat the system implicitly due to the fourth-order derivatives. Let $h_j^n \approx h(j\Delta r, n\Delta t)$ and $\Gamma_j^n \approx \Gamma(j\Delta r, n\Delta t)$ where $j = 0, 1, 2, \ldots, N$ and $\Delta r = \frac{R}{N}$ on the domain $[0, R]$. We use the standard notation for spatial averages of $u_j^n = u(r_j, t_n)$,

$$\bar{u}_{j+\frac{1}{2}}^n \equiv \frac{u_{j+1}^n + u_j^n}{2}. \tag{5.2.3}$$

The numerical method written in flux form is

$$h_j^{n+1} = h_j^n + \Delta t\frac{1}{r_j\Delta r}\left(\mathcal{F}_{j+\frac{1}{2}}^{n+1} - \mathcal{F}_{j-\frac{1}{2}}^{n+1}\right) \tag{5.2.4a}$$

$$\Gamma_j^{n+1} = \Gamma_j^n + \Delta t\frac{1}{r_j\Delta r}\left(\mathcal{G}_{j+\frac{1}{2}}^{n+1} - \mathcal{G}_{j-\frac{1}{2}}^{n+1}\right) \tag{5.2.4b}$$

where the fluxes are separated by (dropping the $n + 1$ superscript)

$$\mathcal{F}_{j+\frac{1}{2}} = \tfrac{1}{2}\mathcal{F}_{j+\frac{1}{2}}^1 + \tfrac{1}{3}\beta\mathcal{F}_{j+\frac{1}{2}}^2 + \tfrac{1}{3}\kappa\mathcal{F}_{j+\frac{1}{2}}^3 \tag{5.2.5a}$$

$$\mathcal{G}_{j+\frac{1}{2}} = \mathcal{G}_{j+\frac{1}{2}}^1 + \tfrac{1}{2}\beta\mathcal{G}_{j+\frac{1}{2}}^2 + \tfrac{1}{2}\kappa\mathcal{G}_{j+\frac{1}{2}}^3 + \delta\mathcal{G}_{j+\frac{1}{2}}^4 \tag{5.2.5b}$$

and the flux functions are expressed as

$$\mathcal{F}^1_{j+\frac{1}{2}} = \overline{r}_{j+\frac{1}{2}} \left(\overline{h}_{j+\frac{1}{2}} \right)^2 \sigma' \left(\overline{\Gamma}_{j+\frac{1}{2}} \right) \frac{\Gamma_{j+1} - \Gamma_j}{\Delta r} \tag{5.2.6a}$$

$$\mathcal{F}^2_{j+\frac{1}{2}} = \overline{r}_{j+\frac{1}{2}} \left(\overline{h}_{j+\frac{1}{2}} \right)^3 \frac{h_{j+1} - h_j}{\Delta r} \tag{5.2.6b}$$

$$\mathcal{F}^3_{j+\frac{1}{2}} = \overline{r}_{j+\frac{1}{2}} \left(\overline{h}_{j+\frac{1}{2}} \right)^3 \frac{\mathcal{E}_{j+2} - \mathcal{E}_j}{2\Delta r} \tag{5.2.6c}$$

$$\mathcal{E}_{j+2} = \frac{h_{j+3} - 2h_{j+2} + h_{j+1}}{\Delta r^2} + \frac{1}{\overline{r}_{j+\frac{3}{2}}} \frac{h_{j+2} - h_{j+1}}{\Delta r} \tag{5.2.6d}$$

$$\mathcal{G}^1_{j+\frac{1}{2}} = \overline{r}_{j+\frac{1}{2}} \overline{h}_{j+\frac{1}{2}} \overline{\Gamma}_{j+\frac{1}{2}} \sigma' \left(\overline{\Gamma}_{j+\frac{1}{2}} \right) \frac{\Gamma_{j+1} - \Gamma_j}{\Delta r} \tag{5.2.6e}$$

$$\mathcal{G}^2_{j+\frac{1}{2}} = \overline{r}_{j+\frac{1}{2}} \left(\overline{h}_{j+\frac{1}{2}} \right)^2 \overline{\Gamma}_{j+\frac{1}{2}} \frac{h_{j+1} - h_j}{\Delta r} \tag{5.2.6f}$$

$$\mathcal{G}^3_{j+\frac{1}{2}} = \overline{r}_{j+\frac{1}{2}} \left(\overline{h}_{j+\frac{1}{2}} \right)^2 \overline{\Gamma}_{j+\frac{1}{2}} \frac{\mathcal{E}_{j+2} - \mathcal{E}_j}{2\Delta r} \tag{5.2.6g}$$

$$\mathcal{G}^4_{j+\frac{1}{2}} = \overline{r}_{j+\frac{1}{2}} \frac{\Gamma_{j+1} - \Gamma_j}{\Delta r}. \tag{5.2.6h}$$

At each time, the scheme is advanced using Newton's method with an exact Jacobian. The boundary conditions (5.2.2) in discrete form are

$$h_0^n = h_1^n, \qquad h_{-2}^n = h_2^n \qquad \Gamma_0^n = \Gamma_1^n \tag{5.2.7}$$

$$h_N^n = 1, \qquad \Gamma_N^n = 0. \tag{5.2.8}$$

The initial conditions are chosen to be in agreement with the experimental profile as discussed in §5.3.1. In the numerical scheme, the edge of the domain R is taken large enough that the influence of the boundary conditions at $r = R$ is minimal over the time of the experiment. In practice, we take $R = 10$ but most of the results are shown on a smaller domain, $r \in [0, 7]$.

5.2.2   Non-dimensional Parameters

The non-dimensional parameters β, κ, δ in (5.2.1) incorporate physical effects such as gravity and surface tension forces, as described in §2.1.8. In this section we investigate the influence of these parameters on the numerical simulations of the height profile and surfactant concentration.

In §5.3.1 we will determine the approximate value for each of the parameters using the non-dimensional grouping from the non-dimensionalization of the equations and the values for the physical parameters in Table 5.1. Here we consider a range for each of the parameters which

includes the approximate value:

$$0.1 \leq \beta \leq 1.0 \tag{5.2.9a}$$

$$0.01 \leq \kappa \leq 0.1 \tag{5.2.9b}$$

$$10^{-5} \leq \delta \leq 10^{-4}. \tag{5.2.9c}$$

We investigate the influence of β and κ on the height and surfactant concentration profiles. Since the value for δ is $O(10^{-5})$ and the parameter only appears in the surfactant equation, we consider this to be a small effect and do not examine the influence of this parameter. We consider an initially uniform film and place a droplet of surfactant on the film; the corresponding initial conditions are

$$h(r,0) = 1, \qquad \Gamma = \begin{cases} 1 - r^{10} & r \leq 1 \\ 0 & r > 0. \end{cases} \tag{5.2.10}$$

As the parameters are varied, we compare the height and surfactant profiles at $t = 5$, which is approximately half way through the experiment.

In Figure 5.6 we fix $\kappa = 0.02$, $\delta = 2.8 \times 10^{-5}$, and vary β. As the parameter β is increased, the disturbance in the height of the film is less pronounced, in the sense that the maximum is decreased and the minimum is increased; the ridge also widens. The location of the maximum in the height also moves slower with larger values of β. The surfactant profile experiences the opposite influence: as β is increased the surfactant steepens and the maximum concentration is higher. The parameter β incorporates gravitational effects; the larger this effect the more damped the height profile. The leading edge of the surfactant approximately corresponds with the maximum in the height profile; since the maximum height moves slower with higher β the surfactant does not spread out as much which causes the distribution to be more compact.

In Figure 5.7 we fix $\beta = 0.5$, $\delta = 2.8 \times 10^{-5}$, and vary κ. We find that the parameter κ has a similar but more minor effect than β on the shape of the height profiles. The main differences are that the maximum height moves faster and the surfactant profiles are dampened as κ is increased. This behavior is explained by the smoothing effect that capillarity introduces to the film.

In §5.3.1 we use the results of this investigation of the effect of β, κ in order to fit the experimental data to the model.

5.2.3   Equation of State

A gradient in the surface tension acts as a driving force to the thin film. This force is incorporated into the system (5.2.1) through the equation of state $\sigma(\Gamma)$ which relates the surface
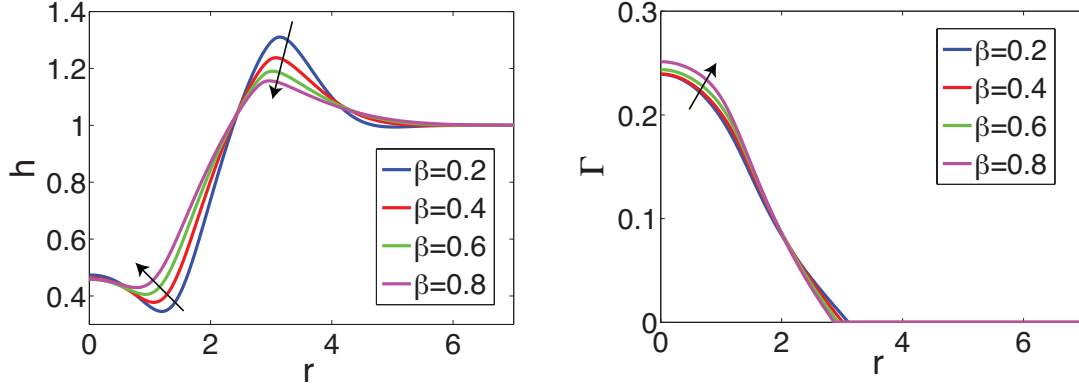
Figure 5.6: The height (left) and surfactant concentration (right) profiles at $t = 5$ with $\beta = 0.2$, 0.4, 0.6, 0.8. The arrows indicate the effect of increasing β.
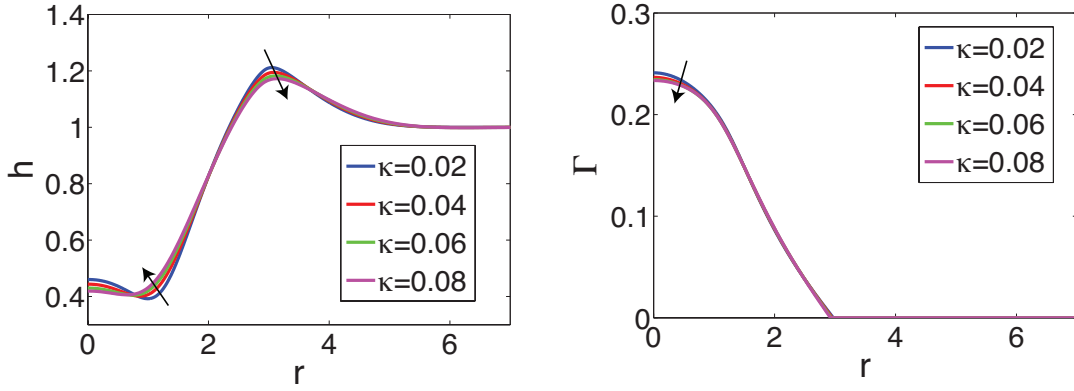
Figure 5.7: The height (left) and surfactant concentration (right) profiles at $t = 5$ with $\beta = 0.02$, 0.04, 0.06, 0.08. The arrows indicate the effect of increasing κ.

tension of the fluid to the surfactant concentration Γ. In particular, the equation of state is included in the equations through its derivative, $\sigma'(\Gamma)$. The following investigation shows that the choice of the equation of state has a substantial impact on the evolution of the film height. However, there has not been a consensus on the form of the equation of state. For this reason, we consider different forms of equation of state and discuss the impact of each choice on the simulations. The different equations of state we consider are shown in Figure 5.8.
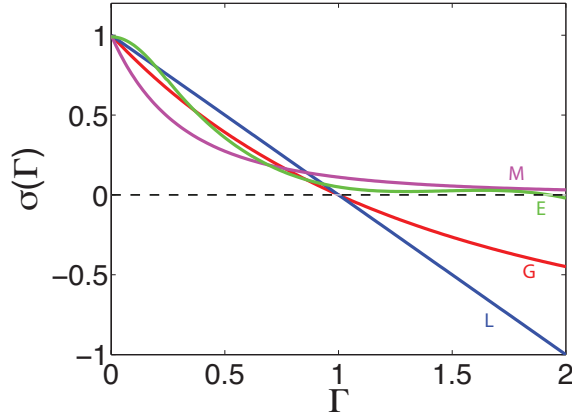
Figure 5.8: The equations of state; L: linear (5.2.11), G: Langmuir (5.2.12), E: measured (5.2.13), M: multiple layer (5.2.14). The dashed line indicates where σ becomes unphysical.

Linear Equation of State

We used the linear equation of state

$$\sigma(\Gamma) = 1 - \Gamma \tag{5.2.11}$$

in Chapters 3-4. The linear equation of state is common to use when examining the system of equations (5.2.1) analytically but has also been utilized in experimental papers; this equation was used in [48, 36, 24, 53]. This choice is made for simplicity; the linear equation of state is a linear approximation to the other equations that we discuss below. There are some key features that should be taken notice of with the linear equation of state. The surface tension is normalized so that $\sigma(0) = 1$. When $\Gamma = 1$ which corresponds to a densely packed monolayer of surfactant molecules, $\sigma(1) = 0$ and if $\Gamma > 1$, $\sigma(\Gamma) < 0$. Thus this equation is only valid when considering less than a saturated monolayer of surfactant, since surface tension cannot be negative. Another issue with this equation is that $\sigma'(\Gamma) = constant$ which suggests the surface tension can decrease endlessly. Also, the Marangoni force $\sigma'(\Gamma)\Gamma_x$ induced by a surfactant concentration gradient is independent of the concentration.

Langmuir Equation of State

The Langmuir equation of state is

$$\sigma(\Gamma) = \frac{\eta + 1}{(1 + \Theta(\eta)\Gamma)^3} - \eta, \qquad \Theta(\eta) = \left(\frac{\eta + 1}{\eta}\right)^{\frac{1}{3}} - 1 \tag{5.2.12}$$

where the parameter η is determined from non-dimensionalization to be $\eta = \frac{\sigma_m}{S} \approx 1.08$. This equation is used in [29, 80]. A more realistic structure for the relation between surface tension and surfactant concentration is achieved through this equation: when there is no surfactant present on the film the introduction of surfactant will cause a large change in the surface tension, however, when the surfactant is close to saturation (a monolayer) then adding more surfactant will not alter the surface tension very much. This equation of state is also restricted for use only when the amount of surfactant is a monolayer. Again, $\sigma(1) = 0$ and $\sigma(\Gamma) < 0$ when $\Gamma > 1$.

Measured Equation of State

Experiments performed by Bull et al. using glycerin and NBD-PC are presented in [13]. As part of the investigation, the surface tension was measured for a range of surfactant concentrations using a tensiometer. A curve was then fit to this data to give an equation of state. We non-dimensionalize this equation in order to compare it to the other equations of state in Figure 5.8

$$\sigma(\Gamma) = \begin{cases} 0.28 \cos{(6.28\Gamma)} + 0.71, & \Gamma < 0.25 \\ 1.26 - 2.6\Gamma + 1.8\Gamma^2 - 0.41\Gamma^3, & 0.25 \leq \Gamma \leq 1.67. \end{cases} \tag{5.2.13}$$

The surfactant concentration Γ has also been non-dimensionalized by the concentration for a monolayer $\Gamma_C \approx 0.3\frac{\mu g}{cm^2}$; this value is determined in [13]. Since this equation is based on an experimental investigation using the same film and surfactant as our experiment, this equation may be the best relation to implement. However, we are unable to use (5.2.13) in the system (5.2.1) because we want to be able to consider surfactant concentration $\Gamma \geq 2$ and this equation becomes negative and hence unphysical in this region. Also, the slope near $\Gamma = 0$ does not satisfy the physical property that the surface tension changes more drastically when surfactant is deposited on a clean fluid surface than on one which already has surfactant present.

Multiple Layer Equation of State

We now seek an equation of state which has similar properties as (5.2.13) but is valid for higher concentrations of surfactant. Borgas and Grotberg [10] use an equation of state

$$\sigma(\Gamma) = (1 + \eta\Gamma)^{-3} \tag{5.2.14}$$

which was created for the case when more than a monolayer of surfactant is being considered. This equation is similar to (5.2.12) for $\Gamma < 1$. As in the Langmuir equation of state, $\eta = \frac{\sigma_m}{S}$ is determined from the non-dimensionalization of the equations. However, the multiple layer

equation of state possesses the critical property that $\sigma \to 0$ as $\Gamma \to \infty$ thus recognizing that the surface tension only changes by a small amount when more surfactant is introduced after a monolayer has been achieved, i.e., $\sigma'(\Gamma) \to 0$ as $\Gamma \to \infty$. Near $\Gamma \to 0$ the slope of σ satisfies the behavior that we physically expect. This formulation is based on properties of surface tension discussed by Sheludko [71] and by an experimental fit by Foda and Cox [27] who worked with an oil layer on water. In [28], a similar equation of state was used for an experiment which investigated the spreading of oleic acid on glycerin.

Comparison of the Equations of State

Figure 5.8 compares the graphs of the equations of state discussed above (5.2.11, 5.2.12, 5.2.13, 5.2.14). As shown the Langmuir (5.2.12), experimental (5.2.13), and multiple layer (5.2.14) equations of state have similar behavior for $\Gamma \leq 1$. However, the multiple layer equation of state (5.2.14) is the only one which stays positive for all Γ. The experimental equation of state was determined by fitting data which was only collected for surfactant concentration up to a little above a monolayer; larger Γ, for which $\sigma(\Gamma) < 0$, are not valid.

We now examine the influence of the choice of equation of state on the numerical solutions. For reasons discussed above, we restrict this comparison to the linear and multiple layer equations of state. Consider solutions generated using (5.2.4) with initial conditions

$$h(r, 0) = 1, \qquad \Gamma(r, 0) = \begin{cases} 1 - r^{10} & r \leq 1 \\ 0 & r > 1 \end{cases} \tag{5.2.15}$$

and non-dimensonal parameters $\beta = 0.5$, $\kappa = 0.02$, $\delta = 2.8 \times 10^{-5}$. Figure 5.9 shows the numerical simulations with the linear equation of state (5.2.11) and the multiple layer equation of state (5.2.14) at $t = 5$. Notice that the choice of equation of state in fact has a substantial influence. In particular, the multiple layer equation of state drives the film and surfactant faster and also creates a larger disturbance in the height of the film. For the remainder of this chapter we will use the multiple layer equations of state (5.2.14) as the equation of state.

5.3 Comparison to Experiment

Having described the effects of various parameters within ranges that include the physically reasonable values, we are ready to compare the experimental data (shown in Figure 5.3) to the predictions of the mathematical model. There are three aspects to make this comparison:

- Shapes of the evolving height $h(r, t)$ and surfactant concentration $\Gamma(r, t)$ profiles

- Propagation rate of film disturbance: maximum height
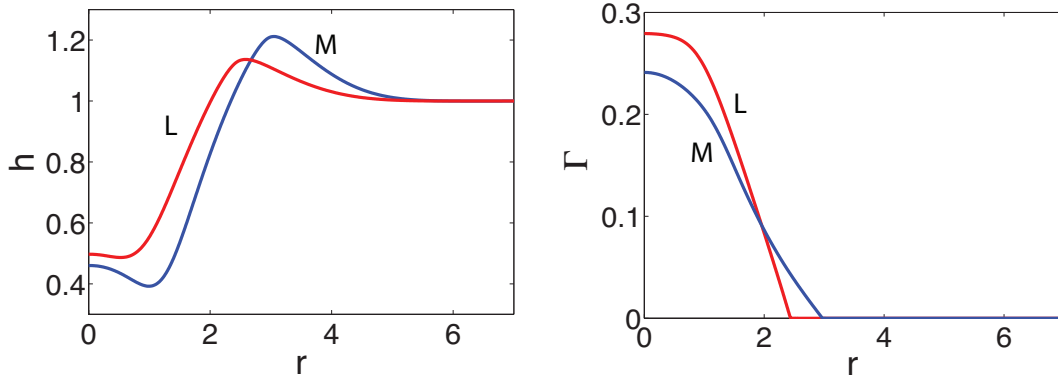
Figure 5.9: The height (left) and surfactant concentration (right) profiles at $t = 5$ with L: linear equation of state (5.2.11) in red and M: multiple layer equation of state (5.2.14) in blue.

- Spreading rate of the surfactant: leading edge

The first goal of this investigation is to compare the shape of the experimental height profile to the corresponding numerically simulated profile. We consider the height profiles to be in alignment if the maximum and minimum of the height profiles occur at approximately the same location as the experimental profiles. In order to achieve this alignment we vary the parameters β, κ, δ, the equation of state $\sigma(\Gamma)$, and time scale, in §5.3.1. An initial attempt at agreement is shown in Figure 5.10, using $\beta = 0.42$, $\kappa = 0.019$, $\delta = 3.05 \times 10^{-5}$ and $t = t^*$, where t^* represents dimensional time. Notice that the surfactant concentration from the experiment differs from the shape of the profile generated from the numerical solutions. We investigate the influence of the surfactant initial condition on the resulting height and surfactant profiles. In §5.3.2, we examine different factors that influence the time scale. In §5.3.3 we compare the spreading of the film height by tracking the location of the maximum of the height profile, marked by • in Figure 5.10(left). In §5.3.4 we describe a numerical method that tracks the leading edge of the surfactant and compare the numerical spreading to the spreading exhibited in the experiment, marked by • in Figure 5.10(right). In §5.3.5 we outline a numerical method to compare the height profile when we input surfactant data into the model rather than simulate the profile using the surfactant equation.

5.3.1 Profile Shape

In this section, we outline the method used to determine the optimal non-dimensional parameters β, κ, δ to align the experimental and simulated height profiles. In §5.2 we examined the influence of these parameters on the profile shape, specifically of the height. Here we determine approximations for these parameters which consist of physical dimensional parameters grouped
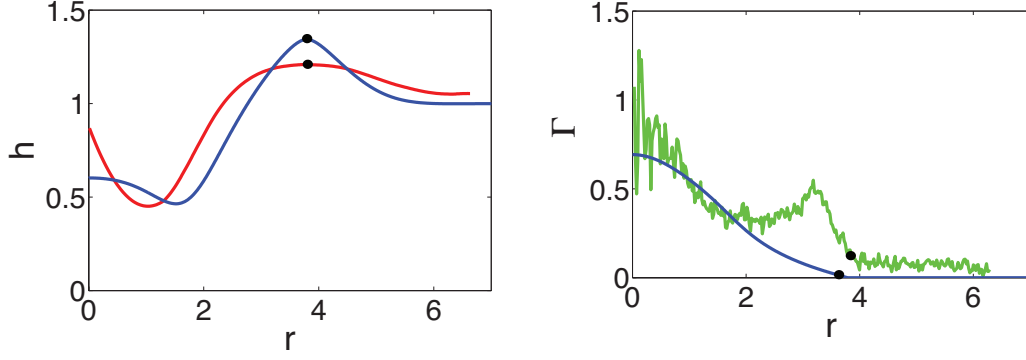
Figure 5.10: Left: The experimental (red) and numerical (blue) height profiles, at $t = 5$. The maximum height is marked with a •. Right: The experimental (green) and numerical (blue) surfactant concentration profiles. The leading edge of the surfactant is marked with a •.

through the non-dimensionalization of the equations. The physical parameters are listed in Table 5.1. Some of these values are determined by the experimental set-up while others are set by chemical or physical properties, such as the viscosity of the glycerin. Where appropriate, sources for the parameter value are cited in the third column.

Table 5.1: Key dimensional parameters

Symbol	Interpretation	Value
ρ	fluid density, glycerin	$1.26 \ g/cm^3$
μ	dynamic viscosity, glycerin	$0.83 \pm .03 \ Pa \cdot s$ [69]
D_s	surface diffusivity, surfactant	$10^{-4} \ cm^2/sec$[67]
σ_0	surface tension, clean glycerin	$63.4 \pm .3 \ dyne/cm$ [81]
σ_m	surfactant-contaminated surface tension	$35.3 \pm .3 \ dyne/cm$[13]
Γ_C	critical monolayer concentration	$0.3 \ \mu g/cm^2$[13]
H_0	initial fluid thickness	$0.98 \pm .03 \ mm$
R_0	lateral dimension	$0.8 \ cm$ (ring radius)

The non-dimensional parameters of (5.2.1) are related to the physical parameters of Table

5.1 by:

$$\beta = \frac{\rho H_0^2 g}{S} = 0.42 \pm .04 \tag{5.3.1a}$$

$$\kappa = \frac{H_0^2 \sigma_m}{R_0^2 S} = 0.019 \pm .002 \tag{5.3.1b}$$

$$\delta = \frac{\mu D_s}{S H_0} = 3.0 \times 10^{-5} \pm .3 \times 10^{-5}, \tag{5.3.1c}$$

where $S = \sigma_0 - \sigma_m \approx 27.9 \; dyne \; cm^{-1}$. The spatial scale r is measured in units of R_0 and non-dimensional time t is related to dimensional time t^* by

$$t = \frac{S H_0}{\mu R_0^2} t^* = (0.52 \pm .09) t^*. \tag{5.3.2}$$

We define the scaling factor

$$T = \frac{S H_0}{\mu R_0^2} \tag{5.3.3}$$

so that $t = T t^*$.

A reasonable approximation to the initial height profile is made using the experimental data collected at short exposure times. However, after the constraining ring is detached from the film it may still be in the view of the camera which causes the ring to obstruct the image of the laser line in this region. Thus throughout the comparison we ignore the height data for $r \leq 1$ since this is the region in which the ring is initially located. When the ring is lifted, a meniscus of fluid forms, but due to the uncertainty in the first experimental image we are not confident of the maximum height of the meniscus. We attempt to match the basic shape of the experimental height profile due to the meniscus as the fluid detaches from the ring with the initial condition

$$h(r,0) = \begin{cases} a \sin\left(2r - \frac{\pi}{3}\right) + (1+a), & 0 \leq r < \frac{11\pi}{12} \\ 1 & r \geq \frac{11\pi}{12} \end{cases} \tag{5.3.4}$$

where a is varied to fit the simulations to the experimental height profile. Figure 5.12(top left) shows this comparison between the initial profiles with $a = 0.15$ in the numerical (5.3.4) and experimental data. While initially the maximum height of the simulation is much smaller than the maximum in the experiment, at later times these maxima are approximately in agreement.

We use the multiple layer equation of state (5.2.14) since it is similar to the form of the equation of state determined experimentally in [13]. We chose this equation of state by performing a numerical investigation of the different equations to determine which choice aligned the

numerical simulations to fit the experimental profiles most accurately. We then systematically vary the parameters β, κ to achieve an optimal fit.

Varying Parameters

Since β was shown to have the largest influence on the structure of the height profile, we first freeze $\kappa = 0.02$, $\delta = 2.8 \times 10^{-5}$ and vary β. We determine that the best visual correlation between the numerical and experimental profiles is achieved when $\beta = 0.5$. Note that this value is slightly larger than that predicted in (5.3.1a) but we still consider it to be reasonable. Next we freeze $\beta = 0.5$, $\delta = 2.8 \times 10^{-5}$ and vary κ to determine the best fit is obtained with $\kappa = 0.02$. This value falls within the range of values (5.3.1b). The time scale is determined by taking a plot of the experimental height at t^* and comparing the plot of the numerical height at varying times t until the maximums occur at approximately the same location. We find that a suitable relation for the time scale is $t = t^*$. However, note that this would give a scaling factor $T = 1$, which is well outside the range of (5.3.2). We then verified this $T = 1$ scaling by comparing a sequence of experimental plots at $t^* = 1, 3, 5, 7, 9$ to numerical plots at the corresponding times.

Initial Surfactant Distribution

Images of the surfactant are collected at long exposure time so the first image is at $t = 1$ sec rather than at $t = 0$ sec. This means that the initial surfactant profile, and the early evolution is not know from the experiment. To address this uncertainty in the initial profile, we consider three forms for the initial surfactant profile as shown in Figure 5.11. We examine the influence of these choices on the film height profile and also the resulting structure of the surfactant distribution.

(a) First, we assume within the constraining ring the surfactant is uniformly distributed, i.e., $\Gamma \approx constant$, and immediately after the ring releases from the fluid there is a jump in the surfactant concentration (from an area with surfactant to an area with no surfactant). From Figure 5.3 we estimate that the initial layer of surfactant within the constraining ring corresponds to $\Gamma = 2$ and outside the ring $\Gamma = 0$. We choose the initial condition to be a smooth interpolation between these values,

$$\Gamma(r,0) = \begin{cases} 2 & r < \frac{\pi}{3} \\ \cos(12r) + 1 & r < \frac{5\pi}{12} \\ 0 & r \geq \frac{5\pi}{12} \end{cases} \tag{5.3.5}$$

which is shown in Figure 5.11a. Figure 5.12 shows the numerical results and experimental data for the height and the numerical results for the surfactant profiles at $t = 0.1, 3, 5, 7, 9$ seconds.

The numerical simulations mimic the basic structure of the experimental height data. The prediction of the time scale from non-dimensionalization (5.3.2) is $t = 0.5t^*$. However, as just discussed, in fact the height profiles agree when the relation $t = t^*$ is used. For the remainder of this section, we discuss possible effects from varying the initial surfactant distribution, postponing further discussion of this discrepancy in the time scale to §5.3.2.

(a) (b) (c)
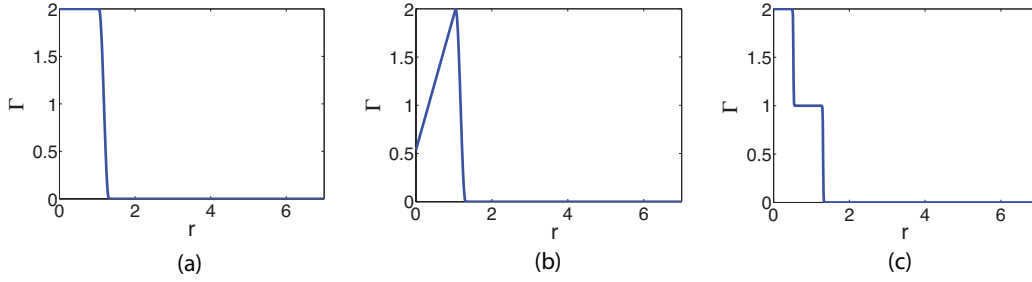
Figure 5.11: Initial conditions for the surfactant concentration profile. (a) corresponds to equation (5.3.5). (b) corresponds to (5.3.6). (c) corresponds to (5.3.7).

(b) The surfactant profile could be affected by the meniscus as the ring lifts, as occurs in the height profile. To mimic the surfactant distribution at the meniscus, we consider the initial condition

$$\Gamma(r,0) = \begin{cases} 1.4r + 2 - \frac{2\pi}{3} & 0 \leq r < \frac{\pi}{3} \\ \cos(12r) + 1 & \frac{\pi}{3} \leq r < \frac{5\pi}{12} \\ 0 & r \geq \frac{5\pi}{12} \end{cases} \tag{5.3.6}$$

which is shown in Figure 5.11b. In Figure 5.13 we show the numerical and experimental data for the height and surfactant profiles at $t = 0.1, 3, 5, 7, 9$ seconds. Even though the initial condition (5.3.6) has a peak, this maximum quickly smooths. The simulations exhibit similar behavior as those generated with Figure 5.11a as initial conditions. However, the ridge is moving slightly slower (which is taken into consideration in the time scale) which is expected since there is less surfactant. We discuss the influence of surfactant mass on the time scale in §5.3.2.

(c) Finally, we consider a profile similar to the shape seen in the experimental data (see Figure 5.3). Initially there is a droplet of surfactant deposited which would take on the form of initial conditions already generated. However, as the surfactant spreads a thinner layer (monolayer) of surfactant protrudes from the reservoir rather than the mass of surfactant merely

smoothing. We attempt to mimic this behavior by implementing the initial condition

$$\Gamma(r, 0) = 0.5 - 0.25 \tanh\left(\frac{r - \frac{\pi}{6}}{0.01}\right) - 0.25 \tanh\left(\frac{r - \frac{5\pi}{12}}{0.01}\right) \tag{5.3.7}$$

as shown in Figure 5.11c. Figure 5.14 shows the evolution of the height and surfactant profiles. The basic behavior of the height profile is captured. However, the surfactant profile is quickly smoothed and by $t = 3\ sec$ no longer has the two step structure exhibited in the experimental data.

Summary

While we are able to capture the basic structure of the height profile for all three choices of initial surfactant profiles, we are unable to simulate a profile similar to that seen in the experimental surfactant data. We can not reasonably expect to match the numerical simulations accurately in either height or surfactant while there is such a discrepancy between the numerical and experimental surfactant profiles. This disagreement raises questions as to the accuracy of the model. We further investigate the accuracy of the surfactant equation in §5.3.5 by neglecting that equation and instead using the data from the experiment to drive the film.
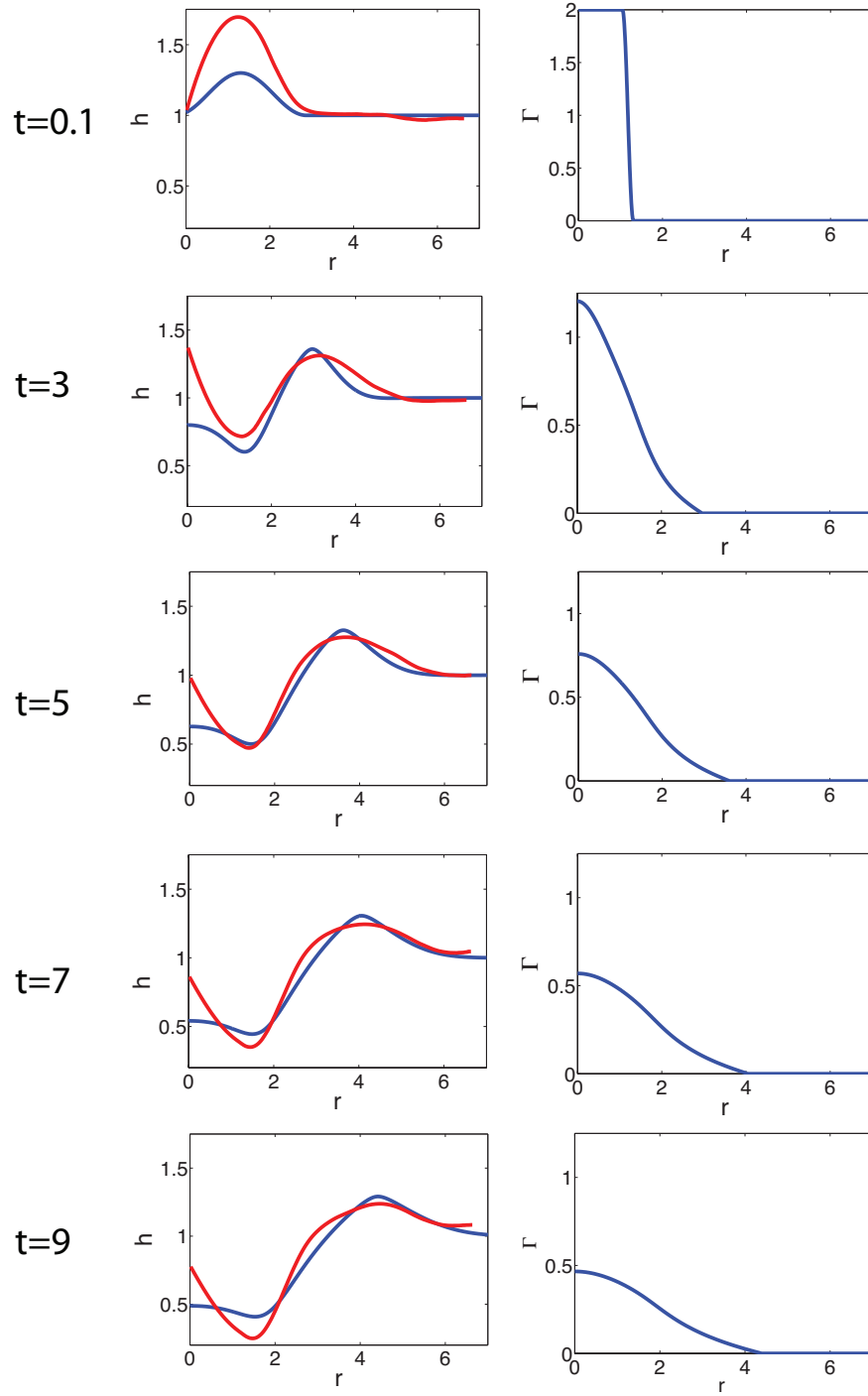
Figure 5.12: Comparison of experimental results (in red) and numerical simulations (in blue) with initial conditions (5.3.4) and (5.3.5) and $\beta = 0.5$, $\kappa = 0.02$, $\delta = 3.0 \times 10^{-5}$, $t = t^*$. Left: height profiles and Right: surfactant profiles at $t = 0.1, 3, 5, 7, 9$ sec.
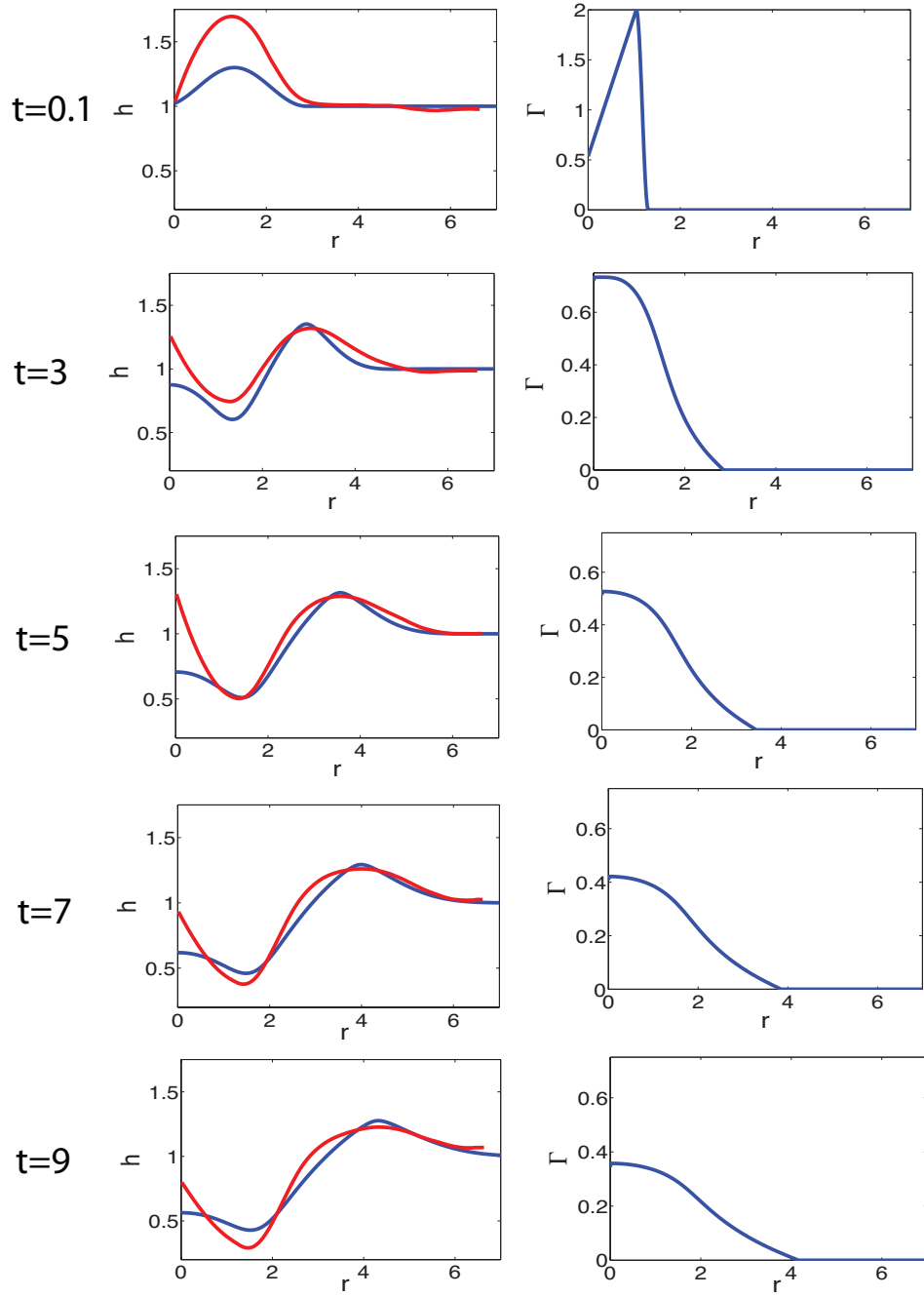
Figure 5.13: Comparison of experimental results (in red) and numerical simulations (in blue) with initial conditions (5.3.4) and (5.3.6) and $\beta = 0.5$, $\kappa = 0.02$, $\delta = 3.0 \times 10^{-5}$, $t = t^*$.. Left: height profiles and Right: surfactant profiles at $t = 0.1, 3, 5, 7, 9$ sec.
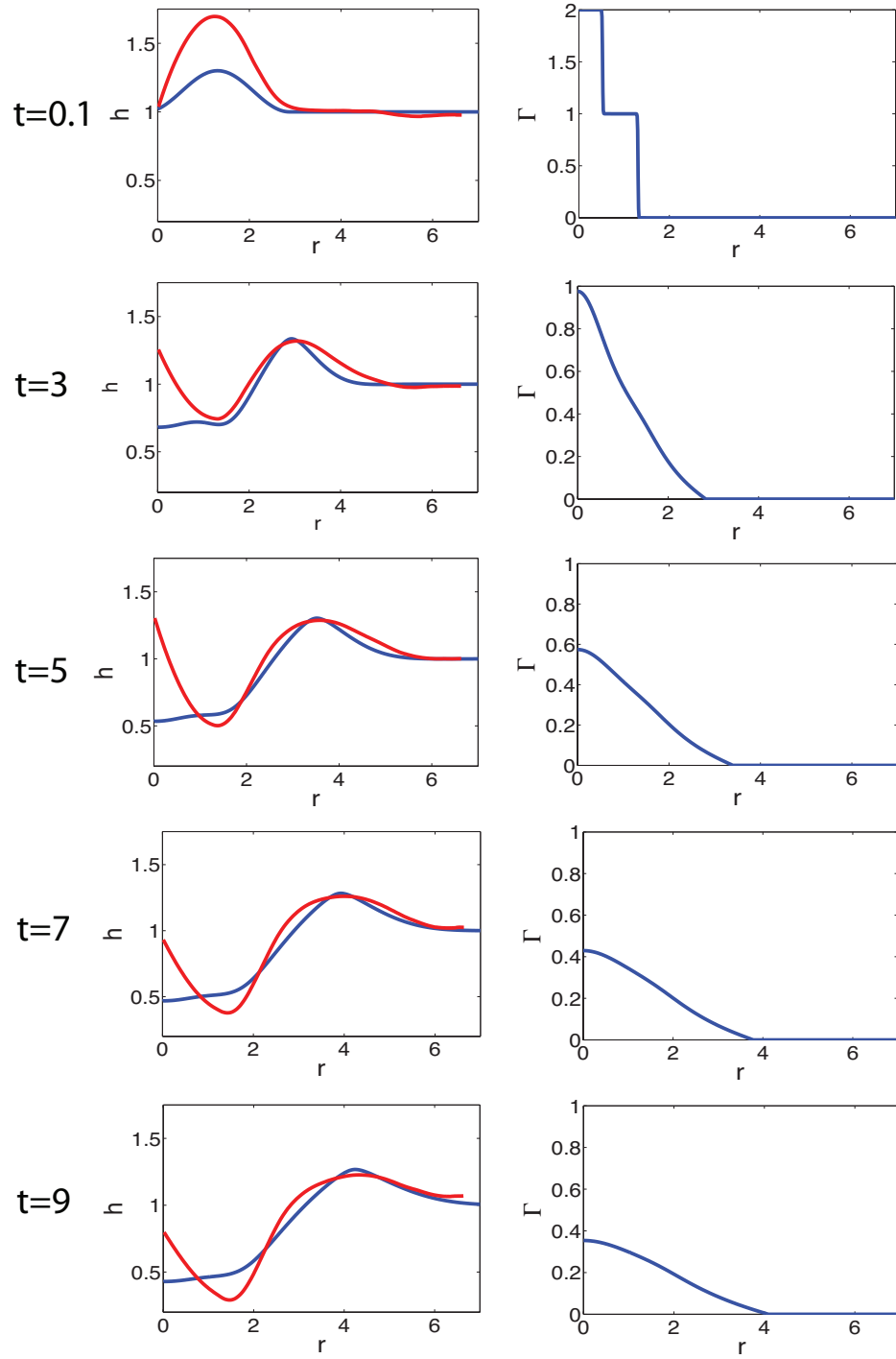
Figure 5.14: Comparison of experimental results (in red) and numerical simulations (in blue) with initial conditions (5.3.4) and (5.3.7) and $\beta = 0.5$, $\kappa = 0.02$, $\delta = 3.0 \times 10^{-5}$, $t = t^*$.. Left: height profiles and Right: surfactant profiles at $t = 0.1, 3, 5, 7, 9$ sec.

5.3.2 Dependence of Time Scale on Surfactant Mass and Length Scale

In §5.2.2, we determined from the non-dimensionalization that the temporal scale is defined as

$$t = Tt^* \approx 0.5t^* \tag{5.3.8}$$

where $T = \frac{SH_0}{\mu R_0^2} \approx 0.5$ is defined by (5.3.3). At each time t^* (in seconds), the experimental height profiles should agree with the simulation height profiles at time t. However, the correspondence between experimental time t^* and simulation time t that we observe is more consistent with $T = 1$. We consider two possible explanations for this discrepancy between time scales: the surfactant mass and the parameter R_0.

Influence of Surfactant Mass

In §4.1.1, we discussed the scale invariance of the system of equations (3.1.4). While this equation is in planar coordinates, the argument for axisymmetric coordinates is analogous. We found that if the surfactant mass is scaled by a parameter $a > 0$ then time is also scaled by a; $(h(r, at), a\Gamma(r, at))$ is a solution to (3.1.4) with mass am if (h, Γ) is a solution with mass m. This argument, however, relies on the use of the linear equation of state. Also, the simplifying assumption $\beta = \kappa = \delta = 0$ is utilized but if these terms were included the parameters would scale like $a\beta$, $a\kappa$, $a\delta$.

The multiple layer equation of state is used in generating the numerical simulations compared to the experimental results. Due to the nonlinearity introduced by this equation of state, the scaling is not as simple. Nevertheless, we expect the the mass of the surfactant to influence the spreading of the film through the time scale. We perform a numerical investigation to determine the influence of the surfactant mass on the time scale. Consider the initial condition

$$\Gamma(r, 0) = \begin{cases} a & 0 \leq r < \frac{\pi}{3} \\ a(0.5\cos(12r) + 0.5) & \frac{\pi}{3} \leq r \leq \frac{5\pi}{12} \\ 0 & r > \frac{5\pi}{12} \end{cases} \tag{5.3.9}$$

where a varies and represents the maximum of the surfactant concentration which is proportional to the surfactant mass. When $a = 2$, this condition corresponds to (5.3.5). We seek an additional scaling factor M which depends on the mass of the surfactant; let $Mt = 0.5t^*$ where M is determined from qualitatively aligning the maximum in the height profile and relating the times used to make this comparison. Figure 5.15 shows the scaling factor M versus the mass of the surfactant (denoted by a the surfactant maximum) required to align the maximum in the numerical and experimental height profiles. This figure suggests that the scaling factor M asymptotes to $M \approx 0.65$ as $a \to \infty$. That is, increasing the surfactant mass has little effect

on the time scale for larger values of a. Since $\sigma' \to 0$ as $\Gamma \to \infty$, the equation of state does not have a significant effect when Γ is well above a monolayer. Consequently, the mass has a substantial influence on the time scale at small values of Γ but after saturation, the additional mass does not have as strong of an impact.
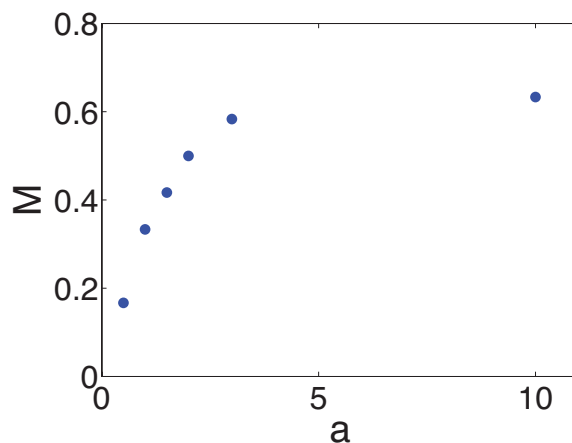
Figure 5.15: The scaling time factor M used when relating numerical and experimental profiles versus the mass of surfactant characterized by a in (5.3.9)

Spatial Scale R_0

In the non-dimensional grouping for the time scale (5.3.3), there are no adjustable parameters. The value for the spreading parameter S is dictated by the properties of surface tension of glycerin; the dynamic viscosity is also intrinsic. The height $H_0 \approx 0.98~mm$ and length $R_0 = 8~mm$ are set by the initial set-up of the experiment. The height scale H_0 is the uniform height of the glycerin before the surfactant is deposited and the length scale R_0 is the radius of the constraining ring. The radius rather than the diameter is used as the length scale because of the assumption that the spreading is axisymmetric. In order to correlate the initial condition of the numerics and experiment these are the relevant spatial scalings.

However, there is a contradiction between the time scale computed from the non-dimensionalization and the one observed in comparing the numerical simulations to the experimental data. The non-dimensionalization suggests that $t \approx 0.5t^*$. Figure 5.16 shows the experimental and numerical data at the initial time $t^* = 0.1$ ($t = 0.05$) (recall that the initial condition for the simulation is different from the experimental plot) and $t^* = 4$ ($t = 2$). The latter profiles obviously do not agree. However, if we adjust the time scale so that $t = t^*$ then Figure 5.12

shows a reasonable fit between the numerical and experimental data.
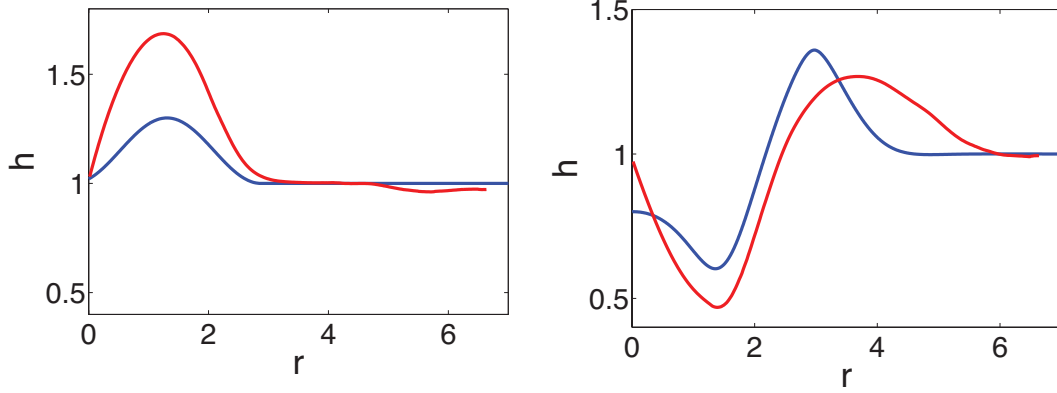
Figure 5.16: The numerical (blue) and experimental (red) height profiles at $t^* = 0.1$ (left) and $t^* = 4$ (right) where $t = 0.5t^*$.

Previous studies on the spreading of surfactant on a thin layer have regarded R_0 as a free parameter [20, 28] in order to adjust the correspondence between experiment and simulated times to achieve agreement. While we expect R_0 to be set by the radius of the ring, we examine the possibility of another length scale being the appropriate choice.

The goal of this calculation is to find a spatial scaling factor R_0 so that the numerical simulation $h(y, \tau_m)$ achieves a maximum at y_m, the location of the maximum in the numerical simulation at time τ_m where $y = \frac{r}{R_0}$. During this investigation, we require that T and R_0 satisfy the relation (5.3.3).

Define

$$\tau = T t^* \tag{5.3.10}$$

where $T = \frac{SH_0}{\mu R_0^2}$. Let S, H_0, μ to fixed. Then the non-dimensional grouping is a formula for T in terms of R_0. If $R_0 = 8\ mm$ then $T \approx 0.5$, which corresponds to the set-up of the experiment. Preserving this property, define

$$T = \frac{32}{R_0^2}. \tag{5.3.11}$$

We want to investigate the dependence of τ on R_0. From (5.3.10) if $t^* = 2$ then $\tau = 2T$;

hence from (5.3.11) $\tau = \frac{64}{R_0^2}$. Solving for R_0,

$$R_0 = \sqrt{\frac{64}{\tau}}, \qquad \text{where } \tau = j\Delta\tau, \ \ j = 0, 1, 2, \ldots. \tag{5.3.12}$$

Next, we determine the spatial location of the maximum in the numerical simulations of the height profile for each time. The numerical simulations are inherently generated in the non-dimensional variable y which corresponds to $y = \frac{r}{R_0}$. The goal of this investigation is to determine the necessary time scale to align the maximum in the numerical simulation and the experimental data at each time. Define $r_m \approx 25 \ mm$ to be the location of the maximum height in the experimental data at $t^* = 2$. We plot the location of the experimental maximum height at $t^* = 2$ in non-dimensional form $\frac{r_m}{R_0}$ in Figure 5.17. This figure is also a parametric plot of the location of the height maximum $y_m(\tau)$ in the numerical simulations and the spatial scaling factor $R_0(\tau)$. The two curves cross at $R_0 \approx 12.65 \ mm$ which suggests the spatial and temporal variables should be scaled like $y = \frac{r}{12.65}$ and $\tau = 0.21t^*$, respectively. Figure 5.18 shows the numerical and experimental results with scaling parameters $R_0 = 12.65$ and $T = 0.21$, at $t^* = 2, 4, 6, 8$.

The result of this calculation is that the experiment and simulation line up if we allow $R_0 = 12.65 \ mm$. However, this value is so far from the physical value $R_0 = 8 \ mm$ that we consider this scaling unrealistic, and conclude that changing R_0 cannot alone account for the discrepancy between the experiment and simulation time scales. This discrepancy between time scales is an issue concerning the accuracy of the system (5.2.1) to model the spreading of thin films.
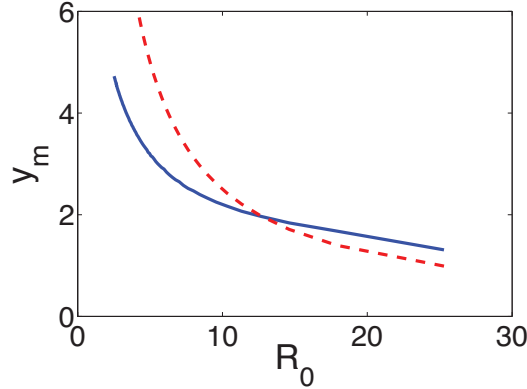
Figure 5.17: The location of the maximum height in the numerical simulations y_m and the relation between the location of the height maximum in the experimental data r_m at $t^* = 4$ to the scaling factor R_0, $\frac{r_m}{R_0}$ (dashed line). Both of these curves are plotted against R_0.
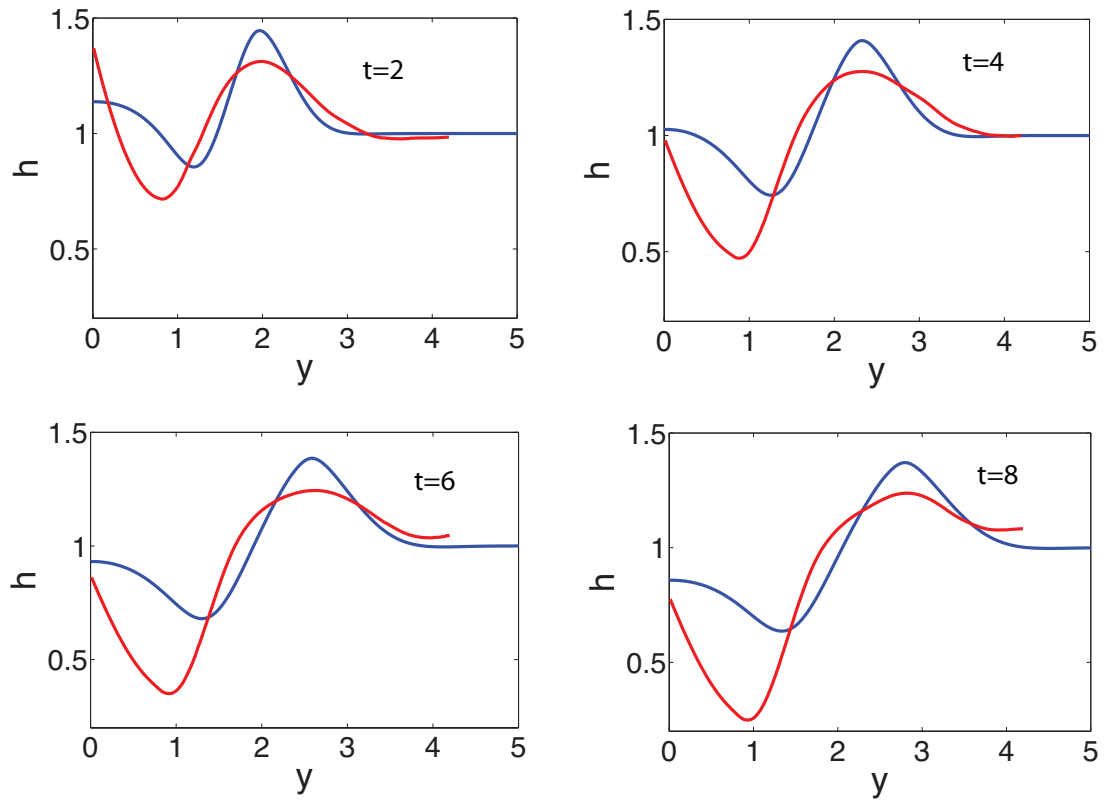
Figure 5.18: The height profile from the numerical simulations (blue) and experiment (red) with $R_0 = 12.65$ and $T = 0.21$.

5.3.3 Location of maximum in height

Another method for comparison of the numerical model to the experiment is through the rate in which the disturbance in the height spreads. We define $r = r_M^s(t)$ and $r = r_M^e(t)$ to be the location of the maximum of the capillary ridge $h_{max}(t) = max_r h(r,t)$ in the simulation and experiment, respectively. We compare r_M^s and r_M^e against time on log-log plots in Figure 5.19 to determine the spreading rate of the film. The numerical data is generated using initial conditions (5.3.4-5.3.5). From this figure, we determine r_M^s spreads at a slower rate than r_M^e which travels like $t^{0.29}$. Also, the locations of the height maxima are comparable which supports the agreement between the numerical and experimental results. This comparison assumes the time scale $t = t^*$.
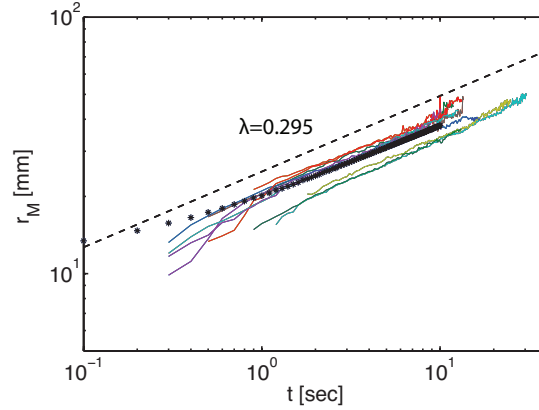
Figure 5.19: Log-log plot of r_M, the location for h_{max}. The solid lines represent the location of h_{max} from the experiment, each color represents a different experimental run. Each $*$ represents the location of the h_{max} from the numerical simulation. The dashed line is a comparison line with slope 0.295.

5.3.4 Location of Leading Edge of Surfactant

In §3.7 we tracked the leading edge of the surfactant $r_0(t)$ for the simplified system (3.7.1) where $\beta = \kappa = \delta = 0$. However, when making the comparison to the experiment it is not reasonable to make the simplifying assumptions that we made in §3.7. For example, gravitational and capillary forces do in fact affect the evolution of the film. Thus we must include the parameters β, κ. However, since in §5.2.2 we determined δ to be $O(10^{-5})$, we can consider the surface diffusion a negligible effect, i.e., take $\delta = 0$. The key property used to transform the support of

the surfactant to a fixed domain while tracking the location of the leading edge of the surfactant was that the support of the surfactant Γ remains bounded for each $t > 0$. Define the surface velocity speed $w(r,t) = h\sigma_r - \beta\left(\frac{1}{2}h^2 h_r\right) + \kappa\left(\frac{1}{2}h^2(h_{rr} + \frac{1}{r}h_r)_r\right)$. Then the argument that the surfactant spreads with finite speed is equivalent to that shown in Lemma 1.

Numerical Method

Consider (5.2.1) with $\beta > 0$, $\kappa > 0$ and $\delta = 0$. As presented in §3.2 we scale the location of the leading edge of surfactant by $\xi = \frac{r}{r_0(t)}$ and consider the transformed variables

$$h(r,t) = \overline{h}(\xi,t), \qquad \Gamma(r,t) = \overline{\Gamma}(\xi,t), \qquad \xi = \frac{r}{r_0(t)}. \tag{5.3.13}$$

Substituting this change of variables into (5.2.1) results in, dropping the $^-$,

$$h_t = \frac{\xi\,\dot{r}_0(t)}{r_0(t)}h_\xi - \frac{1}{\xi r_0(t)^2}\left(\tfrac{1}{2}\xi h^2 \sigma_\xi\right)_\xi \;+\; \beta\frac{1}{r_0(t)^2\xi}\left(\tfrac{1}{3}\xi h^3 h_\xi\right)_\xi \tag{5.3.14a}$$

$$- \; \kappa\frac{1}{r_0(t)^4\xi}\left(\tfrac{1}{3}\xi h^3\left(h_{\xi\xi} + \tfrac{1}{\xi}h_\xi\right)_\xi\right)_\xi$$

$$\Gamma_t = \frac{\xi\dot{r}_0(t)}{r_0(t)}\Gamma_\xi - \frac{1}{\xi r_0(t)^2}\left(\xi h \Gamma \sigma_\xi\right)_\xi \;+\; \beta\frac{1}{r_0(t)^2\xi}\left(\tfrac{1}{2}\xi h^2 \Gamma h_\xi\right)_\xi \tag{5.3.14b}$$

$$- \; \kappa\frac{1}{r_0(t)^4\xi}\left(\tfrac{1}{2}\xi h^2\Gamma\left(h_{\xi\xi} + \tfrac{1}{\xi}h_\xi\right)_\xi\right)_\xi.$$

Notice that the higher order derivatives present in the β, κ terms act only on h, thus the surfactant concentration profile Γ is not smoothed by the addition of these terms. The support of Γ is defined on $0 \leq \xi \leq 1$ but in this case the height profile h cannot be restricted to this domain. The change of variable ξ shifts the height profile thus we work on the reduced domain $0 \leq \xi < 5$. In this section we use initial conditions which correspond to (5.3.4)

$$h_0(r) \;=\; h_0(\xi) = \begin{cases} 0.15\sin\left(2\xi - \frac{\pi}{3}\right) + 1.15, & 0 \leq \xi < \frac{11\pi}{12} \\ 1 & \xi \geq \frac{11\pi}{12}. \end{cases} \tag{5.3.15a}$$

$$\Gamma_0(r) \;=\; \Gamma_0(\xi) = \begin{cases} 1 - \xi^{10}, & \xi < 1 \\ 0, & \xi \geq 1 \end{cases} \tag{5.3.15b}$$

$$r_0(0) \;=\; 1. \tag{5.3.15c}$$

Note that at $t = 0$, $\xi = r$ since $r_0(0) = 1$. We consider boundary conditions

$$h_\xi(0, t) = 0, \qquad \kappa h_{\xi\xi\xi}(0, t) = 0, \qquad \Gamma_\xi(0, t) = 0 \tag{5.3.16a}$$

$$h(\infty) = 1, \qquad \Gamma(1, t) = 0. \tag{5.3.16b}$$

In §3.2, the jump in Γ_ξ at $\xi = 1$ introduced a jump in h for the reduced system. However, due to the smoothing effects present in the β and κ terms, this jump actually occurs in $h_{\xi\xi\xi}$. This behavior is shown in Figure 5.20.
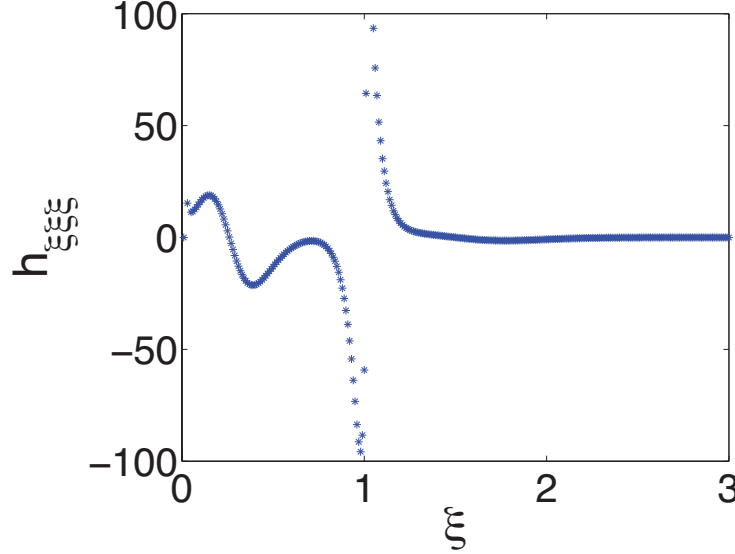
Figure 5.20: Due to the jump in Γ_ξ at $\xi = 1$, $h_{\xi\xi\xi}$ jumps as stipulated by the jump condition of (5.3.14).

Using (5.3.14b) we determine the speed $\dot{r}_0(t)$ of the leading edge of the surfactant noting that $\Gamma_t(1, t) = 0$. Evaluating (5.3.14b) at $\xi = 1^-$

$$-\frac{\dot{r}_0}{r_0}\Gamma_\xi\big|_{\xi=1^-} = -\frac{1}{r_0^2}(h\Gamma\sigma_\xi)_\xi\big|_{\xi=1^-} + \beta\frac{1}{r_0^2}\left(\tfrac{1}{2}h^2\Gamma h_\xi\right)_\xi\big|_{\xi=1^-} - \kappa\frac{1}{r_0^4}\left(\tfrac{1}{2}h^2\Gamma\left(h_{\xi\xi} + \tfrac{1}{\xi}h_\xi\right)\right)_\xi{}_\xi\big|_{\xi=1^-}. \tag{5.3.17}$$

However, $\Gamma(1, t) = 0$ so

$$-\frac{\dot{r}_0}{r_0}\Gamma_\xi^- = -\frac{1}{r_0^2}h\left(\Gamma_\xi^-\right)^2\sigma_\Gamma + \beta\frac{1}{r_0^2}\tfrac{1}{2}h^2\Gamma_\xi^- h_\xi - \kappa\frac{1}{r_0^4}\tfrac{1}{2}h^2\Gamma_\xi\left(h_{\xi\xi} + \tfrac{1}{\xi}h_\xi\right)_\xi\big|_{\xi=1^-}. \tag{5.3.18}$$

110

Dividing through by $\Gamma_\xi \neq 0$, we find that

$$\dot{r}_0 = \frac{1}{r_0} h(1,t) \Gamma_\xi(1^-,t) \sigma'(0) \quad - \quad \beta \frac{1}{r_0} \left(\tfrac{1}{2} h^2(1,t) h_\xi(1,t) \right)$$

$$+ \quad \kappa \frac{1}{r_0^3} \left(\tfrac{1}{2} h^2(1,t) \left(h_{\xi\xi}(\xi,t) + \frac{1}{\xi} h_\xi(\xi,t) \right)_\xi \bigg|_{\xi=1^-} \right). \qquad (5.3.19)$$

Numerical Scheme

This section outlines the finite difference method used to generate numerical results for system (5.3.14-5.3.16, 5.3.19). In this method, the spatial derivatives of the linear terms are upwinded and the nonlinear terms are center differenced. We solve simultaneously for h and Γ.

Let $h_j^n \approx h(j\Delta\xi, n\Delta t)$ and $\Gamma_j^n \approx \Gamma(j\Delta\xi, n\Delta t)$ where $\Delta\xi = \frac{10}{N}$, N is the number of grid-points. We use the standard notation for spatial averages of $u_j^n \approx u(j\Delta\xi, n\Delta t)$,

$$\bar{u}_{j+\frac{1}{2}}^n \equiv \frac{u_{j+1}^n + u_j^n}{2}. \qquad (5.3.20)$$

The discretized equations are

$$h_j^{n+1} = h_j^n + \Delta t \xi_j \frac{x_0^{n+1} - x_0^n}{x_0^n \Delta t} \left(\frac{h_{j+1}^{n+1} - h_j^{n+1}}{\Delta\xi} \right) + \frac{\Delta t}{\xi_j (x_0^n)^2 \Delta\xi} \left(\mathcal{F}_{j+\frac{1}{2}}^{n+1} - \mathcal{F}_{j-\frac{1}{2}}^{n+1} \right) \qquad (5.3.21a)$$

$$\Gamma_j^{n+1} = \Gamma_j^n + \Delta t \xi_j \frac{x_0^{n+1} - x_0^n}{x_0^n \Delta t} \left(\frac{\Gamma_{j+1}^{n+1} - \Gamma_j^{n+1}}{\Delta\xi} \right) + \frac{\Delta t}{\xi_j (x_0^n)^2 \Delta\xi} \left(\mathcal{G}_{j+\frac{1}{2}}^{n+1} - \mathcal{G}_{j-\frac{1}{2}}^{n+1} \right) \qquad (5.3.21b)$$

where $1 \leq j \leq N$ and $n \geq 0$. We separate the fluxes by, (dropping the superscript $n+1$)

$$\mathcal{F}_{j+\frac{1}{2}} = \tfrac{1}{2} \mathcal{F}_{j+\frac{1}{2}}^1 + \tfrac{1}{3} \beta \mathcal{F}_{j+\frac{1}{2}}^2 + \tfrac{1}{3} \kappa \mathcal{F}_{j+\frac{1}{2}}^3 \qquad (5.3.22a)$$

$$\mathcal{G}_{j+\frac{1}{2}} = \mathcal{G}_{j+\frac{1}{2}}^1 + \tfrac{1}{2} \beta \mathcal{G}_{j+\frac{1}{2}}^2 + \tfrac{1}{2} \kappa \mathcal{G}_{j+\frac{1}{2}}^3 + \delta \mathcal{G}_{j+\frac{1}{2}}^4 \qquad (5.3.22b)$$

and express the flux functions as

$$\mathcal{F}^1_{j+\frac{1}{2}} = \overline{\xi}_{j+\frac{1}{2}} \left(\overline{h}_{j+\frac{1}{2}}\right)^2 \sigma'\left(\overline{\Gamma}_{j+\frac{1}{2}}\right) \frac{\Gamma_{j+1} - \Gamma_j}{\Delta\xi} \tag{5.3.23a}$$

$$\mathcal{F}^2_{j+\frac{1}{2}} = \overline{\xi}_{j+\frac{1}{2}} \left(\overline{h}_{j+\frac{1}{2}}\right)^3 \frac{h_{j+1} - h_j}{\Delta\xi} \tag{5.3.23b}$$

$$\mathcal{F}^3_{j+\frac{1}{2}} = \frac{1}{r_0^2}\overline{\xi}_{j+\frac{1}{2}} \left(\overline{h}_{j+\frac{1}{2}}\right)^3 \frac{\mathcal{E}_{j+2} - \mathcal{E}_j}{2\Delta\xi} \tag{5.3.23c}$$

$$\mathcal{E}_{j+2} = \frac{h_{j+3} - 2h_{j+2} + h_{j+1}}{\Delta\xi^2} + \frac{1}{\overline{\xi}_{j+\frac{3}{2}}} \frac{h_{j+2} - h_{j+1}}{\Delta\xi} \tag{5.3.23d}$$

$$\mathcal{G}^1_{j+\frac{1}{2}} = \overline{\xi}_{j+\frac{1}{2}}\overline{h}_{j+\frac{1}{2}}\overline{\Gamma}_{j+\frac{1}{2}}\sigma'\left(\overline{\Gamma}_{j+\frac{1}{2}}\right) \frac{\Gamma_{j+1} - \Gamma_j}{\Delta\xi} \tag{5.3.23e}$$

$$\mathcal{G}^2_{j+\frac{1}{2}} = \overline{\xi}_{j+\frac{1}{2}} \left(\overline{h}_{j+\frac{1}{2}}\right)^2 \overline{\Gamma}_{j+\frac{1}{2}} \frac{h_{j+1} - h_j}{\Delta\xi} \tag{5.3.23f}$$

$$\mathcal{G}^3_{j+\frac{1}{2}} = \frac{1}{r_0^2}\overline{\xi}_{j+\frac{1}{2}} \left(\overline{h}_{j+\frac{1}{2}}\right)^2 \overline{\Gamma}_{j+\frac{1}{2}} \frac{\mathcal{E}_{j+2} - \mathcal{E}_j}{2\Delta\xi} \tag{5.3.23g}$$

$$\mathcal{G}^4_{j+\frac{1}{2}} = \overline{\xi}_{j+\frac{1}{2}} \frac{\Gamma_{j+1} - \Gamma_j}{\Delta\xi}. \tag{5.3.23h}$$

The leading edge of the surfactant is updated explicitly, based on (5.3.19)

$$r_0^{n+1} = r_0^n - \frac{\Delta t}{r_0^n}h_J^n \frac{\Gamma_{J-1}^n}{\Delta\xi}\sigma'(0) - \beta\frac{\Delta t}{2r_0^n}(h_{J+1}^n)^2 \frac{h_J^n - h_{J-1}^n}{2\Delta\xi} \tag{5.3.24}$$

$$+ \quad \kappa\frac{\Delta t}{2(r_0^n)^3}(h_J^n)^2\left[\left(\frac{h_J^n - 3h_{J-1}^n + 3h_{J-2}^n - h_{J-3}^2}{\Delta\xi^3}\right) + \frac{1}{\Delta\xi}\left(\frac{1}{\overline{\xi}_{J+\frac{1}{2}}}\frac{h_{J+1}^n - h_J^n}{\Delta\xi} - \frac{1}{\overline{\xi}_{J-\frac{1}{2}}}\frac{h_J^n - h_{J-1}^n}{\Delta\xi}\right)\right]$$

where J is the grid point such that $\xi_J = 1$. The boundary conditions are

$$h_0^n = h_1^n, \qquad h_N^n = 1 \tag{5.3.25}$$

$$\Gamma_0^n = \Gamma_1^n, \qquad \Gamma_J^n = 0. \tag{5.3.26}$$

Figure 5.21 shows numerical simulations with initial conditions (5.3.15); the surfactant maintains a fixed domain while the height profile is smoothed. Thus we are able to work on a smaller domain than when considering the physical spatial variable r.

Comparison of r_0

We now compare the spreading of the surfactant predicted by the numerical simulations and observed in the experiment. Using (5.3.24), we determine r_0 from the numerical simulations. Figure 5.22 shows the location of the leading edge of surfactant from the numerical simulations and the experiment on a log-log scale. We determine that the numerics and experiment agree
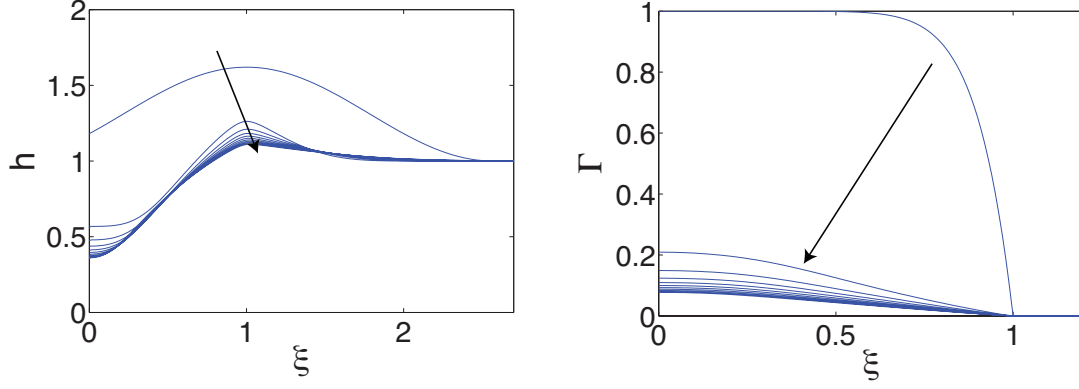
Figure 5.21: Numerical simulations of system (5.3.14-5.3.16, 5.3.19) with $\Delta\xi = 0.01$ at $t = 0, 5, \ldots, 50$.

that r_0 moves like $t^{\frac{1}{4}}$ and that the leading edge of surfactant is approximately at the same location in both the experiment and numerical simulation, again we use the time scale $t = t^*$ for this comparison. Recall this spatial scale is in agreement with the similarity scaling determined in §4.2.1 where $\beta = \kappa = 0$. This result suggests that the surfactant exhibits similar spreading behavior in spite of the values for β, κ. The main driving force of the film is incorporated by the equation of state while the main influence of the β and κ terms is to smooth the profiles. Consequently, they provide a negligible influence on the spreading speed of the film.
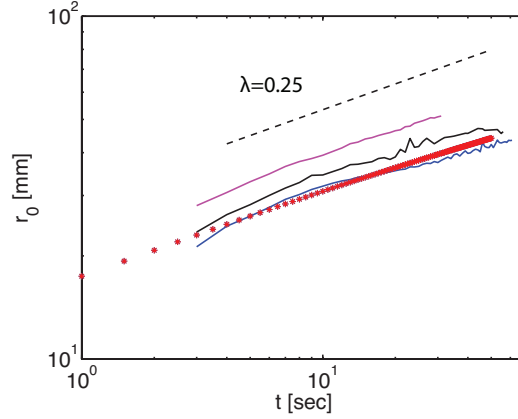
Figure 5.22: Log-log plot of r_0. The solid lines represent the location of the leading edge of the surfactant from the experiment, each color represents a different experimental run. Each $*$ represents the location of the leading edge of the surfactant from the numerical simulation. The dashed line is a comparison line with slope 0.25.

We have successfully connected the spreading of the film and the surfactant between the numerical simulations and experimental data. We found that both the numerics and experiment agree with the spreading predicted analytically in §4.2.1. While we also were able to connect the structure of the height profile, the surfactant profile generated from the numerics does not agree with the experimental surfactant profile. This disagreement calls into question the validity of surfactant equation.

5.3.5   Simulations Using Surfactant Experimental Data

In §5.3.1, we investigated the effect of varying the initial surfactant profile. However, independent of the choice of initial condition, the surfactant profile evolved quickly to a strictly decreasing and concave function. The experimental data does not exhibit this behavior but rather a nearly uniform layer of surfactant spreads from the initial distribution. This spreading causes the distribution to form a double step function which is not strictly concave, as seen in Figure 5.10. Another discrepancy between the experimental and numerical results arises in the implementation of the time scale as discussed in §5.3.2. These significant differences bring into question the validity of the model equations, specifically the equation for the surfactant concentration.

In this section, we discard the surfactant equation and instead use the time dependent experimental surfactant distribution as input for the height equation. We first outline the processing and approximation of the surfactant data, then discuss the numerical method, and finally present a comparison between the experimental and numerical height profiles.

Processing of surfactant data

The experimental data has noise which must be eliminated before it can be input into the numerical method. We first smooth the data using the *smooth* function in MATLAB. This function implements moving averages with a span of 21 points.

In order to record both the height profile and surfactant concentration simultaneously, the camera is set to capture images of the experiment at long exposure time, i. e. one second intervals. However, the numerical method requires the time step Δt to be on the order of $O(10^{-3})$ for stability. Therefore, we interpolate the functions that represent the surfactant profiles to obtain curves which can be used to represent the concentration of the surfactant at intermediate times. First, we use the nonlinear fit function, *nlinfit* in MATLAB to fit the smoothed surfactant data. Since the structure of the surfactant profiles is composed of two steps we use the function

$$\Gamma(r) = a_1^j - a_2^j \tanh\left(\frac{r - a_3^j}{a_4^j}\right) - a_5^j \tanh\left(\frac{r - a_6^j}{a_7^j}\right) \tag{5.3.27}$$

to fit the surfactant profile at each time for which we have data, where $t^* = j, j = 1, 2, \ldots, 10$. This generates coefficients $a_1^j, \ldots, a_7^j$. Next we create functions, $a_i(t^*)$ from these discrete values using *polyfit* in MATLAB. We now have an equation for all time for the surfactant profile of the form

$$\Gamma(r, t) = a_1(2t) - a_2(2t) \tanh\left(\frac{r - a_3(2t)}{a_4(2t)}\right) - a_5(2t) \tanh\left(\frac{r - a_6(2t)}{a_7(2t)}\right). \tag{5.3.28}$$

The coefficients a_i are functions of $2t$ because of the time scale (5.3.3), $t = 0.5t^*$. The fitting functions for $\Gamma(r, t)$ are generated using the experimental time scale t^*, however, in the numerical method the non-dimensional time scale t must be used.

Numerical Method

We update the height profile using the finite difference scheme (5.2.4a) with flux function (5.2.6), boundary conditions (5.2.7) and the surfactant concentration profile using (5.3.28):

$$h_j^{n+1} = h_j^n + \Delta t \frac{1}{r_j \Delta r} \left(\mathcal{F}_{j+\frac{1}{2}}^{n+1} - \mathcal{F}_{j-\frac{1}{2}}^{n+1} \right) \tag{5.3.29a}$$

$$\Gamma_j^{n+1} = a_1(2(n+1)\Delta t) - a_2(2(n+1)\Delta t) \tanh\left(\frac{r - a_3(2(n+1)\Delta t)}{a_4(2(n+1)\Delta t)} \right)$$

$$- a_5(2(n+1)\Delta t) \tanh\left(\frac{r - a_6(2(n+1)\Delta t)}{a_7(2(n+1)\Delta t)} \right). \tag{5.3.29b}$$

The experimental surfactant data we use in this method to compare the height profiles is different from that shown in Figure 5.3; we use a different experimental run due to the unreasonable height data, the maximum height occurs within the ring at $t = 1$ *sec*. Figure 5.23 shows the simulations using initial condition (5.3.4) and parameters $\beta = 0.5$, $\kappa = 0.5$, $\delta = 2.8 \times 10^{-5}$. Note that κ is outside of the range considered reasonable in (5.3.1). This magnitude of κ is necessary to smooth the height profile, otherwise multiple ridges develop and persist due to the steep gradient in the surfactant concentration.

We also observe multiple ridges at very early time in other numerical simulations. However, in the numerical simulations generated using the surfactant equation (5.2.1b), the gradient in the surfactant is quickly smoothed. In this case, the ridge in the height profile from the surfactant gradient and the one from the initial condition (due to the lifting of the ring) combine at very early time and then propagate as one.

By contrast, in the experiment the surfactant distribution does not experience this smoothing and consequently when the experimental values for the surfactant concentration are input into the height equation a second ridge develops and persists. By increasing the capillarity parameter κ, the height profile is smoothed which results in the numerical height profile being more similar to the experimental height profile.
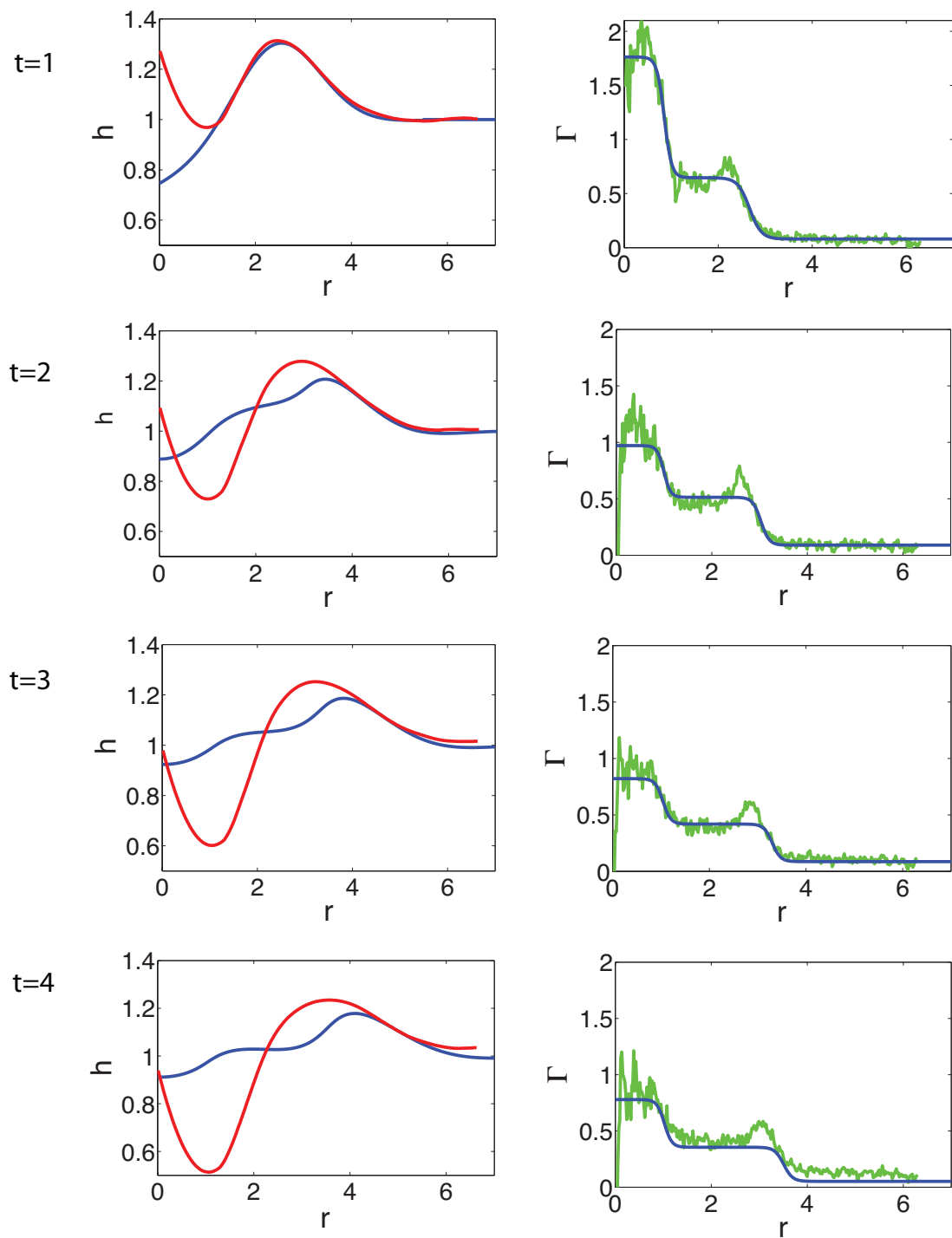
Figure 5.23: Left: Comparison of the height profiles from the numerical simulations (blue) and experimental data (red). Right: The corresponding surfactant profiles from the experiment, smoothed data (blue) and raw data (green). The profiles are shown at $t = 1, 2, 3, 4$ sec.

5.3.6 Discussion

This investigation suggests that the validity of the long accepted thin films equation should be questioned. The surfactant equation produces a profile which smoothes the structure of the surfactant. This smoothed behavior is not observed in the experiment, rather two levels of surfactant develop, one spreading faster than the other and one acting as a reservoir.

There are two prominent issues in aligning the experimental and numerical profiles: the time scale and the incorporation of surface tension. If the surfactant equation is used in the numerical simulation then the profiles can be aligned if the time scale $t = t^*$ is used. However, this time scale does not agree with the one specified by the non-dimensionalization. On the other hand, if the surfactant distribution from the experiment is input into the numerical scheme and the non-dimensional time scale is used then the height profiles from the experiment and simulation align on the expected time scale. This suggests that the experiment is evolving much faster than predicted by the equation modeling the surfactant concentration.

While the time scale appears to be accurate when the experimental surfactant concentration is used, the inclusion of the surface tension through κ does not seem to be correct. In order to produce a reasonable height profile the parameter κ must be an order of magnitude larger than presented by the non-dimensional grouping. The surface tension is predicted in two pieces of the modeling equation, the equation of state and the capillarity coefficient κ. This coefficient incorporates the surface tension due to the curvature of the film. However, the change in surface tension due to the surfactant concentration Γ may also need to be included in this parameter. In the formulation of the modeling system, the equation for the surfactant concentration may have been coupled to the height equation too naively in the sense that the dependence of surface tension on Γ is not fully accounted for.

Chapter 6

Inclined Plane

In this chapter, we consider a thin liquid film on an inclined plane with a drop of insoluble surfactant on the surface of the film. The driving forces of the film are the surface tension gradient and gravity. We consider two cases:

- The inclined substrate is coated with a thin precursor layer and a thicker film is traveling down the plane. Surfactant is present on the surface of the film where these two layers meet. A traveling wave solution exists for the height and surfactant profiles, developed in [47].

- An initially uniform film is flowing down an inclined substrate. A drop of surfactant is deposited on the film causing the film to deform due to the surface tension gradient.

In §6.1, we investigate the stability of the traveling wave solution for the one-dimensional system without the regularizing effects ($\beta = \kappa = \delta = 0$). Using the dispersion relation we find this system is stable to a small perturbation and verify the results with a numerical investigation. In §6.2, we examine the stability of the traveling wave solution for the one-dimension system (2.1.36) which incorporates the regularizing terms. Using the Evans function and stability indicator function we find the analysis is consistent with the solution being stable. In §6.3, we study the stability of the multi-dimensional system. Linearizing about the traveling wave we find that the stability of the solution is independent of the surfactant profile and actually depends on the size of the capillary ridge. This result corresponds to that shown by Bertozzi and Brenner [6] where a thin film on an inclined plane without surfactant was considered. In both §6.2 and §6.3, we investigate the case where the mass of the surfactant is sufficiently small.

In §6.4, we investigate the evolution of an initially uniform film when a drop of surfactant is deposited. When surfactant is introduced, the underlying film develops two waves, one traveling ahead of the surfactant and the other carrying the surfactant.

6.1 Stability of the One Dimensional Simplified System

The following section is based on the work in [60]. In [47], jump conditions for the system (2.1.36) with $\beta = \kappa = \delta = 0$ were formulated, and a surprising new traveling wave was found, in which h is piecewise constant with three jumps, and Γ is continuous and piecewise linear, with jumps in Γ_x corresponding to the jumps in h. We call this a *triple-step* traveling wave. In this section, we present preliminary results related to triple-step traveling waves. We summarize the existence of a traveling wave solution and its overcompressive property. We then analyze the linearization of the PDE system about sections of the wave in which h is constant and Γ is linear. Finally we present numerical results which show how small perturbations propagate within the wave. We determine that the traveling wave associated with the simplified system is stable.

6.1.1 Traveling waves

In this section, we summarize the construction [47, 48] of triple-step traveling wave solutions of the simplified ($\beta = \kappa = \delta = 0$) one dimensional system on the inclined plane (2.1.36),

$$h_t + \left(\tfrac{1}{3}h^3\right)_x - \left(\tfrac{1}{2}h^2\Gamma_x\right)_x = 0 \tag{6.1.1a}$$

$$\Gamma_t + \left(\tfrac{1}{2}h^2\Gamma\right)_x - (h\Gamma\Gamma_x)_x = 0, \tag{6.1.1b}$$

in which h is piecewise constant, and Γ is continuous and piecewise linear.

Triple-step traveling waves.

We outline the construction of the traveling wave solutions for the system (6.1.1) which is described in [47]. Consider an inclined plane covered with a precursor layer of height h_R and an upstream height h_L and assume $h_L > h_R$. Surfactant is present at the interface between the upstream height h_L and downstream height h_R. The resulting boundary conditions are

$$h(-\infty, t) = h_L, \qquad h(\infty, t) = h_R, \qquad \Gamma(-\infty, t) = \Gamma(\infty, t) = 0. \tag{6.1.2}$$

We seek traveling wave solutions of (6.1.1) which are piecewise constant in h and continuous piecewise linear in Γ in the traveling wave variable $\eta = x - st$ such that

$$h(\eta) = \begin{cases} h_L & \eta < \eta_1 \\ h_1 & \eta_1 < \eta < 0 \\ h_2 & 0 < \eta < \eta_2 \\ h_R & \eta_2 < \eta \end{cases} \qquad \Gamma(\eta) = \begin{cases} 0 & \eta \leq \eta_1 \\ \Gamma_{\max} + G_1\eta & \eta_1 \leq \eta \leq 0 \\ \Gamma_{\max} + G_2\eta & 0 \leq \eta \leq \eta_2 \\ 0 & \eta_2 \leq \eta. \end{cases} \tag{6.1.3}$$

Here, η_1, η_2 are related to $\Gamma_{\max}$ so as to make $\Gamma(\eta)$ continuous,

$$\eta_1 = -\frac{\Gamma_{\max}}{G_1} < 0, \qquad \eta_2 = -\frac{\Gamma_{\max}}{G_2} > 0. \tag{6.1.4}$$

At $\eta = \eta_1$ and $\eta = \eta_2$

$$\Gamma(\eta) = 0. \tag{6.1.5}$$

Differentiating with respect to t

$$\begin{aligned} \Gamma_t &= -s\Gamma_\eta \\ &= -sG_i \end{aligned} \tag{6.1.6}$$

where $i = 1, 2$. Using the fact that Γ is linear, (6.1.1b) leads to

$$\Gamma_t = -\tfrac{1}{2}h_i^2 G_i + h_i G_i^2. \tag{6.1.7}$$

Equating (6.1.6) and (6.1.7) determines

$$s = \tfrac{1}{2}h_i^2 - h_i G_i \tag{6.1.8}$$

assuming $G_i \neq 0$. Since we are considering a traveling wave solution, we must ensure that the two expressions $s = \tfrac{1}{2}h_i^2 - h_i G_i$ when $i = 1, 2$ agree using the jump conditions. Since Γ is assumed to be continuous, Γ does not jump but rather Γ_x jumps; the jump condition from (6.1.1b) then simplifies to

$$-\left[\tfrac{1}{2}h^2\right] + [hG] = 0 \tag{6.1.9}$$

thus

$$-\left(\tfrac{1}{2}h_2^2 - \tfrac{1}{2}h_2^2\right) + h_2 G_2 - h_1 G_1 = 0, \tag{6.1.10}$$

and the two speeds in (6.1.8) are the same.

There are three relevant jumps to consider which are categorized by the slope of Γ as discussed in [47]:

- $G_L = 0$ and $G_1 > 0$

  The height of the film corresponding to these regions of the solution are h_L and h_1

respectively. From the jump condition of (6.1.1a) is

$$-s(h_1 - h_L) - \tfrac{1}{2}h_1^2 G_1 + \tfrac{1}{3}(h_1^3 - h_L^3) = 0. \tag{6.1.11}$$

- $G_1 > 0$ and $G_2 < 0$

  The corresponding heights are h_1 and h_2 respectively. The jump condition from (6.1.1a) is

$$-s(h_2 - h_1) - \left(\tfrac{1}{2}h_2^2 G_2 - \tfrac{1}{2}h_1^2 G_1\right) + \tfrac{1}{3}\left(h_2^3 - h_1^3\right) = 0. \tag{6.1.12}$$

- $G_2 < 0$ and $G_R = 0$

  The corresponding heights are h_2 and h_R respectively. Then the jump condition from (6.1.1a) is

$$-s(h_2 - h_R) - \tfrac{1}{2}h_2^2 G_2 + \tfrac{1}{3}(h_2^3 - h_R^3) = 0. \tag{6.1.13}$$

Subtracting (6.1.13) from (6.1.11) and adding (6.1.12) results in

$$-s(h_R - h_L) + \tfrac{1}{3}(h_R^3 - h_L^3) = 0 \tag{6.1.14}$$

which implies the traveling wave speed is

$$s = \tfrac{1}{3}\left(h_R^2 + h_R h_L + h_L^2\right). \tag{6.1.15}$$

Next we define G_i in terms of h_i and the traveling wave speed s. From (6.1.8)

$$h_1 G_1 = \tfrac{1}{2}h_1^2 - s \tag{6.1.16}$$

multiplying by $\tfrac{1}{2}h_1$

$$\tfrac{1}{2}h_1^2 G_1 = \tfrac{1}{4}h_1^3 - \tfrac{1}{2}sh_1. \tag{6.1.17}$$

substituting into (6.1.11) and simplifying results in

$$h_1^3 - 6sh_1 + 4h_L h_R (h_L + h_R) = 0. \tag{6.1.18}$$

The corresponding analysis using (6.1.13) produces an equation for h_2

$$h_2^3 - 6sh_2 + 4h_L h_R (h_L + h_R) = 0. \tag{6.1.19}$$

122

The slopes G_1 and G_2 are determined from (6.1.8) to be

$$G_1 = \frac{h_1^2 - 2s}{2h_1} > 0, \qquad G_2 = \frac{h_2^2 - 2s}{2h_2} < 0. \tag{6.1.20}$$

The traveling wave speed and the structure of the solution are all determined by the height of the film upstream h_L and downstream h_R.

A traveling wave solution of the form (6.1.3) exists when

$$h^3 - 6sh + 4h_L h_R(h_L + h_R) = 0 \tag{6.1.21}$$

has two real positive solutions h_1, h_2, i.e, when

$$q_{crit} = \frac{h_R}{h_L} < \tfrac{1}{2}(\sqrt{3} - 1). \tag{6.1.22}$$

Note that there is always one negative solution of (6.1.21). It is easy to verify the inequalities $h_R < h_2 < h_L < h_1$ when (6.1.22) is satisfied. The inequalities (6.1.20) then follow easily.

The total mass of surfactant in the traveling wave solution (6.1.3) is given by

$$m = \int_{-\infty}^{\infty} \Gamma \, d\eta = \tfrac{1}{2}\Gamma_{\max}(\eta_2 - \eta_1) = \tfrac{1}{2}\Gamma_{\max}^2 \left(\frac{1}{G_1} - \frac{1}{G_2}\right) \geq 0. \tag{6.1.23}$$

Thus, for given upstream and downstream heights h_L, h_R, there is a one-parameter family of traveling waves; either the mass m or $\Gamma_{\max}$ may be used to parametrize the traveling waves. The structure of the solution is shown in Figure 6.1.
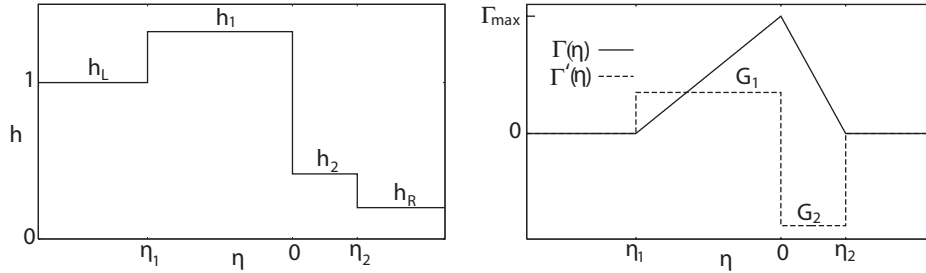
Figure 6.1: Triple-step traveling wave. Height, surfactant concentration and gradient.

The traveling waves are *overcompressive* in the sense that small perturbations introduced ahead of the wave travel at a slower speed than the wave whereas perturbations behind travel faster. More precisely, linearizing the PDE system about the constant upstream or downstream

heights $h = h_L$ or $h = h_R$ and $\Gamma = 0$, we obtain a linear system for the perturbations $\overline{h}, \overline{\Gamma}$:

$$\partial_t \overline{h} + h^2 \partial_x \overline{h} = \tfrac{1}{2} h^2 \partial_{xx} \overline{\Gamma} \tag{6.1.24a}$$

$$\partial_t \overline{\Gamma} + \tfrac{1}{2} h^2 \partial_x \overline{\Gamma} = 0. \tag{6.1.24b}$$

Let $\overline{h}_0(x), \overline{\Gamma}_0(x)$ be initial data:

$$\overline{h}(x,0) = \overline{h}_0(x); \quad \overline{\Gamma}(x,0) = \overline{\Gamma}_0(x). \tag{6.1.25}$$

Then the solution of the Cauchy problem (6.1.24), (6.1.25) involves traveling waves with constant speeds $c_1 = \tfrac{1}{2} h^2, c_2 = h^2$:

$$\overline{h}(x,t) = \overline{h}_0(x - c_2 t) + \overline{\Gamma}'_0(x - c_1 t) - \overline{\Gamma}'_0(x - c_2 t); \quad \overline{\Gamma}(x,t) = \overline{\Gamma}_0(x - c_1 t). \tag{6.1.26}$$

Due to the threshold constraint $h_R/h_L < q_{\mathrm{crit}}$, we find that the wave speeds $h^2, \tfrac{1}{2} h^2$ are greater than the traveling wave speed s for $h = h_L$, and s is larger than both wave speeds for $h = h_R$. In this sense, the wave is over-compressive.

6.1.2 One dimensional stability of triple-step traveling waves

For a nonlinear conservation law

$$h_t + f(h)_x = 0, \tag{6.1.27}$$

in which $f(h)$ is nonlinear, traveling waves are single-step shocks joining two constants $h = h_L, h = h_R$, with speed $s = (f(h_L) - f(h_R))/(h_L - h_R)$. Stability is established by considering perturbations of the two constant states, solving the initial value problem, together with the Rankine-Hugoniot jump condition. For a scalar equation, this is comparatively straightforward. Let $h = h_0$ be a constant, and consider a small perturbation $u :\ h = h_0 + u$. Linearizing about h_0, we find that u satisfies the linear transport equation

$$u_t + f'(h_0) u_x = 0,$$

so that $u(x,t) = u_1(x - ct)$, where $c = f'(h_0)$ is the characteristic speed. Under the Lax entropy condition

$$f'(h_R) < s < f'(h_L),$$

perturbations to the shock wave, initiated away from the shock itself, approach the shock from both sides and modify its location; the shock is considered stable. Proving nonlinear stability involves showing that the full nonlinear problem is well posed. This theory is well established for scalar equations and for strictly hyperbolic systems of equations [70], in which $u \in \mathbb{R}^n$, and

$f : \mathbb{R}^n \rightarrow \mathbb{R}^n$ is continuously differentiable, with distinct and real characteristic speeds, the eigenvalues of the Jacobian $df(u)$.

In the problem (6.1.1-6.1.2), we have a system of two equations for unknowns h and Γ, but the second equation is degenerate parabolic rather than hyperbolic. Traveling waves for the hyperbolic-parabolic system involve constant h and linear Γ. Consequently, the linear system resulting from linearization of (6.1.1) has nonconstant coefficients. The local dispersion relation for this system, obtained by freezing the variable coefficients, gives some information about the short-time evolution of localized perturbations.

The linearized equations

Consider the triple-step traveling wave (6.1.3) of the simplified system (6.1.1). Between jumps in h and Γ_x, h is constant and Γ is linear. In particular, in those sections in which Γ is not identically zero, we have

$$h = h_i, \quad \Gamma = G_i(x - st), \quad s = \tfrac{1}{2}h_i^2 - h_i G_i, \qquad i = 1, 2, \tag{6.1.28}$$

(where we have used (6.1.8) to express the wave speed s in terms of the constants $h_i, G_i,$). For $a > 0$ the equations (6.1.1) are unchanged by the transformation

$$h \rightarrow ah, \quad \Gamma \rightarrow a^2 \Gamma, \quad x \rightarrow ax, \quad t \rightarrow t/a.$$

Consequently, as long as we consider the ith section in isolation, we can take $h_i = 1$, so that $s = \tfrac{1}{2} - G$, in which we write $G = G_i$.

Now consider perturbations of a section of the traveling wave

$$h = 1 + u, \quad \Gamma = G \cdot (x - st) + v. \tag{6.1.29}$$

To maintain $\Gamma > 0$, we consider $x - st > 0$ if $G > 0$, and $x - st < 0$ if $G < 0$. Substituting (6.1.29) into the PDE system, and retaining only terms that are linear in u, v, we obtain the linear system

$$u_t + (1 - G)u_x - \tfrac{1}{2}v_{xx} = 0 \tag{6.1.30a}$$

$$v_t + (\tfrac{1}{2} - G)v_x - \left[(x - st)G(v_x - (1 - G)u)\right]_x = 0. \tag{6.1.30b}$$

It is convenient to consider these equations in a frame moving with constant speed $s = \tfrac{1}{2} - G$.

Accordingly, let $\eta = x - (\frac{1}{2} - G)t$:

$$u_t + \tfrac{1}{2}u_\eta - \tfrac{1}{2}v_{\eta\eta} = 0 \qquad (6.1.31\text{a})$$

$$v_t - \left[\eta G(v_\eta - (1-G)u)\right]_\eta = 0. \qquad (6.1.31\text{b})$$

Carrying out the differentiation in (6.1.31b) and then freezing the coefficient $\eta = \gamma$, we obtain the constant coefficient linear system

$$u_t + \tfrac{1}{2}u_\eta - \tfrac{1}{2}v_{\eta\eta} = 0 \qquad (6.1.32\text{a})$$

$$v_t - Gv_\eta + G(1-G)u - \gamma G v_{\eta\eta} + \gamma G(1-G)u_\eta = 0. \qquad (6.1.32\text{b})$$

We seek solutions of the form

$$u = \tilde{u}e^{i\lambda t + i\xi\eta}, \qquad v = \tilde{v}e^{i\lambda t + i\xi\eta}, \qquad \lambda = a + ib, \qquad (6.1.33)$$

where $\xi > 0$ is the wave number, or spatial frequency and $a, b \in \mathbb{R}$. Writing

$$e^{i\lambda t + i\xi\eta} = e^{-bt}e^{i\xi(\frac{a}{\xi}t + \eta)} = e^{-bt}f(\eta - ct), \qquad c = \frac{-a}{\xi}, \qquad (6.1.34)$$

isolates the wave speed c of the perturbation (relative to $s = \frac{1}{2} - G$); $b > 0$ indicates decay in time and $b < 0$ growth. Substituting (6.1.33) into the linear PDE system (6.1.32), we get simultaneous linear homogeneous equations for $\tilde{u}$ and $\tilde{v}$ which have a solution if and only if the determinant of the coefficient matrix is zero; this leads to the dispersion relation

$$\begin{vmatrix} i(\lambda + \tfrac{1}{2}\xi) & \tfrac{1}{2}\xi^2 \\ G(1-G)(1 + i\xi\gamma) & i(\lambda - G\xi) + \gamma G\xi^2 \end{vmatrix}$$

$$= -\lambda^2 + \lambda G\xi - \tfrac{1}{2}\lambda\xi + i\lambda\gamma G\xi^2 + i\tfrac{1}{2}\gamma G^2\xi^3 + \tfrac{1}{2}G^2\xi^2$$

$$= 0. \qquad (6.1.35)$$

Since this is a quadratic equation in λ, there are two (complex) solutions for each choice of the other parameters. Recalling that $\lambda = a + ib$, we get equations for the real and imaginary parts:

$$-a^2 + b^2 + a\xi\left(G - \tfrac{1}{2}\right) - b\gamma G\xi^2 + \tfrac{1}{2}G^2\xi^2 = 0 \qquad (6.1.36\text{a})$$

$$-2ab + b\xi\left(G - \tfrac{1}{2}\right) + a\gamma G\xi^2 + \tfrac{1}{2}\gamma G^2\xi^3 = 0. \qquad (6.1.36\text{b})$$

Completing the square for both of these equations

$$\left(b - \tfrac{1}{2}\gamma G\xi^2\right)^2 - \left(a - \tfrac{1}{2}\xi\left(G - \tfrac{1}{2}\right)\right)^2 = -\tfrac{1}{4}\xi^2\left(3G^2 - G + \tfrac{1}{4}\right) + \tfrac{1}{4}\gamma^2 G^2 \xi^4 \qquad (6.1.37a)$$

$$\left(a - \tfrac{1}{2}\xi\left(G - \tfrac{1}{2}\right)\right)\left(b - \tfrac{1}{2}\gamma G\xi^2\right) = \tfrac{1}{2}\gamma G\left(G - \tfrac{1}{4}\right)\xi^3. \qquad (6.1.37b)$$

These equations describe hyperbolas in the (a, b) plane with common center,

$$(a_0, b_0) = \left(\tfrac{1}{2}\xi\left(G - \tfrac{1}{2}\right), \tfrac{1}{2}\gamma G\xi^2\right). \qquad (6.1.38)$$

Equation (6.1.37a) represents a hyperbola with asymptotes at $45°$; (6.1.37b) is a hyperbola with asymptotes parallel to the coordinate axes. The orientations of these hyperbolas are determined by the sign of the right hand sides of the respective equations, which depend on the following conditions.

   (i) The right hand side of (6.1.37a) is positive if and only if

$$\gamma^2 \xi^2 > 3 - \frac{1}{G} + \frac{1}{4G^2}. \qquad (6.1.39)$$

   (ii) The right hand side of (6.1.37b) is positive if and only if

$$G > \frac{1}{4}. \qquad (6.1.40)$$

We also note from examining (6.1.36) that without loss of generality we can take $\xi > 0$ due to the symmetry of the solution; if $\xi \to -\xi$ then $a \to -a$ but the sign of $c = \frac{-a}{\xi}$ remains unchanged.

Analysis of the dispersion relation (6.1.37)

In analyzing the dispersion relation in the form (6.1.37), we consider γ and G fixed, and determine the behavior of solutions (a, b) on the wavenumber ξ. We are specifically interested in the signs of a and b, rather than their magnitude, so we focus on identifying in which quadrant of the (a, b) plane the solutions lie. These solutions correspond to the intersection of the hyperbolas. As remarked above, there are two intersections, corresponding to two waves with different speeds and growth/decay rates.

We restrict attention to values of γ, G satisfying $\gamma G > 0$, with $-\infty < G < 0$, or $0 < G < \tfrac{1}{3}$. To explain these inequalities, first note that $\gamma G > 0$ is consistent with the two interior levels $h = h_1, h = h_2$ in the traveling wave. Next consider (6.1.21) as $h_R \to 0^+$

$$h^3 - 2h_L^2 h = 0$$
$$h(h^2 - 2h_L^2) = 0$$

which is satisfied when $h = 0$ or $h = \sqrt{2}h_L$. Since $h_1 > h_2$ we find as $h_R \to 0$

$$h_1 \to \sqrt{2}h_L, \qquad h_2 \to 0 \tag{6.1.41}$$

and from (6.1.20)

$$G_1 \to \frac{\sqrt{2}}{3}h_L, \qquad G_2 \to -\infty. \tag{6.1.42}$$

Thus, with the normalization $h_1 = 1$, we have $G_1 < \frac{1}{3}$. This upper bound on G also guarantees that when (6.1.39) is satisfied, then $\gamma^2 \xi^2 > 2$. Note that the other limit $\frac{h_R}{h_L} \to q_{\text{crit}}$ causes h_1, $h_2 \to h_L$ which implies G_1, $G_2 \to 0$. We deduce that the center (a_0, b_0) of the two hyperbolas, given by (6.1.38), lies in the second quadrant.

We first consider the case $0 < G < \frac{1}{3}, \gamma > 0$ corresponding to the portion $h = h_1, \Gamma = G_1(x - st)$ of the traveling wave. It is convenient to define functions ϕ, ψ of G :

$$\phi(G) = \frac{2(G - \frac{1}{2})^2}{G(1 - 3G)}, \quad \psi(G) = 3 - \frac{1}{G} + \frac{1}{4G^2}. \tag{6.1.43}$$

Proposition 1 *Suppose $0 < G < \frac{1}{3}, \gamma > 0$.*

- *If $\gamma^2 \xi^2 > \phi(G)$, then both intersections of the hyperbolas occur in quadrant II. In this case, both waves decay and move to the right (in the frame moving with the traveling wave speed).*

- *If $\gamma^2 \xi^2 < \phi(G)$, then one intersection of the hyperbolas is in quadrant I and one intersection is in quadrant II. Both waves decay but one moves to the right and the other moves to the left.*

Proof: We consider various cases based on the structure of the hyperbolas, determined by the sign of the right hand side of (6.1.37). The cases are illustrated in Figures 6.2,6.3. In order to determine in which quadrant the hyperbolas intersect we compare the intersections of the hyperbolas with the coordinate axes. Figures 6.2 and 6.3 show examples of where these intersections may occur.

In the figures, dashed lines represent the asymptotes, and C and D represent the intersections of the two hyperbolas. The intersections of the hyperbola (6.1.37a) with the a and b axis are labeled $a_1^{\pm}$ and $b_1^{\pm}$. Intersections of (6.1.37b) are a_2 and b_2.

Setting $b = 0$ in (6.1.37a), (6.1.37b) we find

$$a_1^{\pm} = \frac{\xi}{2}\left[G - \tfrac{1}{2} \pm \sqrt{(G - \tfrac{1}{2})^2 + 2G^2}\right], \quad a_2 = -\tfrac{1}{2}\xi G. \tag{6.1.44}$$

128
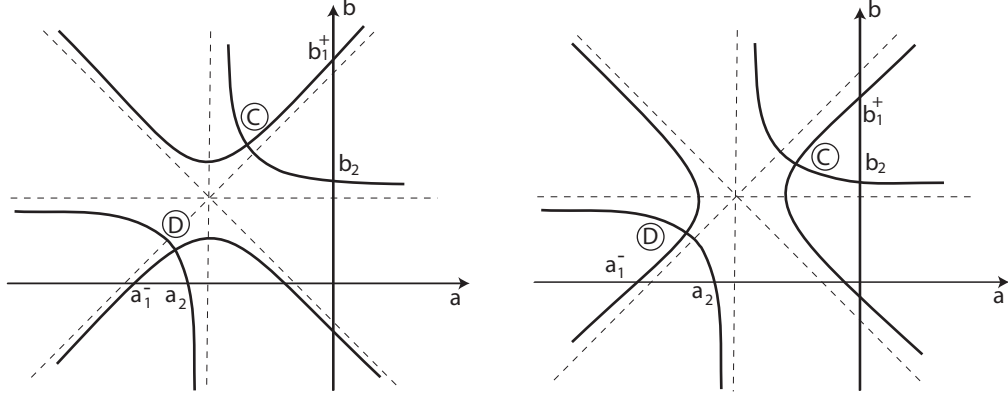
Figure 6.2: $G > \frac{1}{4}$. Left: $\gamma^2 \xi^2 > \psi(G)$; Right: $\gamma^2 \xi^2 < \psi(G)$.

Similarly, setting $a = 0$ in (6.1.37a), (6.1.37b) we find

$$b_1^\pm = \frac{\xi G}{2} \left(\gamma \xi \pm \sqrt{\gamma^2 \xi^2 - 2} \right), \quad b_2 = \tfrac{1}{2} \gamma G \xi^2 - \frac{\gamma G \left(G - \frac{1}{4} \right) \xi^2}{G - \frac{1}{2}}. \tag{6.1.45}$$

Thus

$$a_1^\pm - a_2 = \frac{\xi}{2} \left[2G - \tfrac{1}{2} \pm \sqrt{(G - \tfrac{1}{2})^2 + 2G^2} \right], \tag{6.1.46a}$$

and

$$b_1^\pm - b_2 = \frac{G\xi \left[\pm \left(G - \frac{1}{2} \right) \sqrt{\gamma^2 \xi^2 - 2} + 2\gamma \xi \left(G - \frac{1}{4} \right) \right]}{2(G - \frac{1}{2})}. \tag{6.1.46b}$$

 Now we consider the cases separately, labeled as in Figures 6.2,6.3.

Case I: $G > \frac{1}{4}$.

First consider $\gamma^2 \xi^2 > \psi(G)$ (see Fig. 6.2(Left)). Since $G\xi > 0$ and $G < \frac{1}{3}$, the sign of $(6.1.46b^+)$, is determined by the sign of

$$P(G, \gamma\xi) \equiv \left(G - \tfrac{1}{2} \right) \sqrt{\gamma^2 \xi^2 - 2} + 2\gamma\xi \left(G - \frac{1}{4} \right), \tag{6.1.47}$$

Since $P(G, \gamma\xi) = 0$ when

$$\gamma^2 \xi^2 = \frac{2(G - \frac{1}{2})^2}{G(1 - 3G)} = \phi(G), \tag{6.1.48}$$

we conclude for the intersection C,

- If $\gamma^2 \xi^2 > \phi(G)$ then $b_1^+ - b_2 > 0$. The intersection is in quadrant II.

129

- If $\gamma^2\xi^2 < \phi(G)$ then $b_1^+ - b_2 < 0$. The intersection is in quadrant I.

Note that in the companion case, $G > \frac{1}{4}, \gamma^2\xi^2 < \psi(G)$ (see Fig. 6.2(Right)), $b_1^{\pm}$ are complex when $\gamma^2\xi^2 < 2$ because then the hyperbola does not intersect the b axis. The intersection C is then necessarily in quadrant I. For $\gamma^2\xi^2 > 2$, the argument above implies that C is in quadrant II.

Now we examine the intersection D in Figure 6.2. This intersection occurs in either quadrant II if $a_1^- < a_2$ or quadrant III if $a_1^- > a_2$. But $a_1^- - a_2$ changes sign when

$$Q(G) \equiv 2G - \tfrac{1}{2} - \sqrt{(G - \tfrac{1}{2})^2 + 2G^2} = 0. \tag{6.1.49}$$

Solving for G we find that $G = 0$ or $G = 1$. But $Q < 0$ when $G = 0$ so $Q < 0$ for $0 < G < 1$. Consequently, the intersection D is in quadrant II.

Case II : $0 < G < \frac{1}{4}$.
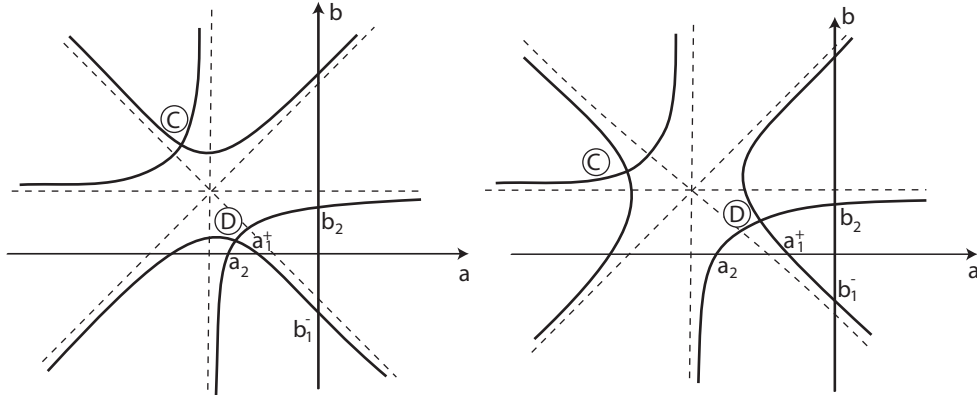
Figure 6.3: $G < \frac{1}{4}$. Left: $\gamma^2\xi^2 > \psi(G)$; Right: $\gamma^2\xi^2 < \psi(G)$.

From the location of the center (in the second quadrant of Figure 6.3), and the orientation of the asymptotes, it is clear that intersection C is in the second quadrant, and we can focus on intersection D. In this case, the sign of $a_1^+ - a_2$ is determined by the sign of

$$\tilde{Q}(G) = 2G - \tfrac{1}{2} + \sqrt{(G - \tfrac{1}{2})^2 + 2G^2}, \tag{6.1.50}$$

which has zeros at $G = 0$ and $G = 1$, but when $G = 1$, $\tilde{Q} > 0$. Thus $\tilde{Q} > 0$ for $0 < G < 1$ and $a_1^+ - a_2 > 0$ which means the intersection occurs in quadrant I or II.

From (6.1.46b), in the case $\gamma^2\xi^2 > \psi(G)$ (see Fig. 6.3 Left), for which both roots are real,

we deduce:

- If $\gamma^2\xi^2 > \phi(G)$ then $b_1^- - b_2 < 0$. Thus the intersection D is in quadrant II.

- If $\gamma^2\xi^2 < \phi(G)$ then $b_1^- - b_2 > 0$. Thus the intersection D is in quadrant I.

The only difference in the companion case $0 < G < \frac{1}{4}$, $\gamma^2\xi^2 < \psi(G)$ (see Fig. 6.3 Right), is that $b_1^\pm$ may be complex, when the hyperbola does not intersect the b axis. But then the intersection D clearly is in quadrant I; otherwise, the intersection D is in quadrant I or II as above. This completes the proof. ■

Next, we consider the case $G < 0, \gamma < 0$ corresponding to the portion $h = h_2, \Gamma = G_2(x - st)$ of the traveling wave. In this case, the right hand side of (6.1.37b) is automatically negative. Thus the only two cases to consider are dependent on the sign of the right hand side of (6.1.37a). Figure 6.3 shows the structure of the hyperbolas.

Proposition 2 *Suppose $G < 0, \gamma < 0$. Then one intersection is in quadrant II and one intersection is in quadrant IV. Thus, one wave moves to the right and decays while a second wave moves to the left and grows.*

Proof: As before, for $G < \frac{1}{4}$, intersection C is necessarily in quadrant II. Regarding the intersection D, first consider the case $\gamma^2\xi^2 < \psi(G)$ (see Fig. 6.3 Right).

If the hyperbola associated with (6.1.37a) does not intersect the b axis (then necessarily $\gamma^2\xi^2 < 2$), then the right arm of the hyperbola lies in the right half plane, so the intersection D of the two hyperbolas occurs in quadrant I or quadrant IV. On the other hand, for $\gamma^2\xi^2 \geq 2$, the hyperbola does intersect the b axis, and we wish to establish the same conclusion.

Since $G < 0$, the lower intersection of the hyperbola (6.1.37a) with the b axis is b_1^+, given by (6.1.45). Moreover, from (6.1.46b), we see that the sign of $b_1^+ - b_2$ depends on the sign of

$$P(G, \gamma\xi) = (G - \tfrac{1}{2})\left[\sqrt{\gamma^2\xi^2 - 2} + 2\gamma\xi(G - \tfrac{1}{4})\right]. \tag{6.1.51}$$

But $P(G, \gamma\xi) \neq 0$ since $\gamma^2\xi^2 < \phi(G)$. In the limit $\gamma^2\xi^2 \to 2^+$ we find that $P(G, \gamma\xi) > 0$. Thus $b_1^+ - b_2 > 0$ establishing that the intersection D of the two hyperbolas occurs in quadrant I or quadrant IV. (Note that in Fig. 6.3 Right, the intersection is shown in quadrant II, which does not occur when $G < 0$.)

Next we compare the a values, to show that in fact, the intersection point D lies in quadrant IV.

From (6.1.46a), we observe that the sign of $a_1^+ - a_2$ depends on the sign of

$$\tilde{Q}(G) = 2G - \tfrac{1}{2} + \sqrt{(G - \tfrac{1}{2})^2 + 2G^2}$$

and following the procedure used with (6.1.49) we find $\tilde{Q} < 0$ when $G = -1$ which means $a_1 - a_2 < 0$. Consequently, the intersection point cannot lie in quadrant I, and must lie in quadrant IV. In the companion case, as for the earlier proposition, the comparisons work the same way, even though the hyperbolas are oriented differently (see Fig. 6.3 Left). ∎

Numerical results

Numerical simulations of the system of equations (6.1.1) help confirm the predictions of the analysis of the dispersion relation. In the simulations, we introduce a small smooth localized perturbation in h into the triple-step traveling wave, away from the jumps, and integrate the equations using a finite difference method that couples an explicit upwind scheme for the convective terms and an implicit scheme for the time-step and the parabolic terms [46]. We use the standard notation for spatial averages of $u_j^n = u(x_j, t_n)$,

$$\bar{u}_{j+1/2}^n \equiv \frac{u_{j+1}^n + u_j^n}{2}. \tag{6.1.52}$$

The nonlinear system

$$h_j^{n+1} - h_j^n - \Delta t \left[\frac{\left(\bar{h}_{j+1/2}^{n+1}\right)^2 \left(\frac{\Gamma_{j+1}^{n+1} - \Gamma_j^{n+1}}{\Delta x}\right) - \left(\bar{h}_{j-1/2}^{n+1}\right)^2 \left(\frac{\Gamma_j^{n+1} - \Gamma_{j-1}^{n+1}}{\Delta x}\right)}{2\Delta x} \right] \tag{6.1.53a}$$

$$+ \Delta t \left(\frac{\left(h_j^n\right)^3 - \left(h_{j-1}^n\right)^3}{3\Delta x} \right) - \epsilon \Delta t \frac{\left(h_{j+1}^{n+1} - 2h_j^{n+1} + h_{j-1}^{n+1}\right)}{\Delta x^2} = 0$$

$$\Gamma_j^{n+1} - \Gamma_j^n - \Delta t \left[\frac{\bar{h}_{j+1/2}^{n+1} \bar{\Gamma}_{j+1/2}^{n+1} \left(\frac{\Gamma_{j+1}^{n+1} - \Gamma_j^{n+1}}{\Delta x}\right) - \bar{h}_{j-1/2}^{n+1} \bar{\Gamma}_{j-1/2}^{n+1} \left(\frac{\Gamma_j^{n+1} - \Gamma_{j-1}^{n+1}}{\Delta x}\right)}{\Delta x} \right] \tag{6.1.53b}$$

$$+ \Delta t \left[\frac{\left(h_j^n\right)^2 \Gamma_j^n - \left(h_{j-1}^n\right)^2 \Gamma_{j-1}^n}{2\Delta x} \right] = 0$$

is solved using Newton's method. An artificial diffusion term is included at the end of the h equation in order to suppress spatial oscillations near jumps in h. In our simulations, we use $\epsilon = 0.001$.

When introduced ahead of or behind the traveling wave, the perturbation propagates towards the middle of the wave from either side, as predicted by the equations linearized around $h = constant$, $\Gamma = 0$ (see (6.1.26) above). The perturbation then encounters the outer discon-
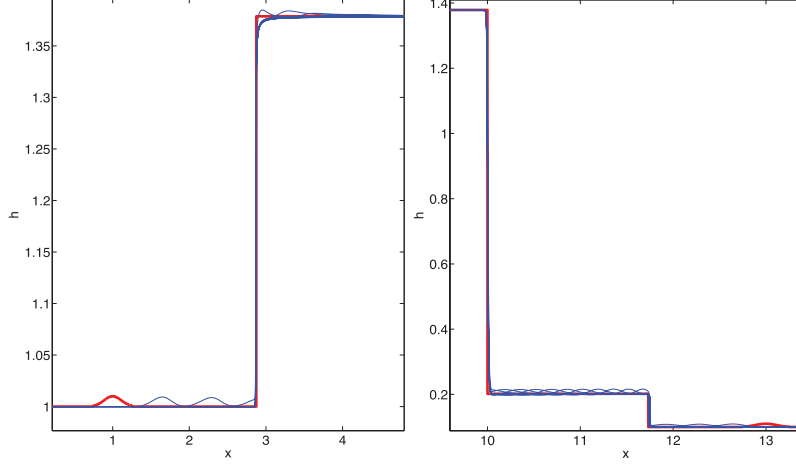
Figure 6.4: Left: Perturbation placed on h_L. Right: Perturbation placed on h_R. Thicker (red) line is the initial condition.

tinuity in h, and passes through with some distortion, as seen in Figure 6.4. Subsequently, we are in the domain of the analysis of the previous subsection, except of course the numerical simulations are not tracking a perturbation with a single wave number, but rather a composition of all wave numbers, with the emphasis being on low wavenumbers - the perturbation is a long wave. When the perturbation is introduced on the levels $h = h_1, h = h_2$, the evolution is
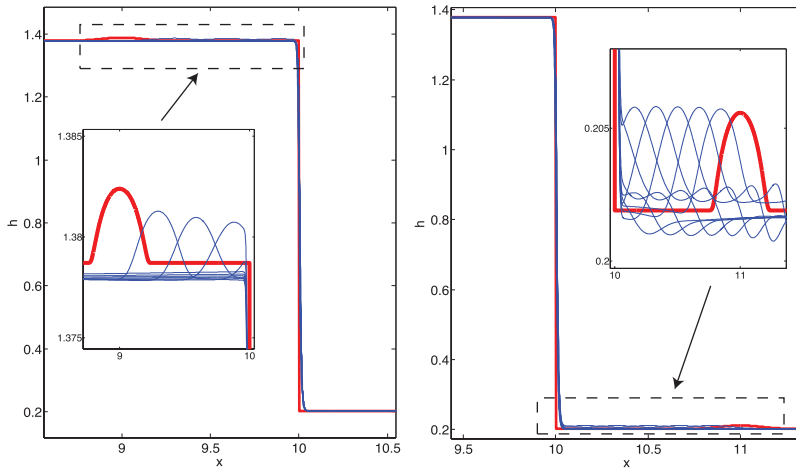
Figure 6.5: Left: Perturbation is placed on h_1. Right: Perturbation is placed on h_2.

exhibited in Figure 6.5. On the higher level ($h = h_1$), the perturbation dies out rapidly, whereas on the lower level ($h = h_2$), the perturbation propagates towards the big central jump in h and

133

is absorbed by it. On this level, there is presumably a small decaying wave moving right as well, but we have not observed it, possibly because it is a small effect at long wavelengths.

6.1.3 Discussion

Since the triple-step wave is readily captured in numerical simulations [47, 48], it should be expected to be stable to one-dimensional perturbations. If it were a shock wave solution of a hyperbolic conservation law (thus with a single step), then stability would be related to short-time preservation of the shock structure under perturbation of initial conditions; such stability is typically associated with the Lax entropy condition, which guarantees that perturbations in the characteristic family of the shock are transported into the shock, where they are absorbed, while other components of the perturbation are transported through the shock and away. However, the traveling wave under consideration here is not a hyperbolic wave, but a traveling wave solution of a system which in essence (in the absence of higher order derivatives) is a scalar conservation law coupled to a degenerate diffusion equation akin to the porous medium equation. At this quasi-hyperbolic level, the new traveling wave behaves like an overcompressive shock. In §6.1.1 we observed that in the linearized equations, perturbations ahead of and behind the wave converge on the wave, as a pair of traveling waves, much as perturbations of a shock travel along characteristics. However, if a perturbation is placed within the traveling wave, then it is not so clear how the solution evolves. In §6.1.2 we analyzed the linearized system at the level of the dispersion relation, which contains information about the direction and growth or decay of perturbations of a specified frequency. In summary, we find that the only perturbations that can grow propagate towards the middle layer. Numerical simulations show that such perturbations are absorbed by the middle layer.

6.2 One dimensional stability: full system

In this section we consider the system of equations (2.1.36) where we assume flow is negligible in the transverse horizontal direction, thus suppressing the y variable

$$h_t - \left(\tfrac{1}{2}h^2\Gamma_x\right)_x + \left(\tfrac{1}{3}h^3\right)_x = \beta\left(\tfrac{1}{3}h^3 h_x\right)_x - \kappa\left(\tfrac{1}{3}h^3 h_{xxx}\right)_x \tag{6.2.1a}$$

$$\Gamma_t - (h\Gamma\Gamma_x)_x + \left(\tfrac{1}{2}h^2\Gamma\right)_x = \beta\left(\tfrac{1}{2}h^2\Gamma h_x\right)_x - \kappa\left(\tfrac{1}{2}h^2\Gamma h_{xxx}\right)_x + \delta\,\Gamma_{xx}. \tag{6.2.1b}$$

We investigate the linearized stability of the smooth traveling wave solutions corresponding to the triple step solution [48]. Using the Evans function and the stability indicator function as presented in [9] we determine the analysis is consistent with stability.

6.2.1 Traveling waves

A traveling wave solution exists of similar form to the triple step solution discussed in §6.1 when $\beta \geq 0$, $\kappa \geq 0$, $\delta > 0$. The effects of β, κ, δ on the triple step solution are analyzed in [48] and the existence of the traveling wave in [51]. In this section we assume that $\beta \geq 0$, $\kappa \geq 0$, $\delta > 0$ and the mass of surfactant is small. Consider the traveling wave solution $h(x,t) = \overline{h}(\overline{x}), \Gamma(x,t) = \overline{\Gamma}(\overline{x})$ where $\overline{x} = x - st$. Substituting into (6.2.1) and integrating once we determine a system of ODEs, dropping the $\overline{}$,

$$-sh + \tfrac{1}{3}h^3 - \tfrac{1}{2}h^2\frac{d\Gamma}{dx} = \tfrac{1}{3}\beta h^3\frac{dh}{dx} - \tfrac{1}{3}\kappa h^3\frac{d^3h}{dx^3} - k_h, \qquad (6.2.2a)$$

$$-s\Gamma + \tfrac{1}{2}h^2\Gamma - h\Gamma\frac{d\Gamma}{dx} = \tfrac{1}{2}\beta h^2\Gamma\frac{dh}{dx} + \delta\frac{d\Gamma}{dx} - \tfrac{1}{2}\kappa h^2\Gamma\frac{d^3h}{dx^3} - k_\Gamma, \qquad (6.2.2b)$$

in which k_h, k_Γ are constants of integration, determined by boundary conditions, which we take in the form

$$h(x \to -\infty) \to h_L, \qquad h(x \to \infty) \to h_R, \qquad (6.2.3a)$$

$$\Gamma(x \to -\infty) \to 0, \qquad \Gamma(x \to \infty) \to 0. \qquad (6.2.3b)$$

Assuming the height approaches a constant at the boundaries with $h^{(j)}(\pm\infty) = 0$, $j = 1, 2, 3$ and $\Gamma'(\pm\infty) = 0$, and the boundary conditions (6.2.3) lead to $k_\Gamma = 0$. Moreover,

$$-sh_L + \tfrac{1}{3}h_L^3 = -k_h \qquad (6.2.4)$$

and

$$-s(h_R - h_L) + \tfrac{1}{3}(h_R^3 - h_L^3) = 0. \qquad (6.2.5)$$

Consequently, the traveling wave speed is $s = \tfrac{1}{3}\left(h_R^2 + h_R h_L + h_L^2\right)$, which is the same speed as in the three step traveling wave in §6.1. Substituting in the traveling wave speed (6.2.5) determines the constant of integration

$$k_h = \tfrac{1}{3}h_L h_R(h_L + h_R). \qquad (6.2.6)$$

The non-negative parameters β, κ, δ control smoothness of the traveling waves. For $\kappa = 0$, it is straightforward to examine a two-dimensional phase plane to show that there is a one-parameter family of traveling waves. Each traveling wave is smooth for $\beta > 0, \delta > 0$, but has reduced smoothness when one of these parameters is zero. This is explained in [48]. For $\kappa > 0$, the situation is more complicated, and there are open issues of existence and uniqueness. A recent paper of Schecter and Manukian [51] provides existence of traveling waves provided a

transversality condition is satisfied. Moreover, this condition guarantees that all the traveling waves are parametrized smoothly by (small values of) $m = \int \Gamma \, dx$ or $\Gamma_{\max}$.

In studying stability to one-dimensional perturbations, we linearize the PDE system and then look for solutions with variables separated, to reduce the problem to an eigenvalue problem for a linear ordinary differential operator, with variable coefficients.

6.2.2 The linearized equations

Consider the PDE system in the moving frame of the traveling wave, i. e. $\bar{x} = x - st$ and dropping the $\bar{\ }$:

$$h_t - s h_x - \left(\tfrac{1}{2} h^2 \Gamma_x\right)_x + \left(\tfrac{1}{3} h^3\right)_x = \beta \left(\tfrac{1}{3} h^3 h_x\right)_x - \kappa \left(\tfrac{1}{3} h^3 h_{xxx}\right)_x \tag{6.2.7a}$$

$$\Gamma_t - s \Gamma_x - (h \Gamma \Gamma_x)_x + \left(\tfrac{1}{2} h^2 \Gamma\right)_x = \beta \left(\tfrac{1}{2} h^2 \Gamma h_x\right)_x - \kappa \left(\tfrac{1}{2} h^2 \Gamma h_{xxx}\right)_x + \delta \, \Gamma_{xx}. \tag{6.2.7b}$$

We linearize the system about a traveling wave solution $h(x,t) = \overline{h}(x), \Gamma(x,t) = 0$. Let

$$h(x,t) = \overline{h}(x) + u(x,t), \quad \Gamma(x,t) = v(x,t).$$

Substituting into (6.2.7) and retaining only linear terms, in u, v

$$u_t - s u_x - \left(\tfrac{1}{2} \bar{h}^2 v_x\right)_x + \left(\bar{h}^2 u\right)_x = \beta \left(\tfrac{1}{3} \bar{h}^3 u_x\right)_x + \beta \left(\bar{h}^2 \bar{h}' u\right)_x \quad - \quad \kappa \left(\tfrac{1}{3} \bar{h}^3 u_{xxx}\right)_x \tag{6.2.8a}$$
$$\qquad\qquad\qquad\qquad\qquad\qquad\qquad\qquad\qquad\qquad - \quad \kappa \left(\bar{h}^2 \bar{h}''' u\right)_x$$

$$v_t - s v_x + \left(\tfrac{1}{2} \bar{h}^2 v\right)_x = \beta \left(\tfrac{1}{2} \bar{h}^2 \bar{h}' v\right)_x - \kappa \left(\tfrac{1}{2} \bar{h}^2 \bar{h}''' v\right)_x + \delta \, v_{xx}. \tag{6.2.8b}$$

Here, we see the simplification in taking the surfactant-free traveling wave $\overline{\Gamma} = 0$: the second equation decouples from the first.

To study spectral stability, we consider the possibility of a solution that is growing exponentially in time. Accordingly, let $\lambda \in \mathbb{C} - \{0\}$, with $Re\lambda \geq 0$, and seek solutions of the form

$$u(x,t) = e^{\lambda t} \phi(x); \quad v(x,t) = e^{\lambda t} \psi(x).$$

Then

$$\lambda \phi - s \phi' - \left(\tfrac{1}{2} \bar{h}^2 \psi'\right)' + \left(\bar{h}^2 \phi\right)' = \beta \left(\tfrac{1}{3} \bar{h}^3 \phi'\right)' + \beta \left(\bar{h}^2 \bar{h}' \phi\right)' \quad - \quad \kappa \left(\tfrac{1}{3} \bar{h}^3 \phi'''\right)' \tag{6.2.9a}$$
$$\qquad\qquad\qquad\qquad\qquad\qquad\qquad\qquad\qquad\qquad - \quad \kappa \left(\bar{h}^2 \bar{h}''' \phi\right)'$$

$$\lambda \psi - s \psi' + \left(\tfrac{1}{2} \bar{h}^2 \psi\right)' = \beta \left(\tfrac{1}{2} \bar{h}^2 \bar{h}' \psi\right)' - \kappa \left(\tfrac{1}{2} \bar{h}^2 \bar{h}''' \psi\right)' + \delta \, \psi''. \tag{6.2.9b}$$

Since the second equation has only ψ as an unknown, we can make an assertion: If λ is an eigenvalue with $Re\lambda \geq 0$, then either it is an eigenvalue for (6.2.9b), or it is an eigenvalue

136

for (6.2.9a) with $\psi = 0$, a case discussed in papers of Howard and Hu [31] and Howard and Zumbrun [32] for the thin film equation with no surfactant. Therefore, we will consider only (6.2.9b).

The Asymptotic Equations

The next step is to consider the system (6.2.9), at the extremes $x \to \pm\infty$. More precisely, we seek a solution of (6.2.9) that decays as $x \to \pm\infty$, and such a solution will approach a linear combination of solutions of the constant coefficient system obtained by letting $x \to \pm\infty$ in the coefficients. From the boundary conditions for $\bar{h}$, we obtain the asymptotic equations

$$\lambda\phi - s\phi' - \left(\tfrac{1}{2}h_\pm^2\psi'\right)' + \left(h_\pm^2\phi\right)' = \beta\left(\tfrac{1}{3}h_\pm^3\phi'\right)' - \kappa\left(\tfrac{1}{3}h_\pm^3\phi'''\right)' \tag{6.2.10a}$$

$$\lambda\psi - s\psi' + \tfrac{1}{2}h_\pm^2\psi' = \delta\,\psi''. \tag{6.2.10b}$$

Rewriting (6.2.10b) slightly,

$$\delta\,\psi'' + (s - \tfrac{1}{2}h_\pm^2)\psi' - \lambda\psi = 0,$$

we see that the characteristic equation for exponential solutions $\psi(x) = e^{\mu x}$ is given by

$$\delta\mu^2 + (s - \tfrac{1}{2}h_\pm^2)\mu - \lambda = 0.$$

Thus,

$$\mu = \frac{1}{2\delta}\left(\tfrac{1}{2}h_\pm^2 - s \pm \sqrt{(s - \tfrac{1}{2}h_\pm^2)^2 + 4\lambda}\right).$$

For real $\lambda > 0$, the roots have opposite signs. Moreover, the roots cannot cross the imaginary axis as λ varies, since if $\mu = ik$ with $k \neq 0$, then $-\delta k^2 + (s - \tfrac{1}{2}h_\pm^2)ik = \lambda$ from (6.2.2). But this would imply that $Re\lambda < 0$, contradicting the assumption that $Re\lambda \geq 0$. Consequently, for each λ, one root is in the right half-plane, and the other is in the left half-plane. We only want the roots corresponding to solutions that decay as $x \to \pm\infty$, so we let $\mu_1 = \frac{1}{2\delta}\left(\tfrac{1}{2}h_-^2 - s + \sqrt{(s - \tfrac{1}{2}h_-^2)^2 + 4\lambda}\right)$ be the root with positive real part, and correspondingly, let $\mu_2 = \frac{1}{2\delta}\left(\tfrac{1}{2}h_+^2 - s - \sqrt{(s - \tfrac{1}{2}h_+^2)^2 + 4\lambda}\right)$ be the root with negative real part.

The Evans function

Now we let $\psi_1(x)$ be the solution of the nonconstant coefficient ODE (6.2.9b) that approaches $e^{\mu_1 x}$ as $x \to -\infty$, and let $\psi_2(x)$ be the solution of the nonconstant coefficient ODE (6.2.9b) that approaches $e^{\mu_2 x}$ as $x \to \infty$. Then the Evans function $D(\lambda)$ is the Wronskian of these two functions, evaluated at $x = 0$:

$$D(\lambda) = \begin{vmatrix} \psi_1(x) & \psi_2(x) \\ \psi_1'(x) & \psi_2'(x) \end{vmatrix}_{x=0}. \tag{6.2.11}$$

It is well known that $D(\lambda)$ can be extended analytically to $\lambda = 0$, and that $D(0) = 0$. The value of the Evans function is that λ is an eigenvalue for (6.2.9b) with $Re\lambda \geq 0$ if and only if $D(\lambda) = 0$. We would like to show that the only zero of $D(\lambda)$ in the right half-plane is $\lambda = 0$.

We consider the *stability indicator function*

$$sgn \left[D'(0) \lim_{\lambda \to \infty} D(\lambda) \right]. \tag{6.2.12}$$

If the indicator function is negative then the system is unstable because the Evans function crosses the x-axis in the right half plane, thus there is a positive eigenvalue. If the function is positive then the analysis is consistent with the system being stable. In this case, we only have consistency since the Evans function could cross the x-axis an even number of times.

We will separately examine the sign of $D'(0)$ and $\lim_{\lambda \to \infty} D(\lambda)$ in order to determine the indicator function. Consider (6.2.9b) and rewrite it as

$$\lambda \psi = (A(x)\psi)' + \delta \psi'' \tag{6.2.13}$$

where

$$A(x) = s - \tfrac{1}{2}\bar{h}^2 + \tfrac{1}{2}\beta \bar{h}^2 \bar{h}' - \tfrac{1}{2}\kappa \bar{h}^2 \bar{h}'''. \tag{6.2.14}$$

Note that

$$A(-\infty) = s - \tfrac{1}{2}h_-^2 < 0 \quad \text{and} \quad A(\infty) = s - \tfrac{1}{2}h_+^2 > 0. \tag{6.2.15}$$

$\lim_{\lambda \to \infty} D(\lambda)$

Consider the change of variables

$$y = \sqrt{\lambda} x, \qquad \frac{d}{dx} = \sqrt{\lambda} \frac{d}{dy}, \tag{6.2.16}$$

and define $\hat{\psi}(y) = \psi(\tfrac{y}{\sqrt{\lambda}})$. Then (6.2.13) becomes, after dividing by λ,

$$\hat{\psi} + \frac{1}{\sqrt{\lambda}} \left(A \left(\frac{y}{\sqrt{\lambda}} \right) \hat{\psi} \right)' = \delta \hat{\psi}''. \tag{6.2.17}$$

Since $A(x)$ and ψ and their derivatives are bounded, taking $\lambda \to \infty$ leads to

$$\hat{\psi} = \delta \hat{\psi}''. \tag{6.2.18}$$

The solutions of (6.2.18) are

$$\hat{\psi}(y) = e^{\pm y/\sqrt{\delta}} \tag{6.2.19}$$

so that

$$\psi(x) = \hat{\psi}(\sqrt{\lambda}x) = e^{\pm\sqrt{\frac{\lambda}{\delta}}x} \tag{6.2.20}$$

to leading order as $\lambda \to \infty$. Now define

$$\psi_1 = e^{\sqrt{\frac{\lambda}{\delta}}x}, \qquad \psi_2 = e^{-\sqrt{\frac{\lambda}{\delta}}x} \tag{6.2.21}$$

and note $\psi_1 \to 0$ as $x \to -\infty$ and $\psi_2 \to 0$ as $x \to \infty$. Then, to leading order, the Evans function (6.2.11) is

$$D(\lambda) = \left| \begin{array}{cc} e^{\sqrt{\frac{\lambda}{\delta}}x} & e^{-\sqrt{\frac{\lambda}{\delta}}x} \\ \sqrt{\frac{\lambda}{\delta}}e^{\sqrt{\frac{\lambda}{\delta}}x} & -\sqrt{\frac{\lambda}{\delta}}e^{-\sqrt{\frac{\lambda}{\delta}}x} \end{array} \right|_{x=0} = -2\sqrt{\frac{\lambda}{\delta}} < 0. \tag{6.2.22}$$

Thus, $\lim_{\lambda \to \infty} D(\lambda) < 0$.

$D'(0)$

To calculate the other factor $D'(0)$ in the stability indicator function, we must first determine the eigenfunctions associated with the eigenvalue $\lambda = 0$. Note that $\lambda = 0$ is a double eigenvalue. One eigenfunction is due to translation invariance of the traveling wave. Since $h = \overline{h}(x+\mu), \Gamma = 0$ is a solution to (6.2.10) for each μ, differentiating with respect to μ at $\mu = 0$ we find the corresponding eigenfunction

$$\left(\begin{array}{c} \varphi^{(1)}(x) \\ \psi^{(1)}(x) \end{array} \right) = \left(\begin{array}{c} h'(x) \\ 0 \end{array} \right). \tag{6.2.23}$$

However, this eigenfunction corresponds to the case $\psi = 0$ which was covered in [31, 32]. The other eigenfunction corresponds to the parameterization of the traveling waves by surfactant mass $m = \int_{-\infty}^{\infty} \Gamma \, dx$

$$\left(\begin{array}{c} \varphi^{(2)}(x) \\ \psi^{(2)}(x) \end{array} \right) = \frac{\partial}{\partial m} \left(\begin{array}{c} h(x) \\ \Gamma(x) \end{array} \right). \tag{6.2.24}$$

Define $u(x) = \frac{d}{dm}\Gamma(x,m)|_{m=0}$. Let $\lambda = 0, \psi = u$ in (6.2.13):

$$\delta u'' + (A(x)u)' = 0. \tag{6.2.25}$$

Integrating once and applying the boundary conditions $u(\pm\infty) = 0$ gives

$$\delta u' + A(x)u = 0 \tag{6.2.26}$$

so that

$$u(x) = e^{-\int_0^x \frac{A(y)}{\delta} dy}. \tag{6.2.27}$$

From (6.2.15), we observe that $u \to 0$ as $x \to \pm\infty$.

Now let $z = \frac{d}{d\lambda}\psi$ and differentiate (6.2.13) with respect to λ at $\lambda = 0$, to obtain

$$u = (A(x)z)' + \delta z''. \tag{6.2.28}$$

Defining $v(x) = \int_0^x u(y)dy$, we can integrate (6.2.28) with respect to x, leading to

$$\delta z' + A(x)z = v(x) + c. \tag{6.2.29}$$

First consider the eigenfunction $\psi = \psi_1$, with $\psi_1(x) \to 0$ as $x \to -\infty$. For the moment, we will assume that $z_1 = \partial_\lambda\psi_1$, $z_1' = \partial_\lambda\psi_1'$ both approach zero as $x \to -\infty$. Then

$$c = c_1 = -v(-\infty) = -\int_0^{-\infty} u(y)dy = \int_{-\infty}^0 u(y)dy. \tag{6.2.30}$$

Similarly for $\psi = \psi_2$ where $\psi_2(x) \to 0$ as $x \to \infty$,

$$c = c_2 = -v(\infty) = -\int_0^\infty u(y)dy \tag{6.2.31}$$

Now define $\tilde{z} = \frac{d}{d\lambda}\psi_2 - \frac{d}{d\lambda}\psi_1 = z_2 - z_1$. Then subtracting the two equations (6.2.29) for $z = z_1, z = z_2$,

$$\delta\tilde{z}' + A(x)\tilde{z} = c_2 - c_1 \tag{6.2.32}$$

$$= -\int_{-\infty}^\infty u(y)dy < 0 \tag{6.2.33}$$

Next, we calculate $D'(0)$. From (6.2.11), we find

$$D'(\lambda) = \psi_2' d_\lambda\psi_1 + \psi_1 d_\lambda\psi_2' - \psi_1' d_\lambda\psi_2 - \psi_2 d_\lambda\psi_1',$$

evaluated at $x = 0$. As $\lambda \to 0$, $\psi_k \to u$, and $\psi_k' \to u'$, $k = 1, 2$. Consequently,

$$D'(0) = \begin{vmatrix} u & \tilde{z} \\ u' & \tilde{z}' \end{vmatrix}_{x=0} \tag{6.2.34}$$

From (6.2.26) we have the relation

$$u' + \frac{A(x)}{\delta}u = 0. \tag{6.2.35}$$

Since matrix row operations preserve the determinant, we multiply the first row by $\frac{A(x)}{\delta}$ and add it to the second row of (6.2.34) to obtain

$$D'(0) = \begin{vmatrix} u & \tilde{z} \\ 0 & \frac{c_2 - c_1}{\delta} \end{vmatrix}_{x=0} = u(0)\frac{c_2 - c_1}{\delta} < 0. \tag{6.2.36}$$

Therefore

$$sgn\left[D'(0)\lim_{\lambda\to\infty}D(\lambda)\right] > 0 \tag{6.2.37}$$

which implies that this analysis is consistent with the system being stable. This analysis is only consistent with stability because the Evans function could cross the positive x axis an even number of times which still allows the stability indicator function to remain positive. The presence of positive eigenvalues would imply the traveling wave is unstable, even though (6.2.37) suggests stability.

6.3   Multidimensional stability

In this section we examine the stability of the traveling wave solution of two-dimensional system (2.1.38) in the presence of a small amount of surfactant by studying the stability of a traveling wave solution to transverse perturbations. The main result is that the additional eigenvalue associated with the surfactant concentration becomes negative once diffusion of surfactant molecules on the free surface is taken into account. This is intuitively obvious, since diffusion has a smoothing, hence stabilizing effect. As a result, linearized stability hinges on the sign of an integral, the same integral identified in the surfactant-free case by Bertozzi and Brenner [6].

We begin with the system of equations (2.1.38) written in a frame moving with speed s,

$$h_t - sh_x + (\tfrac{1}{3}h^3)_x - \nabla \cdot (\tfrac{1}{2}h^2\nabla\Gamma) = \beta\nabla.\left(\tfrac{1}{3}h^3\nabla h\right) - \kappa\nabla.\left(\tfrac{1}{3}h^3\nabla\Delta h\right) \tag{6.3.1a}$$

$$\Gamma_t - s\Gamma_x + \left(\tfrac{1}{2}h^2\Gamma\right)_x - \nabla.(h\Gamma\nabla\Gamma) = \beta\nabla.\left(\tfrac{1}{2}h^2\Gamma\nabla h\right) - \kappa\nabla.\left(\tfrac{1}{2}h^2\Gamma\nabla\Delta h\right) + \delta\,\Delta\Gamma. \tag{6.3.1b}$$

Perturbing about a traveling wave $h = \overline{h}(x)$ with no surfactant (i.e., $\Gamma = 0$), we write

$$h = \overline{h}(x) + H(x, y, t), \quad \Gamma = G(x, y, t). \tag{6.3.2}$$

Substituting into (6.3.1), and retaining only linear terms in H, G, we consider the linearized equations, and seek solutions in the form

$$H(x, y, t) = e^{\lambda t}e^{iqy}\varphi(x), \qquad G(x, y, t) = e^{\lambda t}e^{iqy}\psi(x). \tag{6.3.3}$$

This leads to a system of ODE for the eigenfunctions (φ, ψ), with parameters q, the transverse wavenumber, and λ, the growth rate:

$$\lambda\varphi - s\varphi' \ + \ \left(\overline{h}^2\varphi\right)' - \left(\tfrac{1}{2}\overline{h}^2\psi'\right)' - \tfrac{1}{2}q^2\overline{h}^2\psi = \beta\left(\overline{h}^2\overline{h}'\varphi\right)'$$

$$- \ \kappa\left[\left(\tfrac{1}{3}\overline{h}^3\left(\varphi''' - q^2\varphi'\right)\right)' - \tfrac{1}{3}\overline{h}^3 q^2\left(\varphi'' - q^2\varphi\right) + \left(\overline{h}^2\varphi\overline{h}'''\right)'\right] \quad (6.3.4a)$$

$$\lambda\psi - s\psi' \ + \ \left(\tfrac{1}{2}\overline{h}^2\psi\right)' = \beta\left(\tfrac{1}{2}\overline{h}^2\psi\overline{h}'\right)' - \kappa\left(\tfrac{1}{2}\overline{h}^2\psi\overline{h}'''\right)' + \delta\left(\psi'' - q^2\psi\right). \quad (6.3.4b)$$

When $q = 0$, the analysis reduces to the one dimensional case discussed in §6.2 since (6.3.3) reduces to $H(x, y, t) = e^{\lambda t}\varphi(x)$ and $G(x, y, t) = e^{\lambda t}\psi(x)$. Thus $\lambda = 0$ is a double eigenvalue, with one eigenfunction corresponding to translation invariance of the traveling wave, and an independent eigenfunction corresponding to the parameterization of the traveling wave by surfactant mass m. Since $h = \overline{h}(x + \mu), \Gamma = 0$ is a solution of (6.3.1) for each μ, differentiating with respect to μ at $\mu = 0$, one eigenfunction corresponding to the eigenvalue $\lambda = 0$ is

$$\begin{pmatrix} \varphi_0^{(1)}(x) \\ \psi_0^{(1)}(x) \end{pmatrix} = \begin{pmatrix} h'(x) \\ 0 \end{pmatrix}. \quad (6.3.5)$$

Similarly, since there is a traveling wave for each value of the total surfactant mass $m = \int_{-\infty}^{\infty} \Gamma \, dx$ we see that

$$\begin{pmatrix} \varphi_0^{(2)}(x) \\ \psi_0^{(2)}(x) \end{pmatrix} = \frac{\partial}{\partial m}\begin{pmatrix} h(x) \\ \Gamma(x) \end{pmatrix}\Big|_{m=0} \quad (6.3.6)$$

is also an eigenfunction for $\lambda = 0$ when $q = 0$. Observe that (6.3.4) has the form

$$\lambda\varphi = L_0(x)\varphi + M_0(x)\psi + q^2(L_1(x)\varphi + M_1(x)\psi) + q^4 L_2(x)\varphi \quad (6.3.7a)$$

$$\lambda\psi = K_0(x)\psi - q^2\delta\psi \quad (6.3.7b)$$

where the linear differential operators are represented by

$$L_0 = s\frac{d}{dx} - \frac{d}{dx}\left(h^2\right) - \kappa\left[\frac{d}{dx}\left(\frac{h^3}{3}\frac{d^3}{dx^3}\right) + \frac{d}{dx}\left(h^2\frac{d^3}{dx^3}h\right)\right] + \beta\frac{d}{dx}\left(h^2\frac{d}{dx}h\right) \qquad (6.3.8a)$$

$$M_0 = \frac{d}{dx}\left(\frac{h^2}{2}\frac{d}{dx}\right) \qquad (6.3.8b)$$

$$L_1 = \kappa\left[\frac{d}{dx}\frac{h^3}{3}\frac{d}{dx} + \frac{h^3}{3}\frac{d^2}{dx^2}\right] \qquad (6.3.8c)$$

$$M_1 = \frac{h^2}{2} \qquad (6.3.8d)$$

$$L_2 = \frac{h^2}{2} \qquad (6.3.8e)$$

$$K_0 = s\frac{d}{dx} - \frac{d}{dx}\left(\frac{h^2}{2}\right) - \kappa\frac{d}{dx}\left(\frac{h^2}{2}\frac{d^3}{dx^3}h\right) + \beta\frac{d}{dx}\left(\frac{h^2}{2}\frac{d}{dx}h\right) + \delta\frac{d^2}{dx^2}. \qquad (6.3.8f)$$

Now we assume that eigenvalues and eigenfunctions have power series expansions in terms of q^2, since only q^2 appears in (6.3.7a-6.3.7b). We are interested in how the double eigenvalue $\lambda = 0$ is perturbed by small values of q, we drop the superscripts and write

$$\lambda = aq^2 + O(q^4), \quad \begin{pmatrix} \varphi \\ \psi \end{pmatrix} = \begin{pmatrix} \varphi_0 \\ \psi_0 \end{pmatrix} + q^2\begin{pmatrix} \varphi_1 \\ \psi_1 \end{pmatrix} + O(q^4). \qquad (6.3.9)$$

Substituting into (6.3.7), the $O(1)$ terms cancel, and the $O(q^2)$ terms yield

$$a\begin{pmatrix} \varphi_0 \\ \psi_0 \end{pmatrix} = \begin{pmatrix} L_0 & M_0 \\ 0 & K_0 \end{pmatrix}\begin{pmatrix} \varphi_1 \\ \psi_1 \end{pmatrix} + \begin{pmatrix} L_1 & M_1 \\ 0 & -\delta \end{pmatrix}\begin{pmatrix} \varphi_0 \\ \psi_0 \end{pmatrix}. \qquad (6.3.10)$$

Let

$$A_0 = \begin{pmatrix} L_0 & M_0 \\ 0 & K_0 \end{pmatrix} \qquad (6.3.11)$$

and define $U_0^* = \begin{pmatrix} \varphi^* \\ \psi^* \end{pmatrix}$ by $U_0^* \perp \mathcal{R}(A_0)$, such that

$$0 = (U_0^*, A_0 U) = (A_0^* U_0^*, U), \forall U \in X. \qquad (6.3.12)$$

Note that A_0 has $\lambda = 0$ as a double eigenvalue, so A_0^* also has this property. From the linearized

equations we see that $A_0 U = \frac{d}{dx}(b(x)\mathcal{L}U)$. Thus,

$$
\begin{aligned}
(U^*, A_0 U) &= \int U^* \frac{d}{dx}(b(x)\mathcal{L}U)dx &\text{(6.3.13)}\\
&= -\int \frac{d}{dx}U^*(b(x)\mathcal{L}U)dx \\
&= 0
\end{aligned}
$$

and we conclude the 2-dimensional null space of A_0^* consists of constant vectors in $\mathbb{R}^2$. Taking the action of $U^* = \begin{pmatrix} 1 \\ 0 \end{pmatrix}$ and $U^* = \begin{pmatrix} 0 \\ 1 \end{pmatrix}$ on (6.3.10), we eliminate the (φ_1, ψ_1) terms, leaving

$$
\int_{\mathbb{R}} a \begin{pmatrix} \varphi_0 \\ \psi_0 \end{pmatrix} dx = \int_{\mathbb{R}} \begin{pmatrix} L_1 & M_1 \\ 0 & -\delta \end{pmatrix} \begin{pmatrix} \varphi_0 \\ \psi_0 \end{pmatrix} dx. \tag{6.3.14}
$$

Consider the linear combination of the eigenfunctions

$$
\begin{pmatrix} \varphi_0 \\ \psi_0 \end{pmatrix} = c \begin{pmatrix} \varphi_0^{(1)} \\ 0 \end{pmatrix} + d \begin{pmatrix} \varphi_0^{(2)} \\ \psi_0^{(2)} \end{pmatrix}. \tag{6.3.15}
$$

Substituting (6.3.15) into (6.3.14) we determine

$$
a \begin{bmatrix} \int \left(c\varphi_0^{(1)} + d\varphi_0^{(2)} \right) dx \\ d \int \psi_0^{(2)} dx \end{bmatrix} = \begin{bmatrix} \int L_1 \left(c\varphi_0^{(1)} + d\varphi_0^{(2)} \right) dx + d \int M_1 \psi_0^{(2)} dx \\ -\delta d \int \psi_0^{(2)} dx \end{bmatrix}. \tag{6.3.16}
$$

We immediately deduce one eigenvalue: for $\psi_0 = \psi_0^{(2)} \neq 0$, we have $a = -\delta$, for which $\lambda = -\delta q^2 + O(q^4) \leq 0$, for small q; a stable eigenvalue. The first equation in (6.3.16) then relates c and d

$$
c = -\frac{d \int (L_1 + \delta) \varphi_0^{(2)} dx + \int M_1 \psi_0^{(2)} dx}{\int (L_1 + \delta) \overline{h}' dx}. \tag{6.3.17}
$$

Now consider the eigenfunctions $\begin{pmatrix} \varphi \\ \psi \end{pmatrix} = \begin{pmatrix} \overline{h}'(x) \\ 0 \end{pmatrix}$. In this case, $d = 0$. As in the analysis of Bertozzi and Brenner [6], integrating (6.3.4a) and applying the boundary conditions result in the identity

$$
a \int_{-\infty}^{\infty} \varphi dx = \kappa \int_{-\infty}^{\infty} \frac{\overline{h}^3}{3} \varphi'' dx = \kappa \int_{-\infty}^{\infty} \frac{\overline{h}^3}{3} \overline{h}''' dx. \tag{6.3.18}
$$

Consider the traveling wave solution $h(x, y, t) = \overline{h}(x - st)$ in (6.3.1a). Integrating once and

solving for $\kappa\frac{\overline{h}^3}{3}\overline{h}'''$ results in

$$\kappa\frac{\overline{h}^3}{3}h''' = s\overline{h} - \frac{\overline{h}^3}{3} + \beta\frac{\overline{h}^3}{3}\overline{h}' - k_h \qquad (6.3.19)$$

substituting into (6.3.18) results in

$$\lambda\int_{-\infty}^{\infty}\varphi\,dx = q^2\int_{-\infty}^{\infty} s\overline{h} - \frac{\overline{h}^3}{3} + \beta\frac{\overline{h}^3}{3}\overline{h}' - k_h\,dx. \qquad (6.3.20)$$

Which reduces to

$$\lambda\int_{-\infty}^{\infty}\varphi\,dx = q^2\int_{-\infty}^{\infty} s\overline{h} - \frac{\overline{h}^3}{3} - k_h\,dx \qquad (6.3.21)$$

since $\overline{h}' \to 0$ as $h \to \pm\infty$. The traveling wave speed s (6.2.5) and constant of integration k_h (6.2.6) were determined in §6.2:

$$s = \frac{1}{3}(h_L^2 + h_L h_R + h_R^2) \qquad k_h = \frac{1}{3}h_L h_R(h_L + h_R). \qquad (6.3.22)$$

Thus,

$$\lambda = \frac{q^2}{h_L - h_R}\int_{-\infty}^{\infty}(\overline{h} - h_L)(\overline{h} - h_R)(\overline{h} + h_L + h_R)\,dx. \qquad (6.3.23)$$

The sign of this eigenvalue is dependent on the size of the capillary ridge. The capillary ridge has $h > h_R$, which contributes a positive portion to the integrand, however, the rest of the traveling wave contributes negative values. Thus the capillary ridge has to be large enough to destabilize the wave.

There is one stable eigenvalue and the stability of the other eigenvalue depends on the boundary data h_L and h_R. A more detailed analysis of the case with no surfactant is available in [6]. Note that by continuity, these stability conclusions apply to a small amount of surfactant mass $m > 0$ since the surfactant equation only introduces negative eigenvalues.

6.4 Initially Uniform Height

In this section, we consider an initially uniform film with height $h = 1$ and a small amount of surfactant located on the surface of the film. We consider the simplified system of equations (6.1.1), where $\beta = \kappa = \delta = 0$. In §6.4.1 we use the linearized equations to determine that two waves develop in the presence of a drop of surfactant on the film. This linear analysis suggests that the height h is related to the surfactant concentration Γ: $h = 1 + \Gamma_x$. A numerical investigation surprisingly supports this approximation to high order. In §6.4.2 we further investigate

this relation by implementing $h = 1 + \Gamma_x$ into the governing system of equations to derive a single PDE and investigate the behavior of this equation numerically.

6.4.1 Linearization of Equations

We examine the behavior of an initially uniform film, i.e., $h = 1$ perturbed by a small amount of surfactant. Consider the simplified PDE system (6.1.1)

$$h_t + \left(\tfrac{1}{3}h^3\right)_x - \left(\tfrac{1}{2}h^2\Gamma_x\right)_x = 0 \tag{6.4.1a}$$

$$\Gamma_t + \left(\tfrac{1}{2}h^2\Gamma\right)_x - (h\Gamma\Gamma_x)_x = 0 \tag{6.4.1b}$$

with perturbations of the solution

$$h(x,t) = 1, \qquad \Gamma(x,t) = 0. \tag{6.4.2}$$

In §6.1.1 we considered a small amount of surfactant on a constant film height. By linearizing the equations (6.1.1) about this constant solution we determined (6.1.24). We then found that two traveling waves developed with constant speeds $s_1 = \tfrac{1}{2}h^2$, $s_2 = h^2$ as shown in (6.1.26). Using a slight change in notation, we determine the same result here. We consider initial conditions

$$h(x,0) = 1 + \tilde{h}(x), \qquad \Gamma(x,0) = \tilde{\Gamma}(x) \tag{6.4.3}$$

and assume h, Γ are continuous and piecewise smooth and $\tilde{h}$, $\tilde{\Gamma}$ are small, with compact support. Solving the linearized equations, the perturbations can be expressed in terms of two traveling waves such that

$$\Gamma_1(x,t) = g(x - \tfrac{1}{2}t) \tag{6.4.4}$$

a traveling wave with speed $s = \tfrac{1}{2}$ and

$$h_1(x,t) = f(x - t) + g_x(x - \tfrac{1}{2}t) \tag{6.4.5}$$

where the initial conditions

$$f(x) = \tilde{h}(x), \qquad g(x) = \tilde{\Gamma}(x) \tag{6.4.6}$$

are set by (6.4.3). Thus the presence of surfactant causes two waves to form in the height of the film, one wave travels at the speed $s_1 = 1$ and the other at the speed $s_2 = \tfrac{1}{2}$. Since the surfactant is also traveling at speed $s = \tfrac{1}{2}$ we determine that the faster wave carries no

146

surfactant while the slower includes the surfactant. In the numerical simulations of Figure 6.6, we show that for the nonlinear equations (6.4.1) two waves develop in the height and that the surfactant concentration Γ is carried by the slower moving wave. Observe that the wave without surfactant is traveling at twice the speed of the wave carrying the surfactant. These profiles were generated using the numerical scheme (6.1.53) with $\varepsilon = 0$ and initial conditions

$$h(x,0) = 1, \qquad \Gamma(x,0) = \begin{cases} 0 & \text{if } x < 0.1 \\ 0.2(x - 0.1) & \text{if } x < 0.15 \\ -0.2(x - 0.2) & \text{if } x < 0.2 \\ 0 & \text{if } x \geq 0.2. \end{cases} \tag{6.4.7}$$

Notice that if $f \equiv 0$ in (6.4.5) then $\tilde{h} = g_x$ and $h = 1 + \Gamma_x$. Figure 6.7 shows how the two waves separate and in fact after sufficient time, the behavior of the wave traveling at speed $s_2 = \frac{1}{2}$ is not influenced by the wave traveling at speed $s_1 = 1$. Thus in the wave where $\Gamma > 0$, $f \equiv 0$. We further investigate the behavior of the piece of the solution with $\Gamma > 0$, traveling at speed $s_2 = \frac{1}{2}$.

Consider a continuous surfactant concentration Γ profile in which there is a jump in Γ_x at the maximum of the surfactant concentration. Using the jump conditions for (6.4.1b) we determine the magnitude of the jump in Γ_x:

$$-s[\Gamma] + \left[\tfrac{1}{2}h^2\Gamma\right] - [h\Gamma\Gamma_x] = 0. \tag{6.4.8}$$

Since Γ is continuous, $[\Gamma] = 0$ and we are considering where Γ attains a maximum so $\Gamma \neq 0$. Thus dividing by Γ (6.4.8) reduces to

$$\left[\tfrac{1}{2}h^2\right] - [h\Gamma_x] = 0. \tag{6.4.9}$$

Thus,

$$\tfrac{1}{2}\left(h_+^2 - h_-^2\right) - \left(h_+\Gamma_x^+ - h_-\Gamma_x^-\right) = 0. \tag{6.4.10}$$

Let $h = 1 + \Gamma_x$ then (6.4.10) becomes

$$\tfrac{1}{2}\left((1 + \Gamma_x^+)^2 - (1 - \Gamma_x^-)^2\right) - \left((1 + \Gamma_x^+)\Gamma_x^+ - (1 + \Gamma_x^-)\Gamma_x^-\right) = 0 \tag{6.4.11}$$

which reduces to

$$(\Gamma_x^+)^2 = (\Gamma_x^-)^2. \tag{6.4.12}$$
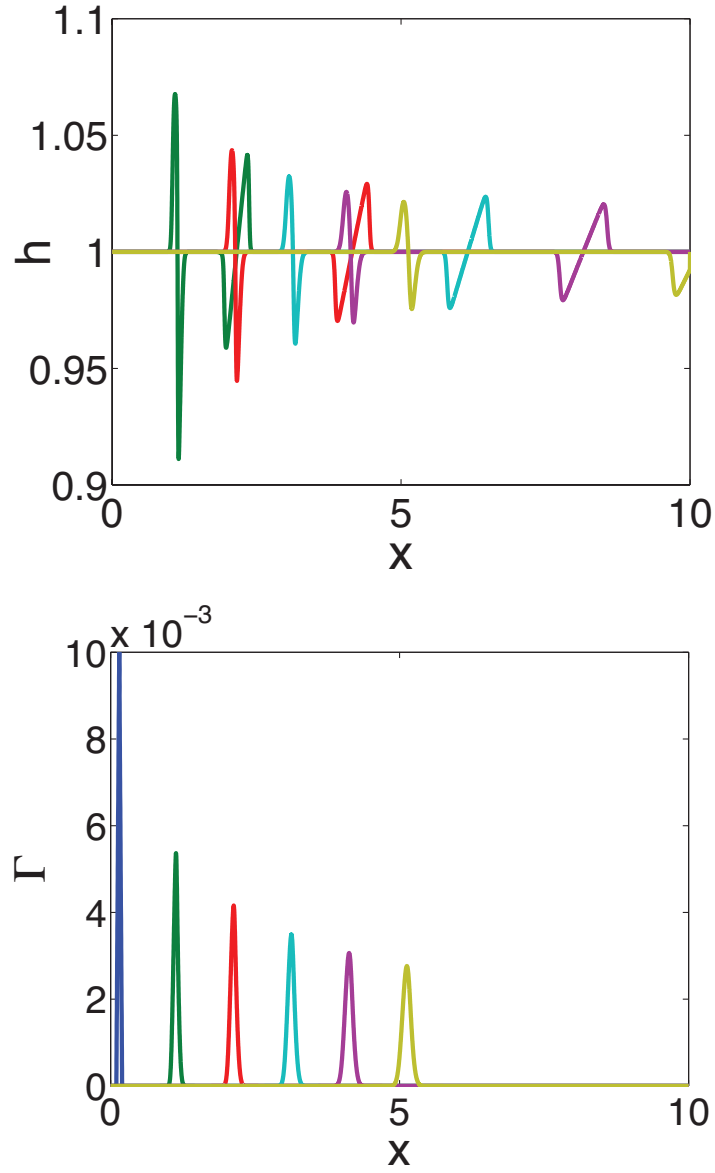
Figure 6.6: The evolution of the height h (top) and surfactant concentration Γ (bottom) profiles for (6.4.1) with initially uniform height and a perturbation of surfactant. The height profile develops two waves, one traveling at the same speed as the surfactant and the other traveling at twice that speed. The profiles are at $t = 0, 2, 4, 6, 8, 10$, each color corresponds to one time and $\Delta x = 0.001$.

Therefore $\Gamma_x^+ = \pm\Gamma_x^-$; we will only consider the case $\Gamma_x^+ = -\Gamma_x^-$ so that one slope is positive
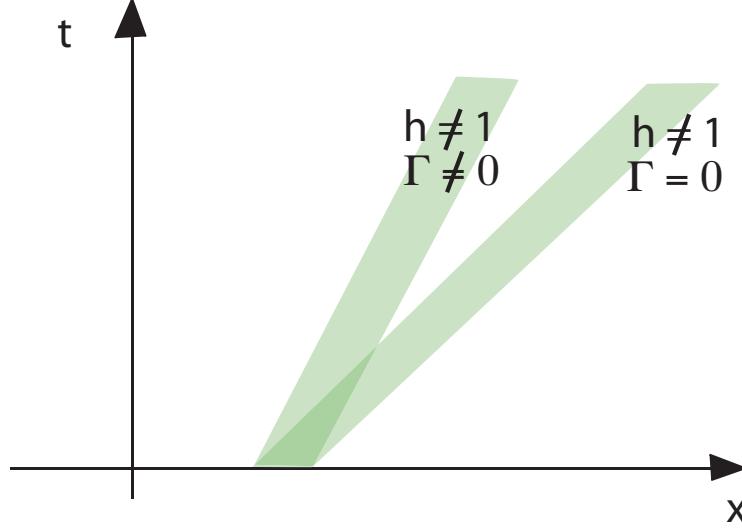
Figure 6.7: The support of the two traveling waves that develop in the height due to the introduction of surfactant. Notice that after sufficient time the two waves are independent of each other.

and the other negative. Consequently,

$$h^- = 1 + \Gamma_x^-, \qquad h^+ = 1 - \Gamma_x^-, \qquad \Gamma_x^+ = -\Gamma_x^-. \tag{6.4.13}$$

Initial conditions (6.4.7) satisfy these jump conditions in Γ. We investigate the jump in h which develops due to the jump in Γ_x. Figure 6.8 shows the height profile plotted against $1 + \Gamma_x$ at $t = 10$ where Γ_x is determined using the finite difference $\Gamma_x \approx \frac{\Gamma_{j+1}^n - \Gamma_j^n}{\Delta x}$. The profiles of h and $1 + \Gamma_x$ appear identical where $\Gamma > 0$ (the wave moving with speed $s = 1$ carries no surfactant). The difference $h - 1 - \Gamma_x$ is shown in Figure 6.9. Notice that the error in the approximation $h = 1 + \Gamma_x$ is on the order of 10^{-5}.

Next we investigate the magnitude of the jumps in the numerical simulations. Figure 6.10 shows Γ_x; observe that where Γ_x jumps from positive to negative at $x \approx 5$, $\Gamma_x^- \approx 0.0214$. From the jump conditions (6.4.13), h^+, h^-, and Γ_x^+ are all determined by Γ_x^-. We compare the values stipulated by the jump conditions to the actual values achieved by the numerical solutions at $t = 10$ as shown in Figure 6.8 and Figure 6.10. The jump conditions suggest that $\Gamma_x^+ = -\Gamma_x^- \approx -0.0214$; from Figure 6.10, the value achieved by the numerical simulations is $\Gamma_x^+ \approx -0.0246$. Now compare the value from the jump condition (6.4.13), $h^- = 1 + \Gamma_x^- \approx 1.0214$ to the height achieved in Figure 6.8, $h^- \approx 1.0214$. Finally we compare the values for $h^+ = 1 - \Gamma_x^- \approx 0.978$ to the values achieved in the numerical solution $h^+ \approx 0.975$. All of the values achieved in the numerical solutions are approximately the values predicted by the jump conditions (6.4.13).
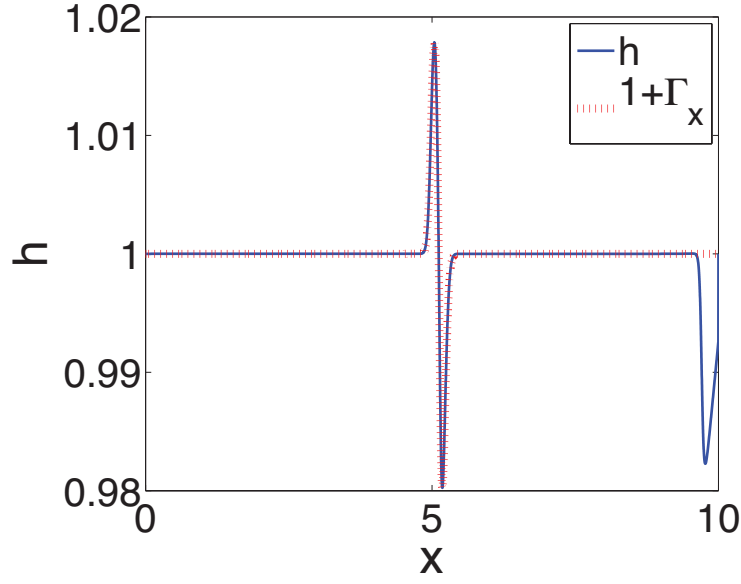
Figure 6.8: The height h and $1 + \Gamma_x$ at $t = 10$ using initial conditions (6.4.2) with $\Delta x = 0.001$.
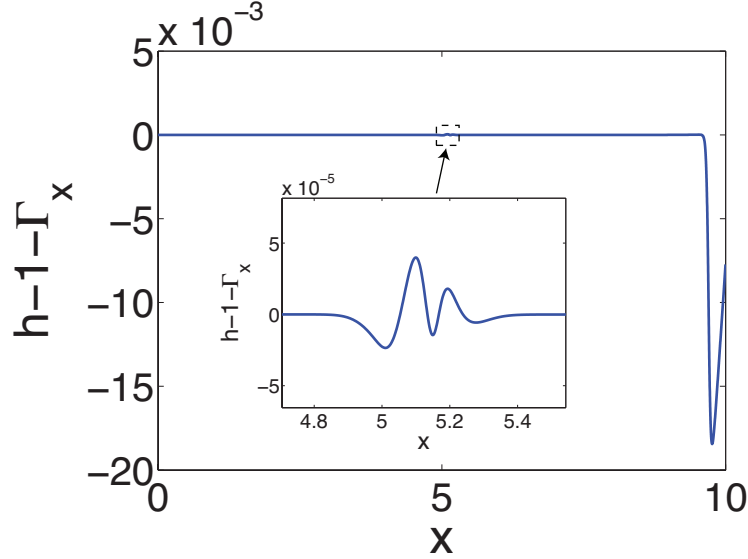
Figure 6.9: The difference between the height h and $1 + \Gamma_x$ at $t = 10$ using initial conditions (6.4.2) with $\Delta x = 0.001$. The inset shows a small error in the location of the jump in Γ_x.

6.4.2 Analysis of (6.4.1) with $h = 1 + \Gamma_x$

From the above numerical investigation, $h = 1 + \Gamma_x$ is a reasonable approximation for the height profile. We now investigate the behavior of the system (6.4.1) when this approximation

150
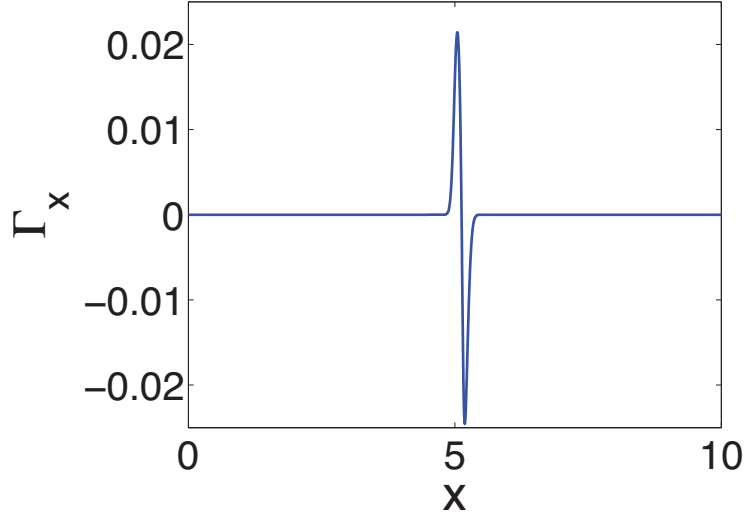
Figure 6.10: Γ_x at $t = 10$ determined using the one-sided finite difference operator $\Gamma_x = \frac{\Gamma_{j+1}^n - \Gamma_j^n}{\Delta x}$ from the numerical simulations using initial conditions (6.4.2) with $\Delta x = 0.001$.

is implemented. Substitute $\Gamma_x = h - 1$ into (6.4.1a)

$$h_t + \tfrac{1}{3}(h^3)_x - \tfrac{1}{2}(h^2(h-1))_x = 0. \tag{6.4.14}$$

This is a conservation law for h

$$h_t + f(h)_x = 0, \qquad f(h) = \tfrac{1}{2}h^2 - \tfrac{1}{6}h^3, \tag{6.4.15}$$

with characteristic speed

$$f'(h) = h - \tfrac{1}{2}h^2. \tag{6.4.16}$$

Notice $f'(1) = \tfrac{1}{2}$ which agrees with the linear analysis and corresponds to the speed of the wave including surfactant. Consider the solutions in a moving frame by defining $y = x - \tfrac{1}{2}t$. Let h(x,t)=1+H(y,t) then (6.4.15) reduces to

$$H_t - \frac{1}{6}(H^3)_y = 0. \tag{6.4.17}$$

We investigate this equation numerically using an explicit upwind scheme

$$H_j^{n+1} = H_j^n + \frac{\Delta t}{6\Delta x}\left((H_{j+1}^n)^3 - (H_j^n)^3\right) \tag{6.4.18}$$

151

with initial condition $H(y, 0) = \Gamma_y(y, 0)$:

$$H(y, 0) = \begin{cases} 0 & \text{if } y \leq 0.8 \\ -2 \cdot 0.05 \cdot (y - 1) \cdot \exp\left(\frac{-1}{1-\left(\frac{y-1}{0.2}\right)^2}\right) \frac{1}{0.2^2\left(1-\left(\frac{1-y}{0.2}\right)^2\right)^2} & \text{if } 0.8 < y < 1.2 \\ 0 & \text{if } y \geq 1.2 \end{cases} \quad (6.4.19)$$

derived from

$$\Gamma(y, 0) = \begin{cases} 0 & \text{if } y \leq 0.8 \\ 0.05 \exp\left(\frac{-1}{1-\left(\frac{y-1}{0.2}\right)^2}\right) & \text{if } 0.8 < y < 1.2 \\ 0 & \text{if } y \geq 1.2. \end{cases} \quad (6.4.20)$$

In Figure 6.11 we show the behavior of (6.4.18) with initial conditions (6.4.19). The profile for the surfactant concentration is determined by $\Gamma = \int_0^y H \, dy$. The leading edge of the disturbance remains stationary at $y = 1.2$ since H is continuous near $y = 1.2$ and $H(1.2, t) = 0$. However, the remainder of the profile moves at a negative speed. Two shocks form and we further investigate the right shock. From (6.4.17),

$$H_t - \tfrac{1}{2}H^2 H_y = 0; \quad (6.4.21)$$

differentiating with respect to y and defining $v = H_y$ we find

$$v_t - \tfrac{1}{2}H^2 v_y = H v^2 \quad (6.4.22)$$

which corresponds to

$$\frac{dv}{dt} = H v^2 \quad (6.4.23)$$

since along characteristics $\frac{dy}{dt} = \tfrac{1}{2}H^2 = constant$. Thus

$$v(y, t) = \frac{c}{1 - cHt} \quad (6.4.24)$$

where c is a constant and $v(y, 0) = H_y(y, 0) = H_y^0$, so

$$v(y, t) = \frac{H_y^0}{1 - H_y^0 H^0 t}. \quad (6.4.25)$$

152

Consequently, $v(y,t)$ blows up as $t \to \frac{1}{(H_y^0 H^0)^-}$ which causes $v(y,t) \to -\infty$. This first happens for $t = \max_y H_y H$, i.e. at a maximum of $H_y H$.

The corresponding surfactant profile $\Gamma = \int_{-\infty}^{\infty} H \, dy - 1$ is smooth at the leading edge but there is a jump in Γ_y at the maximum and also at the trailing edge. The plots are generated using the numerical scheme (6.4.18) with $\Delta y = 0.002$ and $\Delta t = 0.02$; the plots shown are at $t = 0, 5, 10, \ldots, 45$.
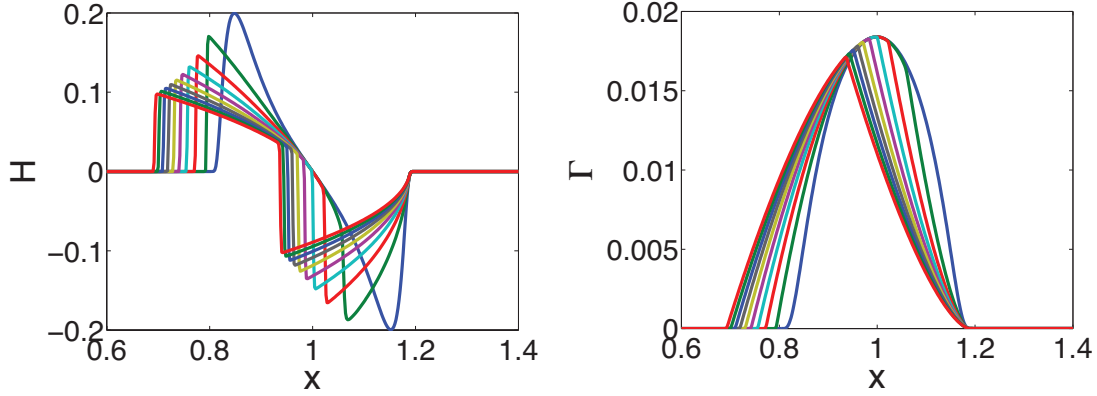
Figure 6.11: The height profiles from (6.4.18) with $\Delta x = 0.002$ and $\Delta t = 0.02$. The plots are at $t = 0, 5, 10, \ldots, 45$. The corresponding surfactant concentration profiles are determined by $\Gamma = \int_0^{\infty} H$.

We have shown various arguments that support the relation $h = 1 + \Gamma_x$. However, these investigations are not conclusive since this is verified analytically only for the linearized equation. Numerical simulations of (6.4.1) capture the expected shock within the profile. However, the shock at the trailing edge is not captured and the leading edge is smoothed. These differences suggest there is still an important structure for the nonlinear evolution of the profile which is not captured by the linear expansion, nor by the approximation $h = 1 + \Gamma_x$.

Chapter 7

Discussion

The deposition of surfactant on a thin liquid film instantly propels the fluid into motion. This motion is a result of a local change in surface tension. We consider a film on a horizontal substrate and on an inclined plane which introduces an additional driving force, due to gravity. We examine the evolution of the film and surfactant concentration on a horizontal surface numerically, analytically, and with an experiment. On the inclined plane, we explore the stability of a traveling wave solution, and perturbations of an initially flat film.

In the absence of gravity, we develop a numerical method in Chapter 3 to simulate the evolution of the height of the film and the surfactant concentration. This method provides the capability of not only simulating the shape of the height and surfactant profiles but also tracking the spreading through the location of the maximum height and the leading edge of the surfactant. In order to obtain a basic understanding of the modeling system, we consider the simplified equations by letting $\beta = \kappa = \delta = 0$. Due to the resulting hyperbolic structure of the height equation, a shock develops in the height profile. This development complicates the generation of a numerical method. If only the height equation was considered it would be logical to use a finite volume method. However, the height equation is coupled to an equation for the surfactant concentration, a parabolic equation, which makes the choice of numerical method more difficult. In order to address the individual issues inherent to the height and surfactant concentration equations concurrently we transform the spatial variable to a fixed domain. We are then able to use the jump conditions of the system to set the boundary condition. This transformation eliminates the issues introduced by each of the equations.

Jensen and Grotberg [35, 34] found a similarity scaling and similarity solution for the simplified system. This solution explained the behavior near the leading edge of the surfactant. However, they were not able to confirm these scalings with numerical results, rather they included the smoothing effects β, κ, δ. In Chapter 4, we verify the numerical results generated on the fixed domain to the scalings and solutions discovered Jensen and Grotberg. We then

further the investigation by exploring the structure of the solution near the center of the droplet of surfactant. We find that this solution is in fact not a similarity solution. This development relies on the use of the numerical simulations to determine the scaling exponents. Once one scaling exponent, for the height, surfactant concentration, or spatial scale, is set for this inner solution the remainder of the solution is defined. Presumably the connection between the inner and outer solution determines this scaling. The numerical results suggest that the inner and outer solutions connect through a jump discontinuity or corner. Such a structure would explain the lack of convergence of the numerical method under grid refinement in this center region of the solution. However, the dip that occurs in the numerical solution moves with the surface velocity instead of the characteristic speed which would contradict the development of a jump or corner.

An innovative experiment in Karen Daniels' lab enables the distortion of the height of the film and the location of the surfactant molecules to be observed simultaneously. One goal of the experiment is to compare the model equations (with the inclusion of the parameters β, κ, δ) to the physical spreading of the film, as described in Chapter 5. If all of the model parameters β, κ, δ, equation of state $\sigma(\Gamma)$, and time scale T are taken to be free parameters then we are able to achieve agreement between the numerical and physical behavior. However, a reasonable range for the parameters is stipulated by the experiment. When these physical values are implemented in the modeling system, the height profiles only line up if we ignore the time scale. Using this time scale we are also able to achieve agreement between the simulations and the experiment for the spreading rate of the film and surfactant. Additionally the location aligns for the simulations and experiment of the maximum in the height as well as the leading edge of the surfactant. However, another discrepancy occurs in the shape of the surfactant profiles. For a variety of the initial conditions implemented in the numerical method, the surfactant profile converges to a concave solution. In contrast, the experimental surfactant concentration profiles clearly exhibit a persistent two step structure. These disagreements call into question the validity of the equation for the surfactant concentration. To further explore the influence of the surfactant profile, we neglect the surfactant equation and instead update the height profile using the experimental surfactant concentration profile. This method provides a reasonable fit for the height profiles, but the modeling parameter κ must be taken to be unreasonably large. This difference traces back to the derivation of the surfactant equation. In the normal stress boundary condition the surface tension caused by the curvature of the film is taken to be constant. However, the surfactant concentration seemingly also affects this role of surface tension which would require the parameter κ to be a function of Γ. This comparison between the modeling system and experiment requires the derivation of the model to be questioned. The equation for the height of the film was originally derived separately and the surfactant equation was later incorporated; this inclusion may have been done too naively.

In Chapter 6 we explore the dynamics of a thin film driven by both gravity an surfactant. We consider the stability of a traveling wave solution on an inclined plane. We make the simplifying assumption that there is only a small amount of surfactant present on the underlying film. This assumption decouples the equation for surfactant concentration from the equation for the height of the film. This analysis could be furthered by studying the stability of the three step traveling wave solution without the assumption of surfactant concentration.

We also examine the evolution of a uniform film driven by both gravity and surfactant. Two waves develop in the film: one traveling at the same speed as the surfactant and the other traveling ahead with no surfactant. The solution for the height profile appears to assume a structure that is dependent on the surfactant concentration. The numerical simulations suggest that the height of the film forms two rarefaction waves which are connected by shock waves; we explore this connection with analysis and simulations. Further analysis is required to confirm this structure.

In this dissertation we explore various aspects of the behavior of a thin film when insoluble surfactant is deposited. While the results provide advances to understanding the spreading dynamics of both the film and surfactant, critical issues are also raised. The numerical method developed provides a more accurate method to track the spreading surfactant. The numerical simulations are beneficial in understanding the structure of the solution for the simplified system of equations. A corresponding experiment produces innovative results in which we observe the evolution of the height of the film and surfactant concentration simultaneously. We are able to successfully connect the spreading behavior between the experiment and model. This comparison raises the need for future investigations into the derivation and accuracy of the equation for the surfactant concentration.

REFERENCES

[1] Navier-stokes equations. `http://www.cfd-online.com/Wiki/Navier-Stokes_equations`, 2009.

[2] J. Ahmad and R.S. Hansen. A simple quantitative treatment of the spreading of monolayers on thin liquid films. *J. Colloid Interface Sci.*, 38:601–604, 1972.

[3] G.I. Barenblatt, M. Bertsch, A.E. Chertock, and V.M. Prostokishin. Self-similar intermediate asymptotics for a degenerate parabolic filtration-absorption equation. *Proc. of the Nat. Acad. of Science*, 97(18):9844 – 9848, 2000.

[4] A.J. Bernoff and T.P. Witelski. Linear stability of source-type similarity solutions of the thin film equation. *Applied Math. Letters*, 15:599 – 606, 2002.

[5] A.L. Bertozzi. The mathematics of moving contact lines in thin liquid films. *Notices of the AMS*, 45(6):689 – 697, 1998.

[6] A.L. Bertozzi and M.P. Brenner. Linear instability and transient growth in driven contact lines. *Physics of Fluids*, 9(3):530–539, 1997.

[7] A.L. Bertozzi, A. Münch, X. Fanton, and A.M. Cazabat. Contact line stability and "undercompressive shocks" in driven thin film flow. *PRL*, 81(23):5169 – 5172, 1998.

[8] A.L. Bertozzi, A. Münch, and M. Shearer. Undercompressive shocks in thin film flows. *Physica D*, 134(4):431 – 464, 1999.

[9] A.L. Bertozzi, A. Münch, M. Shearer, and K. Zumbrun. Stability of compressive and undercompressive thin film travelling waves. *European J. Appl. Math.*, 12(3):253–291, 2001.

[10] M. Borgas and J. Grotberg. Monolayer flow on a thin film. *J. Fluid Mech.*, 193:151 – 170, 1988.

[11] R.J. Braun and A.D. Fitt. Modelling drainage of the precorneal tear film after a blink. *Math. Med. and Bio.*, 20:1–28, 2003.

[12] M. Brenner and A. Bertozzi. Spreading of droplets on a solid surface. *Physical Review Letters*, 71(4):593 – 596, 1993.

[13] J.L. Bull, L.K. Nelson, J.T. Walsh, M.R. Glucksberg, S. Schürch, and J.B. Grotberg. Surfactant-spreading and surface-compression disturbance on a thin viscous film. *J. of Biomech. Eng.*, 121:89 – 98, 1999.

[14] A.M. Cazabat, F. Heslot, S.M. Troian, and P. Carles. Fingering instability of thin spreading films driven by temperature gradients. *Nature*, 346:824–826, 1990.

[15] G.Q Chen, N. Even, and C. Klingenberg. Hyperbolic conservation laws with discontinuous fluxes and hydrodynamic limit for particle systems. *J Diff Eqns*, 245:3095–3126, 2008.

[16] A. Chertock. On the stability of a class of self-similar solutions to the filtration-absorption equation. *Euro. Jnl of Applied Mathematics*, 13:179 – 194, 2002.

[17] A.J. Chorin and J.E. Marsden. *A Mathematical Introduction to Fluid Mechanics*. Springer-Verlag, 1980.

[18] R.V. Craster and O.K. Matar. Dynamics and stability of thin liquid films. *Rev. Mod. Phys.*, 81:1131–1198, 2009.

[19] J.A. Diez and L. Kondic. Computing three-dimensional thin film flows including contact lines. *J. of Comp. Phys.*, 183:274–306, 2002.

[20] A.D. Dussaud, O.K. Matar, and S.M. Troian. Spreading characteristics of an insoluble surfactant film on a thin liquid layer: Comparison between theory and experiment. *J. Fluid Mech.*, 544:23–51, 2005.

[21] B. Edmonstone, O.K Matar, and R.V. Craster. Coating of an inclined plane in the presence of insoluble surfactant. *Jnl of Coll. and Interface Sci.*, 287:261–272, 2005.

[22] B. Edmonstone, O.K. Matar, and R.V. Craster. Surfactant-induced fingering phenomena in thin film flow down an inclined plane. *Physica D*, 209(1–4):62 –79, 2005.

[23] B. Edmonstone, O.K. Matar, and R.V. Craster. A note on the coating of an inclined plane in the presence of soluble surfactant. *Jnl of Coll. and Interface Sci.*, 293:222 –229, 2006.

[24] B.D. Edmonstone, O.K. Matar, and R.V. Craster. Flow of surfactant-laden thin films down and inclined plane. *J. of Eng. Math.*, 50:141–156, 2004.

[25] G. Enhorning, A. Shennan, F. Possmayer, M. Dunn, C. Chen, and J. Milligan. Prevention of neonatal respiratory distress syndrome by tracheal instillation of surfactant: A randomized clinical trial. *Pediatrics*, 76(2):145–153, 1985.

[26] D.W. Fallest, C. Fox, A.M. Lichtenberger, and K.E. Daniels. Fluorescent visualization of a spreading surfactant. *New Journal of Physics*, 2010. (in print, preprint available at http://arxiv.prg/abs/0911/4160).

[27] M. Foda and R.G. Cox. The spreading of thin liquid films on a water-air interface. *J. Fluid Mech*, 101:33–57, 1980.

[28] D.P. Gaver and Grotberg J.B. Droplet spreading on a thin viscous film. *J. of Fluid Mech.*, 235:399 – 414, 1992.

[29] J.B. Gaver, D.P. Grotberg. The dynamics of a localized surfactant on a thin film. *J Fluid Mech.*, 213:127–148, 1990.

[30] A. Heryudono, R.J. Braun, T.A. Driscoll, K.L Maki, and L.P. Cook. Single-equation models for the tear film in a blink cycle: Realistic lid motion. *Math. Med. and Bio.*, 24:347–377, 2007.

[31] P. Howard and C. Hu. Pointwise green's function estimates toward stability for multidimensional fourth-order viscous shock fronts. *J. Diff. Eqns.*, 218:325 – 389, 2005.

[32] P. Howard and K. Zumbrun. Stability of undercompressive shock profiles. *J. Diff. Eqns.*, 225:308 – 360, 2006.

[33] H.E. Huppert. Flow and instability of a viscous current down a slope. *Nature*, 300(5891):427–429, 1982.

[34] O.E. Jensen. Self-similar, surfactant-driven flows. *Phys. of Fluids*, 6:1084 – 1094, 1994.

[35] O.E. Jensen and J.B. Grotberg. Insoluble surfactant spreading on a thin viscous film: Shock evolutions and film rupture. *J. Fluid Mech.*, 230:259–288, 1992.

[36] O.E. Jensen and J.B. Grotberg. The spreading of heat or soluble surfactant along a thin liquid film. *Phys. of Fluids*, 5:58–68, 1993.

[37] O.E. Jensen and S. Naire. The spreading and stability of surfactant-laden drop on a prewetted substrate. *J. Fluid Mech.*, 554:5 –24, 2006.

[38] J.M. Jerrett and J.R. de Bruyn. Fingering instability of a gravitationally driven contact line. *Phys. Fluids A*, 4(2):234 – 242, 1992.

[39] P. Joos and J. Pintens. Spreading kinetics of liquids on liquids. *Jnl of Coll. and Inter. Sci.*, 60(3):507 – 513, 1977.

[40] K. Karlsen and M. Ohlberger. A note on the uniqueness of entropy solutions of nonlinear degenerate parabolic equations. *J. Math. Anal. and Appl.*, 275:439–458, 2002.

[41] K. Karlsen and N. Risebro. On the uniqueness and stabiliry of entropy solutions of nonlinear degenerate parabolic equations with rough coefficients. *Dis. and Cont. Dyn. Sys.*, 9:1081–1104, 2003.

[42] P.E. King-Smith, B.A. Fink, K.K. Nichols, R.J. Braun, and G.B. McFadden. The contribution of lipid layer movement to tear film thinning and breakup. *Invest. Ophthal. Vis. Sci.*, 50:2747–2756, 2009.

[43] P.E. King-Smith, J.J. Nichols, K.K. Nichols, B.A. Fink, and R.J. Braun. Contributions of evaporation and other mechanisms to tear film thinning and break-up. *Optometry and Vision Science*, 85:623–630, 2009.

[44] S.N Kruzkov. First order quasilinear equations in several independent variables. *Math. USSR*, 10:217–243, 1970.

[45] R. LeVeque. *Finite Volume Methods for Hyperbolic Problems.* Cambridge University Press, 2002.

[46] R. LeVeque. *Finite Difference Methods for Ordinary and Partial Differential Equations.* SIAM, 2007.

[47] R. Levy and M. Shearer. The motion of a thin liquid film driven by surfactant and gravity. *SIAM J. Appl. Math.*, 66(5):1588 – 1609, 2006.

[48] R. Levy, M. Shearer, and T. Witelski. Gravity-driven thin liquid films with insoluble surfactant: Smooth traveling waves. *European J. Appl. Math.*, 18:679 – 708, 2008.

[49] E.N. Ludviksson, V. Lightfoot. The dynamics of thin liquid films in the presence of surface-tension gradients. *AIChE J.*, 17:1166–1173, 1971.

[50] K.L. Maki, R.J. Braun, T.A. Driscoll, and P.E. King-Smith. An overset grid method for the study of reflex tearing. *Math. Med. and Bio.*, pages 1–28, 2008.

[51] V. Manukian and S. Schecter. Travelling waves for a thin liquid film with surfactant on an inclined plane. *Nonlinearity*, 22(1):85 – 122, 2009.

[52] C. Marangoni. On the expansion of a drop of liquid floating on the surface of another liquid. *Tipographia dei fratelli Fusi, Pavia*, 1865.

[53] O.K. Matar and S.M. Troian. Spreading of a surfactant monolayer on a thin liquid film: Onset and evolution of digitated structures. *Chaos: An Interdisciplinary Journal of Nonlinear Science*, 9(1):141 – 153, 1999.

[54] S. McLaughlin. The electrostatic properties of membranes. *Annual Review of Biophysics and Biophysical Chemistry*, 18:113–136, 1998.

[55] T.A. Merrit, M. Hallman, B.T. Bloom, C. Berry, K. Benirschke, D. Sahn, T. Key, D. Edwards, A.L. Jarvenpaa, M. Pohjavuori, K. Kankaanpaa, M. Kunnas, H. Paatero, J. Rapola, and J. Jaaskelainen. Prophylactic treatmeant of very premature infants with human surfactant. *The New England Journal of Medicine*, 315:785–790, 1986.

[56] A. Münch and A.L. Bertozzi. Rarefaction - undercompressive fronts in driven films. *Physics of Fluids*, 11(10):2812 – 2814, 1999.

[57] T.G. Myers. Thin films with high surface tension. *SIAM Review*, 40(3):441–462, 1998.

[58] S.E. Orchard. Surface levelling in viscous liquids and gels. *Appl. Sci. Res. A*, 11:451–464, 1962.

[59] S.H. Oron, A. Davis and S.G. Bankoff. Long-scale evolution of thin liquid films. *Rev. Mod. Phys.*, 69:931–980, 1997.

[60] E. Peterson, M. Shearer, T. Witelski, and R. Levy. Stability of traveling waves on thin liquid films driven by gravity and surfactant. *Proceedings, 12th International Conference on Hyperbolic Problems: Theory, Numerics, Applications*, 67:855–867, 2009.

[61] A. Pockels. Surface tension. *Nature*, 43(1115):437–439, 1891.

[62] M. Renardy. On an equation describing the spreading of surfactants on thin films. *Nonlinear Analysis, Theory, Methods and Applications*, 26:1207–1219, 1996.

[63] M. Renardy. A singularly perturbed problem related to surfactant spreading on thin films. *Nonlinear Analysis, Theory, Methods and Applications*, 27:287–296, 1996.

[64] M. Renardy. A degenerate parabolic-hyperbolic system modeling the spreading of surfactants. *SIAM J. Math. Anal.*, 28:1048–1063, 1997.

[65] M. Renardy and R.C. Rogers. *An Introduction to Partial Differential Equations*. Springer-Verlag, 2004.

[66] O. Reynolds. An experimental investigation of circumstances determine whether the motion of water shall be direct or sinuous, and of the law of resistance in parallel channels. *Philosophical Transaction of the Royal Society of London*, 174:935–982, 1883.

[67] E.K. Sakata and J.C. Berg. Surface diffusion on monolayers. *Industrial and Engineering Chemistry Fundamentals*, 8:570–575, 1969.

[68] M. Schneemilch and A.M. Cazabat. Shock separation in wetting films driven by thermal gradients. *Langmuir*, 16:9850 – 9856, 2000.

[69] J.B. Segur and H.E. Oberstar. Viscosity of glycerol and its aqueous solutions. *Industrial and Engineering Chemistry*, 43(9):2117–2120, 1951.

[70] D. Serre. *Systesm of Conservation Laws 1: Hyperbolicity, Entropies, Shock Waves*. Cambridge Univeristy Press, 1999.

[71] A. Sheludko. *Colloid Chemistry*. Elsevier, 1966.

[72] N.P.D. Smith, S.E. Orchard, and A.J. Rhind-Tutt. The physics of brush marks. *J. Oil Col. Chem. Assoc.*, 44:618–633, 1961.

[73] H.A. Stone. A simple derivation of the time-dependent convective-diffusion equation for surfactant transport along a deforming interface. *Physics of Fluids A*, 2:111–112, 1990.

[74] J. Sur, A.L. Bertozzi, and R.P. Behringer. Reverse undercompressive shock structures in driven thin film flows. *PRL*, 90(12), 2003.

[75] L.H. Tanner. The spreading of silicone oil drops on horizontal surfaces. *J. Phys. (D)*, 12:1473 – 1484, 1979.

[76] J. Thomson. On certain curious motions observable at the sufaces of wine and other alcoholic liquors. *Philos. Mag.*, 10:330, 1855.

[77] S.M. Troian, E. Herbolzheimer, and S.A. Safran. Model for the fingering instability of spreading surfactant drops. *PRL*, 65(3):333 – 336, 1990.

[78] S.M. Troian, X.L. Wu, and S.A. Safran. Fingering instability in thin wetting films. *PRL*, 62(13):1496 – 1500, 1989.

[79] J.L. Vazquez. *The Porous Medium Equation: Mathematical Theory*. Oxford Science Publications, 2007.

[80] M.R.E. Warner, R.V. Craster, and O.K. Matar. Fingering phenomena created by a soluble surfactant deposition on a thin liquid film. *Phys. of Fluids*, 16(8):2933–2951, 2004.

[81] M. Wulf, S. Michel, K. Grundke, O.I. del Rio, D.Y. Kwok, and A.W. Neumann. Simultaneous determination of surface tension and density of polymer melts using axisymmetric drop shape analysis. *Journal of Colloid and Interface Science*, 210(1):172–181, 1999.